RESPONSE OF ULTRA-THIN CONTINUOUSLY REINFORCED CONCRETE PAVEMENT TO TRAFFIC LOADING

M.S. SMIT

RESPONSE OF ULTRA-THIN CONTINUOUSLY REINFORCED CONCRETE PAVEMENT TO TRAFFIC LOADING

MARTHA SOPHIA SMIT

A thesis submitted in partial fulfilment of the requirements for the degree of

PHILOSOPHIAE DOCTOR (ENGINEERING)

in the

FACULTY OF ENGINEERING, BUILT-ENVIRONMENT AND INFORMATION TECHNOLOGY

UNIVERSITY OF PRETORIA

APRIL 2020

ABSTRACT

RESPONSE OF ULTRA-THIN CONTINUOUSLY REINFORCED CONCRETE PAVEMENT TO TRAFFIC LOADING

M.S. SMIT

Supervisor: Professor E.P. Kearsley

Department: Civil Engineering

University: University of Pretoria

Degree: Philosophiae Doctor (Engineering)

Ultra-Thin Continuously Reinforced Concrete Pavement (UTCRCP) is an innovative pavement type that has the potential to fulfil South Africa's pavement repair strategy requirements. It consists of a 50 mm thick High Strength Steel Fibre Reinforced Concrete (HS-SFRC) layer that is reinforced with 50 x 50 mm aperture steel bar mesh, placed on a newly constructed or rehabilitated pavement. The current design procedure for UTCRCP was extrapolated from conventional concrete design procedures, incorporating the improved flexural properties of the HS-SFRC to design for fatigue cracking. However, the alternative nature of the thin HS-SFRC layer in comparison to a thick normal strength concrete layer has led to the proposal that the response of UTCRCP to traffic loading should be reconsidered to improve its design approach.

A literature study revealed that the wheel load configuration, the relative stiffness of the concrete layer and its foundation and the complex response of foundation materials to stress influence the response of pavements to traffic loading. The effect of these aspects was investigated by making use of scaled physical modelling, as well as Finite Element (FE) modelling that incorporated Linear Elastic (LE) and advanced material models.

The effect of load configuration on thin asphalt and thin concrete layers was investigated using LE FE modelling. A three-layer system of bound layer, base and subgrade was modelled. It was found that the response of a thin concrete layer is similar to that of a thin asphalt layer subjected

to axle loading in that the maximum deflection is at the load location and that a hogging type deflection is induced in the axle centreline. The stress induced at the top of the concrete layer due to this hogging moment was high, indicating the necessity of including significant steel in both the transverse and longitudinal directions of UTCRCP. The difference in substructure response (in terms of horizontal and vertical displacement), modelled using single wheel or axle loading, showed that the compression of the substructure in the axle centreline can be critical, while it is ignored when load configurations are simplified to single wheel loading.

A multivariable analysis of the concrete layer thickness and base material stiffness was conducted using LE FE modelling. A similar three-layer system of bound layer, base and subgrade was used. It was found that the location of the maximum deflection is in the axle centreline for pavements incorporating thick concrete layers, while the maximum deflection is in the wheel centreline for pavements incorporating thin concrete layers. The response of thin concrete pavements was more dependent on the substructure.

The physical modelling consisted of 1:10 scale models tested in a geotechnical centrifuge. The models consisted of either thick concrete layer or thin concrete layer on compacted dry sand, as well as a thin concrete layer on a cement stabilized base supported by compacted dry sand. The most notable finding was that a rut forms in the wheel path of thin concrete layers on sand, although it cannot be observed from the surface. It was observed that the concrete layer rebounds when the pavement is unloaded, forming a gap between the concrete layer and substructure.

An advanced material model for sand was used to explore the effect of incorporating the stress-dependent, elasto-plastic behaviour of granular materials in UTCRCP. A FE model, similar to the three-layer system of the LE FE modelling, was used and the base layer was modelled using a soil model called Nor-Sand, which is based on the critical state framework. The initial void ratio, lateral earth pressure at-rest and overconsolidation ratio were varied. It was found that the combination of the strain hardening and the stress dependence of the elastic material stiffness resulted in higher induced stresses close to the load location. The gap formation observed during the physical modelling was confirmed by the capability of Nor-Sand to model permanent deformation.

Overall, the results of this investigation indicate that the response of UTCRCP to traffic loading differs significantly from that of rigid concrete pavements. The thin HS-SFRC layer is subjected to high tensile stresses and deflects significantly into the substructure at the load location. It is proposed that UTCRCP should be designed to limit rutting, as well as that stress dependent, elasto-plastic material models should be used to optimize its layer arrangement.

ACKNOWLEDGEMENTS

I wish to express my appreciation to the following persons that made this project possible:

- My supervisor, Prof Elsabé Kearsley, for her advice, guidance, enthusiasm and patience throughout the course of my PhD studies.
- Prof Ashraf Osman, for his support during my exchange at Durham University and continued guidance in numerical modelling and geotechnical aspects.
- Prof S.W. Jacobsz, for his valuable input on this document and other papers and presentations on the research done for this study.
- Prof James Maina, for always having an open door when I had questions related to pavement engineering practice, modelling and testing.
- The technical staff at the University of Pretoria, especially Johan Scholtz and Derek Mostert, for their assistance during the physical modelling stage of this study.
- Dylan Armfield, for configuring my computer to run user subroutines in ABAQUS and teaching me that you can do almost anything with a computer if you are patient.
- My Head of Department, Prof Wynand Steyn, and colleagues for supporting me to finish my studies while being employed at the University of Pretoria.

I also wish to acknowledge the following organisations that funded parts of my PhD studies:

- The Southern Africa Research Conference, for their generous study bursary.
- The Newton Fund UK (Grant ES/N013905) for supporting the PhD exchange between University of Pretoria and Durham University.
- The Knowledge Interchange and Collaboration funding of the National Research Fund which made it possible for me to attend international conferences.

The number of full-time post-graduates at the Department of Civil Engineering at UP grew from four students during the first year of my Masters to approximately 40 students in 2020. It has been a privilege to be part of this growth and a joy to interact with intelligent and motivated peers. I would like to thank Ione Loots, Hendrik Louw, Stuart Hofmeyr, Megan Weyers, Paul le Roux and Tiago Gaspar, in particular, for their encouragement and regular tea breaks.

I would also like to thank my friends, old and new, and my family. Hopefully we can be together to celebrate the end of this phase of my career soon.

TABLE OF CONTENTS

LIST OF TABLES

PAGE

LIST OF FIGURES

PAGE

NOMENCLATURE

List of Symbols

Symbol	Description	Units
	Stress related symbols	
$\sigma_1, \sigma_2, \sigma_3$	Principal stresses	Pa
σ_h	Horizontal stress/pressure	Pa
σ_v, σ_z	Vertical stress/pressure	Pa
p'	Mean effective principal stress	Pa
q	Deviator stress/applied stress	Pa
p'_0	Initial mean effective principal stress	Pa
q_r	Repeated deviator stress	Pa
θ	Bulk stress	Pa
η	Stress ratio $\left(=\frac{q}{p'}\right)$	
K_0	Coefficient of lateral earth pressure at-rest	
	Strength related symbols	
φ'	Effective angle of friction	°
φ'_{max}	Maximum effective friction angle	°
σ_b	Flexural strength	Pa
σ_c	Unconfined compressive strength	Pa
	Material stiffness property related symbols	
E_{BL}	Young's modulus of bound layer	Pa
E_c	Young's modulus of concrete	Pa
E_p	Young's modulus of pipe	Pa
E_r	Resilient modulus	Pa
E_s	Young's modulus of soil	Pa
G	Shear modulus	Pa
G_r	Resilient shear modulus	Pa
K_B	Bulk modulus	Pa
k	Modulus of subgrade reaction	N/m^3
ν_c	Poisson's Ratio of concrete	
ν_s	Poisson's Ratio of soil	

Dimensional symbols		
a	Radius of circular load	m
d	Footing thickness	m
l	Footing length	m
h	Concrete layer thickness	m
h_1	Thickness of structural layer	m
i	Trough width parameter (or distance from maximum settlement to inflection point)	m
I_{BL}	Moment of Inertia of bound layer	m^4
I_p	Moment of Inertia of pipe	m^4
r_0	Outer radius of pipe	m
S_{max}	Maximum settlement	m
S_v	Vertical soil settlement	m
V_s	Volume of solids	m^3
V_v	Volume of voids	m^3
x	Distance from load location or maximum deflection	m
z	Depth	m
δ	Deflection	m

Regression coefficient symbols	
C	Regression coefficient
K, K_1, K_2, K_3	Regression coefficient
m	Regression coefficient
n	Regression coefficient

Relative stiffness descriptors		
K_s	Foundation system stiffness	
l_k	Radius of relative stiffness for spring foundations	m
l_e	Radius of relative stiffness for elastic foundations	m
R	Relative rigidity factor	

Response surface methodology symbols	
α	Distance from centre point to axial point
y	Response
$\beta_0, \beta_A, \beta_B, \beta_{AB}, \beta_{AA}, \beta_{BB}$	Regression coefficient

x_A, x_B	Independent variables
$x_A x_B$	Interaction effect between variables
x_A^2, x_B^2	Quadratic effect of a single variable
ϵ	Observed noise/error
y'	Transformed response
t	Transformation constant
Λ	Power transformation value

Nor-Sand material input parameter symbols	
M	Critical stress ratio in triaxial compression
e_{max}	Maximum void ratio
e_{min}	Minimum void ratio
A	Shear modulus constant
n	Pressure exponent
ν	Poisson's Ratio of sand
N	Flow rule value
h	Plastic hardening modulus
χ	Maximum dilatancy coefficient

Nor-Sand theory symbols	
Γ	Critical void ratio at 1 kPa cut-off
λ	Slope of CSL in $\ln p - e$ space.
ψ	State parameter

Other symbols		
e	Void ratio	
γ	Unit weight	N/m^3
ε	Strain	m/m
μ	Coefficient of friction	
υ	Specific volume	

List of Abbreviations

ANOVA	Analysis of Variance
APT	Accelerated Pavement Testing
BL	Bound Layer

CCD	Central Composite Design
CL	Centreline
CPT	Centrifuge Pavement Tester
CSL	Critical State Line
DIC	Digital Image Correlation
FE	Finite Element
GLM-ANOVA	General Linear Model Analysis of Variance
HS-SFRC	High Strength Steel Fibre Reinforced Concrete
HVS	Heavy Vehicle Simulator
ITS	Indirect Tensile Strength
JDMD	Joint Deflection Measurement Device
LE	Linear Elastic
LVDT	Linear Variable Differential Transducer
MDD	Multi Depth Deflectometer
MEPD	Mechanistic-Empirical Pavement Design
MLLE	Multi-Layer Linear Elastic
NCL	Normal Consolidation Line
NSC	Normal Strength Concrete
OCR	Overconsolidation ratio
S/C	Swelling/Compression
S-N	Stress level – fatigue life
SFRC	Steel Fibre Reinforced Concrete
SW	Single wheel
UCS	Unconfined Compressive Strength
UTCRCP	Ultra-Thin Continuously Reinforced Concrete Pavements
VDD	Vertical Displacement Distribution
2D	Two-dimensional
3D	Three-dimensional

1 INTRODUCTION

1.1 BACKGROUND

Cracking, which is caused by environmental and traffic loading, is the principle failure mechanism of concrete pavements. Wide, uncontrollable cracks allow the ingress of moisture which results in loss of support. These cracks also change the stress distribution in the concrete slab of a concrete pavement and its substructure (Huang, 1993). Cracks form when the tensile stress exceeds the tensile strength of the concrete surface layer. Different concrete pavement types have been developed to accommodate these stresses and prevent wide, uncontrollable cracks.

In concrete members, thermally induced tensile stress can be significant. Thermally induced stresses are controlled by limiting the effective length of concrete slabs. This resulted in the development of Jointed Concrete Pavements (JCP). Most failures in JCP are related to the joints, which also need to be sealed regularly to prevent moisture from entering the substructure. The approach of Continuously Reinforced Concrete Pavements (CRCP) is to eliminate these joints and introduces longitudinal steel reinforcing to control crack widths thus preventing moisture ingress. The predominant distress type in CRCP is edge punchout, which occurs when the interlock and support at transverse cracks had deteriorated and longitudinal cracks start forming due to traffic loading (Huang, 1993).

Ultra-Thin Continuously Reinforced Concrete Pavement (UTCRCP) consists of a 50 mm High Strength Steel Fibre Reinforced Concrete (HS-SFRC) overlay that is cast continuously. The concrete overlay is additionally reinforced with 5.7 mm diameter, 50 x 50 mm welded deformed steel bar mesh. As with CRCP, UTCRCP eliminates potential problems with joints due to its continuous nature. The steel mesh and HS-SFRC controls crack widths, preventing moisture ingress. It also provides superior post-crack carrying capacity which mitigates failures typical of CRCP, such as edge punchout. HS-SFRC also makes it possible to reduce the concrete slab thickness reducing the volume of material required (Briggs *et al.*, 2016).

The thin, heavily reinforced HS-SFRC overlay is placed on pavement systems that require rehabilitation or forms part of a new pavement system. The design methodology of UTCRCP was extrapolated from conventional concrete pavement design methodology where concrete layer thickness is typically greater than 150 mm (SANRAL, 2013). The applicability of conventional concrete pavement design methodology to the innovative pavement system has been questioned in the past. The main critique, and focus, being that the fracture of HS-SFRC should be modelled more accurately to predict the system's performance (Denneman, 2011;

Elsaigh, 2007). This focus in terms of UTCRCP and HS-SFRC agrees with the statement by Ioannides (2006) that fracture mechanics is one of the future directions of concrete pavement research and design.

Less attention has been given to the effect of the reduced flexural stiffness of the thin HS-SFRC layer of UTCRCP in comparison to the relatively thick Normal Strength Concrete (NSC) layer of conventional concrete pavements and how this should inform the UTCRCP design approach. The principal traffic associated failure mechanism of conventional concrete pavement is fatigue cracking of the concrete layer. Rutting is not considered as a traffic associated failure mechanism for conventional concrete pavements and the response of the substructure to traffic loading is considered unimportant as long as the variability of the substructure is limited. During the mechanistic analyses of conventional concrete pavement, the substructure is often reduced to an array of springs and complex load configurations are usually ignored with the load location on the concrete slab being of greater importance.

The alternative nature of UTCRCP, with its very thin HS-SFRC layer that has a high material stiffness and ductility, leads to the proposal that its response to traffic loading should be reconsidered. The response of UTCRCP to traffic loading should be investigated by focussing on the effect of load configuration, relative stiffness of the concrete layer and substructure, and the substructure behaviour.

1.2 STUDY OBJECTIVES

The objective of this study is to determine the response of UTCRCP to traffic loading by considering load configuration, relative stiffness of the concrete layer and substructure, as well as the stress-dependent, elasto-plastic behaviour of granular materials. The aspects considered were selected to allow a broad understanding of the response of UTCRCP to be developed in the context of conventional (flexible or rigid) pavement types.

The pavement response was investigated by considering the overall pavement response as well as the substructure response. The overall pavement response was not only described by selected critical parameters (vertical displacement, stress and strain in the concrete layer and substructure in the wheel centreline) but also the transverse and longitudinal deflection bowls, while the substructure response was described by a range of parameters such as vertical displacement, horizontal displacement and material stiffness contour plots.

Secondary aims included determining the effect of:

- relative layer stiffness and load configuration on road pavement response modelled using Linear Elastic (LE) Finite Element (FE) modelling,
- relative stiffness and load configuration on road pavement response modelled using results from centrifuge modelling, and
- incorporating advanced material models for soil in the FE modelling of road pavements and comparing it to the response modelled using linear elasticity and centrifuge modelling.

The secondary aims were selected to build on each other allowing a more thorough understanding of the response of UTCRCP to traffic loading. Investigating pavement response using LE FE modelling gives an indication of the response that may be observed from the centrifuge modelling. The LE FE modelling also gives a reference for comparison to conventional structural analyses methods when the advanced materials model is implemented in a FE model with a similar geometry. Using the advanced material model for soil enables the researcher to develop a more thorough understanding of the response observed from the centrifuge testing.

1.3 SCOPE OF STUDY

In this study the response of UTCRCP to traffic loading was investigated considering load configuration, relative layer stiffness and the stress-dependent, elasto-plastic behaviour of granular materials. A combination of centrifuge modelling and FE modelling that incorporated linear elasticity and advanced material models were used.

The study was limited in the following ways:

- Cyclic loading and principal stress rotation were not included in the FE modelling of the road pavement. The FE pavement models were simply subjected to a pressure over an area.
- Variation in the magnitude of loading, overloading and wander were not considered.
- Interaction at the wheel-pavement surface interface, as well as the shape of the load area, fell outside the scope of this study.
- Interlayer interaction of the bound layers and the base (or substructure) was not considered.
- The effect of cracking of HS-SFRC layers on pavement response was not considered.
- Centrifuge models were subjected to a limited number of cyclic loads, and the pavement response up to only 60 load cycles was discussed in this thesis.

- For the centrifuge modelling and advanced soil material modelling part, the behaviour of thin concrete layers on dry sand was investigated. Granular materials typically used in pavements were not considered.
- The intention of the study was to improve the understanding of UTCRCP and not to optimize the design or develop design guidelines.
- Partially saturated subgrade and granular materials commonly occur in pavements, as well as the behaviour of partially saturated soils in terms of effective stress is not yet completely understood. The effect of partially saturated soils falls outside the scope of this study.

1.4 METHODOLOGY

The following methodology was implemented to investigate the response of UTCRCP to traffic loading:

- A literature study was conducted where the pavement design philosophy for flexible and rigid pavements, the response of pavement substructure to traffic loading and structural analyses of pavements were explored. Background of UTCRCP was given and previous research relevant to this project was reported. Cement stabilization of granular materials and its potential use in UTCRCP were discussed. The effect of load configuration and concepts of relative stiffness and soil-structure interaction was explored. Questions related to the pavement design and practical application of UTCRCP were identified.
- The effect of relative stiffness and load configuration were investigated using LE FE modelling. This was done in the following sequence:
  a) Comparing the effect of single wheel and axle load configurations on thin asphalt and thin concrete pavement models.
  b) Comparing the response of a thin concrete pavement subjected to load over a circular area and strip loading.
  c) Comparing the deflected shapes of slabs-on-grade determined from beam-on-elastic support equations for different bound layer-support condition combinations.
  d) Conducting a parametric study where the concrete layer thickness and base material stiffness were varied simultaneously.
  e) Considering the effect of cement stabilized base layers in pavements with ultra-thin concrete layers.
  f) Exploring deflection bowl inflection points as wheel load interaction indicators for different relative stiffnesses

- Centrifuge modelling was used to compare the response of pavements that incorporate ultra-thin HS-SFRC bound layers, thick normal strength concrete layers and cement stabilized bases. Variations of axle loading were applied using either strip loading or an axle with rolling wheels. Cyclic loading was applied, and vertical displacement was used to monitor the pavement response. The results of the centrifuge modelling were processed, analysed and discussed per load application method.
- The effect of incorporating a stress-dependent, elasto-plastic material model based on the critical state framework in FE modelling of pavements was determined. This was done in two phases. In the first phase the effect of modelling the base as a sand, using the Nor-Sand model, was explored by varying the initial void ratio, coefficient of lateral earth pressure at-rest and overconsolidation ratio. In the second phase, the Nor-Sand material input parameters were determined for the sand used in the centrifuge modelling and the measured pavement response was compared to the numerically modelled pavement response.
- Conclusions were made regarding the aims of the study and the practical applications questions were answered. Recommendations for future research were also made.

1.5 ORGANIZATION OF REPORT

This thesis document comprises of several chapters which include:

Chapter 1 that serves as an introduction to the report.

Chapter 2 contains a summary of literature relevant to this study.

In Chapter 3 the LE FE and other numerical models used to investigate relative stiffness and load configuration are described. The chapter also contains the results and discussion of the respective numerical models.

Chapter 4 contains the LE FE analyses performed to investigate the effect of relative stiffness on concrete pavements. Both the concrete thickness and base material stiffness were varied in this parametric study.

In Chapter 5 the centrifuge modelling conducted to investigate the response of concrete layers on compacted sand is described. The chapter described the experimental setup of the strip loading and rolling wheel loads models. Properties of materials used in the physical models are given. The measured pavement response is presented and discussed.

In Chapter 6 the stress-dependent, elasto-plastic material model based on the critical state framework, Nor-Sand, was used to determine the effect of more representative soil material models on FE modelling results. A brief overview of the constitutive model's capabilities, material input parameters, model input parameters and use in ABAQUS/Standard (Dassault Systemes Simulia Corp, 2016) was given. The effect of the model input parameters was used to explore the effect of the incorporation of an advanced soil materials model.

In Chapter 7 the measured response obtained during the centrifuge modelling was compared to that modelled using Nor-Sand. The material model was first calibrated to fit the stress-strain response measured using triaxial testing to determine the material input parameters.

Chapter 8 consists of the conclusions made from the results of this study. Recommendations are given for the design and application and future research of UTCRCP.

2 LITERATURE REVIEW

2.1 INTRODUCTION

In this chapter background is given on the design of road pavements. The reduced thickness of the concrete layer in UTCRCP, results in the substructure having a greater influence on the pavement behaviour. Aspects of the soil mechanics of pavements are discussed and an introduction to the critical state framework is given. The structural analysis of road pavements is explored.

Background is given on UTCRCP and HS-SFRC, along with an overview of previous research on UTCRCP deemed relevant to this project. The numerical modelling of the pavement substructure is discussed. The potential use of cement stabilized granular materials in UTCRCP is recognized and mechanical properties are given. The effect of load configuration on pavement response, considering wheel and axle arrangements, is discussed. Load configurations used for physical modelling of road pavements is summarised. Plane strain simplification of road pavements is also considered.

The concepts of soil-structure interaction and relative stiffness in a variety of civil engineering systems, including road pavements, are discussed. Background is given on the use of deflection bowls in pavement engineering. The chapter is concluded with a summary of the most important aspects discussed.

2.2 PAVEMENT DESIGN

Pavements consist of a system of layers of unbound and bound materials placed on each other and supported by the subgrade (Huang, 1993). The purpose of pavements is to allow wheeled vehicles to operate safely (Brown & Selig, 1991). Werkmeister *et al.* (2004) summarised that pavement design is a process intended to find the most economical combination of layer thickness and material types for pavements, considering the properties of the subgrade and the environmental and traffic loading during the service life of the road.

Although environmental loading has a significant influence on pavement performance, the focus of this study is on design to prevent traffic associated failure mechanisms: differential vertical deformation (rutting) and fatigue cracking (Brown & Selig, 1991). Pavements can be simplified to a stiff layer on top of a less stiff layer. When a load is applied to the simplified system, the less stiff layer supports the stiff layer and reduces the horizontal tensile stresses that manifest at the bottom of the stiff layer. Simultaneously, the stiff layer protects the less stiff

layer from high vertical compressive stresses. The vertical compressive stress that manifests at the top of the less stiff layer and the horizontal tensile stress that manifests at the bottom of the stiff layer are considered to be critical stresses (Brown & Selig, 1991). Design to prevent traffic associated failure mechanisms is an optimization to minimize these critical stresses (Huang, 1993).

The uppermost layer of pavements usually consists of a bound material such as asphalt or concrete. The subbase and subgrade are considered as the foundation layers of pavements. The system of layers placed on the foundation is considered to be the structural layer of pavements (Brown & Selig, 1991). Broadly there are two types of pavement, flexible and rigid pavement. Typically, concrete pavements are deemed to be rigid pavement and asphalt pavements are deemed to be flexible pavement.

Figure 2.1 shows the division between the structural and foundation layers of conventional flexible and rigid pavements. For the purposes of this study, the substructure of a pavement refers to all layers underneath the uppermost layer. The uppermost layer is typically a bound layer of asphalt or concrete. The concrete layer of rigid pavements is structurally dominant, and it is usually assumed that as long as variability in the substructure is limited, the substructure's properties can largely be ignored (Brown & Selig, 1991). The asphalt layer is not as structurally dominant as concrete. The typical design approach for flexible pavements is that stress exerted on the surface is spread gradually with depth through layers of materials that become weaker further from the surface. Pavements that incorporate this approach of gradual load spreading, and layer strength reduction, with depth are referred to as balanced pavements.

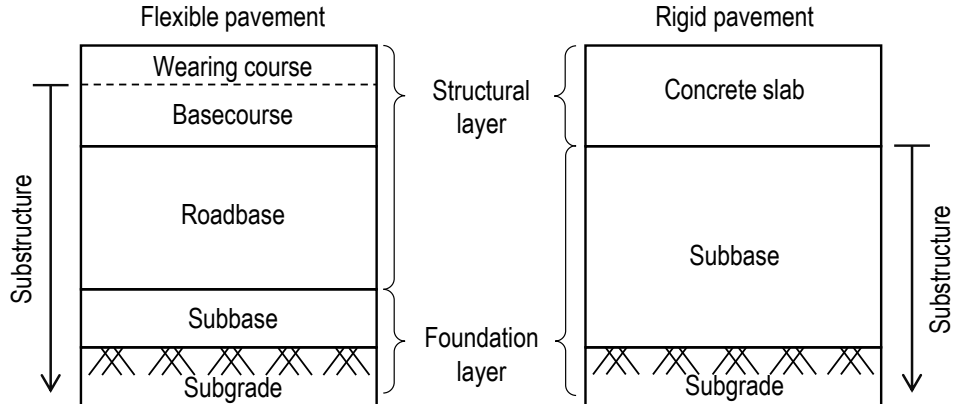

Figure 2.1 Structural and foundation layers, and substructure, of flexible and rigid pavements (adapted from O'Flaherty (1967))

In terms of traffic associated failure mechanisms, fatigue cracking is considered for rigid pavement, while rutting is ignored. Fatigue cracking and rutting are considered for flexible pavement.

2.3 RESPONSE OF PAVEMENT SUBSTRUCTURE TO TRAFFIC LOADING

The substructure of a pavement consists of one or more layers of stabilized granular material over subgrade soil. The stabilized pavement layers are bound and unbound granular layers. Loading of the substructure of pavements is a soil mechanics problem and effective stress conditions dictate pavement response to traffic loading. The stress conditions and effect of applied stress change throughout the course of the pavement life. Broadly, there are four stress phases throughout pavement life: construction, initial loading, service phase and failure. The main stress characteristics of pavement substructures are low effective stresses and repeated loading pulses well below yield (Brown & Selig, 1991).

The effective stress conditions of a pavement structure are dependent on the same factors than any soil mechanics problem. The vertical effective stress is dependent on the weight above the layer (or soil element) in question and the water table position, while the vertical effective stress and the coefficient of lateral earth pressure at-rest are used to determine the horizontal effective stress. A relationship exists between the overconsolidation ratio (OCR) and the coefficient of lateral earth pressure at-rest (K_0). The relationship between K_0 and the OCR of subgrade has been investigated and reported by Mayne & Kulhawy (1982). The relationship between K_0 and the OCR of subgrade and granular material that have been remoulded and stabilized by compaction is more complex and has been investigated by Duncan & Seed (1987), Duncan *et al.* (1991) and Chen & Fang (2008).

Pavement elements are subjected to complex stress conditions under moving wheel loads (Brown, 1996). Figure 2.2 illustrates the general stress regime experienced by a pavement element within the plane of a wheel track. There is a vertical and horizontal stress pulse as a wheel moves over the element, which is accompanied by a double pulse of shear stress with a sign reversal in the vertical and horizontal plane. This type of loading is referred to as principal stress rotation.

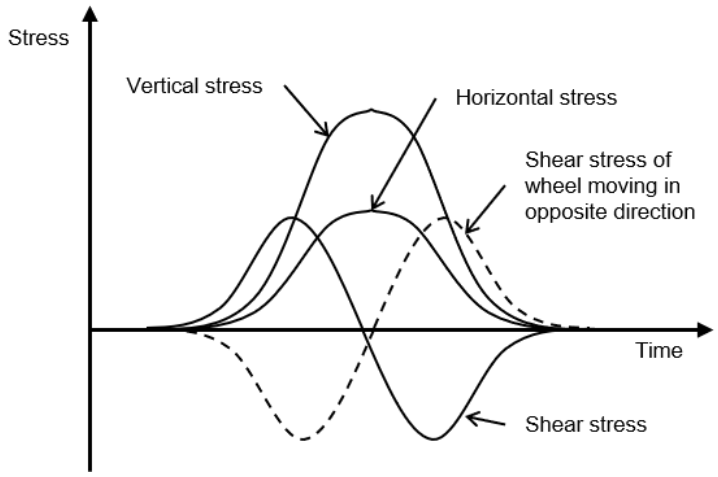

Figure 2.2 Variation of stresses with time (Brown, 1996)

Partially saturated subgrade and granular materials commonly occur in pavements and the behaviour of partially saturated soils in terms of effective stress is not yet completely understood. The effect of partially saturated soils falls outside the scope of this study.

2.3.1 Compaction, overconsolidation and lateral earth pressure at-rest

Initial stress conditions in a pavement substructure before initial loading determines pavement performance. The initial stress conditions are influenced by a range of factors. The initial stress conditions in the subgrade depend on whether the pavement is built in cut or on fill, construction traffic and stabilisation. The initial stress conditions of the granular layers depend on construction traffic and stabilisation.

During construction, the subgrade and the layers of granular materials that are placed on the subgrade, are compacted to obtain higher shear strength and reduce compressibility (Craig, 2004). The effect of compaction on the lateral earth pressure at-rest is analogous to overconsolidation (Brown, 1996). Lateral stresses accumulate in the granular layers and the coefficient of earth pressure at-rest $\left(K_0 = \frac{\sigma_h}{\sigma_v}\right)$ can be greater than 1. The degree of compaction and the lateral earth pressure at-rest are interdependent and has an influence on the behaviour of the pavement.

Compaction is a form of mechanical stabilisation. The purpose is to increase the density of soil by packing its particles closer and expelling air. Shear strength is increased by compaction and compressibility decreased. There is no significant change in water content during compaction. Consolidation is the process of dissipation of excess pore water pressure that is accompanied by an increase in effective stress and reduction in volume. Overconsolidation occurs when the maximum value of effective stress (termed the pre-consolidation stress) in the past has been

greater than the present value (Craig, 2004). Overconsolidation is measured using the overconsolidation ratio (OCR), which is the ratio of the maximum stress to the current stress.

Both consolidation and compaction result in a reduced volume. In both cases the reduction in volume is achieved by raising the effective stress. When the source of higher effective stress is removed, both soil elements are in a state of overconsolidation. In the case of pavement layers that have been compacted, the effect is referred to as apparent overconsolidation (Brown & Selig, 1991) and compaction represents a form of overconsolidation (Duncan & Seed, 1987).

Mayne & Kulhawy (1982) showed that K_0 for an overconsolidated clay or sand can be estimated from the OCR and effective angle of friction (φ') using Equation 2.1. Upon reloading of the soil, the relationship becomes more complex and incorporates regression coefficients.

$$K_0 = (1 - \sin\varphi')OCR^{\sin\varphi'} \qquad \textbf{Equation 2.1}$$

Chen & Fang (2008) measured the vertical and lateral earth pressure in air-dry Ottowa sand compacted in a rigid 1.5 x 1.5 x 1.6 m soil bin. The sand was compacted in 300 mm layers. They concluded that the effect of vibratory compaction on vertical pressure is negligible and that the relationship of $\sigma_v = \gamma z$ is adequate. They also compared the measured results with the relationships of lateral earth pressure with depth due to compaction proposed by Broms (1971), Duncan & Seed (1987) and Duncan *et al.* (1991). It was concluded that the lateral earth pressure can be taken as assuming passive conditions to a depth of 300 mm and then reduce to the relationship of $K_0 = 1 - \sin\varphi'$ (Jaky's equation (Craig, 2004)) at a depth of 850 mm.

An apparent OCR would be in the range of 2 to 5 in oedometer tests for compacted fill (Brown & Selig, 1991). K_0 and OCR can be back-calculated by matching deflection bowls and making use of multi-objective inverse analyses (Levenberg & Garg, 2014). Additional information required to back-calculate K_0 and OCR included the measured stress of the instrumented pavement and the resilient moduli of granular materials. In the study by Levenberg & Garg (2014) an OCR value of 27 was determined for the subbase and 207 was determined for base. These values fall outside the range for which Equation 2.1 can be used. In the study it was found that K_0 decreased from top to bottom from 7.5 to 1.8 for subbase with a thickness of 925 mm. The estimated K_0 value for the base layer was 13. Initial stress conditions do not affect linear-elastic modelling and typically K_0 for stress-dependent material behaviour is assumed to be 1 (Brown, 1996).

2.3.2 The critical state framework and traffic loading

The behaviour of soils is best explained within the critical state framework. Craig (2004) summarised that the critical state concept *"... relates the effective stresses and corresponding specific volume of clay during shearing under drained or undrained conditions, thus unifying the characteristics of shear strength and deformation"*. The concept demonstrates that all possible states of soil exist within a characteristic surface. In other words, normally consolidated and overconsolidated specimens tested in drained or undrained conditions fall within the surface. A thorough description of critical state soil mechanics can be found in The Mechanics of Soils by Atkinson & Bransby (1978). Models based on the critical state framework were initially developed for saturated clay but have since been extended for soils other than clay and even to partially saturated conditions (Fern *et al.*, 2016; Jefferies, 1993).

The stress parameters used in the critical state framework are the mean effective principal stress (p') and deviator stress (q), which are determined using Equation 2.2 and Equation 2.3.

$$p' = \frac{1}{3}(\sigma'_1 + 2\sigma'_3) \qquad \textbf{Equation 2.2}$$

$$q = (\sigma'_1 - \sigma'_3) \qquad \textbf{Equation 2.3}$$

Specific volume (v), or void ratio (e), are the parameters used to describe volumetric behaviour. Equation 2.4 shows the relationship between specific volume and void ratio, as well as volume of voids (V_v) and volume of solids (V_s).

$$v = 1 + e = 1 + \frac{V_v}{V_s} \qquad \textbf{Equation 2.4}$$

Figure 2.3 (a) shows the characteristic surface, also referred to as the state boundary surface, in $p' - q - v$ space within which all possible states of soil exist. Some important characteristics of the critical state concept are the normal consolidation line, swelling/compression lines and critical state line. The normal consolidation line and critical state line are indicated in Figure 2.3 (a). The swelling/compression lines can be seen in Figure 2.3 (b), which shows all three important characteristics in $p' - v$ space. The swelling/compression lines are within the state boundary surface. An infinite number of swelling/compression lines exist in in $p' - v$ space, parallel to the schematic ones in the Figure 2.3 (b).

When an overconsolidated soil element is subjected to additional stress in drained conditions, the soil element compresses (and reduces in volume) on the compression/swelling line. When the soil element reaches the normal consolidation line it is experiencing the highest stress it has ever experienced. It is no longer in an overconsolidated state, and the specific volume of the soil element decreases along the normal consolidation line, at a faster rate.

When the soil element reaches the normal consolidation line in Figure 2.3 (b) permanent deformation occurs. When the stress decreases, the specific volume of the soil element will increase parallel to the original swelling line but at lower volume. If the mean effective principal stress decreases before reaching the normal consolidation line, the volume would increase on the original swelling/compression line and no permanent deformation would have occurred.

A soil element reaches the critical state line at ultimate failure, where yielding occurs at constant volume under constant effective stress. In the context of road pavements, soil behaviour before reaching the critical state line, is of interest.

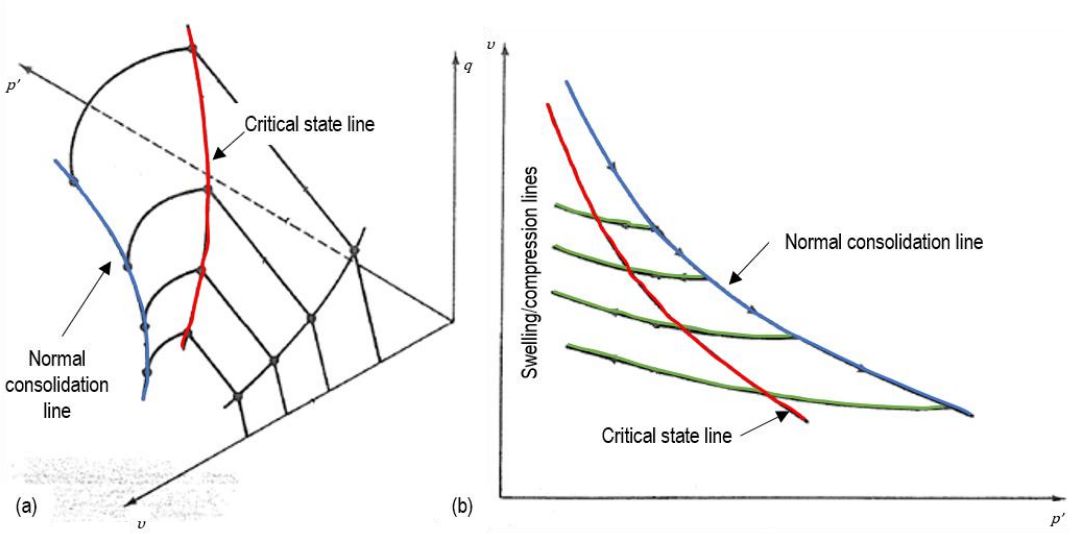

Figure 2.3 (a) The characteristic surface in *p'-q-υ* space and (b) swelling/compression lines in the *p'-υ* space (adapted from Atkinson & Bransby (1978))

Although pavement substructures are subjected to complex stress conditions through traffic loading, the main characteristics of pavement substructures are low effective stresses and repeated loading pulses well below yield (Brown & Selig, 1991).

Figure 2.4 shows the stress paths of two soil elements that have the same yield surface. The soil elements exist at different in-situ stress conditions and are loaded with the same magnitude of transient wheel load. The soil element in Scenario 1 is far from the yield surface even when it is loaded. The soil element would not deform permanently and would behave as a resilient material. The soil element in Scenario 2 is closer to the yield surface in an unloaded state. The

traffic induced stress causes the effective stress to move beyond the yield surface and permanent deformation occurs (Brown, 1996).

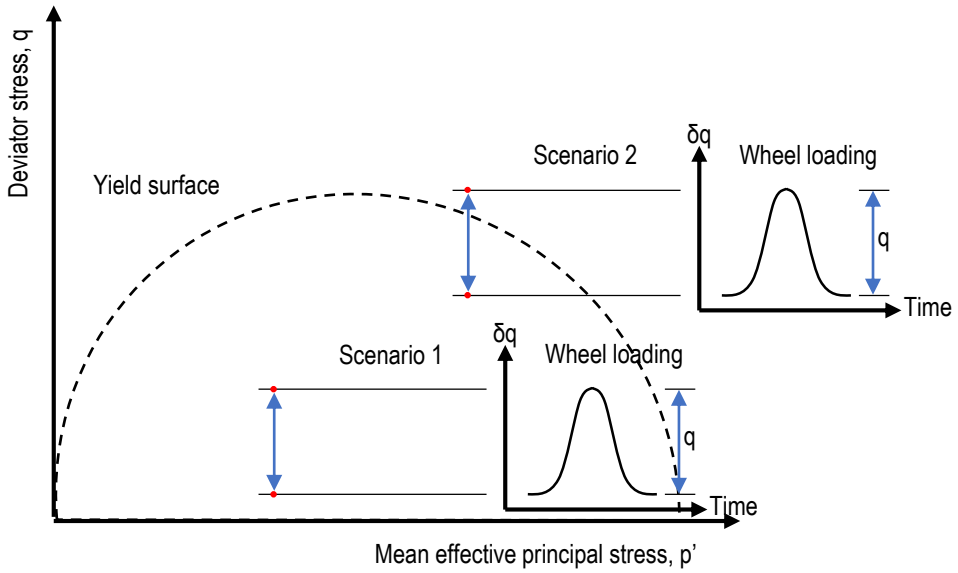

Figure 2.4 Stress paths for wheel loading (adapted from Brown (1996))

2.3.3 Response of soil material to repeated loading

The elasto-plastic behaviour, and critical state framework, where plastic strain only occurs when the stress conditions probe past the static yield surface, is not entirely applicable for repeated transient loading. It has been shown that the plastic strain associated with a single cycle of transient stress past the static yield surface is not significant, but that the accumulation of the plastic strain due to repeated loading can become significant. It has also been shown that plastic strain accumulates in granular material and subgrade under conditions of repeated loading even if the yield surface has not been passed (O'Reilly & Brown, 1991).

The accumulation of plastic strain due to repeated loading is caused by the gradual change of the soil particles and particle assembly. Soil particles crush and break when their strength is exceeded. Crushing can start at relatively low stresses and gradually change the particle assembly. Soil particles also slide and roll over each other to result in the particle assembly becoming less dense (dilation) or more dense (contraction) (Lekarp *et al.*, 2000a, 2000b).

The response of soil material to cyclic loading is analysed on a macroscopic level using stress-strain curves. Figure 2.5 is a schematic diagram of the stress-strain response of soil. The curve of each load cycle is non-linear with an elastic and plastic strain component. Under ideal stress conditions for pavements, the plastic strain component progressively becomes smaller as more load cycles are applied until it is negligible in comparison to the elastic component. The soil material is said to have reached resilience at this point (Huang, 1993; Lekarp *et al.*, 2000a,

2000b). The resilient modulus (E_r) is determined as a secant modulus of the stress-strain curve and this is the material stiffness that is typically used, analogous to the Young's Modulus or Modulus of Elasticity, in structural analysis programs.

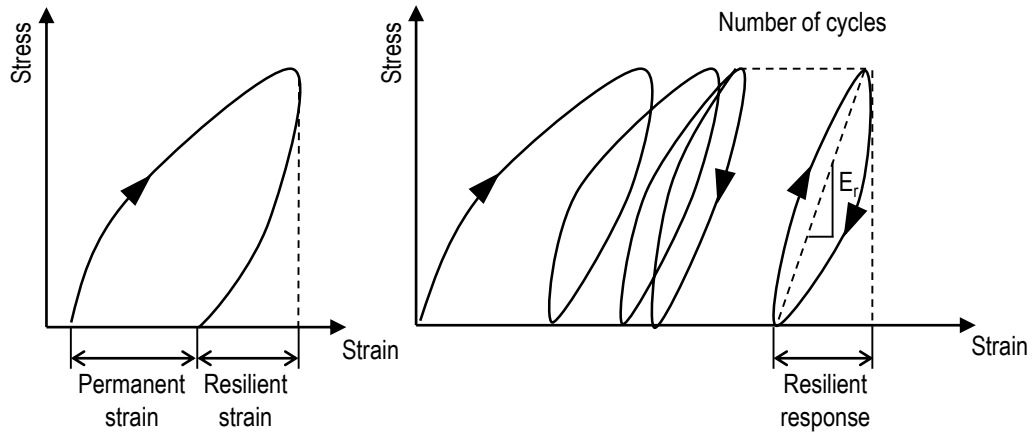

Figure 2.5 Stress-strain response of granular material (adapted from O'Reilly & Brown (1991))

Numerous factors influence the stress-strain response of soils. These factors broadly fall into two categories; stress related and soil composition related factors. Stress related factors include; confining and deviator stress, stress history and number of load applications. Soil composition related factors include: density, grading, moisture content, aggregate type and particle shape. In this discussion stress related factors are the focus and the only soil composition related factor of interest is density.

The stress state is one of the most important factors that influence the stress-strain behaviour of soil. The resilient modulus increases considerably with an increase in confining pressure and is comparatively less dependent on deviator stress. The influence of stress on the development of permanent deformation is better described by a stress ratio of deviatoric stress over confining pressure (or mean effective principal stress), where the manner in which permanent deformation accumulates falls within certain ranges of the ratio.

Stress history (often described by the OCR) has an effect on initial resilient behaviour. Within a certain stress ratio range, the influence of stress history on resilient behaviour becomes negligible as more loads are applied (the initial stress history having been "overridden"). Following on this, the resilient behaviour is independent of the stress level sequence. The accumulation of permanent strain is dependent on stress history and the stress level sequence. Less permanent strain occurs when the stress level is increased progressively, instead of applying the highest stress immediately. This is a consequence of progressive particle rearrangement and densification (Lekarp *et al.*, 2000b). Pavements are subjected to principal

stress rotation due to being loaded by moving wheels. It is known that principal stress rotation increases the accumulation of permanent strain (Lekarp *et al.*, 2000b).

Generally, the resilient modulus increases with increase in density, because the number of particle contacts per particle increases. Resistance to the accumulation of permanent deformation is improved by higher densities. It has also been shown that as compactive effort (and density) decreased, permanent deformation typically grew rapidly when principle stress rotation is applied (Kim & Tutumluer, 2005).

2.3.4 Shakedown and failure

It has been mentioned that the plastic strain component of the stress-strain curve becomes negligible under ideal stress conditions for pavements. Whether or not soil material reaches resilient behaviour, is dependent on the stress ratio (η), i.e. the deviatoric stress over the confining pressure (or mean effective principal stress) that it is subjected to, as seen in Equation 2.5.

$$\eta = \frac{q}{p'}$$ **Equation 2.5**

A threshold stress ratio exists above which significant plastic strain accumulates. The shakedown concept states that there is a critical stress level between stable (predominantly resilient) and unstable (significant permanent) pavement deformation (Werkmeister *et al.*, 2004).

There are three observed behaviours for granular materials and soil subgrade, which are referred to as “plastic shakedown”, “intermediate response-plastic creep” and “incremental collapse”. For plastic shakedown and intermediate response-plastic creep the stress level is low enough that the response is stable. For incremental collapse the stress level is higher and very close to critical stress level that results in the pavement response being unstable. Significant permanent deformation occurs with every load application. This type of stress range would lead to rapid failure of the pavement.

Figure 2.6 shows the accumulation of permanent strain for crushed carboniferous limestone that is subjected to three different stress paths (Pappin (1979) as cited by Brown (1996)). The stress ratio of A is relatively high, and the accumulation of permanent deformation is intermediate. The stress path of B reaches very close to failure (transiently) and the accumulation of permanent deformation is much more significant (even though the stress ratio

is similar). The stress path of C is the shortest and furthest away from the failure line. The accumulation of permanent deformation is the smallest for this sample.

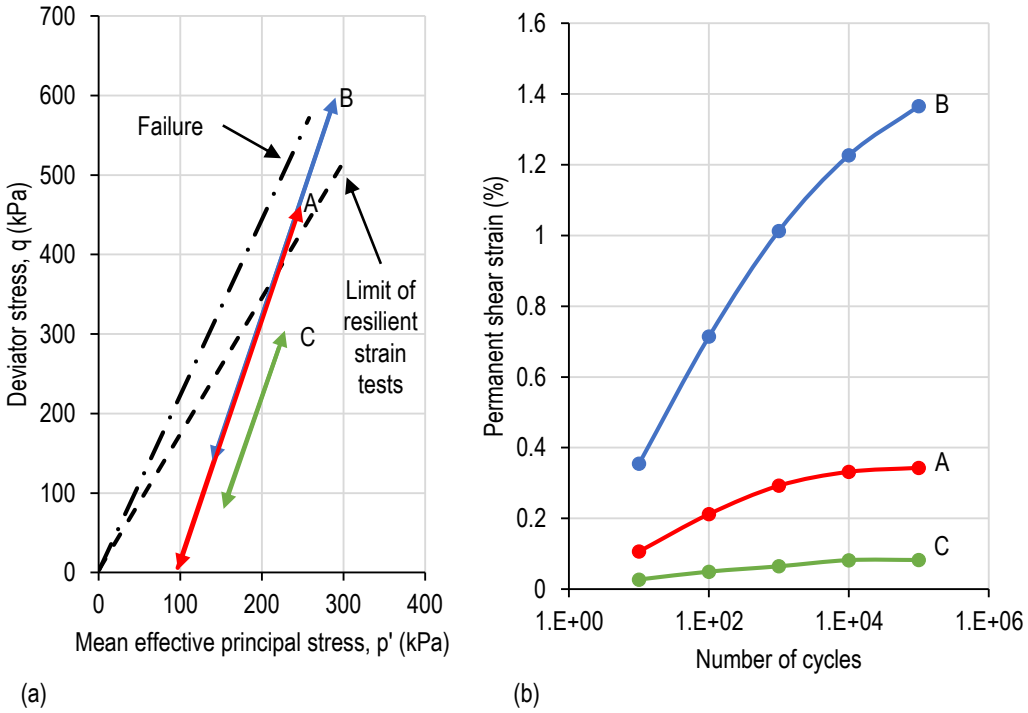

Figure 2.6 Effect of repeated loading with (a) stress paths applied and (b) accumulation of permanent strain (adapted from Brown (1996) as adapted from Pappin (1979))

2.4 STRUCTURAL ANALYSIS OF PAVEMENT

Pavement design has long been an empirical discipline where the relationships between design inputs and pavement failure were derived through a combination of engineering experience and experimental observations (Theyse *et al*, 1996: Li *et al.*, 2011). In the past 50 years there has been a move to the Mechanistic-Empirical Pavement Design (MEPD) approach. It considers input parameters such as traffic, climate, pavement structure and material properties, but most importantly the design approach incorporates the principles of engineering mechanics for the structural analyses of pavements to predict critical stresses.

2.4.1 Historical development of structural analysis of pavement

Analytical methods were used at the inception of the structural analyses of pavements. Westergaard (1926) developed analytical solutions that obeyed the restrictions of medium thick plate theory, to determine stresses in concrete pavements. His solutions were the result of the reduction of the analyses of pavements to a problem of the mathematical theory of elasticity,

where a homogenous, isotropic, elastic solid slab rests on a support that reacts proportional to the deflection of the slab in the vertical direction.

The slab thickness remains constant. The complexity of soil behaviour is simplified to series of springs. The modulus of subgrade reaction, pioneered by Winkler in 1867 (Ioannides, 2006), is used to assign stiffness to the springs. A characteristic system length, referred to as the radius of relative stiffness, is used repeatedly in the analyses. Westergaard (1926) considered three load cases which were corner, edge and central loading.

For corner loading, a wheel load acts close to a rectangular corner of a large slab. The critical stress is at the top of the slab. Edge loading is on the edge of a large slab and a considerable distance from the slab corners. The critical stress is at the bottom of the slab. For central loading the wheel load is at a considerable distance from all edges of the slab and the critical stress is at the bottom of the slab. The critical stress of all three load cases is tension stress.

The principle of simplifying concrete pavements to a slab on idealised soil foundation, where stress and strain within the foundation is ignored, is still very popular and is often referred to as a slab-on-grade simplification (Elsaigh, 2007). Finite Element (FE) analyses of pavements also uses this concept, where an idealised foundation of springs is used and the concrete slab is modelled using finite elements (Ioannides, 2006; Khazanovich *et al.*, 2000).

Burmister (1945a, 1945b, 1945c) introduced layered elastic theory when he developed analytical solutions for two-layered and three-layered systems. Since then layered elastic theory has been extended to any arbitrary number of layers and is referred to as Multi Layered Linear-Elastic (MLLE) theory. It allows the calculation of stresses in all the pavement layers. Its application has been predominantly in flexible pavement, where the critical stresses in the substructure are considered for design.

MLLE theory assumes linear-elasticity for all layers. A Modulus of Elasticity and Poisson's Ratio is assigned to each layer. The Modulus of Elasticity is usually a secant modulus and resilient. The thickness of the layers remains constant and layers extend infinitely in the horizontal direction. Self-weight as well as initial stresses and strains are ignored. Continuity between the layers, except the uppermost layer is assumed. For the solutions proposed by both Westergaard and Burmister the load is applied over circular areas and superposition can be used to simulate various load configurations.

2.4.2 Design for traffic load induced critical stress and strain

The traffic associated failure mechanism of rigid pavement is deemed to be fatigue cracking, while the traffic associated failure mechanisms of flexible pavements are fatigue cracking and

rutting. The critical stress and strain determined from the structural analysis programs are used to predict the fatigue life of the pavement component, ultimately ensuring the pavement design life.

Rigid pavements are designed to limit fatigue cracking by determining the load induced tensile stresses in the concrete layer. This stress is used to calculate the stress level, which is the ratio of the calculated tensile stress to the flexural strength. The stress level is limited to ensure the desired number of load cycles can be absorbed. The horizontal tensile stress in the concrete layer can be reduced by altering the concrete layer properties or increasing the strength and stiffness of the foundation layer.

A similar process is used to limit fatigue cracking of the asphalt layer in flexible pavements. Rutting is typically designed for by limiting the vertical compressive strain at the top of the subgrade. Structural analysis is used to determine the vertical compressive strain. The design procedure propose that rutting can be limited by having good quality control on the surface and base layers, but the vertical compressive strain can also be reduced by altering the properties of the layers above the subgrade.

2.4.3 Specialized structural analysis of pavement

Numerous programs, that incorporate the concepts of slab-on-grade and MLLE, have been developed for routine pavement analyses. Typically, these programs assume linear-elasticity of all bound and unbound materials. For more advanced pavement analyses, where higher accuracy is required, the non-linearity and stress-dependency of unbound materials are often incorporated. Dynamic loading is also modelled. In these cases, FE methods are usually used.

In the context of concrete pavements, it is not common practice to incorporate the complexity of unbound materials. A testament to this statement is the practice of simplifying the unbound material to a spring. Although concrete is also popularly modelled as a linear-elastic material, there has been a move towards including fracture mechanics as an important material characteristic to be included in the mechanistic analyses of concrete pavements (Ioannides, 2006). Numerical modelling of steel-fibre reinforced concrete has also been a prominent topic of research, where cracking is particularly of interest because the influence of the steel fibres is only activated after the concrete cracks (Barros & Figueiras, 2001).

2.5 ULTRA-THIN CONTINUOUSLY REINFORCED CONCRETE PAVEMENT (UTCRCP)

UTCRCP is a type of pavement for which the distinguishing feature is that the uppermost layer consists of a 50 mm thick continuously cast slab of HS-SFRC (Kannemeyer *et al.*, 2007).

Approximately 80 kg/m^3 hooked-ended steel fibres are used in the HS-SFRC. The concrete layer is additionally reinforced in the longitudinal and transverse direction with 5.7 mm steel bar mesh with an aperture of 50 mm. The concrete layer is intended to be placed on existing pavement as rehabilitation, or to be designed and constructed as part of new pavements where it acts as the primary structural layer (Kannemeyer *et al.*, 2007).

The concept of UTCRCP was developed from the need to mitigate problems that are experienced with conventional concrete pavements. These problems are related to crack formation and design methodologies adopted to control crack formation (Huang, 1993; O'Flaherty, 1967). UTCRCP eliminates joints and as a result, problems associated with joints. The high steel bar mesh content controls crack widths in the slabs. The high reinforcement content (steel bar mesh and steel fibres) provides superior post crack load-carrying capacity and mitigates problems, such as edge-punchout, experienced with Continuously Reinforced Concrete Pavement (CRCP) (Huang, 1993).

2.5.1 High Strength Steel Fibre Reinforced Concrete (HS-SFRC)

The addition of steel fibres to concrete produces a composite material with ductile tensile mechanical behaviour (Owen, 2009). This behaviour is also described as post-cracking strength and is brought about by steel fibres bridging cracks that form in the concrete matrix when it is subjected to tensile stress. The steel fibres maintain tensile resistance until they break or pull out of the concrete. Steel Fibre Reinforced Concrete (SFRC) uses NSC and steel fibre contents of varying percentages. HS-SFRC uses concrete with compressive cube strengths greater than 80 MPa (Neville & Brooks, 2010) and steel fibre contents of varying percentages.

The post-cracking strength can be illustrated by the flexural stress-deflection response of beam specimens tested under displacement control. In Figure 2.7 the flexural stress-deflection behaviour of high strength concrete with no steel fibres is compared to HS-SFRC with increasing steel fibre contents (Kearsley & Mostert, 2010). The unreinforced high strength concrete beam failed in a brittle manner. All the HS-SFRC beams maintained load in the post-peak stage, while increasing steel fibre content improved the post-crack carrying capacity further. The flexural strength of the beam with the highest steel fibre content increased significantly (Kearsley & Mostert, 2010).

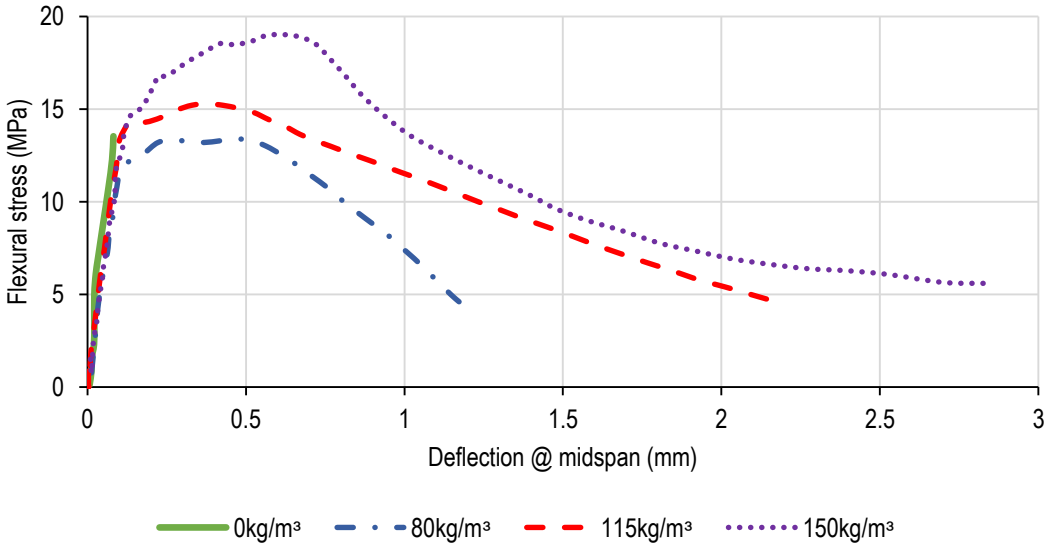

Figure 2.7 Effect of steel fibres on flexural behaviour (adapted from Kearsley & Mostert (2010))

In airfield and road pavement implementation, an SFRC slab would be subjected to repetitive loading. Fatigue behaviour of SFRC is important in the context of repetitive loading. Fatigue failure occurs in structural components that are repeatedly loaded to a stress level significantly smaller than its yield strength. In concrete, fatigue is associated with the progressive growth of microcracks, which gradually change the mechanical properties on a macrolevel (Lee & Barr, 2004).

The mechanism by which steel fibres affect fatigue behaviour is similar to how they affect flexural behaviour. They bridge microcracks, transferring load across the crack thus reducing stress at crack tips, slowing down the growth of cracks and increasing the resistance to irrecoverable strain. Stress level – fatigue life (S-N) curves are used to quantify fatigue strength. The number of cycles to fatigue failure is plotted for the stress level, which is the quotient of the repeatedly applied stress and the static (monotonic) strength. A standard testing procedure is used to determine the S-N curves of concrete beams (Huang, 1993). The static strength is required to determine the curves. Typically, it is determined by three-point or four-point bending of beams with the same dimensions as tested for fatigue. Figure 2.8 shows how the inclusion of steel fibres increases the fatigue life of concrete (Lee & Barr, 2004). Although no real limit has been found up to 20 million cycles, it has been speculated that concrete will not fail by fatigue when the stress level is smaller than 0.5.

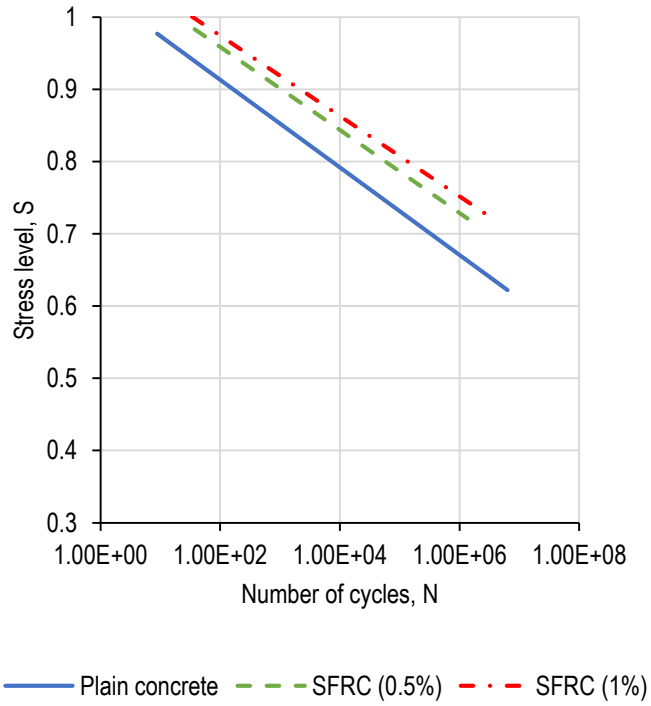

Figure 2.8 Stress level – fatigue life curves for plain concrete and SFRC under flexural loading (Lee & Barr, 2004)

Figure 2.9 shows the improvement of flexural strength of HS-SFRC in comparison to plain NSC. Both the results for HS-SFRC contained 1% steel fibres by volume. The difference in strength of the HS-SFRC is explained by different materials being used. A flexural strength of 11.7 MPa for 91.7 MPa compressive strength has been reported for the standard mixture proportions and materials used for UTCRCP (Kearsley *et al.*, 2014). A Modulus of Elasticity of 41 GPa was reported for the same concrete mix, while a resilient modulus of 49.7 GPa was reported by Denneman *et al.* (2010) for a similar mix design with 120 kg/m^3 steel fibres instead of 80 kg/m^3.

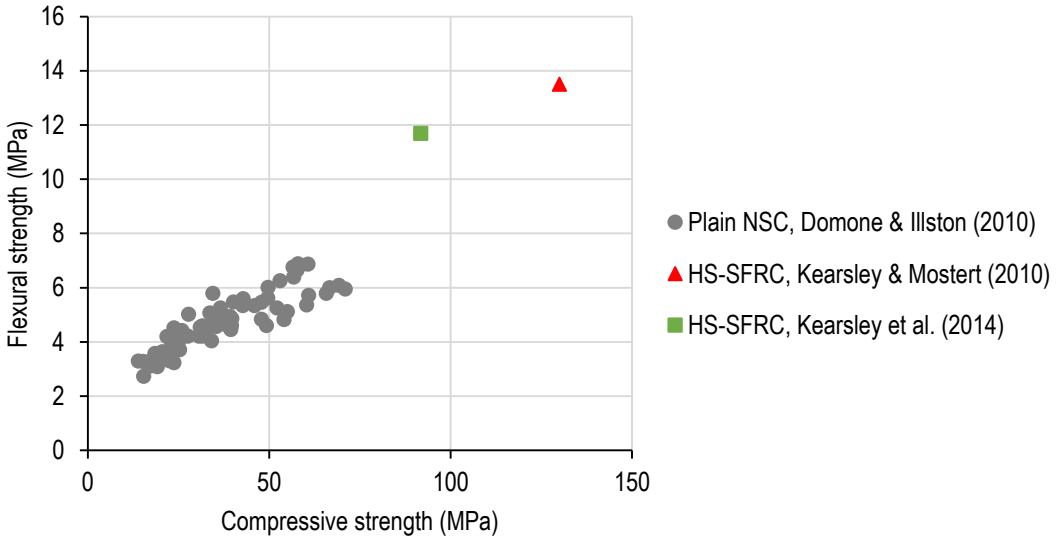

Figure 2.9 Compressive strength vs flexural strength for plain NSC and HS-SFRC (adapted from Domone & Illston, 2010; Kearsley *et al.*, 2014; Kearsley & Mostert, 2010)

High reinforcement content (steel bar mesh and steel fibres) of concrete members improve the tensile mechanical behaviour, thus allowing for the reduction of concrete slab thickness (Barros & Figueiras, 1998; Belletti *et al.*, 2008; Briggs *et al.*, 2016; Kannemeyer *et al.*, 2007; Roesler *et al.*, 2012; Strauss *et al.*, 2007). The concept of UTCRCP was developed to exploit the reduced thickness and post-crack carrying capacity of HS-SFRC.

In addition to an increase in tensile stress, a reduction in thickness of the concrete layer would result in increased deflection of a pavement. HS-SFRC reinforced with steel mesh can absorb the additional stress and rebound from high deflections, but care should be taken in the design of the substructure that will also be subjected to higher strains and stresses. It is suggested that, as for flexible pavement design, rutting should be considered as a traffic associated failure mechanism for UTCRCP.

2.6 DEVELOPMENT OF UTCRCP AND PREVIOUS RESEARCH ON ULTRA-THIN SFRC

With the potential of UTCRCP and other ultra-thin SFRC pavements recognized, a considerable amount of research has been done on this type of pavement system to improve understanding of its response to loading and its design methodology. In the following section, aspects of the design of UTCRCP and research conducted on the pavement type, deemed relevant to this research, are discussed.

Part of the research published is Accelerated Pavement Testing (APT) of UTCRCP. APT is the practice of estimating the response and performance of pavements to traffic loading by subjecting actual or prototype pavement systems to controlled, accelerated wheel loading. It simulates the accumulation of damage in a compressed time. APT forms a crucial part in bridging the understanding of laboratory work, site situations and theory (Brown, 2004), and by extension, developing MEPD.

2.6.1 Design of UTCRCP in South Africa

cncPAVE is a concrete pavement design program that incorporates mechanistic-empirical principles. The program has been adjusted to include the design of UTCRCP (Strauss *et al.*, 2007). It uses multi-layer analysis software, while spring foundations are typically used for the analyses of concrete pavements (Ioannides, 2006). This is because there are limits to medium thick plate theory for UTCRCP to be valid and to simplify the analyses of asphalt pavements that are rehabilitated using concrete (Strauss, 2018).

As mentioned in Section 2.5.1, the introduction of steel fibres increases the flexural strength, increases the load transfer capabilities at cracks and improves the fatigue characteristics of the concrete. Three-dimensional (3D) FE analyses of the pavement under dynamic loading was used to do a sensitivity analyses of a variety of parameters (slab thickness, voids under the slab, percentage reinforcement, position of steel, load transfer characteristics at cracks) (Strauss *et al.*, 2007). As for conventional concrete pavements, cracking of the concrete was considered as a failure mechanism. The effect of the formation of voids on the stress in the concrete layer was considered, although rutting was not considered as a failure mechanism.

For the sensitivity analyses done by Strauss *et al.* (2007), symmetry along the axle centreline was assumed for the 3D FE analyses. The results of the sensitivity analyses were used to calibrate the cncPAVE structural analyses models. The design procedure was verified through observations of UTCRCP test sections subjected to APT, using a Heavy Vehicle Simulator (HVS), where a dual-wheel was used.

2.6.2 Accelerated pavement testing of ultra-thin SFRC pavements

Internationally, ultra-thin SFRC pavements fall under the category of ultra-thin white-topping (Pereira *et al.*, 2006; Chen *et al.*, 2016). APT, using an HVS, has been used to investigate the response of ultra-thin HS-SFRC slabs on weak, medium and strong substructures, as well as slabs with partial support (Kannemeyer *et al.*, 2007). The weak substructure consisted of ripped and recompacted in-situ material. The medium and strong substructures consisted respectively of 150 mm and 300 mm thick, 4% cement stabilized in-situ material. The partially supported

pavement section had an 800 mm wide transverse cavity. The pavements were subjected to a range of loads that included 80 kN dual wheel loading and 140 kN aircraft wheel loading. The surface displacements were measured using Joint Deflection Measurement Devices (JDMD). Kannemeyer *et al.* (2007) found that all the pavement models performed well in dry conditions and cycles of wetting had to be introduced to ensure pavement failure.

Figure 2.10 shows the performance of the pavement under APT through the peak deflection and permanent deformation plot as a function of number of load cycles. From the peak deflection in Figure 2.10 (a) and the permanent deformation in Figure 2.10 (b) it can be seen that the section with partial support failed first. The permanent deformation accumulated steadily in the pavement with the weak substructure. It was reported that cracks formed parallel to the loading direction, approximately 300 mm from the wheel path and loss of support was identified between the concrete and the recompacted in-situ material. The deflection and permanent deformation in the medium and strong substructure were similar, with the strong substructure performing marginally better.

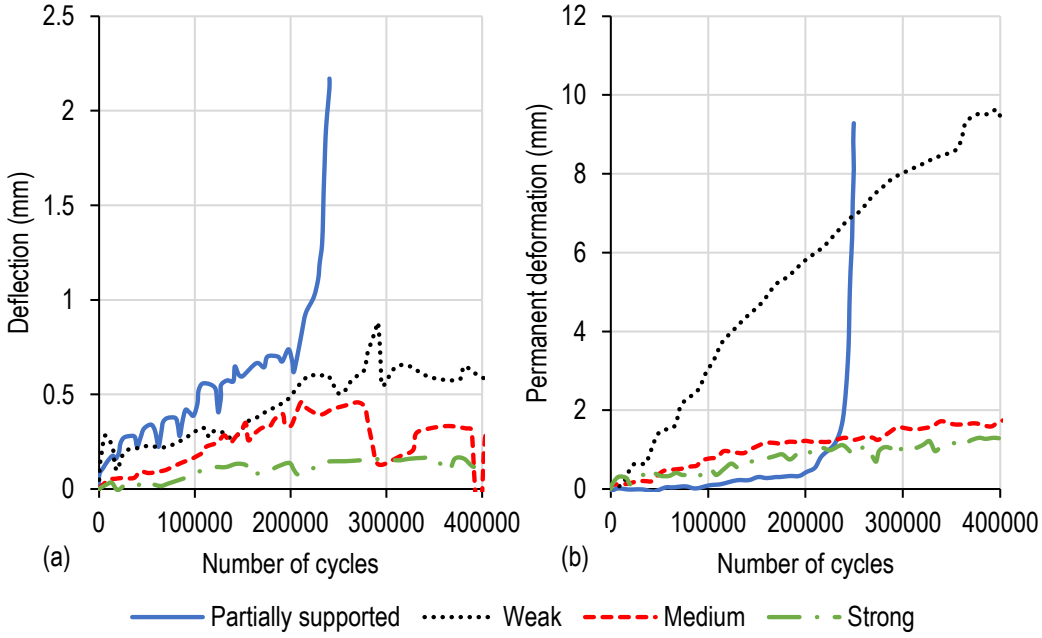

Figure 2.10 Response of UTCRCP on various support conditions considering (a) deflection and (b) permanent deformation (adapted from Kannemeyer *et al.* (2007))

Gerber (2011) monitored the response of UTCRCP to APT by installing Multi-Depth Deflectometers (MDDs) approximately in the middle of the thin HS-SFRC layer and approximately in the middle of one of the granular layers. The pavement composition, MDD installation depths and the measured response can be viewed in Figure 2.11. The load configuration was a dual set of tyres which could be loaded up to 80 kN, which is double the

magnitude of per axle side of a standard axle wheel load (E80). Even though Figure 2.11 shows up to 1.6 million load cycles, in total 2.5 million load cycles were applied. Cycles of wetting were introduced after 0.3 million load cycles.

The maximum vertical deflection versus number of load cycles was reported. The deflection at 170 mm below the surface in the granular layer remained approximately constant. The deflection measured in the ultra-thin HS-SFRC layer increased as more cycles were applied. After 0.125 million cycles the load was increased from 75 kN to 80 kN where after the deflection increased notably. After approximately 1 million cycles the maximum deflection at the concrete layer stabilized. The deflection value predicted by cncPAVE of 0.109 mm was exceed and 1.8 mm was measured after 2.25 million cycles (not shown in Figure 2.11).

The increasing maximum vertical deflection measured in the middle of the ultra-thin concrete layer, in comparison to the relatively stable (not increasing) maximum vertical deflection at a depth of 170 mm in the granular layer indicates that the load spreading is wide enough that the most stress is absorbed in the layer above the 170 mm depth where the MDD was placed.

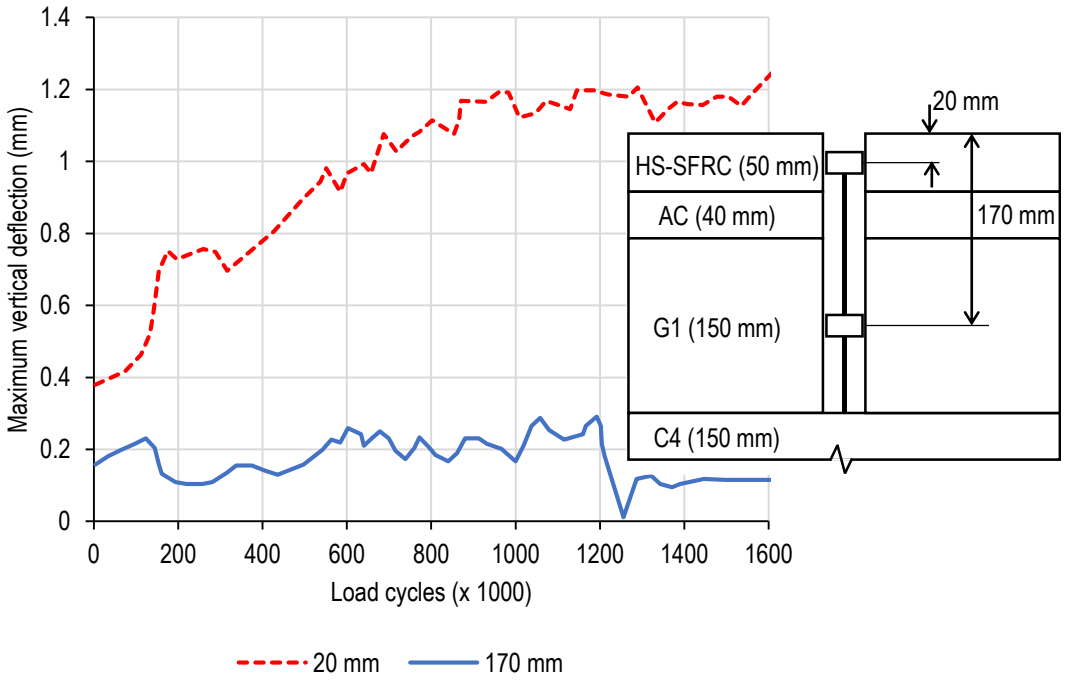

Figure 2.11 Vertical deflection and instrumentation (adapted from Gerber (2011))

Roesler *et al.* (2012) conducted a study where APT was used to determine the performance of concrete pavement (plain concrete and SFRC) for which the slab geometry was optimised to reduce the slab thickness. It was found that the slab thickness could be reduced up to 90 mm for a slab size of 1800 x 1800 mm on granular base. It was observed that structural fibres

improved the fatigue life of the 90 mm slabs and that its cracking performance varied with the stiffness of the soil. As anticipated, the systems with thin slabs showed high deflection and it was recognised that the substructure must be specified to reduce the accumulation of permanent deformation.

2.6.3 Steel bar mesh reinforcing

UTCRCP is additionally reinforced with 5.7 mm diameters, 50 mm aperture steel bar mesh. The effect of the mesh aperture was investigated by Kearsley & Mostert, (2010). Disks with a diameter of 600 mm and thickness of 55 mm were tested. The disks were supported on ball bearings at three equally spaced points on the circular edge and a displacement-controlled load was applied in the disk centre. Three mesh apertures were tested: 50 x 50 mm, 50 x 100 mm and 100 x 100 mm. The fibre content remained constant at 80 kg/m^3.

Figure 2.12 shows that an aperture of 50 x 50 mm could absorb and sustain the highest load. This was expected because this disk had the highest steel content. The response of the 50 x 100 mm and 100 x 100 mm disks were similar, showing that there is little benefit in using rectangular mesh apertures in terms of load absorption with the direction of least steel content determining the behaviour.

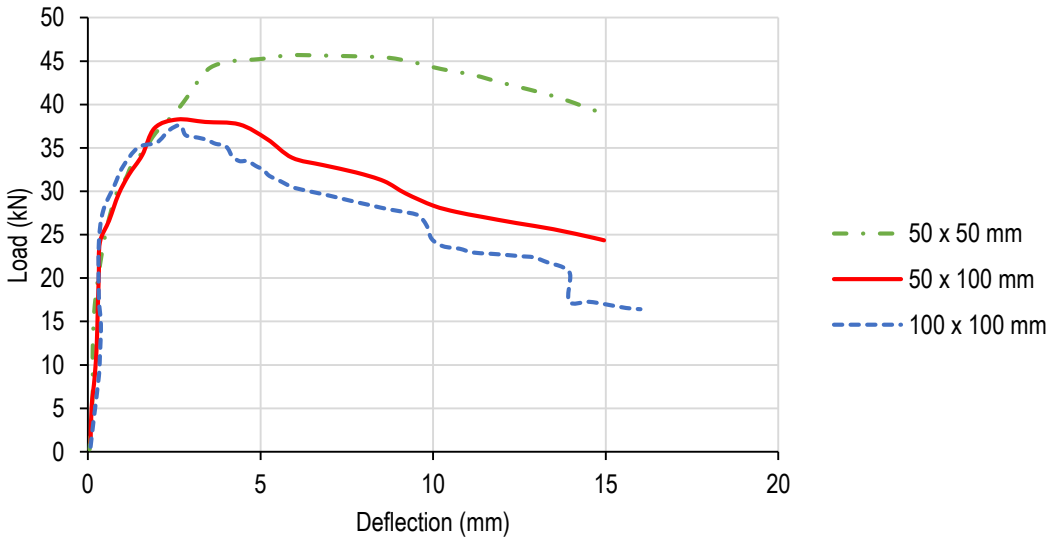

Figure 2.12 Effect of mesh aperture on disk load-deflection

2.6.4 Numerical modelling of SFRC slabs-on-grade

Belletti *et al.* (2008) focused on the fracture behaviour of SFRC. They recognised that traditional concrete pavement design, based on the Westergaard's approach considers first

crack as failure, which is not applicable to SFRC slabs because fibres only activate after first cracking.

Including non-linearity in the spring response would enable the correct modelling of the slab-on-grade problem. The soil response was simplified to a trilinear function which took the no-tension behaviour and bilinear shape of the compression part into account. Uplift could also be accounted for by this spring response. The numerical model was compared to experimental data where a 3000 x 3000 mm, 150 mm thick SFRC slab with hooked-ended steel fibres was placed on steel springs and loaded. The sensitivity of the system stiffness to the spring model was considered by calculating the deflection at the centre of a slab using four different spring model configurations;

1) Linear with compression and tension
2) Linear with only compression
3) Non-linear with compression and tension
4) Non-linear with only compression

Figure 2.13 illustrates that the trilinear spring response results in the most representative numerical response. Giving the spring response tension behaviour resulted in the most stiff slab-on-grade system. Including non-linear spring behaviour resulted in a less stiff response. A linear, no tension behaviour spring resulted in a system that was slightly stiffer than the response that was selected as the most representative. It is relevant to note that the spring function only starts affecting the system stiffness after approximately 200 kN, which is much higher than a standard axle load of 80 kN.

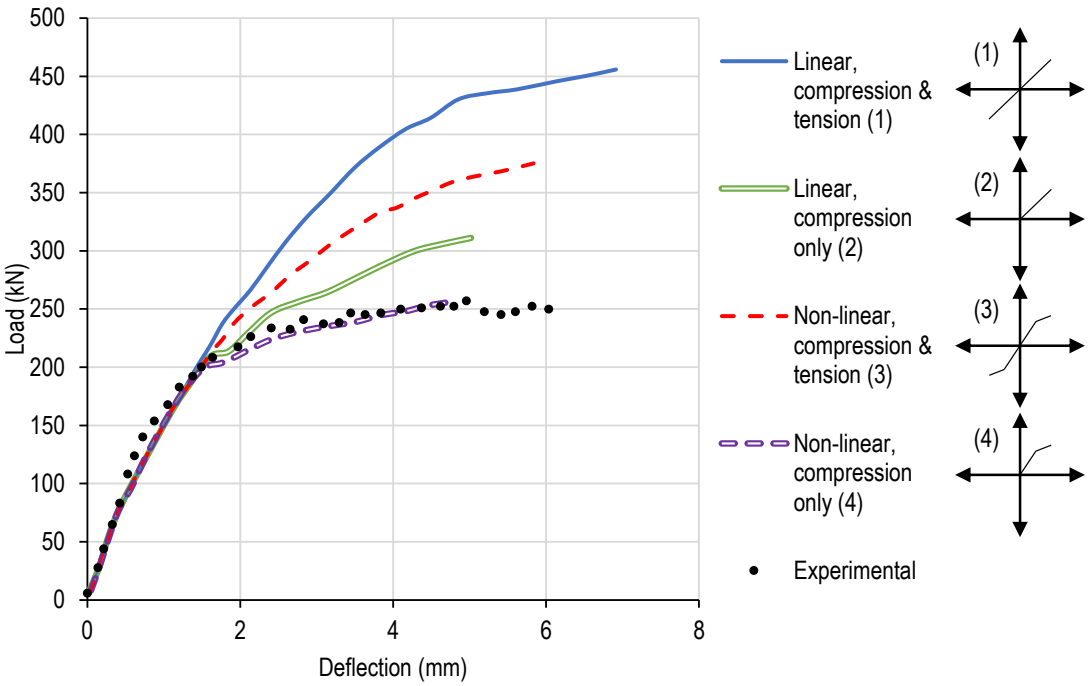

Figure 2.13 Effect of spring stiffness variation of response of SFRC slabs to load (adapted from Belletti *et al.*, (2008))

From 1998 to 2001, Barros & Figueiras (1998, 1999, 2001) published three papers investigating the behaviour of SFRC slabs-on-grade. Their research was primarily concerned with the numerical modelling of SFRC, but they did recognise the necessity to incorporate aspects of the complexity of soil response to loading. Finite element techniques were used. The SFRC response was modelled under the framework of smeared crack concepts. Shell elements were used for the slab. The soil foundation was simulated by springs orthogonal to the laminate structure. The foundation accounted for the non-linear, elasto-plastic response of soil to loading, as well as the loss of contact between slab and soil.

Including some form of non-linearity and no-tension behaviour inevitably improves the representativeness of the numerical models. The numerical model Belletti *et al.* (2008) developed, could model a 150 mm thick SFRC slab-on-grade, while the numerical model Barros & Figueiras (1998) developed was used for a 75 mm SFRC slab-on-grade.

UTCRCP consists of a HS-SFRC that is only 50 mm thick, indicating that more representative numerical models of the substructure are required to accurately model the pavement response to loading. More representative models have been developed for the numerical modelling of flexible pavements (Kim *et al.*, 2009). UTCRCP should perhaps be considered as a flexible pavement and be modelled using these models.

2.7 NUMERCIAL MODELLING OF PAVEMENT SUBSTRUCTURE

The substructure of road pavements consists of granular materials and subgrade. The stress-strain behaviour of these two soil materials are modelled numerically for the mechanistic analyses of pavements. Material models can be elastic or elasto-plastic. For elastic assumptions the resilient modulus is usually used.

As mentioned, the resilient behaviour is dependent on an array of factors and can be modelled numerically with varying degrees of complexity. According to Van Aswegen (2013), advanced material models for soil material used in MEPD consider stress sensitivity. Predictably, these models also have varying degrees of complexity, where factors such as moisture content, suction and density are considered. Simplified approaches have been adopted for design.

Although the granular layers and subgrade are both soil materials and are influenced by similar factors, they are also dissimilar enough that different numerical models have been developed for both (Brown, 1996). Numerical models for resilient behaviour fall in two categories, where models are based on either the resilient modulus and Poisson's Ratio, or use a shear-volumetric approach (Lekarp *et al.*, 2000a).

When linear-elasticity is assumed, stresses have a wider zone of influence than for more representative constitutive models. Brown & Selig (1991) stated that numerical analyses of the subgrade must take the non-linear-elastic properties into account and that this can be done in principle by modelling material stiffness as stress-dependent to reflect non-linearity. Poisson's Ratio is also stress dependent. The relationship between Poisson's Ratio and stress has been modelled, but the effect falls outside the scope of the current study.

2.7.1 Resilient modulus – stress relationships

Over more than a decade, two empirical relationships between resilient modulus of subgrade and effective stress were developed (Brown, 1996). Both were power-law relationships and incorporated some form of a stress ratio. The first relationship was deduced by testing reconstituted clay over a range of initial specific volumes, effective stresses and OCRs. Equation 2.6 shows the relationship:

$$E_r = K\left(\frac{p'_0}{q_r}\right)^n \qquad \textbf{Equation 2.6}$$

where K and n are regression coefficients depend on the soil type. The initial mean effective principal stress and the repeated deviator stress are respectively denoted by p'_0 and q_r. An

improved experimental procedure yielded a similar expression relating the resilient shear modulus to initial mean effective principal stress and repeated deviator stress as seen in Equation 2.7:

$$G_r = \frac{q_r}{C}\left(\frac{p'_0}{q_r}\right)^m \qquad \textbf{Equation 2.7}$$

where C and m are regression coefficients dependant on soil type. This relationship was developed for shear strains between 100 and 500 microstrain and stress ratio (η) values from 0.2 to 0.6. More empirical relationships have been developed that replaces p'_0 with suction and where multiple linear regression is used to relate the resilient modulus to p'_0, q_r and the plastic limit (Brown, 1996; Lekarp *et al.*, 2000a).

As for subgrade, modelling of granular materials is complex. Simplified approaches, such as the $K-\theta$ model (Sweere (1990) as referenced by Lekarp *et al.* (2000a)), have been adopted for design. This model relates the resilient modulus (E_r) to the bulk stress also using a power-law relationship as expressed in Equation 2.8:

$$E_r = K_1\theta^{K_2} \qquad \textbf{Equation 2.8}$$

where K_1 and K_2 are regression coefficients and the bulk stress is determined as $\theta = \sigma_1 + \sigma_2 + \sigma_3$ or $\theta = 3p'$. The $K-\theta$ model was further developed by Uzan (1985) to include the effect of deviator stress (q) as seen in Equation 2.9:

$$E_r = K_1\theta^{K_2}q^{K_3} \qquad \textbf{Equation 2.9}$$

where K_1, K_2 and K_3 are regression coefficients. Lekarp *et al.* (2000b) states that the Uzan-model has been shown to be superior to the $K-\theta$ model, and that it seems likely to become more popular than its predecessor. The $K-\theta$ and Uzan models were further developed to include the effect of density by incorporating porosity. Models have also been developed to include the effect of moisture using parameters such as saturation, suction and water content. It has been shown that these models cannot predict behaviour at higher load levels (Hjelmstad & Taciroglu, 2000). The effect of principal stress rotation on resilient moduli models was incorporated by Chou & Tutumluer (2001) using previously reported repeated load triaxial test data. These models produced a high degree of accuracy by simultaneously analysing the static and dynamic components of the applied mean and deviator stresses.

2.7.2 Application of critical state soil mechanics in pavement engineering

Constitutive models based on critical state theory have been used to analyse the response of pavements to loading. Zaghloul & White (1993) used the Cam-Clay model (Roscoe & Burland, 1968; Schofield & Wroth, 1968) for the subgrade in a study where FE analysis was used to investigate the effect of traffic loading on pavement rutting. Dondi (1994) also used the Cam-Clay model to model the subgrade in a study investigating the effect of geosynthetic reinforcement on the relative improvement of pavement system performance. 3D FE analysis was used in both these studies.

More recently the subgrade was again modelled using the Cam-Clay model to investigate the effect of base strength and thickness, and subgrade quality on fatigue and rutting strains and vertical deflection (Saad *et al.*, 2005). They found that more representative modelling of the substructure resulted in significantly greater rutting strains but had a less significant influence on the critical parameters of the asphalt bound layer. The same authors used Cam-Clay to investigate the effect of geosynthetic reinforcement placement on pavement response (Saad *et al.*, 2006).

2.8 CEMENT STABILIZED GRANULAR MATERIALS

Soil stabilization is a process of soil improvement. Cement stabilization is one of the methods used for this purpose. Other methods include mechanical, lime and lime-pozzolan stabilization as well as bituminous stabilization. Cement stabilization is a popular method, second only to mechanical stabilization. One of the less obvious reasons for its popularity is that almost any soil can by stabilized using Portland cement if the correct combination of water, compaction and curing is utilized (O'Flaherty, 1967). Lime and lime-pozzolan stabilization can have a cementation effect, but it also has the ability of changing the soil gradation chemically.

Three types of cement stabilization have been used in pavement engineering: soil-cement, cement-modified soil and plastic soil-cement. Soil-cement is a hardened material of pulverized soil, Portland cement and water mixed, mechanically compacted and cured. It contains the necessary amount of water and cement to allow the soil to harden, as well as an adequate amount of water to compact the material densely. Soil-cement has poor abrasion properties and is used in the road base and/or the subbase (O'Flaherty, 1967).

Cement modified soils are a combination of cement with soils that would be unsuitable to be used in the pavement structure unless they are modified. These are soils with high water-holding capacities and volume change characteristics that would result in pavement distortion. It is not economical to stabilize them to adhere to criteria for soil-cement, but their physical

properties can be improved (O'Flaherty, 1967). The resulting hardened material is intended to fragment under traffic loading. Plastic soil-cement is a mortar-like mixture and is primarily used for erosion control. Because cement-bound materials are prone to cracking they are considered to belong in the flexible pavement categorization, nevertheless they are used in both types of pavement (O'Flaherty, 1967).

In South Africa cement stabilization is often used because it is an economical way of improving marginal granular materials (De Beer, 1990). The resulting material falls under "cement modified soils" and should be classified as C3 and C4 (SANRAL, 2013). Cement stabilization is also used in inverted pavements where a granular base is placed on a cemented subbase. This is done to create an anvil on which the granular material can be densely compacted. As with cement modified soils the material is expected to crack and assume the characteristics of a granular material (referred to as "equivalent granular state"). This is a form of traffic moulding and a balanced pavement (where the strength of the pavement layers reduces with depth) is formed in the process.

Soil-cement materials, C1 and C2, are not designed to become granular-like materials with traffic loading. They tend to crack in a more discrete fashion and do not result in balanced pavements (Jordaan, 1984). Reflection cracking is caused by the cement stabilized base layers that cause stresses in the overlaying asphaltic layers (Visser, 2017) and often occurs when soil-cement materials are used.

It has been established that the substructure of pavements with thin HS-SFRC should be designed for poorer load spreading and high deflections. The use of soil-cement materials, C1 and C2, to ensure gradual load spreading with depth could be considered as a design solution. The possibility of a form of reflection cracking should however be recognized. If a C1 or C2 material in the base cracks, it is unlikely that the stresses caused in overlaying layer would cause cracks in the HS-SFRC. It is possible that the cracked base could cause stress concentrations in the underlying layer and result in augmented deterioration of the subbase.

2.8.1 Mechanical properties of cement stabilized granular materials

The Unconfined Compressive Strength (UCS), Indirect Tensile Strength (ITS) and flexural strength of the different strength classes of cement stabilized materials are summarised in Table 2.1 (Department of Transport, 1996). The flexural strength is determined as a fraction of the UCS. Although the fatigue performance of cement stabilized materials is complex (Lv *et al.*, 2019), cement contents from 3% to 4%, loaded to a stress level of 0.5 generally reached between 1 and 10 million load cycles in terms of flexural fatigue after 28 days of curing (Xie *et al.*, 2018).

Table 2.1 Strength properties of cement stabilized material (adapted from Department of Transport (1996))

Material	UCS[#] (MPa)	ITS* (kPa)	Flexural strength (MPa)
C1: Cemented crushed stone or gravel	6.0. to 12.0	-	1.2 to 2.4[$]
C2: Cemented crushed stone or gravel	3.5 to 6.0	> 400	0.7 to 1.2[$]
C3: Cemented natural gravel	1.5 to 3.5	> 250	0.5 to 1.17[$$]
C4: Cemented natural gravel	0.75 to 1.5	> 200	0.25 to 0.5[$$]
# @ 100% Mod. AASHTO (MPa) (TMH 1 Method A14, 1979) * @ 95 – 97 % Mod. AASHTO compaction, (SABITA Manual 14, 1993) $ High strength materials (C1 & C2): Flexural strength = 0.2*UCS $$ Low strength materials (C3 & C4): Flexural strength = 0.33*UCS			

The material stiffness, in terms of Young's Modulus, of the different strength classes of cement stabilized materials are summarised in Table 2.2. The material stiffness of cracked cement stabilized material is significantly reduced. When the material is cracked, the material stiffness is affected by whether the overlaying layer is bound or unbound. This is in part because confinement is influenced by the state of the overlaying layer. The Young's Modulus of uncracked cement stabilized granular material ranges between a minimum of 2 GPa for C4 and 30 GPa for C1. The range for C1 materials is also wide and falls between 7 GPa to 30 GPa.

Table 2.2 Material stiffness of cement stabilized material (adapted from Department of Transport (1986))

Material	Young's Modulus (GPa)		
	Pre- cracked phase	Post-cracked phase	
		Under bound materials	Under cracked or untreated materials
C1: Cemented crushed stone or gravel	7 to 30	1.5	1.2
C2: Cemented crushed stone or gravel	4 to 14	1	0.75
C3: Cemented natural gravel	3 to 10	0.75	0.5
C4: Cemented natural gravel	2 to 7	0.5	0.3

The material stiffness can be estimated from the UCS or flexural strength. Relationships have been established for cemented crushed stone or gravel and for cemented natural gravel. Equation 2.10 and Equation 2.11 show the relationship of the Young's Modulus (E) to flexural strength (σ_b) and UCS (σ_c) for C1 and C2 materials, respectively. Equation 2.12 and Equation

2.13, show the relationship of the Young's Modulus (E) to flexural strength (σ_b) and UCS (σ_c) for C3 and C4 materials.

$$E = 8\sigma_b + 3500$$ **Equation 2.10**

$$E = 4.16\sigma_c^{0.88} + 3484$$ **Equation 2.11**

$$E = 10\sigma_b + 1000$$ **Equation 2.12**

$$E = 5.13\sigma_c^{0.88} + 1098$$ **Equation 2.13**

It has been demonstrated through back-calculation of deflection that the initial material stiffness, in terms of Young's Modulus, of cement stabilized layers is in the order of 3 to 4 GPa (Department of Transport, 1986). The Pavement Number design method uses a maximum effective long-term stiffness of 1500 MPa for C1 and C2, 550 MPa for C3 and 400 MPa for C4 (SANRAL, 2013).

2.9 LOAD CONFIGURATION

The traffic loading of pavements is variable. A variety of wheel and axle configurations are used that are also loaded to different degrees. The velocity at which wheels roll have an influence on the stress that is exerted on the pavement. Stationary wheels cause the highest stress. Vehicles also wander while travelling, not always applying the same stress in exactly the same transverse location throughout the pavement life (O'Flaherty, 1967; SANRAL, 2013).

In the mechanistic-empirical design approach, traffic loading is thoroughly characterized by a full axle-load spectrum. The magnitude, wheel load configuration and frequency of traffic loading are used to determine the loads that the pavement will be subjected to in each time increment of damage accumulation (Li *et al.*, 2011). Typically, the load spectra are linked back to an equivalent standard axle wheel load for ease of use (Department of Transport, 1991; De Bruin & Jordaan, 2004; SANRAL, 2013). The design process is evolving to consider load spectra instead of converting all loads to a standard axle wheel load. A range of load configurations are considered by routine pavement analysis programs.

2.9.1 Wheel and axle arrangements

Several wheel and axle arrangements are commonly used for vehicles. Single axle, single wheel arrangements are extended to single axle, dual wheel arrangements and tandem or tridem axle, dual wheel arrangements. Recently there has been a move toward using wide-based super single tyres. Routine pavement analyses programs, that assume linear-elasticity, use superposition to

determine the effect of multiple wheel loads. It has been shown that critical pavement responses under multiple wheel loads are substantially different from each other (Kim, 2007).

Figure 2.14 shows some of the load configurations that are used. The figure shows the typical spacing of wheels and axles, as well as the distance from wheel arrangement centreline to the axle centreline. The effect of multiple wheel load interaction has been investigated using physical and numerical modelling (Kim, 2007). In these investigations the wheel arrangements of one side of an axle are typically considered, ignoring the potential interaction between the wheel arrangements at opposite ends of an axle.

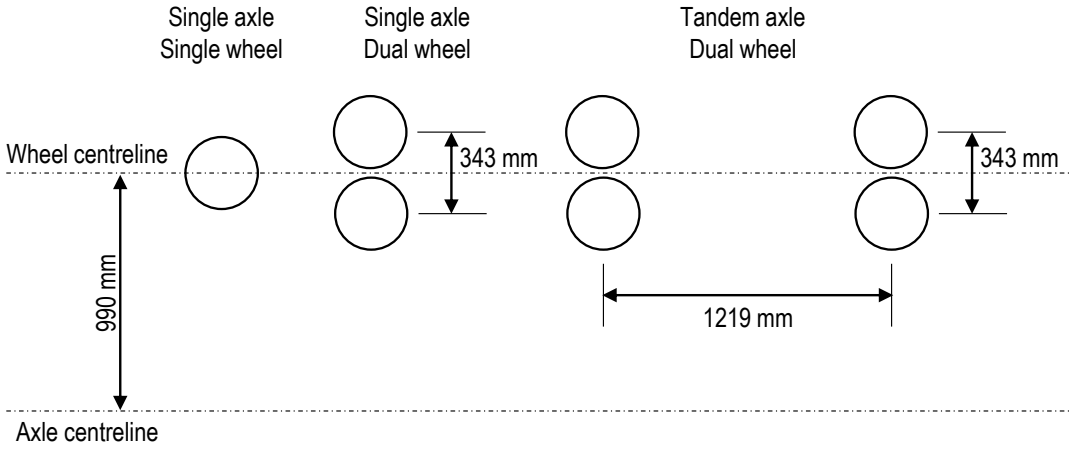

Figure 2.14 Wheel and axle arrangements (adapted from Huang (1993) and Kim (2007))

2.9.2 Stress distribution caused by load configuration

The vertical stress caused by multiple wheel loads do not interact at shallow depths. At greater depths, the vertical stress distributions start overlapping and the pavement material that is situated at this depth is subjected to a higher stress between the two wheels of a tandem axle than if no superposition is taken into account. If the behaviour of the substructure is investigated, overlapping stress fields of wheel loads become important. In Figure 2.15 the vertical stress distribution with depth of a single axle arrangement is compared to that of a tandem axle arrangement. The superimposed vertical stress between the two axles of the tandem axle arrangement is illustrated.

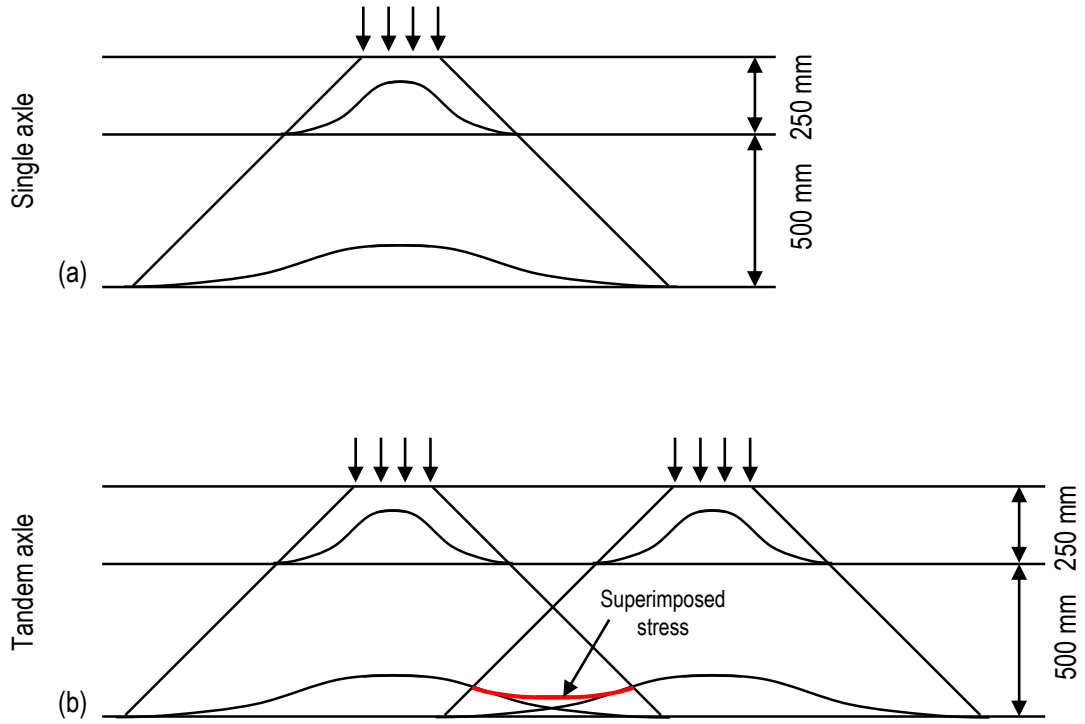

Figure 2.15 Vertical stress distribution of (a) single axle and (b) tandem axle loads in the longitudinal direction of a road pavement (adapted from Kim (2007))

The typical distance between the axles in a tandem axle arrangement is 1 219 mm and the typical distance between the end axles of a tridem axle arrangement is 2 438 mm. The distance between the wheel arrangements at the ends of an axle is in the range of 1 980 mm (Huang, 1993). This distance is within a range that is recognised to have an effect and it is anticipated that the zones of influence of the wheel loads from the axle ends overlap and interact from a certain depth. This stress overlap and interaction are often ignored for conventional flexible and rigid pavement design.

The alternative nature of UTCRCP, with a very thin concrete layer that has a much higher material stiffness than asphalt, leads to the proposal that the interaction between the wheel arrangement at the ends of an axle should be considered in the design process. Thus far APT done on UTCRCP in South Africa has only considered one side of an axle.

2.9.3 Load configurations used in physical modelling of pavements

APT is done using load simulators of which the fundamental feature is moving wheels that apply the load repeatedly. Examples of load simulators are the Hamburg wheel-tracking device (Su Jung *et al.*, 1993), Nottingham Pavement Test Facility (Juspi, 2007) and Cambridge Airfield Pavement Tester (Bowman & Haigh, 2016). All three load simulators make use of wheels that move along a beam that it is attached to. The beam makes use of a lever system to

apply load. APT is also done using a circular test track, where wheels are attached to a rotating arm (Hernández *et al.*, 2016). Pavement models are often tested in a controlled laboratory environment.

Other examples are the HVS and the Model Mobile Load Simulator (MMLS) (De Beer, 1990; Kannemeyer *et al.*, 2007; Van de Ven & De Fortier Smit, 2000). For the HVS, wheels also move along a beam. The load mechanism of the MLLS is slightly more complex and involves a number of wheels that are attached to a circular chain (Van de Ven & De Fortier Smit, 2000). HVS and MLLS are moved to different sites to test pavements. Pavements are tested up to speeds of 20 km/h and rates of 800 passes per hour (Bowman & Haigh, 2016; CSIR, 2017; Dynatest, 2017).

Depending on the load simulator, pavements can be loaded uni- and bi-directionally. Bi-directional loading results in greater permanent deformation for the same number of passes than if uni-directional loading was applied (Chan, 1990). Although accelerated pavement testing facilities can be adjusted to examine the effect of axle loading and wander (Bowman & Haigh, 2016; Donovan *et al.*, 2016; Ferretti & Bignozzi, 2012), APT predominantly only considers one side of an axle with single or dual wheels ignoring the potential interaction between wheel arrangements at opposite ends of axles. One of the shortcomings of APT done on UTCRCP in South Africa is that only one side of an axle is considered, usually using a dual wheel (Kannemeyer *et al.*, 2007).

Recently there has been a move toward scaled physical modelling in conjunction with a geotechnical centrifuge (Bayton *et al.*, 2018; Dave, 2018; Kearsley *et al.*, 2014; Lukiantchuki *et al.*, 2018; Saboya *et al.*, 2020; Smit *et al.*, 2018a, 2018b). A variety of load configurations have been used. As part of the scaled physical modelling, pavements were loaded using strip loads, resulting in the assumption of plane strain conditions

2.9.4 Plane strain simplification for road pavements

Ideally, road pavements become a plane strain problem when permanent deformation is considered. This is because no net strains accumulate in a pavements' longitudinal direction and the strains that develop in the transverse direction accumulate to form rutting (Brown & Selig, 1991). If the permanently deformed shape of a pavement is of interest and applying a rolling wheel load is not an option, assuming plane strain conditions would make it possible to investigate different aspects of pavement behaviour (rather than applying a static load over an area in a 3D model). Strip loading excludes the contribution that principal stress rotation (unidirectional or bidirectional) would have on the degree of permanent deformation. In terms of numerical modelling, plane strain models are computationally inexpensive.

In Figure 2.16 the difference between applying equal pressure over a strip area and square area is illustrated. Strip loading, and by extension a plane strain assumption for road pavements, results in higher stresses reaching greater depths. Horizontally, the zone of influence of strip loading is wider.

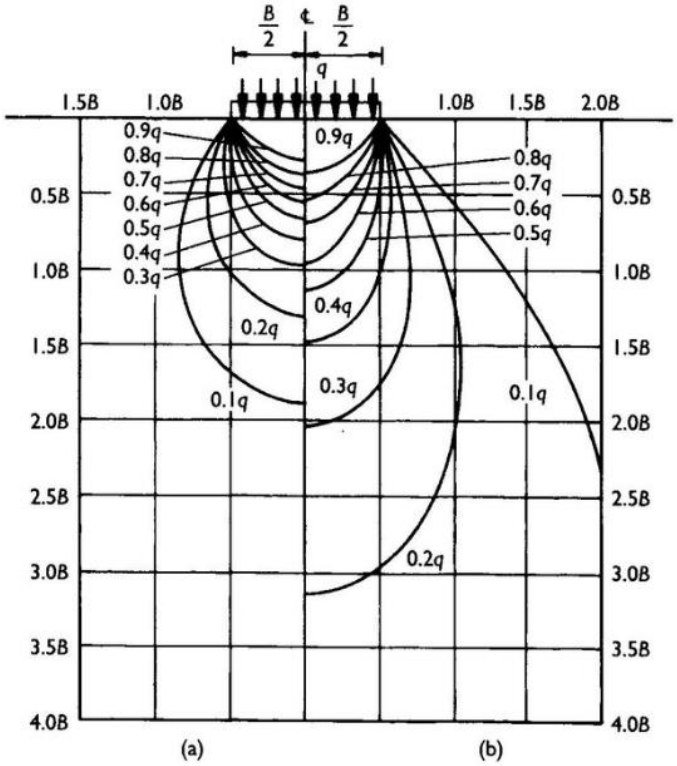

Figure 2.16 Vertical stress isobars of pressure applied over (a) a square area and (b) a strip area (Powrie, 2004)

The extent of stress zone overlap in pavements is dependent on the relative stiffness of adjacent layers and the soil-structure interaction of the structural and substructure components of pavements.

2.10 SOIL-STRUCTURE INTERACTION AND RELATIVE STIFFNESS

Soil-structure interaction is the process in which structural displacement and soil displacement are dependent on each other. The movement of the structure directly influences the response behaviour of the soil and the soil movement influences the response of the structure (Hallak, 2012; Lemmen, 2015). The relationship between the stiffness of structural elements and the stiffness of the soil controls the contact stress distribution between the soil and structural element, which controls the interaction (Aiban & Znidarcic, 1995; Laue & Arnold, 2008; Vorster *et al.*, 2005). The contact stress distribution can vary with the magnitude of load and time.

The stiffness of a body is defined as the resistance of that body to deformation under applied load. It is dependent on the geometry and boundary conditions of the body as well as the stiffness properties of materials in the body (Clayton, 2011). Material stiffness properties are typically a description of the relationship of stress and strain of the material. Numerous approaches to describing the stress-strain relationship exist and the most applicable approach is dependent on the context of the problem.

The concept of relative stiffness is used to predict and describe the soil-structure interaction and, by extension, response of civil engineering structural systems to loading. Different formulations of relative stiffness are used for different systems. Generally, the concept attempts to take the stiffnesses of different components of a structure into account. It is especially used in geotechnical engineering for the design or investigation of pipe and tunnelling systems, retaining walls as well as foundations, which includes piles and footings.

Ranges of relative stiffness are used to categorise soil-structure interaction. For certain systems soil-structure interaction can broadly be categorized into “interaction” and “no interaction”, where “interaction” may have a number of subcategories (Lemmen *et al.*, 2017; Vorster *et al.*, 2005). Relative stiffness ranges to categorise soil-structure interaction have been established for pipes and footings.

Although concrete pavements are normally deemed to be rigid pavements, the limited thickness of UTCRCP may result in flexible pavement behaviour where the soil-structure interaction between the concrete and the substructure determines its response to traffic loading. The effect of relative stiffness on soil-structure interaction in pavements should thus be studied. Before relative stiffness in pavements is discussed, some background of the concept of relative stiffness and its effect on soil-structure interaction for pipes and foundations is given.

2.10.1 Soil-structure interaction and relative stiffness of pipes

The dissimilarity between pipes and pavements is indisputable. Elements of the geometry of the problems are incomparable. Pavements consist of layers of pavement materials, while pipe systems are typically circular pipes within a body of soil. Pipe-soil interaction is induced by soil settlement close to the pipeline (and surface loading close to the pipeline). Relative pipe-soil stiffness has been investigated for variations of soil settlement. A simple variation is loss of support underneath the pipe, perpendicular to the direction of the pipe for a certain width (as illustrated in Figure 2.17). This is a scenario that occurs when tunnelling underneath pipes.

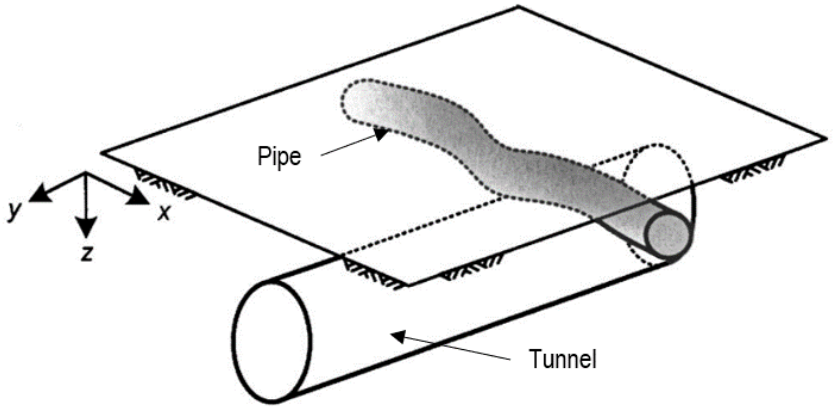

Figure 2.17 Simple pipe loss of support variation (Vorster *et al.*, 2005)

The loss of support results in a settlement trough. The relative stiffness parameter for pipe-soil interaction incorporates the distance from the tunnel centreline, or maximum displacement, to the point of inflection in the settlement trough (Vorster *et al.*, 2005). Pipe-soil interaction, and their relative stiffness parameters, should be considered due to the similarity of settlement troughs and deflection plots of loaded pavements. Deflection plots of pavements are commonly used in pavement engineering and some concepts that have been developed for pipe-soil interaction should be transferable to pavement engineering.

The relative stiffness parameter for bending of pipelines is referred to as the relative rigidity factor (R). It is based on elasticity models. It defines the relationship between the flexural as well as the axial stiffness of the pipe and the material stiffness of the soil (Klar *et al.*, 2005). Equation 2.14 shows the relationship:

$$R = \frac{E_p I_p}{E_s r_0 i^3} \qquad \textbf{Equation 2.14}$$

Where $E_p I_p$ is the flexural rigidity of the pipe and E_s is the material stiffness of the soil. The outer radius of the pipeline is incorporated through r_0 and the distance from the buried tunnel centreline to the inflection point of the greenfield surface settlement trough is incorporated by i. Greenfield surface settlement is the settlement of the soil due to loss of support without the potential effects of a pipe. Figure 2.18 is a schematic of a pipe-tunnel-soil system that shows the outer radius of the pipe and the inflection point of a greenfield surface settlement trough.

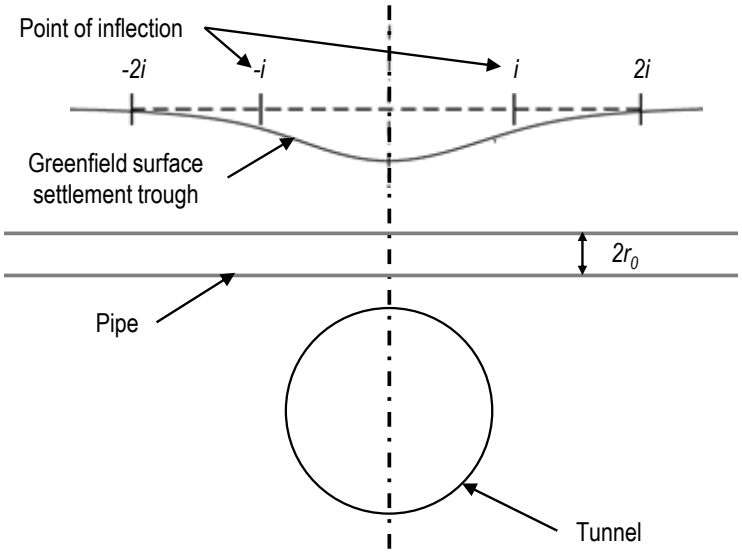

Figure 2.18 Components of soil tunnel-pipeline system geometry incorporated in relative rigidity factor (adapted from Vorster *et al.* (2005))

Assuming that a pipeline does not fracture, it behaves in two distinct ways. It either interacts with the surrounding soil or does not interact with the surrounding soil. For R smaller than 0.1, the response is described as flexible and the pipeline approximately follows the greenfield soil displacement profile. There is little or no interaction between the pipe and surrounding soil. For R equal to or greater than 5, the response is described as rigid. The influence of the soil displacement profile on the response of the pipe is reduced and the soil-pipe interaction becomes important. Various mechanisms govern the behaviour of buried pipelines and local mechanisms are driven by soil-pipe interaction.

Gaussian curves, of the form in Equation 2.15, are commonly used to describe vertical soil settlement due to tunnelling:

$$S_v(x) = S_{max} e^{-\frac{1}{2}\left(\frac{x}{i}\right)^2} \qquad \textbf{Equation 2.15}$$

Where S_{max} is the maximum settlement and i , also referred to as the trough width parameter, is the distance from the maximum deflection to the inflection point. It has been shown that this curve is not satisfactory to describe the settlement of soil and it has been modified to include a shape function parameter that controls the profile width and an alpha parameter to ensure that i remains the distance to the inflection point. The effect of S_{max} and i are shown in Figure 2.19.

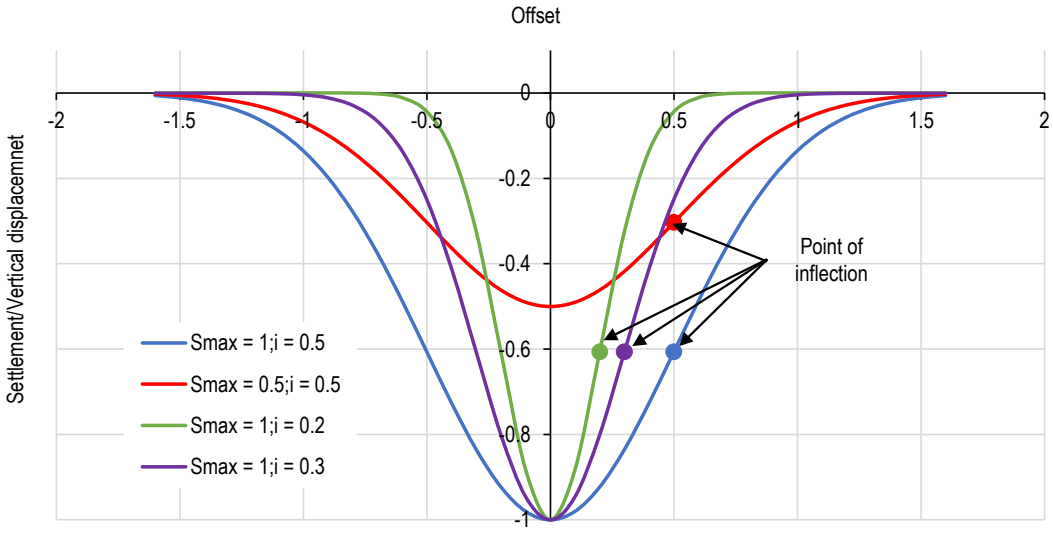

Figure 2.19 Effect of S_{max} and i on Gaussian curve shape

2.10.2 Soil-structure interaction and relative stiffness of foundations

The similarities between concrete footings and concrete pavements are indisputable and for some designs, the dimensions fall within the same ranges. Laue & Arnold (2008) tested raft foundations that were 5500 mm by 5500 mm with a depth of 200 mm. It has been shown that jointed concrete pavements with a joint spacing in the range of 5500 mm perform well (Huang, 1993). Lane widths of high-speed, high volume highways are 3600 mm. The thickness of conventional concrete pavements range between 150 mm and 300 mm. The loading of pavements and footings are often simplified to arrangements of point loads, or pressures over areas. In the following discussion, a foundation refers to a footing and the ground supporting it.

Relative stiffness influences the stress distribution below a footing. A uniform stress distribution, as assumed for footing design, is only true if the footing is completely flexible and a constant load is applied over the entire footing area (Craig, 2004). The stress distribution changes as a footing becomes more rigid (or stiff). The contact stress distribution is dependent on the supporting ground type. A rigid footing on sand has a stress distribution that is concave with increased stress at the edges of the footing. Figure 2.20 shows the difference between the stress distribution of flexible and rigid footings on sand. Once the footing is no longer completely flexible, the stress distribution also becomes dependent on the fraction of failure load that is being applied. The evolution of the theoretical stress distribution is illustrated in Figure 2.21. The stress distribution alters from convex at low loads to concave at failure.

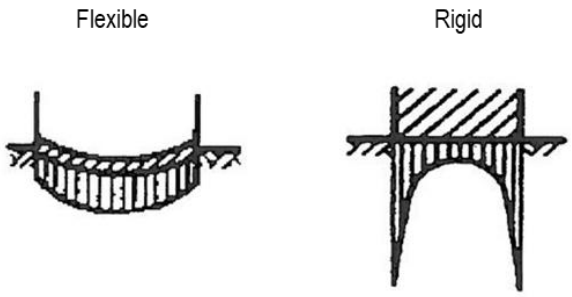

Figure 2.20 Stress distribution of flexible and rigid footings (Laue & Arnold, 2008)

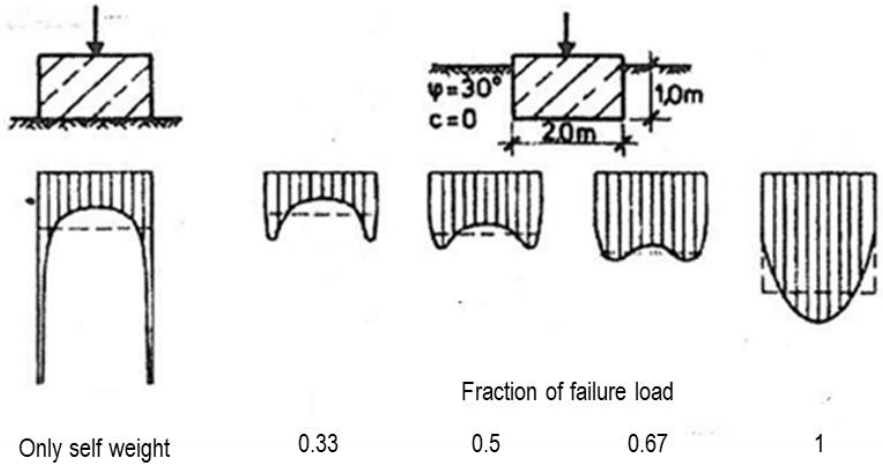

Figure 2.21 Stress distribution change with increasing load (Laue & Arnold, 2008)

A relative stiffness parameter has been developed to predict the behaviour of raft foundations (Beuth Verlag GmbH, 1974). In this text the parameter is referred to as foundation system stiffness (K_s). Lemmen *et al.* (2017) found good correlation between the predicted response of the parameter and measured response of scaled physical models of strip footings, which indicated that foundation system stiffness can be used for foundations other than raft foundations.

Equation 2.16 allows for foundation systems to be categorised as flexible, semi-flexible, semi-rigid and rigid:

$$K_s = \left(\frac{1}{12}\right)\left(\frac{E_c}{E_s}\right)\left(\frac{d}{l}\right)^3 \qquad \textbf{Equation 2.16}$$

Where E_c and E_s are the material stiffness, in terms of Young's Modulus, of the concrete in the footing and soil it rests on respectively. The thickness of the footing is d and the length of both

sides is l. The ratio of the thickness and length give a measure of the footing slenderness. Table 2.3 contains the ranges of foundation system stiffness for the respective system stiffness classifications (flexible, semi-flexible, semi-rigid and rigid).

Table 2.3 System stiffness categories and ranges

System stiffness category	K_s range
Absolutely flexible	0
Semi-flexible	0 – 0.01
Semi-rigid	0.01 – 0.1
Rigid	0.1 - ∞

Lemmen *et al.* (2017) investigated the response of footings of various stiffnesses on sand using centrifuge modelling. The thickness of the footings was varied, while the plan dimensions remained constant. At full scale, the plan dimensions were 4500 mm by 4500 mm and the thicknesses that were tested were 90 mm, 200 mm, 300 mm, 480 mm, 750 mm, 1050 mm and 1500 mm. The contact stress distributions and load-settlement of footings were discussed as a function of foundation system stiffness.

The shape of contact stress distribution evolved with increasing load. At the same load, three classes of contact stress distribution were identified. Rigid foundations showed a concave stress distribution that increased slightly from the footing centre toward the footing edge. Lemmen *et al.*, (2017) stated that these contact stress distributions could be considered uniform. The contact stress distribution of the semi-rigid and semi-flexible foundations increased from the footing edge to the footing centre. For the semi-rigid foundation, the increase was convex in nature. The semi-flexible foundation, which had a footing thickness of 90 mm, had a stress distribution that increased approximately linearly toward the footing centre. The semi-flexible footing bent excessively and there was loss of contact between concrete and sand at the footing edge.

It was found that the slope of the load-settlement curve reduced rapidly as the foundation system stiffness increased. It stabilized once a system stiffness of greater than 0.1, or the rigid category, was reached. (Of the footings that were tested, a thickness of 480 mm at full scale and greater classified as rigid.) The tendency of the slope of the load-settlement curve for rigid foundations to be the same means that the behaviour of all rigid foundations was similar.

It was summarised that the behaviour of rigid foundations was independent of actual relative stiffness and minimal soil-structure interaction took place. The deflection of the footing was

negligible, and the settlement of rigid foundations was only dependent on the properties of the supporting ground. For semi-flexible and semi-stiff foundations, both the deformation of the footing and the sand influenced the behaviour of the foundations. The effect of loss of contact is also a point of interest in soil-structure interaction.

2.10.3 Discussion on soil-structure interaction and relative stiffness

Soil-structure interaction plays a role in both pipelines and foundations. Both system types use the concept of relative stiffness to classify the soil-structure interaction that should be anticipated and the overall response of the system.

The classifications, or categories, of relative stiffness range from flexible to rigid. At the ends of the relative stiffness ranges (flexible and rigid) soil-structure interaction is unimportant, and the soil properties become the controlling factor of the system behaviour. When a soil-pipeline system is flexible, interaction is unimportant, and the pipe take the form of the Greenfields settlement curve. When a foundation system is rigid there the interaction is also unimportant because the deflection in the footing is minimal and the settlement is dependent on the supporting ground properties.

Soil-structure interaction is important for semi-flexible and semi-rigid systems, where the deformation of the structure and deformation in the soil impact each other significantly. UTCRCP has been referred to a semi-rigid pavement and it is anticipated that soil-structure interaction will influence its behaviour.

The relative stiffness parameters that were discussed assume elasticity. The exception is the Greenfield's trough width used to calculate the relative rigidity factor for pipe-soil-tunnel systems, which would include true soil behaviour. The behaviour of soil is stress dependent. True relative stiffness changes as load is applied and this will influence interaction in systems.

2.11 SOIL-STRUCTURE INTERACTION AND RELATIVE STIFFNESS OF PAVEMENTS

The distinction between soil and structure is straightforward for foundations and pipelines. The material used for the structure is typically concrete or steel, for which the material properties differ significantly from that of soil (and linear-elasticity is considered to be appropriate). The geometry of the structure is also different than that of the soil. The structure is a body with a finite geometry, such as a rectangular cuboid or a hollow cylinder with a wall thickness, which is typically placed on top of or within a semi-infinite mass of soil.

Pavements consist of a system of layers of unbound and bound materials placed on each other and supported by the subgrade (Huang, 1993). The uppermost layer of pavements usually consists of a bound material such as asphalt or concrete. The subgrade is considered as the foundation of pavements. The system of layers is considered as the structure of pavements (Brown & Selig, 1991). In the case of pavements, soil-structure interaction could be used to consider the interaction between the system of layers and the subgrade. An equivalent stiffness for the layer system, or structure, could be used to determine a relative stiffness parameter.

It should be noted that the properties of the adjacent layers vary in terms of using different materials and using the same materials that are compacted to different densities. Each layer has its own material stiffness properties and adjacent layers will have different relative stiffnesses.

For rigid pavements, the thick concrete layer alone is the structural layer and is placed on a subbase and subgrade that are the foundation. This makes it is easier to make the distinction between soil and structure. In this report, the surfacing bound layer is considered to be the structure and the supporting layers (base, subbase and subgrade) are considered as the soil. The relative stiffness between these two components can be used to investigate the response of pavement systems to load and predict soil-structure interaction. In other words, the bound material, lying on unbound material is the soil-structure system under consideration.

There are two well-known relative stiffness parameters that are used in pavement design. A modular ratio limit is used in the Pavement Number design method developed for flexible pavements. The modular ratio uses the material stiffness of adjacent layers to enforce gradual load spreading with pavement depth. The radius of relative stiffness is used for the analyses of slabs-on-grade, which is used for the design of rigid pavements.

2.11.1 Modular ratio

The modular or modulus ratio was initially introduced by Burmister (1945a) in his paper *"Theory for stresses and displacements in layered systems I"*. It is the ratio of the Young's Modulus of each layer divided by the Young's Modulus of the layer underneath it. It is a measure of relative material stiffness and the relative load spreading ability of adjacent layers in pavements.

Figure 2.22 shows the effect of modular ratio on the vertical distribution of vertical stress (σ_z) in a pavement simplified to a two-layer system consisting of a structural and supporting layer (Burmister, 1958). It shows the vertical stress distribution under the centre of a circular load area. The two layers act together as an elastic, composite system (Burmister, 1945a). The layers

are continuously in contact. Shear resistance is fully active between them and there is full continuity of stress and displacement across the interface. A Poisson's Ratio of 0.5 is assumed.

The vertical stress distribution is also dependent on the ratio between the thickness of the structural layer and the radius (a) of the circular area load. The vertical stress distribution is normalized to the applied stress (q) and the depth is expressed as multiples of the radius $\left(\frac{z}{a}\right)$. In the case illustrated in Figure 2.22, the radius of the circular load area is the same as the thickness of the structural layer (h_1). If a radius of 152.4 mm is assumed, as by Kim (2007), the depth of the structural layer is 152.4 mm.

The decrease in the vertical stress, at the layer interface, as the modular ratio increases shows the improved load spreading ability of materials with high material stiffnesses. For a Boussinesq stress distribution, where the modular ratio is 1, the normalized vertical stress at the interface is 0.68. When the modular ratio is 100, the normalized vertical stress reduces to 0.08 at the interface. A normal strength concrete would typically have a material stiffness, in terms of Young's Modulus, of 30 GPa and be placed on a substructure that has a material stiffness, in terms of Young's Modulus, of less than 300 MPa. The modular ratio would be greater than 100, and the vertical stress at the interface would be reduced to approximately 10% of the pressure on the circular load area.

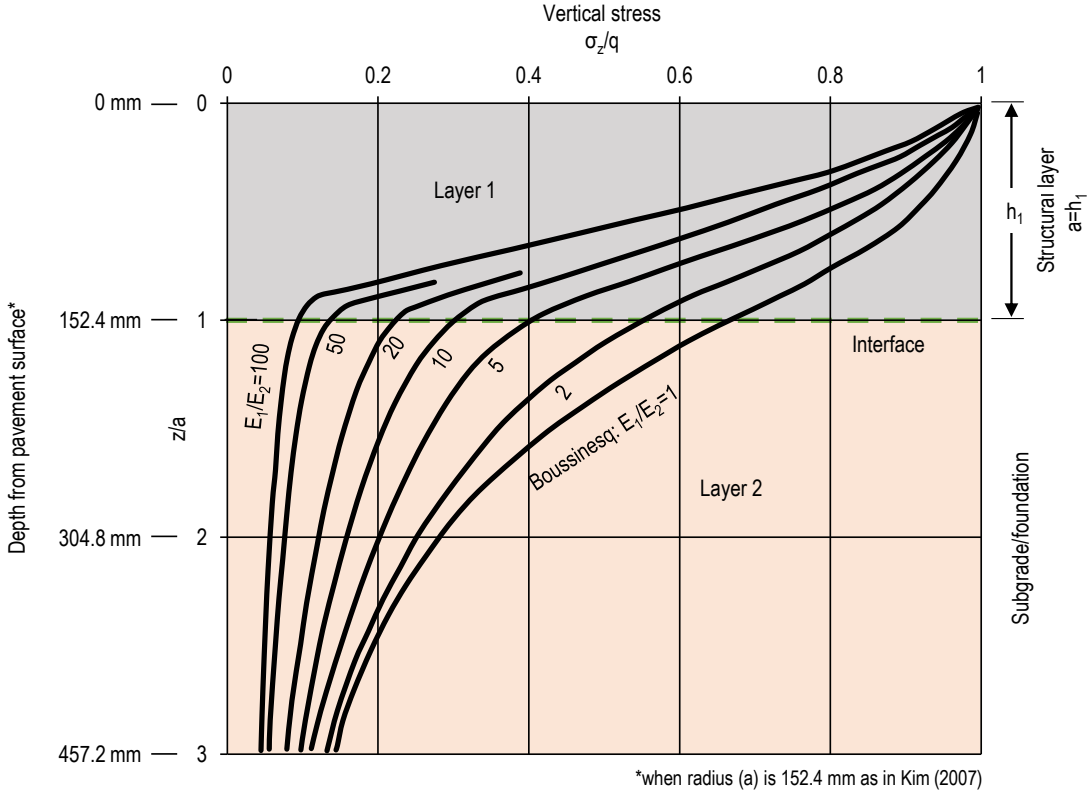

Figure 2.22 Effect of modular ratio on vertical stress distribution (adapted from Burmister, (1958))

Figure 2.23 shows the effect of the modular ratio and structural layer thickness on the vertical stress at the structural layer-substructure interface in the centreline of the circular load area (Huang, 1969). The structural layer thickness is expressed as multiples of the circular load area radius $\left(\frac{h_1}{a}\right)$. Assuming a radius of 152.4 mm, as by Kim (2007), the range of structural layer thickness shown in this chart extends from 76.2 mm to 304.8 mm.

The contour lines show how the stress at the interface decreases non-linearly as the thickness of the structural layer increases. The effect of increasing the thickness is less pronounced for high modular ratio two-layer systems. It can be seen that reducing the thickness of a concrete pavement to as little as 50 mm, can significantly increase the stresses in the supporting layers, resulting in high localized stresses in the substructure.

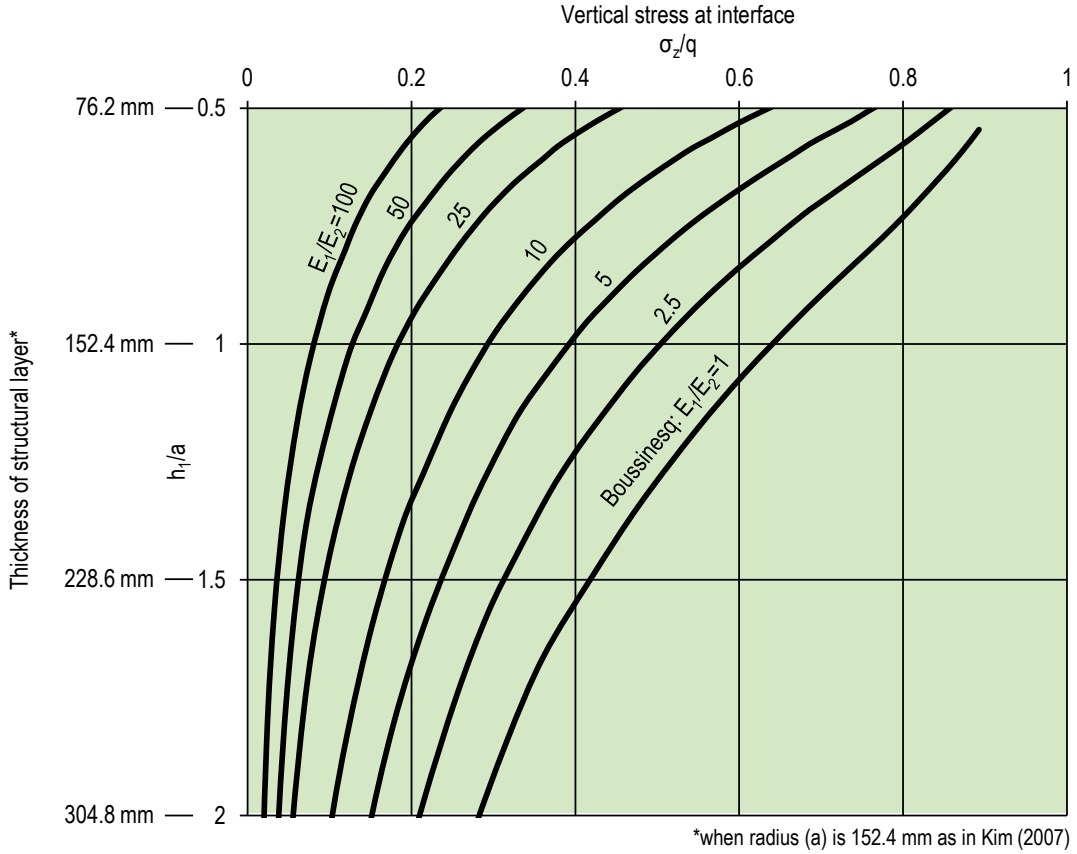

Figure 2.23 Effect of modular ratio on vertical stress at structural layer-substructure interface with increasing structural layer thickness (adapted from Huang (1969))

Assuming perfect continuity between layers, large shear stresses will result if modular ratios between adjacent layers are high. When the overlaying layer is much stiffer than the support, it tends to bend into the support, increasing shear stresses and tensile stresses in itself. These

stresses are only mobilised when the pavement is loaded, and deflection takes place. A design method proposed by Burmister (1962), mentioned in Brown (1967), recommends that ideally there should be a small difference in material stiffness between adjacent layers. Deflection and shear stresses are the critical parameters in the design method and should not exceed permissible values.

The concept of limiting the modular ratio has been extended to other design methods. Pavements that limit the modular ratio between adjacent layers spreads load progressively with depth, ensuring that layers with decreasing strengths are not overloaded. These pavements are referred to as balanced pavements (SANRAL, 2013).

The Pavement Number design method incorporates a modular ratio limit to ensure that balanced pavements are built. The design method is used for Category A and B roads, designed for traffic between 1 and 30 million equivalent standard axles and roads with thin asphalt surfacing. The Pavement Number design method uses an effective long-term stiffness, which has a maximum allowable limit, to determine modular ratios. Typical modular ratio limits range between 2 to 1.2 for unbound granular materials (G1 to G10), 9 to 3 for cement bound granular materials (C1 to C4) and 2 to 5 for materials that incorporate asphalt and bitumen (SANRAL, 2013). The modular ratio between concrete and granular material or subgrade is typically very high.

2.11.2 Radius of relative stiffness

Westergaard (1926) introduced the radius of relative stiffness in his analytical solutions to determine stresses in concrete pavements. It is a characteristic length of a pavement system. The concept of a characteristic length is used in the mechanics of a diverse range of structural systems, such as pile foundations and beams-on-elastic foundations (Ioannides, 2006). It is a linear dimension, comparable to the radius of gyration. The radius of relative stiffness for systems that use spring foundations, denoted by l_k, is defined by Equation 2.17:

$$l_k = \sqrt[4]{\frac{E_c h^3}{12(1-{\nu_c}^2)k}} \qquad \textbf{Equation 2.17}$$

Where the stiffness properties of the concrete slab are the material stiffness (Young's Modulus), E_c, and Poisson's Ratio, ν_c, and the thickness, h. The stiffness of the supporting layer is quantified by the modulus of subgrade reaction, k. The modulus of subgrade reaction is determined using a plate bearing test or it can be back-calculated from the deflected shape of pavements (Bowles, 1996; Westergaard, 1926).

The radius of relative stiffness remains constant if E_c and k are multiplied by the same factor. The influence of the thickness of the slab on the radius of relative stiffness is raised to the power of three. Increasing the modulus of subgrade reaction reduces the radius of relative stiffness.

The radius of relative stiffness calculated by Westergaard (1926) ranged from 430 mm to 1385 mm and it is stated that a typical value is 914 mm. It has also been stated that the radius of relative stiffness should fall between 570 mm and 2032 mm, where the lower limit is selected considering that pavement systems with low radius of relative stiffness values cannot be modelled adequately using a slab-on-grade model (ARA & Division, 2004; Gerber, 2011).

Ioannides (2006) mentioned that the series of equations proposed by Losberg (1960), which are in a form analogous to those proposed Westergaard (1926), can be used as alternative formulation of the radius of relative stiffness. Equation 2.18 shows the formulation and how the modulus of subgrade reaction is replaced by the material stiffness (Young's Modulus), E_s, and Poisson's Ratio, ν_s, of the subgrade:

$$l_e = \sqrt[3]{\frac{E_c h^3 (1 - \nu_s^2)}{6(1 - \nu_c{}^2) E_s}} \qquad \textbf{Equation 2.18}$$

The radius of relative stiffness has rarely been used as a parameter to predict pavement behaviour. Recently, the radius of relative stiffness was used to predict the maximum flexural edge stress in concrete pavements in a simplified approach using regression equations (Vishwakarma & Ingle, 2017). The effect of panel size and radius of relative stiffness on the critical stresses in concrete pavements was also investigated by the same authors (Vishwakarma & Ingle, 2018).

The radius of relative stiffness contains most of the components that the relative stiffness descriptors of other civil engineering systems use to predict the soil-structure interaction of the systems. It has the potential to be used to categorise the soil-structure interaction of pavement systems, as well as wheel load interaction.

The equivalent of the radius of relative stiffness in Westergaard's solutions in the basic beam-on-elastic support is the reciprocal of β. Equation 2.19 shows that β contains a variation of the same variables that are used to calculate the radius of relative stiffness. It does not incorporate the Poisson's Ratio.

$$\beta = \sqrt[4]{\frac{k}{4E_c I}} \qquad \textbf{Equation 2.19}$$

2.12 DEFLECTION BOWLS OF PAVEMENTS

Deflection bowls are the result of the response of the pavement structure to applied load. It consists of a partially circular, deflected indentation that forms around the loaded area (Horak, 2008). The applied load generates stress in the system that dissipates with depth (Brown, 1996; Huang, 1993). Deflection bowls are also referred to as deflection basins.

Deflection bowls are used for condition assessment of road pavements. This is done by back-calculating material stiffnesses of pavement components iteratively until the calculated deflection bowl fits the measured deflection bowl (Brown & Selig, 1991). Typically, layered elastic theory is used, but spring foundations have also been used for the back-calculation of rigid pavements. The structural capacity of layers is determined by comparing the iteratively determined material stiffnesses with expected values for the pavement design life.

Deflection bowls are determined using non-intrusive measurement techniques such as the Falling Weight Deflectometer (FWD), Benkelman beam or deflectographs (SANRAL, 2014). An FWD makes use of an impulse force created by dropping a predetermined weight from a predetermined height to cause deflections, which are typically measured using equally spaced velocity transducers. Deflection bowls can also be determined using in-situ displacement measurement of the pavement layers. Multi-Depth Deflectometers (MDDs), a measurement device that is retrofitted into pavement layers, are used for this purpose. The measured deflection bowls are dependent on pavement structural aspects and load aspects, as well as instrumentation and climate.

The entire deflection bowl is useful for the analyses of pavements (Horak, 2008). Deflection bowls have three distinct zones of curvature. Figure 2.24 shows the zones. The positive curvature at the load location gauges the structural conditions of the upper layers. The middle pavement layers are measured by the inflected zone and is predominantly influenced by the pavement structural composition. The lower layers are represented by the reverse curvature zone furthest from the load location. The depth of the pavement governs the reverse curvature zone. In flexible pavements the positive curvature zone typically occur within a radius of 300 mm and the inflection zone lies within a radius of 300 mm to 600 mm. The reverse curvature zone stretches from 600 mm to approximately 2000 mm away from the load location.

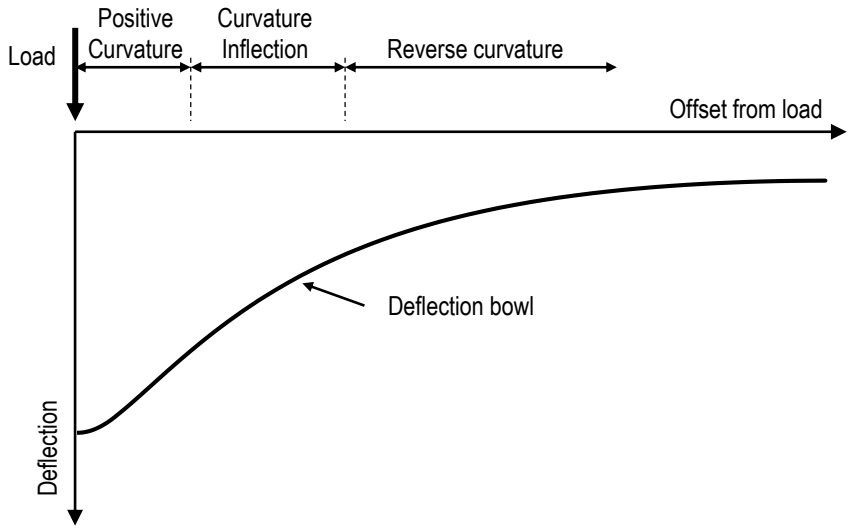

Figure 2.24 Zones of curvature of deflection bowl (adapted from Horak (2008))

Principles of dimensional analysis have been used to interpret deflection bowl data of rigid pavements. A relationship between the radius of relative stiffness and the average deflection of a deflection bowl has been determined.

The solutions from the back-calculations are not unique if the pavement geometry and material properties are not adequately defined and back-calculation programs are user sensitive. This has resulted in very different back-calculated results from the same program for the same pavement cross sections. Other problems with back-calculation are related to the theoretical assumptions of material continuity, homogeneity and elastic behaviour and static loading. Linear-elasticity has been noted as a particular shortcoming, where the match between the measured and computed surface deflection can be improved by modelling the subgrade using a non-linear material stiffness (Brown *et al.*, 1986 quoted by Brown 1996). Another issue with the back-calculation, is that the material stiffnesses cannot be guaranteed to be reasonable results, especially when thin pavement layers are used. When thin layers are used, deflection bowls become insensitive to the material stiffness of the thin layers and matches can be derived for unrealistic moduli.

2.13 SUMMARY

Pavement design is a process in which critical stresses of pavements are minimized. Pavement type determines which stresses are considered critical. The structural analysis of pavements is used to predict critical stresses and their magnitude. A series of assumptions have to be made

to enable structural analyses. With the advancement of computational technology, it has become viable to model pavement systems to greater complexity.

An overview of the complex behaviour of pavement substructure was given. The effect of compaction, overconsolidation and lateral earth pressure at-rest on the initial stress state in the pavement substructure was explored. An introduction to traffic loading in the critical state framework was given and the effect of stress ratio on the response of granular material and pavement performance was discussed.

From the summary of previous research on UTCRCP and HS-SFRC it was found that the design methodology of UTCRCP in South Africa was extrapolated from conventional concrete pavement design methodology to incorporate the improved characteristics of concrete due to the inclusion of high strength concrete and steel fibres. MLLE is used for structural analyses in cncPAVE. APT of UTCRCP in South Africa showed that the concrete slab performed well regardless of support and that cycles of wetting had to be introduced to force the pavement to fail. Gerber (2011) also introduced wetting to force failure. He found that the deflection of the concrete layer was notable and that it increased as more load cycles were applied. The deflection at a depth of 170 mm remained relatively constant, not increasing as more load cycles were applied. Roesler *et al.* (2012) remarked that thin concrete overlays tended to deflect excessively and that the supporting structure needs to be designed to prevent it. In terms of steel mesh spacing it was found that there is little benefit in using rectangular mesh apertures in concrete slabs, because the direction of least steel content determines the load absorption.

A review of the numerical modelling of SFRC slabs-on-grade showed that including more complex material models for the foundation results in a more accurate numerical modelling of the response. This being said, the extent of complexity of the research was limited to varying the spring stiffness. The inclusion of elasto-plastic behaviour of granular material and subgrade in analysis of concrete pavements is limited.

The numerical modelling of granular materials for pavements problems was reviewed to find that stress-dependent material stiffness models are used relatively often for flexible pavements. The use of elasto-plastic material models in industry is limited, with more application in research. Material models based on the critical state framework, such as the Cam-Clay model, are rarely used and primarily for the subgrade. In the cases where the Cam-Clay model was used, it was found that greater rutting strains were predicted, although the critical parameters of the asphalt layer was not affected significantly.

Cement stabilized granular materials are often used in road pavements. Incorporating cement stabilized bases in UTCRCP has the potential to force gradual load spreading with depth.

Cement stabilized layer are sometimes meant to deteriorate to its equivalent granular state. Insufficient degradation can result in reflection cracking in asphalt pavements. The use of cement stabilized materials in UTCRCP is of interest because it is anticipated that, instead of reflection cracking, stress concentrations will occur in the substructure, resulting in its accelerated deterioration.

The stress overlap at opposite ends of an axle is often ignored in the analyses of conventional flexible and rigid pavements. The alternative nature of UTCRCP, with a very thin concrete layer (50 mm) that has a much higher material stiffness than asphalt, leads to the proposal that the interaction between the wheel arrangements at the ends of an axle should be considered in the design process. The use of physical modelling of road pavements was explored. APT is used to evaluate the performance of pavements. It was found that load configurations that consider wheels arrangements on opposite sides of axles are rarely considered when doing APT. There have however been developments into modelling wheel wander and the effect of unidirectional and bi-directional loading is well understood. A shortcoming of APT on UTCRCP was that loading was applied through a dual wheel considering one side of an axle. The recent development of using centrifuge modelling for pavement problems was also investigated, finding that a variety of load configurations and ways to measure the pavement response have been applied.

The effect of relative stiffness on the soil-structure interaction of civil engineering systems was discussed. The differences between pavements and other civil engineering systems were highlighted, while the use of relative stiffness to predict pavement behaviour was proposed. Relative stiffness parameters for pavements, such as modular ratio and radius of relative stiffness, were discussed. The use of deflection bowls was also discussed.

The superior flexural strength and post-crack load carrying capacity of HS-SFRC results in an overlay that can withstand millions of axle loads without failing. The significantly reduced thickness, and flexural stiffness, does however allow the pavement system to deflect notably. Observed behaviour of UTCRCP indicates it is not a rigid pavement, however it has also been shown that it can withstand millions of cycles under conditions of poor support. The response of UTCRCP to traffic loading should be investigated considering load configuration, relative stiffness and substructure behaviour to assist in determining suitable design assumptions for this not-rigid concrete pavement.

Based on the literature reviewed the following questions related to the pavement design and practical application of UTCRCP were identified:

- Is it viable to simplify traffic loading configurations to strip loading and how does strip loading and 3D loading affect pavement response?
- Can concepts of relative stiffness be used to predict the extent of wheel load interaction and if a pavement should be modelled as a flexible pavement?
- Should UTCRCP be modelled as a flexible pavement where the substructure properties are important, and rutting is a traffic associated failure mechanism?
- Is it useful to incorporate stress-dependent, elasto-plastic soil material models to numerically model the substructure of pavements that use thin concrete overlays?
- Is it necessary to include significant amounts of steel reinforcement in the longitudinal and transverse direction?
- Is it useful to incorporate cement stabilized bases in UTCRCP to improve load spreading?
- Should numerical and physical modelling of UTCRCP use axle loading instead of a single wheel and are important aspects of the pavement response ignored if axle loading is not used?

3 EFFECT OF LOAD CONFIGURATION AND RELATIVE STIFFNESS ON ROAD PAVEMENT RESPONSE TO TRAFFIC LOADING

3.1 INTRODUCTION

The stress distribution in UTCRCP, with its very thin HS-SFRC layer, has the potential to be significantly different to that of conventional flexible and rigid pavement types. The effect of load configuration and relative stiffness on road pavement response should be explored to improve our understanding of the response of UTCRCP to traffic loading.

Three approaches were used to investigate the effect of load configuration and relative stiffness on the road pavement response:

1. The potential interaction between wheel arrangements at opposite ends of axles is usually ignored. The effect of wheel and axle load configuration on thin asphalt and thin concrete pavements was investigated using 3D FE modelling.
2. It has been noted that the permanent deformation of road pavements is a plane strain problem in circumstances with no wander. The difference between 3D and plane strain models, or circular and strip loading, of a thin concrete pavement was investigated using FE modelling.
3. The extent of wheel load interaction is dependent on the relative stiffness of a pavement structure. Beam-on-elastic-support calculations were used to investigate wheel load interaction for pavements with different relative stiffnesses.

In this chapter, 3D and plane strain FE modelling, in the general-use FE analyses program ABAQUS/Standard (Dassault Systemes Simulia Corp, 2016), were used to allow control over all boundary conditions and other assumptions. An isotropic, LE constitutive material models were used for all FE modelling. A three-layer road pavement system, with a bound layer, base layer and subgrade, was used. In this research a bound layer refers to a pavement layer that consists of a material such as asphalt or Portland cement concrete which is usually the uppermost layer (or surfacing) of the pavement.

A 3D FE road pavement model was adapted from literature. The effect of changing the load configuration from single wheel load to two-wheel axle load for asphalt and concrete was compared by changing the material properties of the bound layer. The 3D concrete bound layer FE model with two-wheel axle loading was simplified to a plane strain model to support the findings in Chapter 5 where physical models of road pavements were tested using strip loading. The effect of relative stiffness on the wheel load interaction in the basic beam-on-elastic support

formulation was also investigated. This was done to enable an elementary understanding of the effect of the components of analytical models. Two point loads were applied to simulate the wheel loads at opposite ends of an axle. Combinations of bound layer thickness and material stiffness and support stiffness were used to vary the relative stiffness.

To investigate pavement response the sensitivity of the selected critical parameters (vertical displacement, stress and strain in the concrete layer and substructure in the wheel centreline) for pavement design were considered, along with the deflection of the pavement surface and contour plots of vertical and horizontal displacement of the substructure.

3.2 REPLICA OF FE MODEL BY KIM (2007)

The pavement model used in this chapter was adapted from Kim (2007), who used 3D FE analyses to consider the effect of non-linear pavement foundation behaviour. Initially, the domain size of a 3D FE model with negligible boundary effects was determined. This was done to make the model comparable to MLLE models. MLLE assumes that horizontal and vertical boundaries are infinitely far from where the load is applied. Kim (2007) compared selected critical parameters of the 3D model with those from the MLLE program, KENLAYER. The required depth and horizontal distance were expressed in terms of the radius (a) of the circular area over which the load is applied. It was determined that a depth of $140a$ and horizontal distance of $20a$ were sufficient for negligible boundary effects. This 3D model was replicated and adjusted to investigate the effect of load configuration and relative stiffness.

The general-use FE analyses program ABAQUS/Standard (Dassault Systemes Simulia Corp, 2016) was used. As in Kim (2007), a three-layer system was modelled. Isotropic, linear-elastic material properties were assumed for each layer. The thicknesses and the material properties of the respective layers used by Kim (2007) are listed in Table 3.1. The properties used by Kim (2007) for asphalt bound layer were initially retained. Tension cut-off for the base and subgrade was not modelled, thus the redistribution of stresses due to the inability of soils to sustain low levels of tension was not considered. The layers were modelled as one part, ignoring interaction between the layers. The sensitivity of the pavement response to Poisson's Ratio and bound layer-substructure interaction are summarised in Appendix A.

In ABAQUS, a Young's Modulus and a Poisson's Ratio have to be defined for linear-elasticity. In pavement engineering, the Young's Modulus would typically be a secant modulus of the axial stress-strain response of the respective materials. The secant modulus may be of the resilient response or the stress-strain response at any stage of the pavement life. Unless stated otherwise, material stiffness refers to Young's Modulus in this study.

Table 3.1 Layer thicknesses and material properties

Layer	Thickness (mm)	Young's Modulus (MPa)	Poisson's Ratio
Bound Layer (BL)	76	2 759	0.35
Base	305	207	0.4
Subgrade	140a-(BL+Base)	41	0.45

Similar to Kim (2007) the depth and horizontal distance were 140a and 20a respectively. The load was applied over a circular area with a radius of 152.4 mm. A pressure of 550 kPa was used to represent a standard axle wheel load of 80 kN, where 40 kN is applied per side of the axle. Quarter symmetry was assumed. The axis of symmetry in the transverse and longitudinal direction was taken as the centreline of the circular load area in the respective directions. Roller support boundary conditions were used for the vertical boundaries and at the bottom of the model. Although Kim (2007) did not report the mesh arrangement in detail, an attempt was made to replicate it. Figure 3.1 shows the geometry and mesh reported by Kim (2007) and Figure 3.2 shows the mesh used in the replica model.

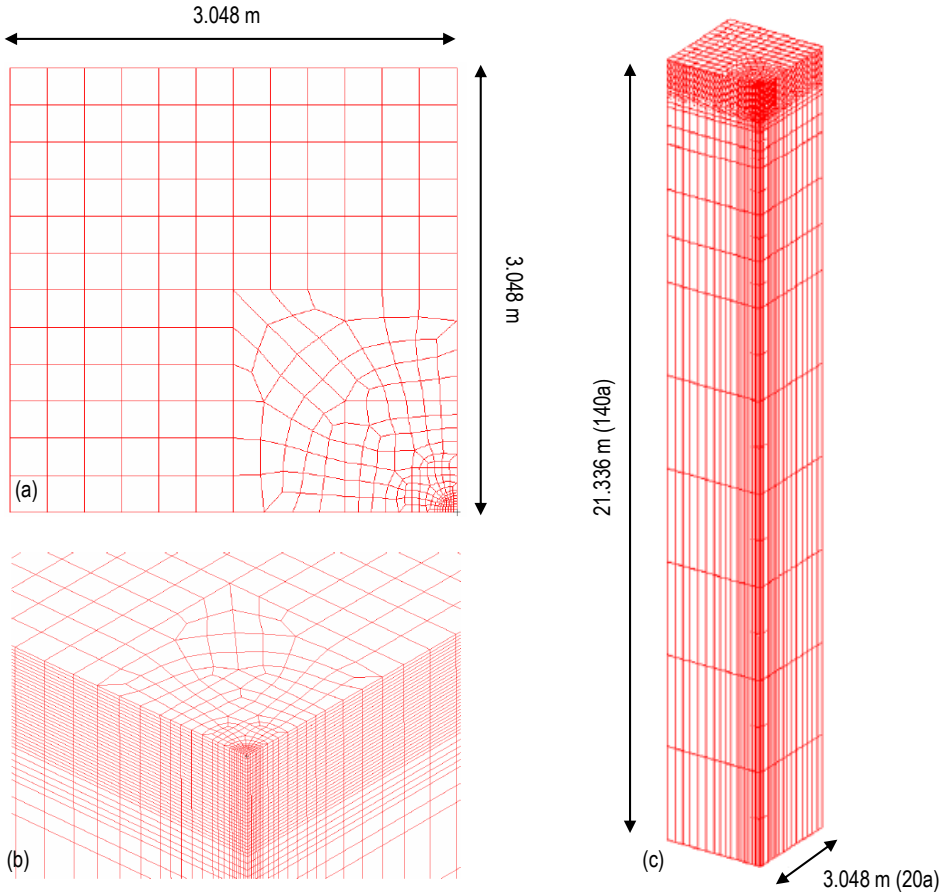

Figure 3.1 Model dimensions and mesh of Kim (2007) (a) plan view, (b) top isometric view and (c) full depth isometric view

The element type used was 20 node quadratic brick elements with reduced integration (C3D20R). Swept meshing was used. The mesh fineness decreased further from the zone of interest where the pressure is applied. Figure 3.2 (a) gives a plan view of the mesh. In terms of depth, six elements were fitted into the 76 mm bound layer, resulting in an element height of 12.67 mm. The same element height was used for the base. The element height was progressively increased to 5 m in the subgrade toward the bottom of the model. Figure 3.2 (b) shows how the aspect ratio of the elements further away from the zone of interest falls outside the normally accepted limits with an aspect ratio smaller than 5 generally deemed to be acceptable (MacDonald, 2011). The use of quadratic elements partially mitigates the effect of element aspect ratio (Cho *et al.*, 1996).

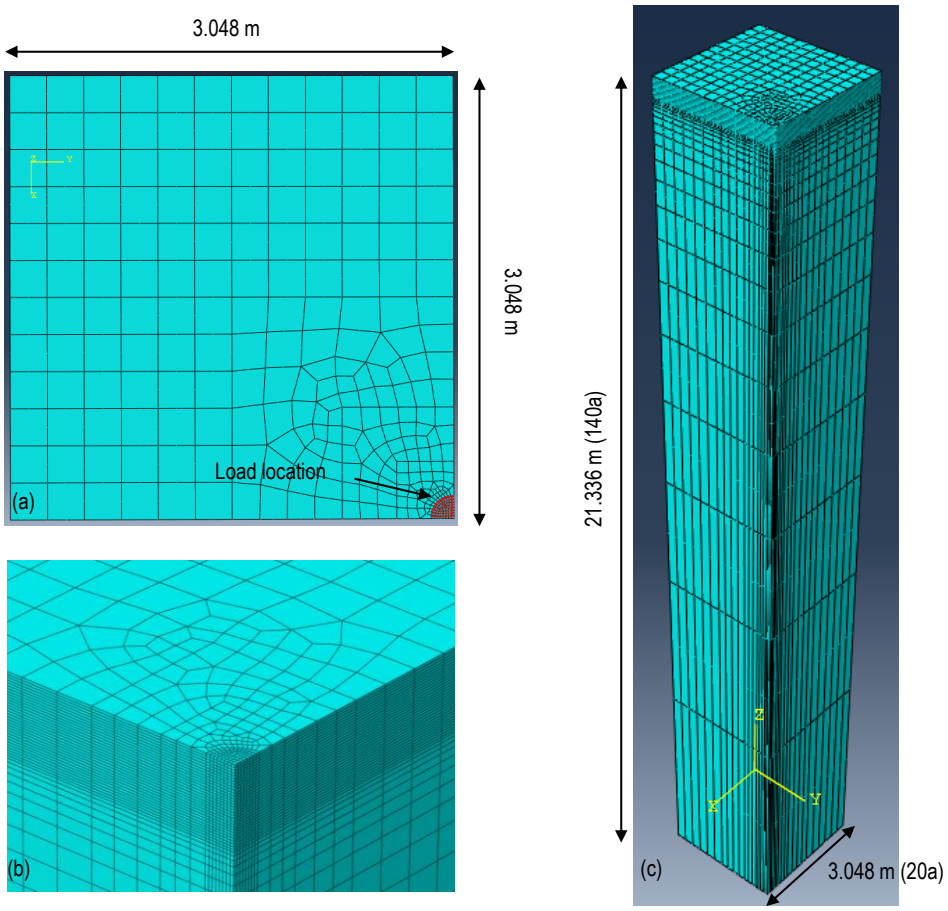

Figure 3.2 Model dimensions and mesh of replica (a) plan view, (b) top isometric view and (c) full depth isometric view

The critical parameters considered by Kim (2007) were all measured along the wheel centreline and included the vertical deflection of the model surface, transverse horizontal tensile stress at the bottom of the bound layer, as well as the vertical stress and strain at the top of the subgrade. The locations of the critical stresses are shown in Figure 3.3. Values extrapolated to the nodes were reported. Tensile stress and strain were taken as positive.

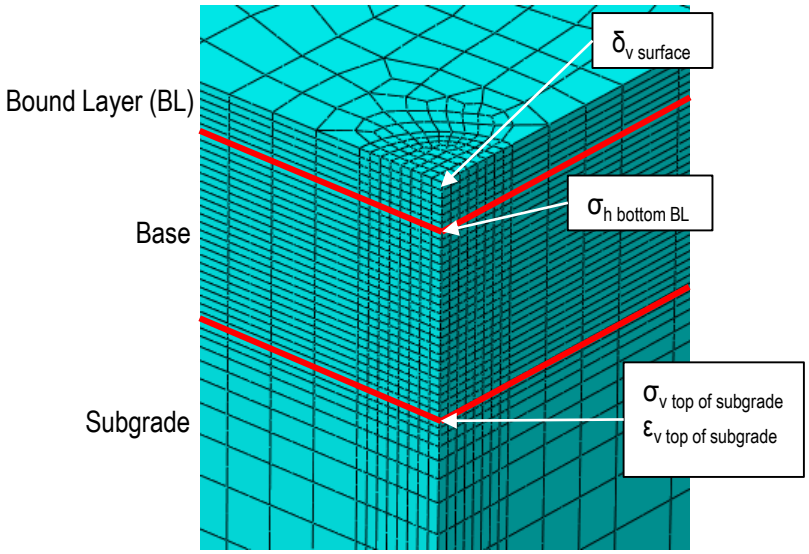

Figure 3.3 Locations of critical parameters

The critical parameters reported by Kim (2007) and those extracted from the replica model are summarised in Table 3.2. The number of elements used per model is also reported. More elements were used in the replica model. The only parameter that was not in good agreement with that reported by Kim (2007) was the tensile stress at the bottom of the asphalt bound layer. The replica values were verified by using locally available FE analysis and MLLE software i.e. Finite Element Method for Pavement Analysis (FEMPA) (Maina *et al.*, 2008) and General Analysis of Multi-layered Elastic Systems (GAMES) (Maina & Matsui, 2004). All four critical parameters from the additional analyses were in good agreement with those extracted from the replica.

Table 3.2 Comparison of critical parameters of Kim (2007), replica, FEMPA and GAMES

Model	Critical parameter				Number of elements
	$\delta_{v\ surface}$ (mm)	$\sigma_{h\ bottom\ of\ BL}$ (kPa)	$\sigma_{v\ top\ of\ subgrade}$ (kPa)	$\varepsilon_{v\ top\ of\ subgrade}$ (μm/m)	
Kim (2007)	-0.909	770	-40	-930	15 168
Replica	-0.913	1364	-41.7	-974	16 430
FEMPA	-0.923	1328	-39.6	-961	
GAMES	-0.924	1353	-41.8	-975	

3.3 EFFECT OF LOAD CONFIGURATION ON THIN BOUND LAYER PAVEMENTS

To simulate the effect of having a thin HS-SFRC bound layer (instead of asphalt as in the replica models), the material stiffness and Poisson's Ratio of the bound layer were changed. The layer thicknesses remained constant as well as the material properties for the base and subgrade. The material property of the bound layer remained isotropic, linear-elastic. Typical material properties for HS-SFRC were used. A material stiffness of 40 000 MPa and a Poisson's Ratio of 0.17 were selected (Kearsley *et al.*, 2014). The effect of cracking was not considered. The model with HS-SFRC material properties is referred to as the concrete model. The model with asphalt material properties is referred to as the asphalt model.

To investigate the effect of modelling an axle with a wheel at each end, instead of a single wheel, the geometry of the replica model was adjusted. The typical axle length to the wheel centreline at opposite ends is 1.98 m. As with the single wheel model, load was applied as a pressure on a circular area. The radius remained constant at 152.4 mm. Quarter symmetry was used. Figure 3.4 shows the adjusted geometry. All thicknesses remained constant, while the bound layer material properties were varied between that selected for asphalt and concrete.

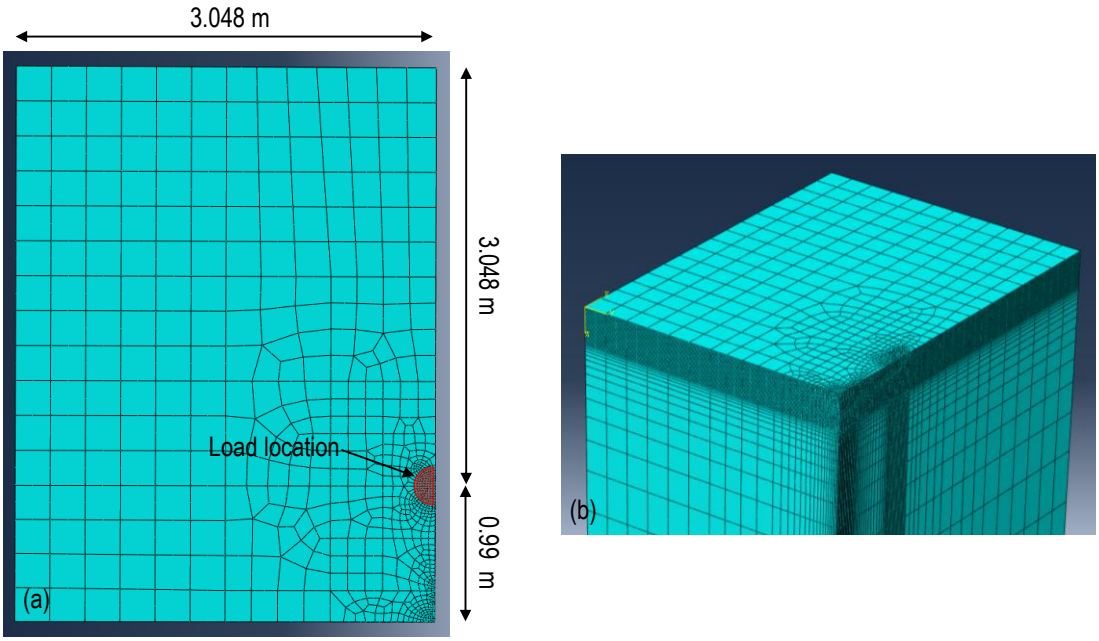

Figure 3.4 Axle model with (a) plan view and (b) isometric view

3.3.1 Effect of bound layer type

Table 3.3 shows the critical parameters obtained from the asphalt and concrete models. The selected material stiffness of concrete was approximately fifteen times greater than that selected for asphalt. It was anticipated that the response would be significantly different. The vertical

deflection of the surface of the concrete model was less than that of the asphalt model, the tensile stress was greater, while the stress and strain at the top of the subgrade was approximately halved.

The high tensile stress shows how the concrete layer dominated as a structural layer. It also confirms the necessity of incorporating HS-SFRC to ensure that the stress level (tensile stress over strength) remains low and that the materials' good fatigue performance is taken advantage of. The lower stress and strain at the top of the subgrade show how the concrete layer radiates (or spreads) the load (and stress) further from the load location, also resulting in a lower vertical deflection.

Table 3.3 Critical parameters of asphalt and concrete pavements

Bound layer type	Critical parameter			
	$\delta_{v\ surface}$ (mm)	$\sigma_{h\ bottom\ of\ BL}$ (kPa)	$\sigma_{v\ top\ of\ subgrade}$ (kPa)	$\varepsilon_{v\ top\ of\ subgrade}$ (μm/m)
Asphalt	-0.913	1364	-41.7	-974
Concrete	-0.59	4747	-21.9	-473

The deflection bowl and normalized deflection bowl of the surface of the asphalt and concrete models can be seen in Figure 3.5. The figure shows how the asphalt layer deflected more than the concrete from the wheel centreline to approximately 0.75 m away from the wheel centreline, where after the deflected shape was similar. The calculated deflection was normalized with respect to the maximum deflection of the respective models. The normalized deflected shape illustrates how a larger proportion of the maximum deflection was spread more widely for the concrete model.

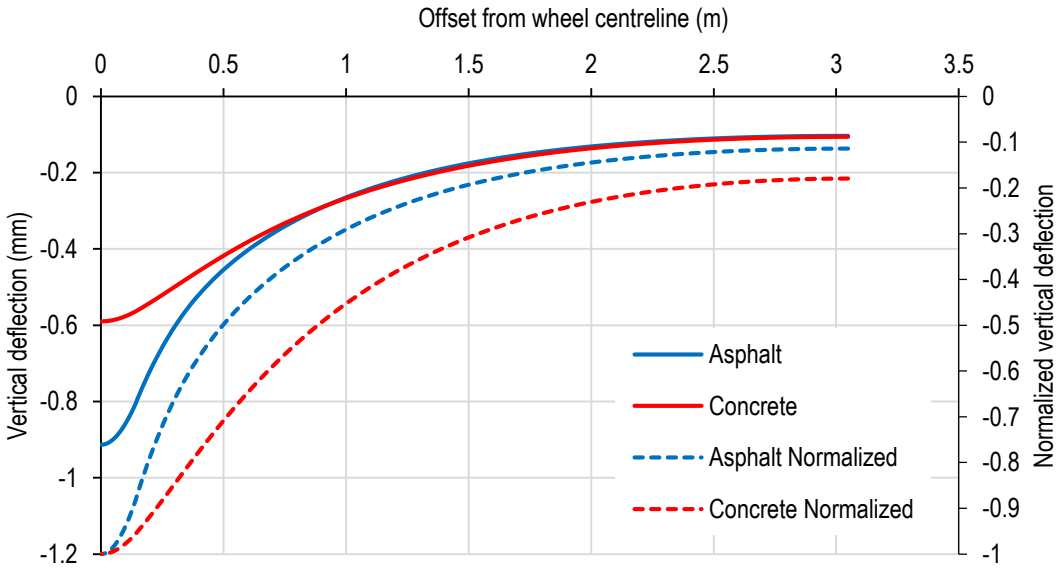

Figure 3.5 Deflection and normalized deflection bowl of asphalt and concrete pavement

Figure 3.6 shows contour plots of the vertical and horizontal displacement of the asphalt and concrete models up to a depth of 5 m. The total model depth was 21.336 m. Note that downward vertical displacement is negative and horizontal displacement to the right is positive. Figure 3.6 (a) shows that the vertical displacement was greater for the asphalt model in the immediate vicinity of the load location. From the -0.3 mm vertical displacement contour, the magnitude of displacement of the asphalt and concrete models became similar. Vertical displacement of - 0.14 mm occurred at a depth of approximately 3.5 m. The -0.14 mm vertical displacement contour line was slightly narrower towards the top of the model for the asphalt and also reached deeper into the model than for the concrete.

The horizontal displacement, Figure 3.6 (b), was order of magnitude smaller than the vertical displacement for both models. The further from the load location, the more similar the displacement of the models were, although the horizontal displacement of the asphalt model reached deeper. For both models the contour lines had a similar shape, indicating that the substructure response for the two bound layer types was similar and that rutting might be a traffic associated failure mechanism for pavements that use thin concrete layers as it is for flexible pavements.

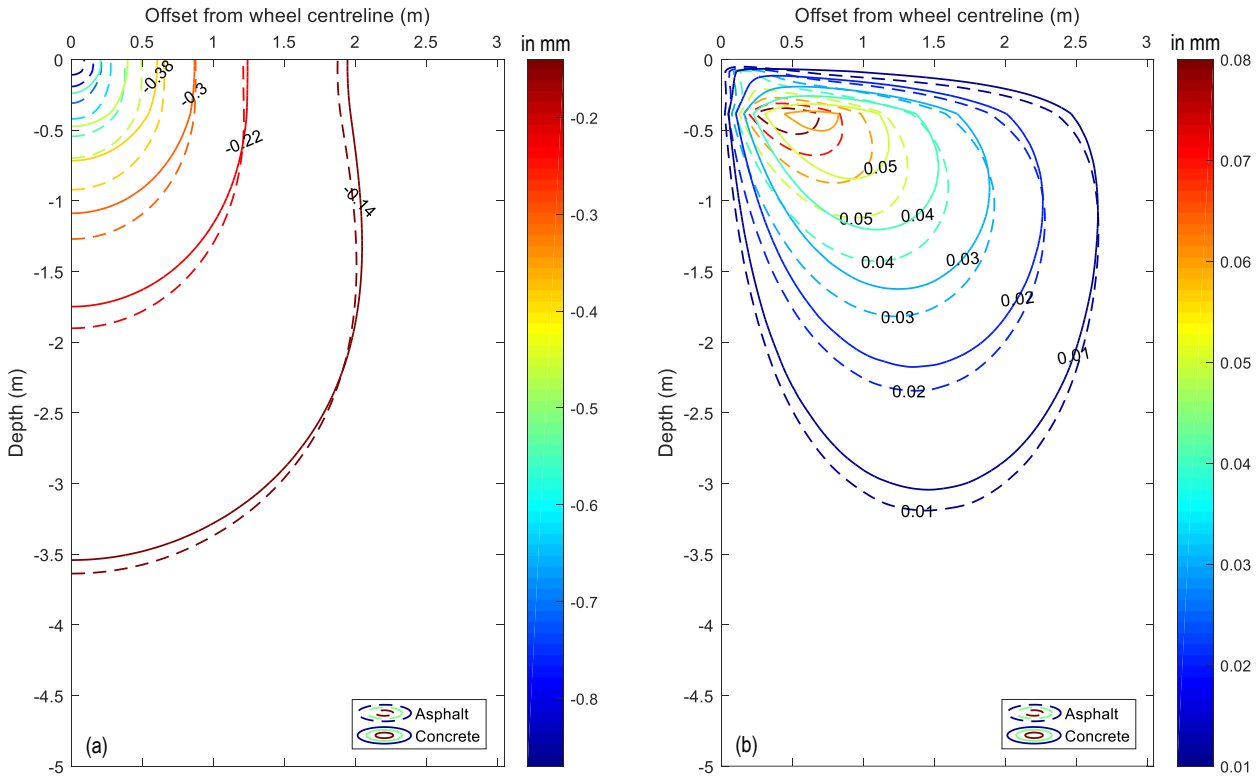

Figure 3.6 Contour plot of the (a) vertical and (b) horizontal displacement

3.3.2 Effect of load configuration

The same critical parameters discussed in Section 3.2 were compared to investigate the effect of load configuration on the asphalt and concrete models. Table 3.4 contains the critical parameters. It also contains the percentage difference for each critical parameter, calculated using Equation 3.1. The critical parameters of the Single Wheel (SW) models were used as the original values.

$$\text{Difference (\%)} = \frac{\text{Original value} - \text{New value}}{\text{Original value}} \text{x}100 \qquad \textbf{Equation 3.1}$$

The vertical displacement along the wheel centreline for both the asphalt and concrete models was greater when an axle was modelled. This is because the full 80 kN of a standard axle wheel load was applied when an axle was modelled. The percentage difference in vertical deflection was greater for the concrete model. This can be explained by referring to the response of the SW models in Section 3.2. The deflection bowl of the concrete model was wider and thus the interaction between two deflection bowls placed at a distance apart (in this case 1.98 m) should be greater. Due to the wider deflection bowls, the vertical displacement contours of the SW concrete model were also wider. This means that a greater proportion of the vertical displacement would overlap (and be superimposed) for the axle load concrete model.

The effect of axle loading on the asphalt model in terms of transverse horizontal tensile stress at the bottom of the bound layer was very small, while it was slightly more pronounced for the concrete model. A similar observation could be made regarding the vertical stress and strain at the top of the subgrade.

Table 3.4 Critical parameters of asphalt and concrete, single wheel and axle loading models

Bound layer type	Load configuration	Critical parameter			
		$\delta_{v\ surface}$ (mm)	$\sigma_{h\ bottom\ of\ BL}$ (kPa)	$\sigma_{v\ top\ of\ subgrade}$ (kPa)	$\varepsilon_{v\ top\ of\ subgrade}$ (μm/m)
Asphalt	SW	-0.913	1364	-41.7	-974
	Axle	-1.011	1362	-41.9	-965
	Difference (%)	-10.75	0.092	-0.508	0.879
Concrete	SW	-0.59	4747	-21.9	-473
	Axle	-0.692	4637	-22.3	-466
	Difference (%)	-17.32	2.314	-1.791	1.395

In terms of the stress and strain critical parameters, the benefit of modelling an axle instead a single wheel was marginal. The vertical surface deflection was affected more significantly. The effect of modelling an axle was more pronounced for the concrete model. Although the critical parameters indicate that the effect of the load configuration was marginal the deflection bowls and substructure response were also considered.

Figure 3.7 shows the transverse deflection bowls for asphalt and concrete when the models were loaded using a single wheel or an axle. The deflection bowls of the SW models would be the same in the transverse and longitudinal directions of the pavement. The axle centreline (CL) and wheel centreline (CL) are indicated. The overall deflections of the axle models were greater because 80 kN, instead of only 40 kN, was applied and the displacement caused by the respective wheel loads overlap.

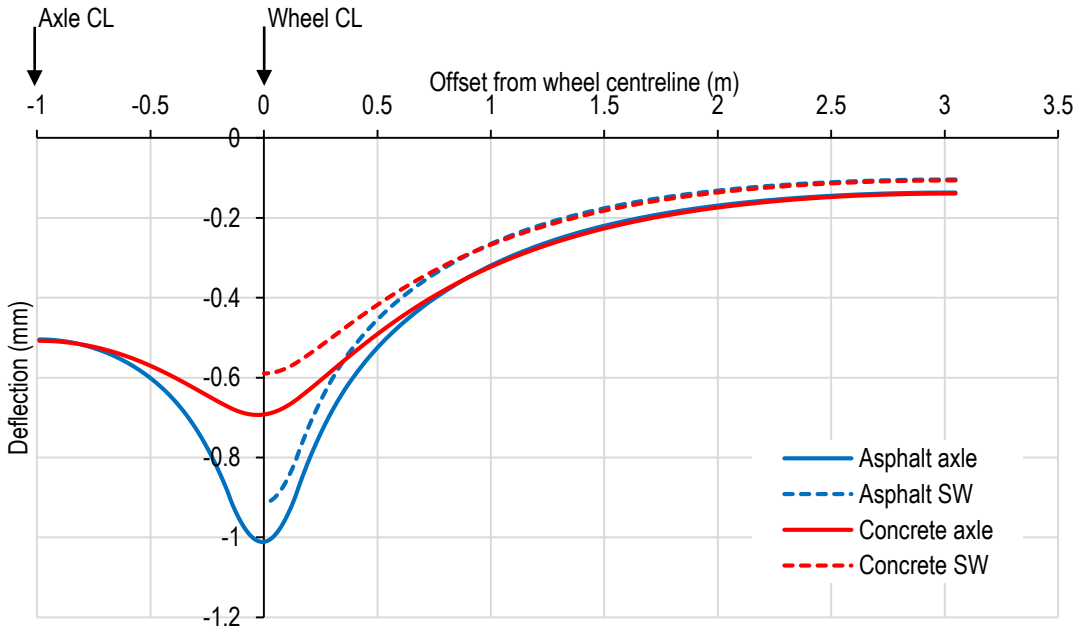

Figure 3.7 Transverse deflection bowls of asphalt and concrete, single wheel and axle loading models

In Figure 3.8 the deflection bowls were normalized to the maximum deflection of the respective models. The deflection from the centreline of the axle to an offset of 1 m is shown. The symmetry assumption of the SW model means that the same deflection is measured at either side of the wheel centreline. The figure highlights the difference in deflection that occurs between the centreline of the wheel and the centreline of the axle if a single wheel is modelled instead of an axle. From the wheel centreline to the free end (that is from 0 m towards 1 m) there is a small difference between single wheel and axle loading for both asphalt and concrete. From the wheel centreline to the axle centreline (0 m to -1 m), deflected shape diverges.

Figure 3.8 also shows that the difference between single wheel and axle loading was slightly more severe for the concrete model than for the asphalt model. For the asphalt model the difference remains small up to an offset of approximately -0.15 m (left from the wheel centreline). From this figure it is noted that there was a considerable difference between the deflection bowls of single wheel and axle load configurations for both asphalt and concrete road pavements. For matching deflection, the LE modelling of both pavements would benefit from modelling axle loading instead of a single wheel loading. The LE modelling of representative load configurations becomes more important when the relative stiffness between the bound layer and substructure is greater.

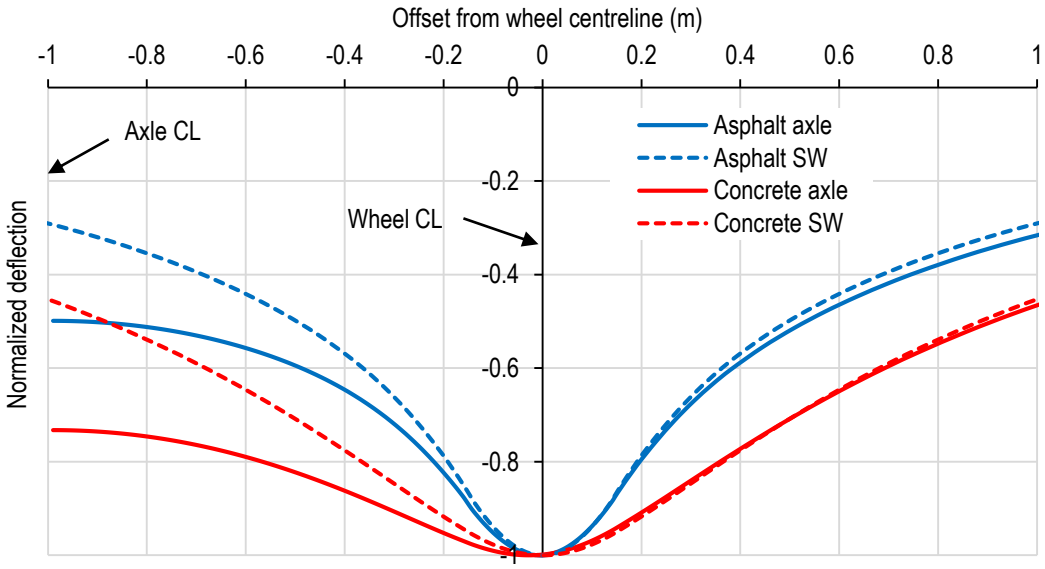

Figure 3.8 Transverse deflection bowls from axle centreline to 1 m to the right of the wheel centreline of asphalt and concrete, single wheel and axle loading models

The difference between the curvature of the deflection bowls for the axle and SW models indicates that there is a difference in transverse horizontal stress in the bound layers of the respective models. Figure 3.9 shows the vertical distribution of transverse horizontal stress in the bound layer at the axle centreline of the axle models as well as the transverse horizontal stress at an offset of 0.96 m from the wheel centreline for the SW models. An offset of 0.96 m was selected because it is the same distance from the wheel centreline as half an axle.

The bound layer of both axle models experienced a hogging moment along the axle centreline, which resulted in a tensile stress being induced at the top of the bound layers. The tensile stress at the top of the concrete and asphalt bound layers were 702 kPa and 86.3 kPa respectively. The tensile stress at the top of the SW concrete layer at an offset of 0.96 m was 372 kPa and the tensile stress at the top of the SW asphalt layer at an offset of 0.96 m was 75.0 kPa. The transverse horizontal tensile stress modelled at the top of the concrete layer in the axle centreline was more than double of what would have been modelled at an offset of 0.96 m had only a single wheel been used. The stress in the axle centreline will increase further when the concrete in the wheel centreline cracks. The effect of load configuration was not as severe for the asphalt models, where the tensile stress at the top of the asphalt layer did not vary much. The horizontal stress in asphalt bound layer at an offset of 0.96 mm remained tensile throughout the whole depth of the layer.

The high tensile stresses induced in the wheel centreline (as reported in Table 3.4) and axle centreline indicate the importance of steel reinforcement in the transverse direction. This should be in addition to high steel areas in the longitudinal direction. In the original UTCRCP design,

the aperture of 50 x 50 mm for steel bar mesh accounted for high tensile stresses longitudinally and transversally. The effect of using even more complex load configurations, such as more than one axle, should be investigated.

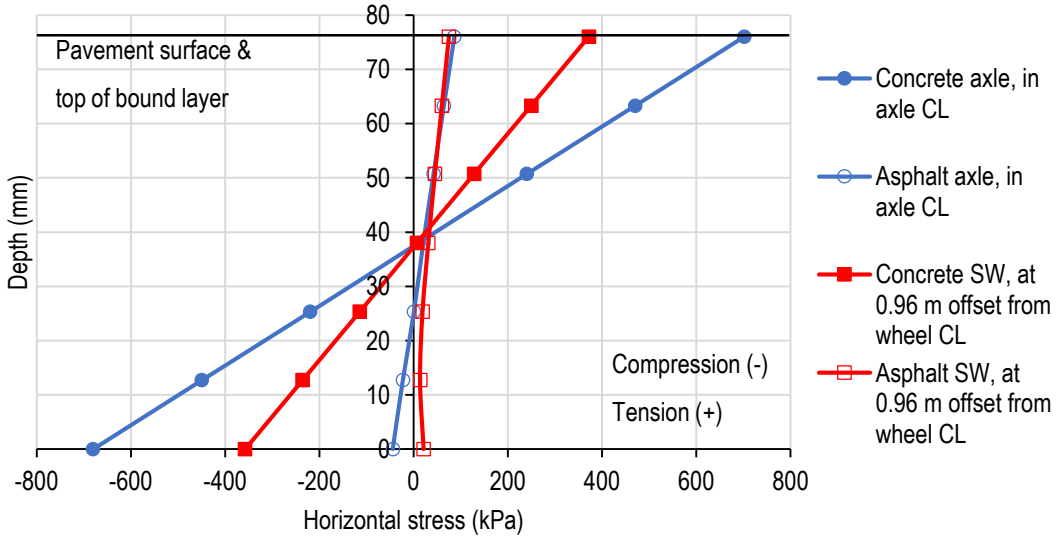

Figure 3.9 Vertical distribution of transverse horizontal stress in bound layers in the axle centreline & 0.96 m offset from wheel centreline

The difference in deflected shape indicated that the displacement, stress and strain, in the substructure of the SW and axle models would also differ. The deflected shape of the concrete and asphalt axle models were similar in that the maximum deflection was in the wheel centreline and that there was hogging type deflection in the axle centreline. From this it could be observed that rutting may occur along the wheelpath of pavements that incorporate 76 mm concrete layers.

As the main focus of the project was to investigate the response of an ultra-thin concrete pavement to traffic loading, the difference between the vertical and horizontal displacement of the substructure for single wheel and axle loading is only discussed for the concrete model. Although the displacement in the substructure can be deduced from the deflection plots, examining contour plots of the vertical and horizontal displacement can help to establish a more complete understanding of the pavement response.

Figure 3.10 (a) contains a contour plot of the vertical displacement of the concrete model with single wheel load configuration and axle load configuration. As discussed in the previous section, the displacement was larger for the axle model. The contours for the SW model were symmetrical around the wheel centreline. The contours of the axle model were symmetrical around the axle centreline. In the wheel centreline, the contours of the axle model were

approximately symmetrical to a depth of -0.5 m, where after the horizontal location of the maximum displacement moved toward the axle centreline. From between a depth of -1 m and -1.5 m the maximum deflection was along the axle centreline. The -0.18 mm vertical displacement contour of the axle model was deeper and wider than that of the SW model. The same could be observed for the other contours.

Figure 3.10 (b) contains a contour plot of the horizontal displacement of the SW and axle load concrete models. The horizontal displacement is order of magnitude smaller than the vertical displacement. The displacement contours for the SW model are symmetrical around the centreline of the wheel. The contour lines of the axle model are not symmetrical around the wheel centreline regardless of depth.

The most striking difference was that for the axle load model, a shape that reached past the 0 m offset to the centreline of the axle, displaces horizontally to the right, away from the centreline of the axle. A much smaller, and shallower, area displaces toward the axle centreline. The magnitude of horizontal displacement was greater for the axle model. The 0.06 mm contour of the axle model stretched from 0.25 m to 1.5 m horizontal offset, and -0.5 m to -1.25 m vertical depth, while the same contour of the axle model only stretched from 0.5 m to 0.8 m horizontal offset, and -0.4 m to -0.7 m vertical depth. At a depth of 5 m the vertical displacement was slightly less than -0.18 mm and the horizontal displacement was slightly more than 0.01 mm.

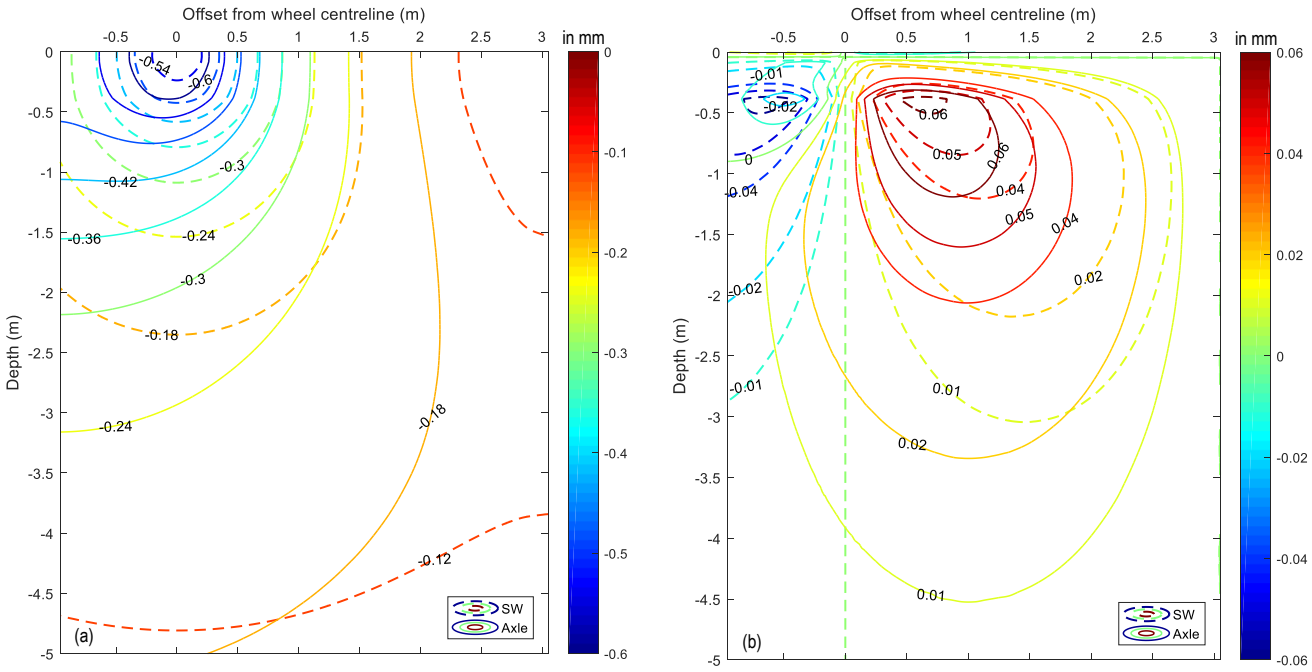

Figure 3.10 Contour plot of (a) vertical displacement and (b) horizontal displacement of single wheel and axle loading of the concrete model

3.3.3 Inflection point and relative stiffness

The inflection point is the point on a curve where a change in direction of curvature occurs, i.e. where the curvature is zero. The inflection point of the deflection bowls were determined as the locations where the second derivative is equal to zero. In medium thick plate theory, the moment is defined as the second derivative of deflection (also referred to as the curvature) multiplied by the flexural stiffness (EI). The inflection point of the second derivative of deflection is the zero moment point and is typically theoretically one radius of relative stiffness from the centre of the load.

In Figure 3.11 the offset of the inflection points (of the asphalt and concrete, single wheel and axle models) from the wheel centreline can be seen with respect to radius of relative stiffness. The radius of relative stiffness for spring foundation systems was used as in Equation 2.8. The modulus of subgrade reaction required in Equation 2.17 was determined by modelling a plate load test using finite elements (as described in Appendix B). The modulus of subgrade reaction of the substructure with a base material stiffness of 207 MPa and a subgrade material stiffness of 40 MPa was 0.129 N/mm^3.

The radius of relative stiffness of the concrete model was greater than for the asphalt model. The radius of relative stiffness was greater than the offset of inflection point from the wheel centreline, but in the same range of magnitude. When the load configuration was changed to axle loading, the offset of the inflection point was further from the wheel centreline. The difference in offset for the concrete models was 60 mm, in comparison to the 49 mm for the asphalt model.

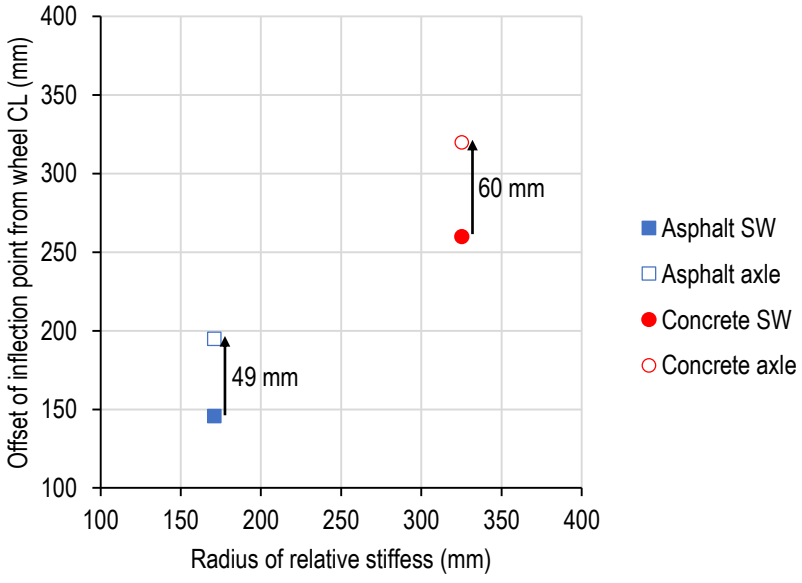

Figure 3.11 Effect of load configuration on inflection point offset

This figure shows that there is more wheel load interaction between wheels at opposite ends of an axle for high relative stiffness combinations of bound layer and substructure. Similar to soil-structure interaction, wheel load interaction is dependent on relative stiffness of the bound layer and substructure and complex load configurations should be taken into account for certain ranges of relative stiffness.

3.4 PLANE STRAIN FE MODELLING OF THIN CONCRETE PAVEMENTS

The difference between 3D and plane strain models, or loading applied over a circular area and a strip, was investigated using FE modelling of a thin concrete pavement. The purpose of this investigation was to support the findings in Chapter 5, where road pavements were subjected to strip loading during the physical modelling phase of the project. The domain of the 3D model was large enough that there would be insignificant boundary effects. The domain size of the plane strain model was determined for single wheel loading of asphalt and concrete bound layers. A depth of $140a$ (the same as for 3D models) and width of $35a$ were selected.

The 3D axle load model, for which the load was applied over a circular area, was altered to a plane strain axle load model. The thicknesses of the bound layer, base and subgrade remained the same as in Table 3.1. The properties of the substructure remained constant. Concrete properties were assigned to the bound layer. A pressure of 550 kPa was applied over a width of 304.8 mm, which was the same as the diameter of the circular area used for the 3D FE models.

The critical parameter values calculated for the 3D and plane strain concrete models can be seen in Table 3.5. The critical parameters of the plane strain model were greater than that of the 3D model. The vertical displacement was an order of magnitude greater for the plane strain model. The other critical parameters were between three and six times greater. The percentage difference for the respective critical parameters, as calculated using Equation 3.1, was significant. The percentage difference was the greatest for the vertical displacement and the smallest for the horizontal tensile stress at the bottom of the concrete layer.

Table 3.5 Critical parameters of 3D and plane strain concrete model

Model type	Critical parameter			
	$\delta_{v\ surface}$ (mm)	$\sigma_{h\ bottom\ of\ BL}$ (kPa)	$\sigma_{v\ top\ of\ subgrade}$ (kPa)	$\varepsilon_{v\ top\ of\ subgrade}$ (μm/m)
Plane strain model	-7.765	13287	-116	-1702
3D model	-0.692	4637	-22.3	-466
Difference (%)	-1022	-187	-420	-265

The deflection bowls of the 3D and plane strain models can be seen in Figure 3.12. As the surface deflection critical parameter indicated, the deflection was order of magnitude greater for the plane strain model. It is however not only the vertical deflection that differed. The shape of the two deflection bowls were also dissimilar. The figure shows that the domain of the plane strain model was more than 2 m wider than the 3D model.

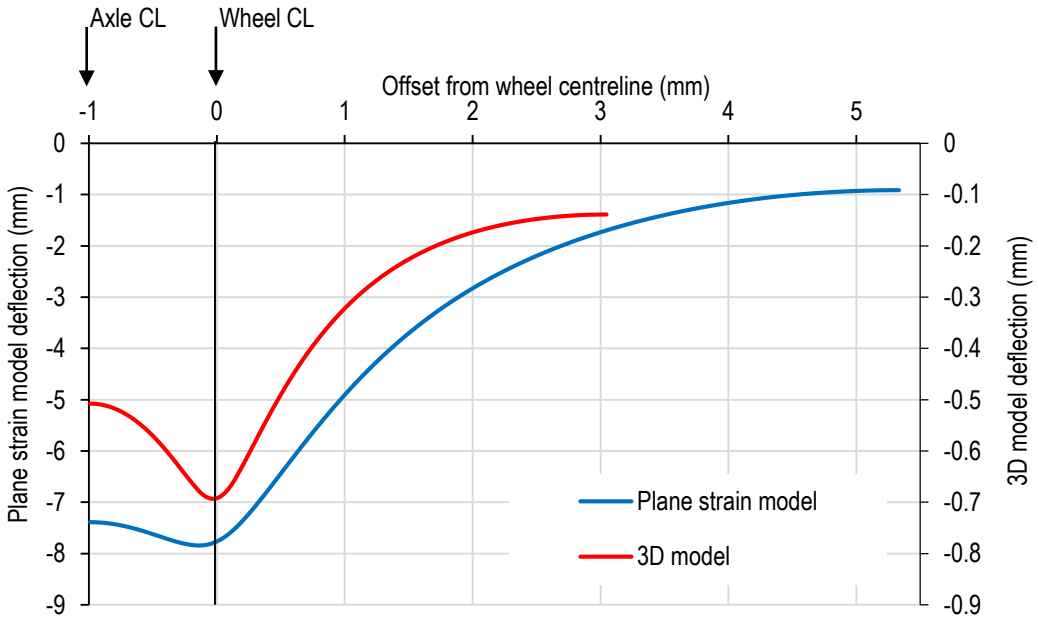

Figure 3.12 Deflection bowls of plane strain and 3D concrete models

The wider and deeper influence zone of the square footing (in the case of the 3D model the load was applied over a circular area) versus strip footing is illustrated in Figure 2.16 with stress isobars (Powrie, 2004). The normalized deflection bowls can be seen in Figure 3.13. The difference in deflected shape was apparent. Figure 2.16 can be used to explain the difference. The plane strain deflection bowl from the wheel centreline to free-end for the plane strain model was wider than the 3D deflection bowl. The extent of hogging type deflection in the axle centreline was reduced. This is due to the zones of influence of the respective wheels overlapping at a shallower depth for strip loading.

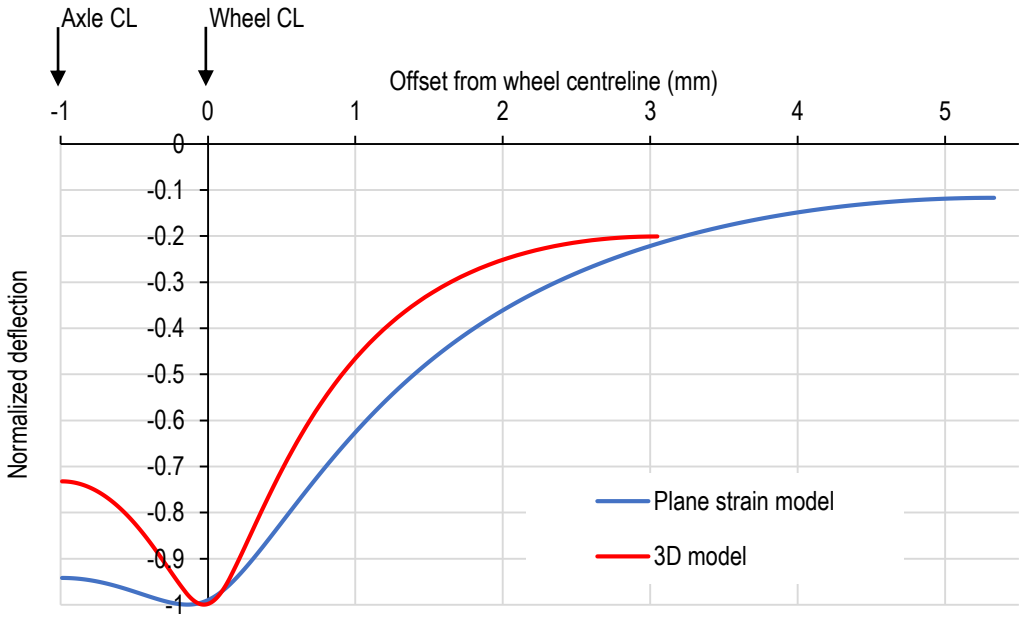

Figure 3.13 Normalized deflection bowls of plane strain and 3D concrete models

Figure 3.14 shows the vertical displacement contours of the 3D and plane strain concrete models. The contour plot is to a depth of 5 m. The vertical displacement of the plane strain model was order of magnitude greater than that of the 3D model. The contours of the plane strain model show that the load influence zones overlapped at a shallower depth, resulting in a contour plot that is symmetrical around the axle centreline. The vertical displacement contours of the 3D model start with the maximum vertical displacement below the wheel centreline and progressively moved toward the axle centreline with depth. Figure 3.15 shows the horizontal displacement contours of the 3D and plane strain concrete models. The horizontal displacement contours of the plane strain model were predominantly symmetrical around the axle centreline.

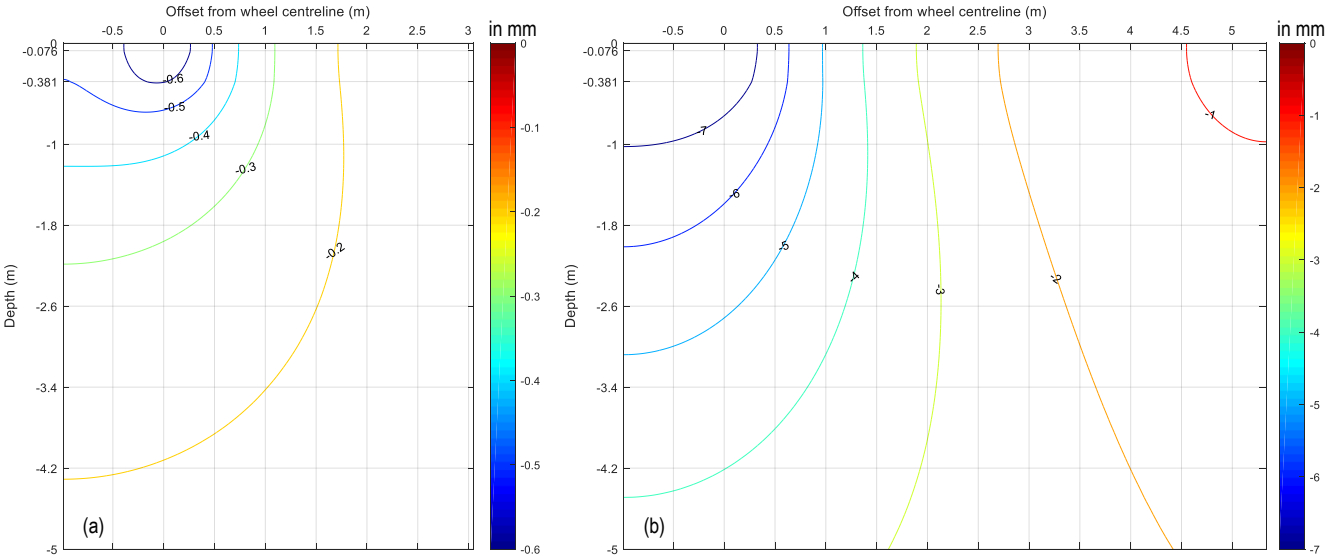

Figure 3.14 Vertical displacement contour plot of (a) 3D and (b) plane strain concrete models

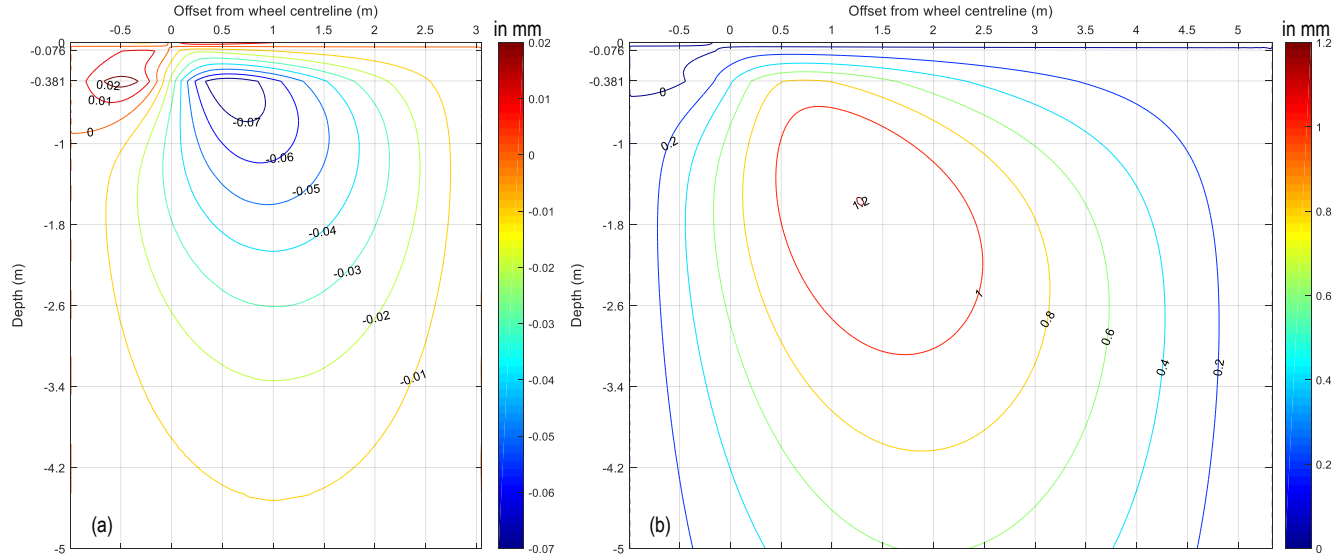

Figure 3.15 Horizontal displacement contour plot of (a) 3D and (b) plane strain concrete models

3.5 BEAM-ON-ELASTIC SUPPORT SIMPLIFICATION

From the Section 3.3 it is clear that the extent of wheel load interaction is dependent on the relative stiffness of the bound layer and substructure. In the following section the effect of relative stiffness on the extent of wheel load interaction was investigated using the beam-on-elastic support formulation. This was done even though the beam-on-elastic support formulation would reduce pavement modelling to a two-dimensional (2D) problem.

Different combinations of bound layer (or beam) thickness and material stiffness (Young's modulus), as well as support stiffness (modulus of subgrade reaction) were used. Three types

of bound layers were combined with two support stiffnesses. The bound layer types were: Thin Asphalt, Thick Concrete and Thin Concrete. Thin Asphalt and Thick Concrete represent conventional flexible pavement and rigid pavement, respectively. Thin Concrete represents UTCRCP.

The basic beam-on-elastic support formulation for a point-load on an infinitely long beam was used (Ugural & Fenster, 2012). The formulation is defined in Equation 3.2:

$$v(x) = \frac{P\beta}{2k} e^{-\beta x}(\cos \beta x + \sin \beta x) \qquad \textbf{Equation 3.2}$$

Where:

$$\beta = \sqrt[4]{\frac{k}{4E_{BL}I_{BL}}} \qquad \textbf{Equation 3.3}$$

And:

P = point load applied (N)
k = modulus of subgrade reaction (N/mm^2)
x = distance from load application location (mm)
E_{BL} = Young's Modulus of bound layer (MPa)
I_{BL} = Moment of Inertia of bound layer (mm^4)

Axle loading was simulated by superimposing the deflection of two point loads at an offset. An offset of 2 m was selected, with a point load 1 m to the left of the axle centreline and another 1 m to the right of the centreline. Each point load was 40 kN to represent standard axle loading. The properties of the bound layer types can be viewed in Table 3.6 (Kearsley *et al.*, 2014; Kim, 2007). Loose and dense sand were selected for the support. Table 3.7 contains the relevant moduli of subgrade reaction (Bowles, 1996).

Table 3.6 Properties of bound layer types

Bound layer type	Thickness (mm)	Young's Modulus (MPa)	Poisson's Ratio
Thin Asphalt	50	2 759	0.35
Thick Concrete	300	40 000	0.17
Thin Concrete	50	40 000	0.17

Table 3.7 Modulus of subgrade reaction of support types

Support type	Modulus of subgrade reaction (N/mm^3)
Loose sand	0.016
Dense sand	0.128

3.5.1 Deflection of bound layer and support combinations

Figure 3.16 shows the deflection produced by the left and right point-loads, as well as the superimposed deflection of each bound layer type on loose and dense sand. The centreline of the axle had an offset of 0 m. Note that the scale of the y-axis is different for each bound layer type. The extent of deflection bowl overlap for the respective point-loads (left and right) can be observed. Generally, three types of overlapping can be seen; no overlapping, partial overlapping and complete overlapping.

In Figure 3.16 (a) no overlapping occurred for thin asphalt on dense sand. The left and right deflection bowls did not influence each other when they were superimposed. Figure 3.16 (b) shows complete overlapping for the thick concrete. The deflection bowls overlapped enough that the superimposed shape results in a single trough with its maximum deflection along the axle centreline. Regardless of support stiffness, the deflected shape of the thick concrete layer resulted in complete overlapping.

Two types of partial overlapping could be observed for the bound layer – support combinations considered. For the first type, the upward deflecting section, left and right of the centreline, overlapped. The superimposed deflected shape resulted in a hogging type deflection along the centreline. This type of partial overlapping can be seen for thin asphalt on loose sand (Figure 3.16 (a) and thin concrete on dense sand (Figure 3.16 (c)). It is referred to as small partial overlap. For the second type, the downward deflecting section of the left and right deflection bowls overlapped. However, two troughs at the point-load location and a peak along the centreline were still present. The second type of overlapping can be seen for thin concrete on loose sand (Figure 3.16 (c)). It is referred to as large partial overlap.

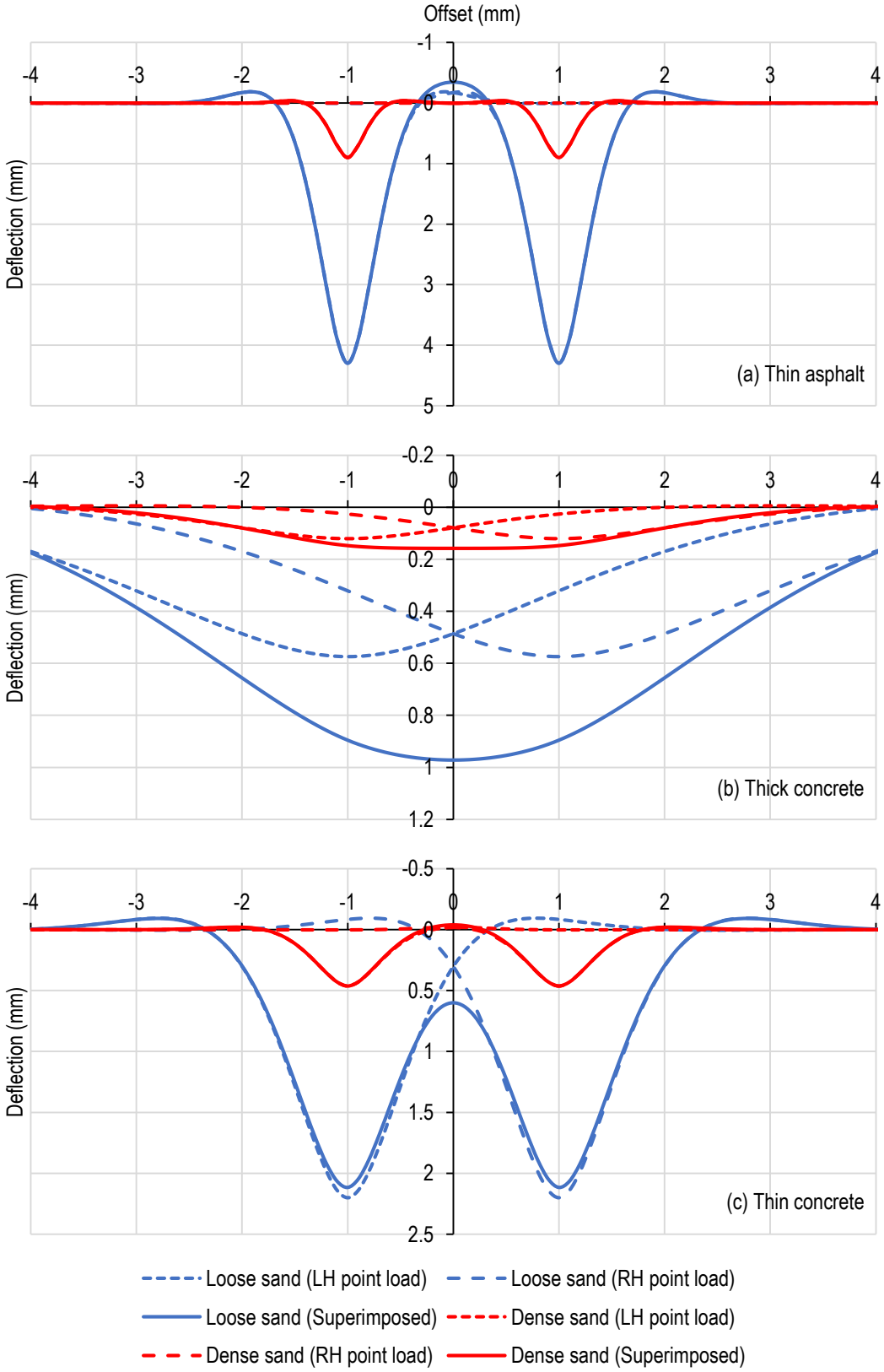

Figure 3.16 Left, right and superimposed deflection bowls of (a) thin asphalt, (b) thick concrete and (c) thin concrete

Figure 3.17 (a) shows the superimposed response of the three bound layer types on loose sand and Figure 3.17 (b) shows the superimposed response of the three bound layer types on dense sand. Note that the y-axis scale of the two graphs differ, with less deflection calculated for the dense sand support. The maximum deflection for both thin bound layers (Thin Asphalt and Thin Concrete) were at the load locations. The thin concrete deflected less, and the deflection bowls were wider than the thin asphalt. The maximum deflection for both thick concrete models were along the centreline of the axle. The deflected shape and extent of overlap is a consequence of the bound layer – support relative stiffness.

The bound layer – support combinations for which the deflection bowls overlapped completely had single curvature for the deflected shape. This indicates that the bottom of the bound layer was always in tension. The other combinations did not have single curvature for the deflected shape. The sign of the curvature changed between positive and negative with offset. The two types of partial overlapping did not have single curvature, with the section around the axle centreline in negative curvature and the section around the load location in positive curvature. This indicates that the bending moment of the bound layer changed sign with distance from the load location; a section of the bound layer at the axle centreline experiences tensile stress at its top and a section of the bound layer at the load location experiences tensile stress at its bottom.

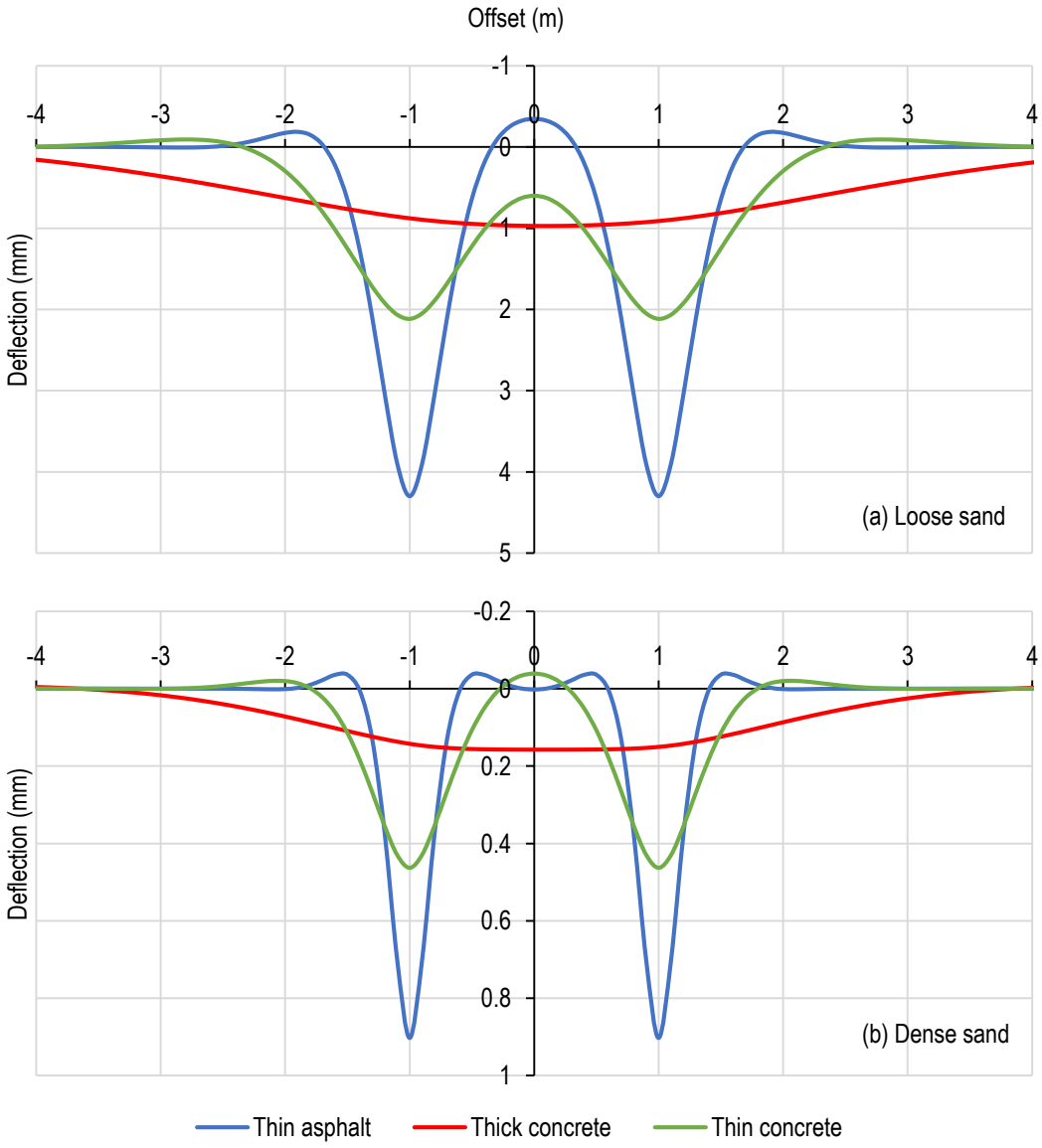

Figure 3.17 Two-wheel axle deflection on (a) loose sand and (b) dense sand

The beam-on-elastic support is an (over) simplification of a road pavement structure. It reduces the structure and loading to two dimensions and the springs, that represent the substructure, only exert resistance in the vertical direction. Examining the deflected shapes of the different combinations does, however, allow the development of a conceptual understanding of the interaction between bound layer type and support stiffness as well as the interaction between wheel loads. As the response of the road pavement substructure is of interest, it would be beneficial to investigate the interaction between bound layer and support stiffness by using 3D FE modelling, where the substructure is modelled as a continuous solid (and not a set of springs) so that displacement and strains can be determined.

3.5.2 Effect of relative stiffness on the deflected shape caused by axle loads

The radius of relative stiffness is a measure of the stiffness of a slab relative to its support. It can be calculated for a 3D slab on a bed of springs using Equation 2.17, which incorporates the Young's Modulus, Poisson's Ratio and thickness of the slab and modulus of subgrade reaction of the substructure.

The beam-on-elastic support simplification used in the Section 3.5 is not a 3D model. By comparing Equation 2.17 and Equation 2.19 (or Equation 3.3) the reciprocal of β can be used as the equivalent of radius of relative stiffness for the 2D model of beam-on-elastic support. The same variables are used to determine β as for the radius of relative stiffness and the reciprocal of β has a linear dimension with a base unit of meter. A linear relationship exists between the radius of relative stiffness and reciprocal of β calculated for the same bound layer – support combinations. The radius of relative stiffness is smaller than the reciprocal of β for the same bound layer – support combinations.

Figure 3.18 shows the reciprocal of β calculated for the bound layer – support combinations used. The inflection point of the deflection bowl for the thin asphalt on dense sand was the closest to the load location, resulting in narrow deflection bowls. The reciprocal of β for thin asphalt on loose sand and thin concrete on dense sand were similar and that for thin concrete on loose sand was larger. There are ranges of the reciprocal of β that correlate with the types of overlapping discussed in Section 3.5.1.

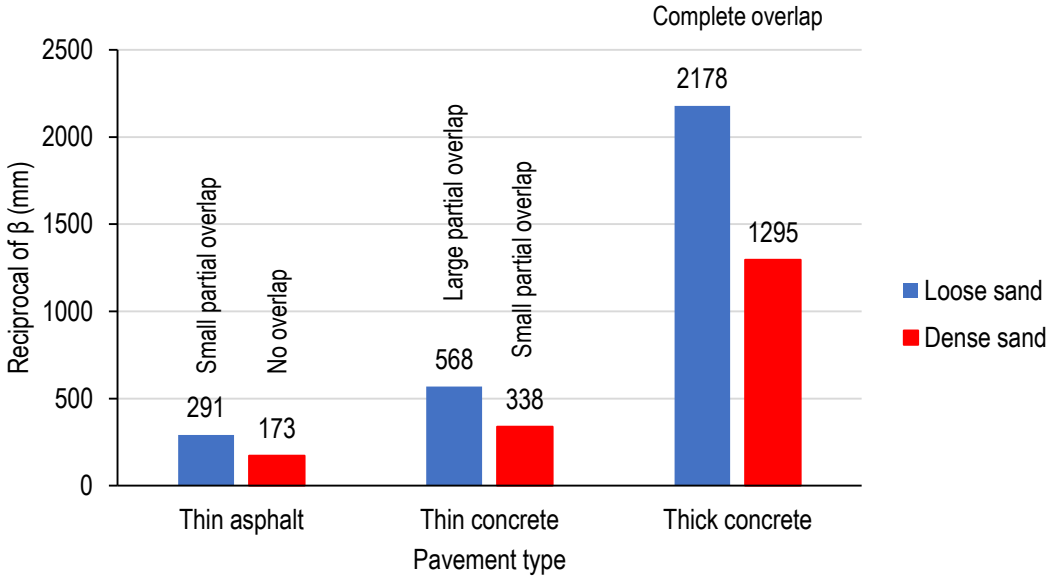

Figure 3.18 Reciprocal of β for bound layer – support combinations

3.6 SUMMARY

Changing the material properties of the bound layer from that of asphalt to concrete caused a decrease in the maximum deflection, as well as stress and strain at the top of the subgrade. It increased the transverse horizontal tensile stress at the bottom of the bound layer. When considering the normalized deflected shape, it could be seen that the deflection bowl of the concrete model was wider than for the asphalt model.

Considering the critical parameters, applying a two-wheel axle affected the concrete model more than the asphalt model. In terms of stress in the bound layer, loading a pavement with a two-wheel axle load results in a hogging moment occurring in the axle centreline, where transverse horizontal tensile stress is induced at the top of the layer. The induced stress was significantly larger for the concrete model and will increase further when the concrete layer cracks in the wheel centreline. The high transverse horizontal stresses induced in the thin HS-SFRC layer highlight the importance of reinforcing the layer in the transverse and longitudinal directions.

The comparison of the deflected shape and displacement contour plots of the asphalt and concrete models support the proposal that UTCRCP should be designed for rutting. The deflected shape and displacement contour plots also indicate that both pavement types would benefit from modelling two-wheel axles. This is because of the difference in response and that the accumulation of permanent strain modelled would not be representative using a single wheel.

The permanent deformation of road pavements is a plane strain problem when there is no wander. The vertical and horizontal zone of influence is larger for strip loads. The displacement of the plane strain model was an order of magnitude greater than the 3D model. The normalized transverse deflection bowls of the plane strain and 3D models also differed significantly due to the larger zone of influence of strip loading. The stress and strain critical parameters were not affected as significantly as the surface deflection in the wheel centreline.

The effect of load configuration is dependent on the relative stiffness of pavement systems. The interaction of wheels at opposite ends of an axle for different relative stiffnesses was investigated using the beam-on-elastic support simplification. Three types of wheel load interaction were observed: no overlapping, partial overlapping and complete overlapping. Partial overlapping could also be subdivided into two types: small partial overlapping and large partial overlapping. The thin concrete bound layer placed on dense sand had large partial overlapping, while the thin concrete bound layer on loose sand had small partial overlapping.

The radius of relative stiffness concept is applicable to the 3D analysis of pavements. The equivalent of the radius of relative stiffness for the beam-on-elastic-support formulation is the reciprocal of β. Ranges of relative stiffness could be used to predict the extent of wheel load interaction, pavement response and how the pavement should be modelled and designed.

A positive relationship exists between radius of relative stiffness and inflection point determined from the transverse deflection bowls of the 3D models. The radius of relative stiffness was greater for the concrete model than the asphalt model. The inflection point of the concrete model was also further from the wheel centreline. Changing the load configuration from single wheel to axle loading widened the deflection bowl and pushed the inflection point further from the wheel centreline.

The following questions identified in the literature review (Section 2.13) can be partially addressed from the summary in Chapter 3:

- Should UTCRCP be modelled as a flexible pavement where the substructure properties are important, and rutting is a traffic associated failure mechanism?

  Yes, the deflected shape of a thin concrete layer was similar to the deflected shape of a thin asphalt layer on the same substructure, in that there was a distinctive trough around the load location. As a result, the substructure was subjected to a similar stress distribution, even though the stress was smaller. This indicates that traffic loading of UTCRCP would results in a rut forming along the wheelpath

- Should numerical and physical modelling of UTCRCP use axle loading instead of a single wheel and are important aspects of the pavement response ignored if axle loading is not used?

  Yes, the LE modelling indicated that there is interaction between wheels at opposite ends of a 1.98 m axle. This interaction results in a hogging moment along the axle centreline that is significantly greater for thin concrete layers than for thin asphalt layers. Additionally, the stress distribution in a substructure under axle loading results in the maximum stress and strain being along the axle centreline beyond a certain depth.

- Is it viable to simplify loading configurations to strip loading and how does strip loading and 3D loading affect pavement response?

  Not only was the magnitude of displacement, stress and strain greater for the strip loading, the deflected shape of the two load configurations (where the same pressure was used) was also dissimilar. The zones of influence of the strip loading model overlapped more,

resulting in greater deflection in the axle centreline. Reducing the applied pressure when using strip loading to match deflected shapes could be considered for physical modelling.

- Can concepts of relative stiffness be used to predict the extent of wheel load interaction and if a pavement should be modelled as a flexible pavement?

Yes, relative stiffness can be used to determine the extent of wheel load interaction and whether a trough might form around the load location and a hogging moment would form along the axle centreline if axle loading is used.

- Is it necessary to include significant amounts of steel reinforcement in the longitudinal and transverse direction?

Yes, the transverse deflected shape and induced tensile stresses, in the concrete bound layer along the wheel and axle centreline indicate that it is essential to include significant steel reinforcement in the transverse direction. This is in addition to the longitudinal reinforcement, which is included to control thermally induced cracking.

This chapter showed that the extent of wheel load interaction and pavement response was dependent on the relative stiffness between the bound layer and substructure. To further improve our understanding of the response of UTCRCP traffic loading, the effect of relative stiffness on concrete pavement response should be explored.

4 EFFECT OF CONCRETE LAYER THICKNESS AND BASE MATERIAL STIFFNESS ON ROAD PAVEMENT RESPONSE TO TRAFFIC LOADING

4.1 INTRODUCTION

It was seen in the previous chapter that the extent to which the wheel loads at opposite ends of an axle interact is dependent on the relative stiffness between the bound layer and the substructure of the road pavements. The road pavement response, in terms of selected critical parameters (vertical displacement, stress and strain in the concrete layer and substructure in the wheel centreline), deflected shape and substructure displacement, is also affected by the load configuration and relative stiffness.

The effect of concrete layer thickness and substructure material stiffness on road pavement response should be explored to improve our understanding of the response of UTCRCP to traffic loading. The effect was investigated using two parametric studies of combinations of concrete layer thickness and substructure material stiffness;

1. The concrete layer thickness and base material stiffness were varied simultaneously using Response Surface Methodology (RSM).
2. The base material stiffness was increased incrementally, while the concrete layer thickness and subgrade material stiffness remained constant. Increasing the base material stiffness gave an indication of the effect of cement stabilization on the response of pavement with thin HS-SFRC bound layers.

In this chapter, 3D FE modelling, in the general-use FE analyses program ABAQUS/Standard (Dassault Systemes Simulia Corp, 2016), was used to allow control over all boundary conditions and other assumptions. The replica model adjusted for axle loading was used as a basis. DesignExpert (Stat-Ease Corporation, 2019) was used for RSM. The pavement response was measured using similar parameters as in Chapter 3.

4.2 MULTIVARIABLE ANALYSIS OF CONCRETE LAYER THICKNESS AND BASE MATERIAL STIFFNESS

The effect of relative stiffness was investigated using RSM. The relative stiffness was varied by varying the concrete layer thickness and base material stiffness simultaneously.

4.2.1 Response surface methodology

Response surface methodology is a set of mathematical and statistical techniques that enables the efficient modelling and analyses of responses that are dependent on multiple variables (Montgomery, 2001). Response surface designs define the framework of an experiment (or parametric study). It determines the combination of variable values and number of combinations required to fit a surface function of a selected order. The response surface design used in this study was Central Composite Design (CCD). It can be used to develop second-order polynomials, which makes it possible to model curvature. Equation 4.1 shows the general form of a second-order polynomial for two factors:

$$y = \beta_0 + \beta_A x_A + \beta_B x_B + \beta_{AB} x_A x_B + \beta_{AA} x_A^2 + \beta_{BB} x_B^2 + \epsilon \qquad \textbf{Equation 4.1}$$

Where:

$\beta_0, \beta_A, \beta_B, \beta_{AB}, \beta_{AA}, \beta_{BB}$ = regression coefficients
x_A, x_B = independent variables
$x_A x_B$ = interaction effect between variables
x_A^2, x_B^2 = quadratic effect of a single variable
ϵ = observed noise or error

CCD for two variables consists of four factorial points, four axial points and a centre point. Each point defines a combination of variable values and are referred to as sets in this research. Figure 4.1 shows the three different types of points for a two factor CCD. Axial points are situated a distance α away from the centre point. The value of α for two factor CCD is 1.414. This makes the surface plot rotatable, which means that a constant prediction variance at all equidistant points from the design centre is provided (Montgomery, 2001).

A response of a parametric study is recorded using selected parameters from the various sets and are used to investigate the effect of the independent variables. Regression models are developed to predict the effect of the variables and their interaction. Design Expert (Stat-Ease Corporation, 2019) is a program that makes is easy to compile and evaluate the regression models generated from parameters used to measure the response.

The program also outlines a procedure to fit a regression model to response data. The first step of the procedure consists of inspection of the fit summary, which provides information on the appropriateness of the order of higher degree polynomials used to model a response. The second step is the model selection, which is typically informed by the fit summary unless prior knowledge of the response is available. For the third step an Analysis of Variance (ANOVA)

of the selected model is conducted. The F-test, sum of squares and mean square are used for the ANOVA. The significance of the mathematical models and the respective terms are evaluated. The coefficients of the terms are given for coded and actual factors.

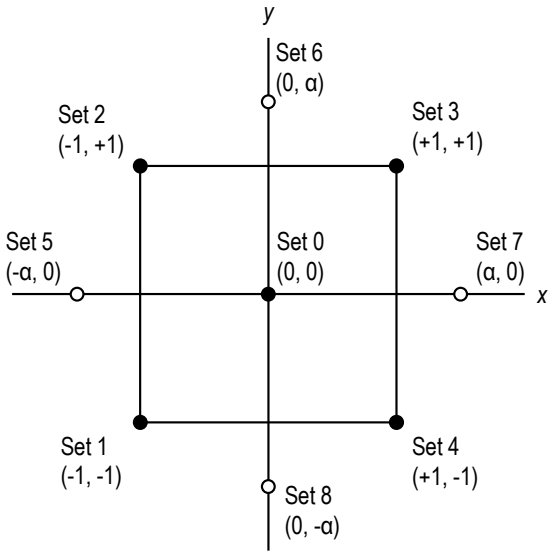

Figure 4.1 Central composite design (Montgomery, 2001)

The fourth step of the procedure is to check diagnostics or residual plots to determine if the assumptions that have to be made to do regression analysis hold (Vining, 2011). If required, transformation of the response data is recommended, and a suitable mathematical function is suggested. If transformation is required, the same procedure has to be followed from the first step. The procedure is described thoroughly when using DesignExpert (Stat-Ease Corporation, 2019) and a summary is given in Smit (2015).

Using numerical modelling, in conjunction with RSM, enables the efficient investigation of the effect of concrete layer thickness and base material stiffness within a specified range. Although RSM is more commonly used for physical experiments, it is used in this case to get a sense of the effect that the pavement components would have on the road pavement response.

4.2.2 FE model setup and critical parameters

The replica model adjusted for the axle load configuration, presented in Chapter 3, was used as a basis. The concrete material properties remained constant with a material stiffness (Young's Modulus) of 40 000 MPa and Poisson's Ratio of 0.17. The base thickness and Poisson's Ratio remained constant, at 305 mm and 0.4 respectively. The subgrade depth (20.955 m) and material properties (Young's Modulus of 41 MPa and Poisson's Ratio of 0.45) remained constant. No interaction between the layers was modelled and the layers were assumed to be

perfectly bonded. The plan arrangement of the mesh remained the same. The element size of the bound layer remained unchanged at a height of 12.6 mm.

The concrete layer thickness and base material stiffness were varied simultaneously using the values prescribed by the CCD. Table 4.1 shows the coded variable levels (correlating to Figure 4.1) and the actual values of concrete layer thickness and base material stiffness that were used.

The base material stiffness, Young's Modulus, was varied from 40 MPa to 700 MPa. These were the minimum and maximum effective long-term stiffness values for granular materials used in the Pavement Number design method (SANRAL, 2013). The concrete layer thickness was varied from 30 mm to 346 mm to include the effect of thicknesses smaller than 50 mm (the thickness of UTCRCP) and greater than 300 mm (the typical thickness of conventional concrete pavement).

Table 4.1 Central composite design variable combination

Multivariable combination	Coded variable level		Variables	
	x	y	Thickness (mm)	Material stiffness (MPa)
Set 0	0	0	188	370
Set 1	-1	-1	76	137
Set 2	-1	1	76	603
Set 3	1	1	300	603
Set 4	1	-1	300	137
Set 5	-1.414	0	30	370
Set 6	0	1.414	188	700
Set 7	1.414	0	346	370
Set 8	0	-1.414	188	40

The critical parameters used in Chapter 3 were used to develop response surface models. These were the vertical deflection of the model surface, transverse horizontal tensile stress at the bottom of the bound layer and vertical stress and strain at the top of the subgrade. All the critical parameters were situated in the wheel centreline. The critical parameter values of the respective sets can be viewed in Table 4.2.

Table 4.2 Response of critical parameters

Multivariable combination (Thickness, Material stiffness)	Critical parameter			
	$\delta_{v\ surface}$ (mm)	$\sigma_{h\ bottom\ of\ BL}$ (kPa)	$\sigma_{v\ top\ of\ subgrade}$ (kPa)	$\varepsilon_{v\ top\ of\ subgrade}$ (μm/m)
Set 0 (188 mm, 370 MPa)	-0.389	1287	-6.81	-118
Set 1 (76 mm, 137 MPa)	-0.733	5055	-23.8	-488
Set 2 (76 mm, 603 MPa)	-0.571	3265	-16.7	-345
Set 3 (300 mm, 603 MPa)	-0.293	579	-3.60	-52.7
Set 4 (300 mm, 137 MPa)	-0.303	631	-3.74	-52.7
Set 5 (30 mm, 370 MPa)	-0.868	6027	-36.3	-829
Set 6 (188 mm, 700 MPa)	-0.371	1172	-6.32	-109
Set 7 (346 mm, 370 MPa)	-0.277	465	-3.10	-42.2
Set 8 (188 mm, 40 MPa)	-0.425	1452	-6.93	-126

In this study a General Linear Model Analysis of Variance (GLM-ANOVA) and the response surface plots (determined using the procedure described Section 4.1.1) were reported and discussed. The model equations and ANOVA can be viewed in Appendix C. The deflection bowls and displacement contour plots of the models were also reported and discussed.

4.2.3 Preliminary model analyses

GLM-ANOVA was performed to determine the dependence of the critical parameters on the independent variables. Higher-order terms were excluded to perform a general linear model analysis. The GLM-ANOVA values can be seen in Table 4.3. The F-test was used. An independent variable must have a large F-value to have a significant effect on the critical parameter. The F-value (or variance ratio) is the ratio of the model mean square over the residual mean square and shows the relative contribution of the model variance to the residual variance. The probability associated with the F-value is the probability of obtaining the specific F-value if the term did not have an effect on the response. The probability (p-value) should be smaller than 0.05 to be considered significant. The percentage contribution is determined from the sum of squares of the respective independent variables.

The F-values, p-values and percentage contribution of all the critical parameters indicated that concrete layer thickness dominated the response of road pavements. The contribution of the base material stiffness to the compressive stress and strain at the top of the subgrade was less than the contribution of the variable to the surface deflection and tensile stress at the bottom of

the concrete layer. This could be caused by the zones of influence of the respective wheel loads overlapping for certain combinations of variables.

Table 4.3 GLM-ANOVA for critical parameters

Dependent variables	Independent variables	Statistical parameters				Contribution (%)
		Sum of squares	F-value	p-value	p<0.05	
$\delta_{v\ surface}$ (mm)	Thickness	0.298	45.66	5.00E-05	Y	97.48
	Material stiffness	0.008	1.18	0.3026	N	2.52
$\sigma_{h\ bottom\ of\ BL}$ (kPa)	Thickness	2.80E+07	34.16	1.63E-04	Y	97.82
	Material stiffness	6.25E+05	0.76	0.4031	N	2.18
$\sigma_{v\ top\ of\ subgrade}$ (kPa)	Thickness	801.9	25.30	5.14E-04	Y	98.99
	Material stiffness	8.197	0.26	0.6221	N	1.01
$\varepsilon_{v\ top\ of\ subgrade}$ (μm/m)	Thickness	4.23E+05	22.44	7.96E-04	Y	99.18
	Material stiffness	3484	0.18	0.6764	N	0.82

4.2.4 Critical parameter response surface models

Quadratic surface models were derived for all the critical responses. The diagnostics and residual plots of the untransformed regression models indicated that transformation of all the critical parameters was required. Power transformation, as seen in Equation 4.2, was used for all the critical parameters. A constant is denoted by t and the power value is denoted by Λ. The values of λ ranged from -0.22 to -0.99, which is also an inverse transformation. The constant t remained zero for all the transformation of all the surface models.

$$y' = (y + t)^{\Lambda} \qquad \textbf{Equation 4.2}$$

The coefficient of determination (R^2) and model p-value of each model indicated that the response surface models were adequate to model the effect of concrete layer thickness and base material stiffness on the critical parameters. The model equations and ANOVA can be viewed in Appendix C. The p-values of the respective terms in the surface equation must be smaller than 0.05 to be significant. The concrete layer thickness term (A) and quadratic effect (A^2) were always significant. The base material stiffness term (B) was significant for all the models. The interaction term (AB) was not significant for the horizontal stress at the bottom of the concrete layer model. The quadratic effect term for the base material stiffness (B^2) was only significant response surface model of the vertical deflection. Comparing the coefficients of the coded equations make it possible to predict the relative contribution of the terms to the response.

Figure 4.2 shows the contour plots of the response surface models derived for the critical parameters using Design Expert (Stat-Ease Corporation, 2019). Note that because there was no sign change for the critical parameters in the variable domain investigated, all critical parameters were given as positive. As the GLM-ANOVA and inspection of the quadratic response surface equations indicated, the critical parameters were predominantly dependent on the concrete layer thickness. The dominant effect is related to the concept of flexural stiffness of rectangular sections where the effect of thickness is raised to the power of three. The contour plots of the response surface make it easier to interpret the developed models and the effect of the two pavement components.

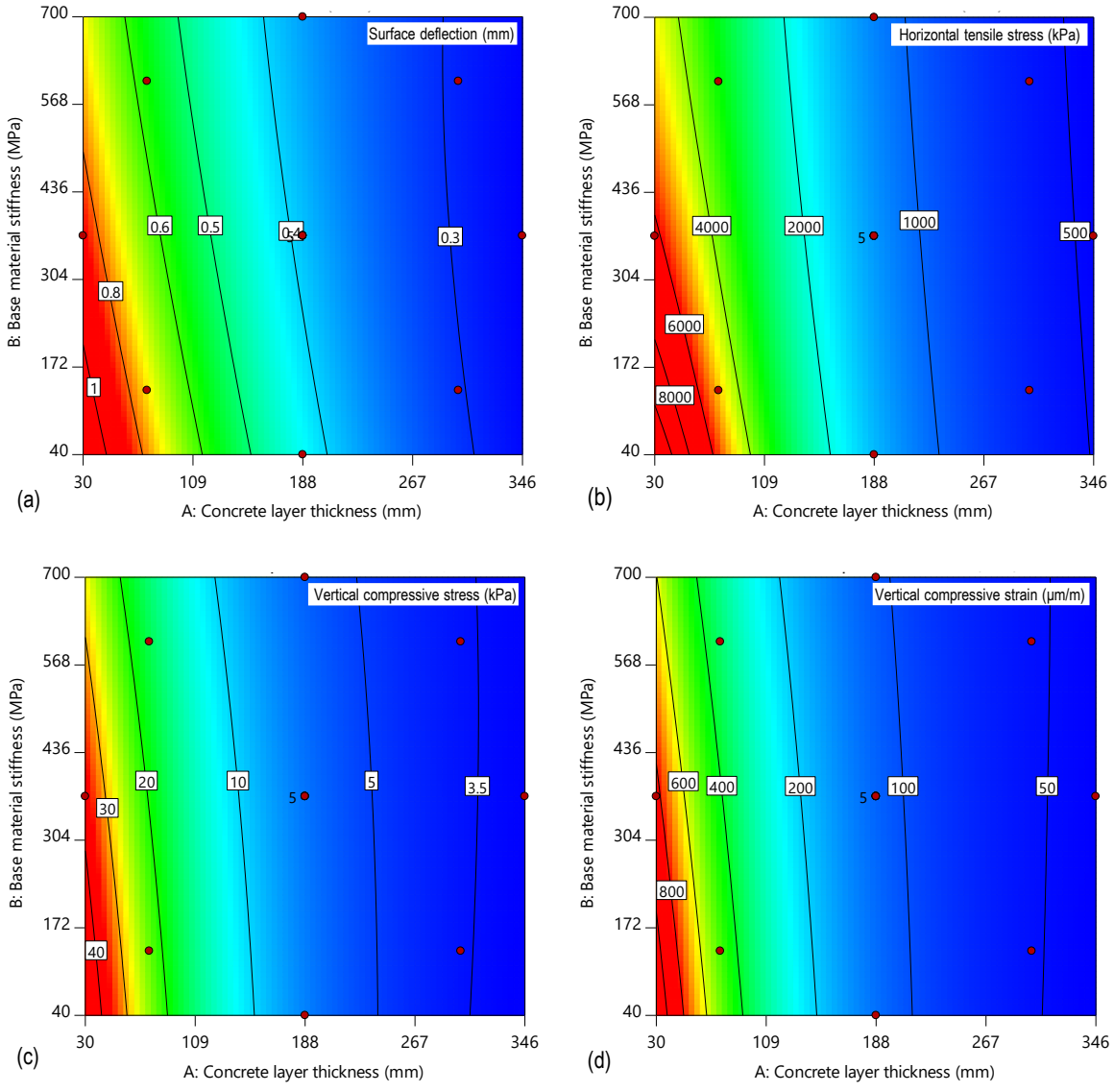

Figure 4.2 Response surface plots of (a) surface deflection, (b) transverse horizontal tensile stress at bottom of bound layer, (c) compressive stress at top of subgrade and (d) compressive strain at top of subgrade

The pavement response did not vary much for a concrete layer thickness of approximately 150 mm to 346 mm. There was a steep increase in the critical parameter magnitude from 150 mm to 30 mm thickness. The steep increase was more prominent for the deflection and horizontal stress at the bottom of the concrete layer. The spacing of the contour lines for these critical parameters pivoted toward the left, indicating that the contribution of base material stiffness to the pavement response increased as the thickness decreases. This effect was the most pronounced for the horizontal stress at the bottom of the concrete layer.

4.2.5 Transverse deflection bowls

Figure 4.3 and Figure 4.4 show the transverse deflection bowls of all the combinations of concrete layer thickness and base material stiffness analysed. Figure 4.3 shows the deflection bowls of the factorial points of the CCD (i.e. the values on the corners of the CCD square in Figure 4.1). It also includes the deflection bowls of the centre point as a reference. In Figure 4.3, the maximum deflection of Set 1 (76 mm, 137 MPa) and Set 2 (76 mm, 603 MPa) was at the centreline of the circular load area. These deflection bowls did not have single curvature. The shape of the deflection bowl had a trough around the load location with hogging (upward deflection) in the axle centreline. Set 1 had greater overall deflection because of the lower base material stiffness.

The deflection bowls of Set 3 (300 mm, 603 MPa) and Set 4 (300 mm, 137 MPa) show that changing the base material stiffness had little effect on the magnitude and shape of the deflection bowls of thick concrete pavements. The maximum deflections of these sets were along the axle centreline and the shape of the deflection bowl was similar to single curvature. Set 0 showed a slight trough in the wheel centreline and hogging in the axle centreline, although the deflected shape was less distinct than for the 76 mm models.

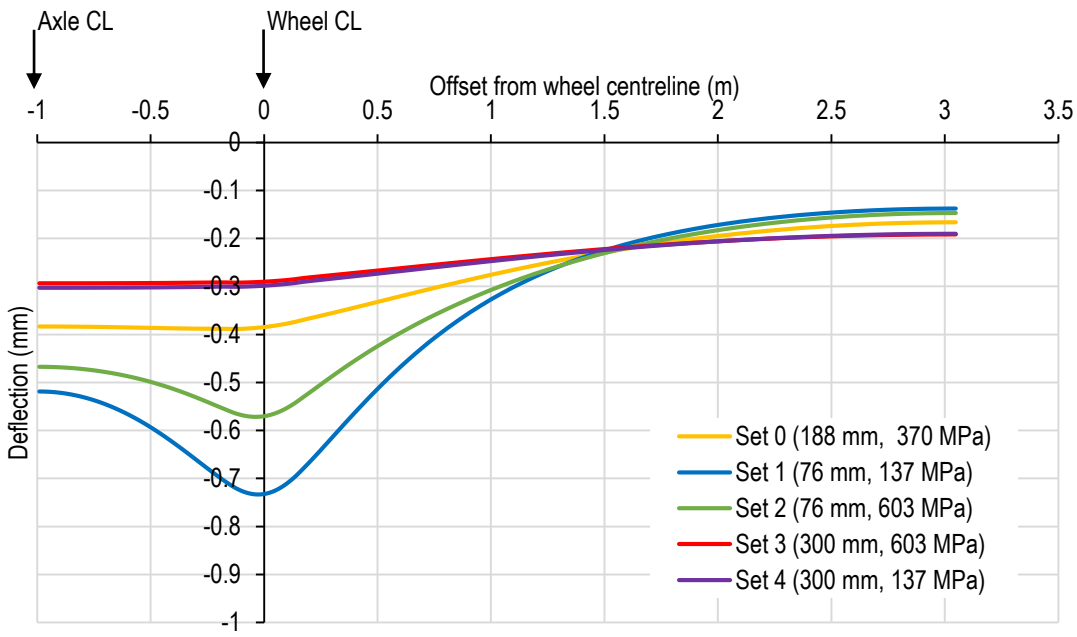

Figure 4.3 Deflection bowls for factorial points and centre point

Figure 4.4 shows the deflection bowls of the axial points. These are the extreme values. As with Figure 4.3, it includes the deflection bowls of the centre point as a reference. In Figure 4.4 Set 0 (188 mm, 370 MPa), Set 6 (188 mm, 700 MPa) and Set 8 (188 mm, 40 MPa) had the same thickness. The shape and magnitude of their deflection plots did not vary much although the base material stiffness varied significantly between from 40 MPa to 700 MPa. Set 7 (346 mm, 370 MPa) deflected the least and experienced the least curvature. Set 5 (30 mm, 370 MPa) had the greatest deflection, with the concrete layer bending significantly into the substructure. The shape of the deflection bowl was similar to that of Set 1 and Set 2.

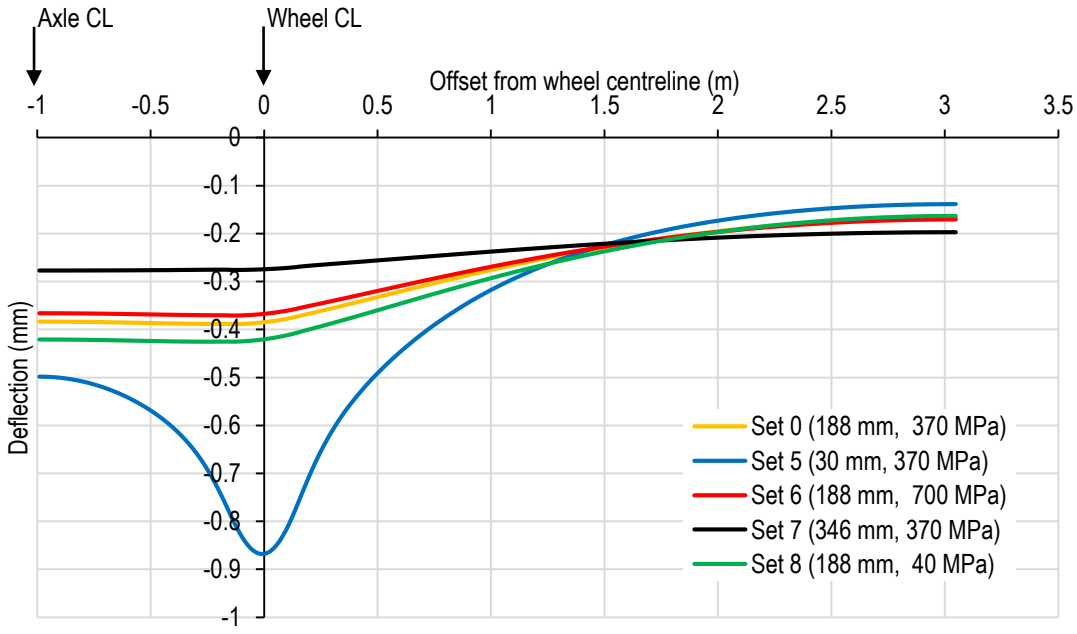

Figure 4.4 Deflection bowls for axial points and centre point

None of the transverse deflection bowls of the multivariable analyses of the 3D model had the deflected shape that was similar to that determined using the beam-on-elastic support simplification which was referred to as small partial overlap. The vertical displacement in the axle centreline was always downward.

4.2.6 Displacement contour plots

Although the displacement in the substructure can be deduced from the deflection plots examining contour plots of the vertical and horizontal displacement allows a more thorough understanding of pavement response. Figure 4.5 and Figure 4.6 are the contour plots of vertical and horizontal displacement of a selection of the models.

The shape of vertical displacement contour plot of Set 0 (188 mm, 370 MPa), Set 3 (300 mm, 603 MPa) and Set 7 (346 mm, 370 MPa) in Figure 4.5 was generally the same. The magnitude decreased as thickness increased. The thickness of these sets was greater than 150 mm and the deflection bowls had a similar shape. There was minimal differential vertical deflection between the wheel and axle centreline. The horizontal displacement was order of magnitude smaller than the vertical displacement and shows that all movement was toward the right, away from the axle centreline.

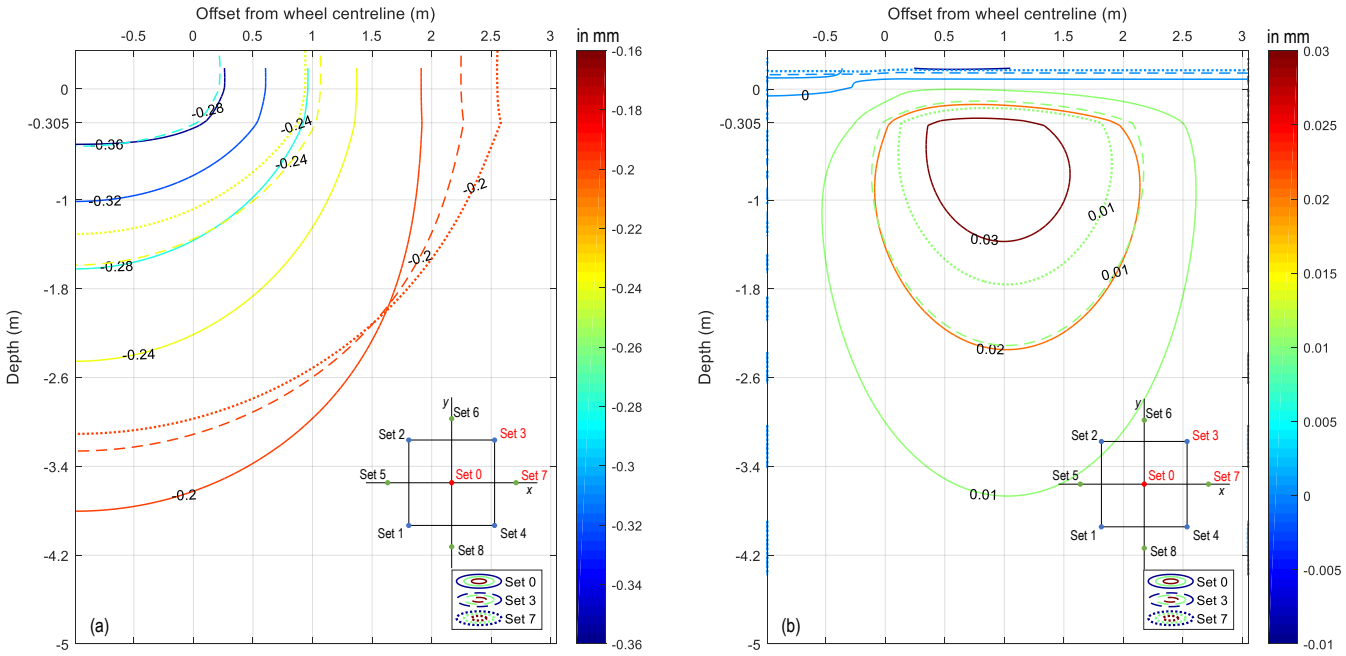

Figure 4.5 Contour plots of (a) vertical and (b) horizontal displacement of Set 0, Set 3 and Set 7

Figure 4.6 shows the vertical and horizontal displacement contour plots of Set 0 (188 mm, 370 MPa), Set 1 (76 mm, 137 MPa) and Set 5 (30 mm, 370 MPa). The deflection bowls in Figure 4.3 and Figure 4.4 respectively showed that Set 1 and Set 5 deflected into the substructure with a distinct trough around the load location and hogging type deflection toward the axle centreline. The vertical displacement contours form concentric-like circles around the load location at shallow depths. Between depths of 0.305 m and 1 m, the horizontal location of maximum vertical deflection moves toward the axle centreline. The deflection bowl of Set 0 was pronounced. The 0.32 mm and 0.24 mm contour lines are at a shallower depth than for Set 1 and Set 5 and the maximum displacement is around the centreline of the axle.

The horizontal displacement is order of magnitude smaller than the vertical displacement. For Set 1 and Set 5 there is movement towards the left and right of the load location. The section of substructure that displaces toward the right stretches past the wheel centreline to axle centreline. The section of substructure that displaces to the axle centreline is small. It stretched from the wheel centreline to the axle centreline in width and the depth is relatively shallow. For Set 0 there is only movement to the right, with minimal horizontal displacement at shallow depths.

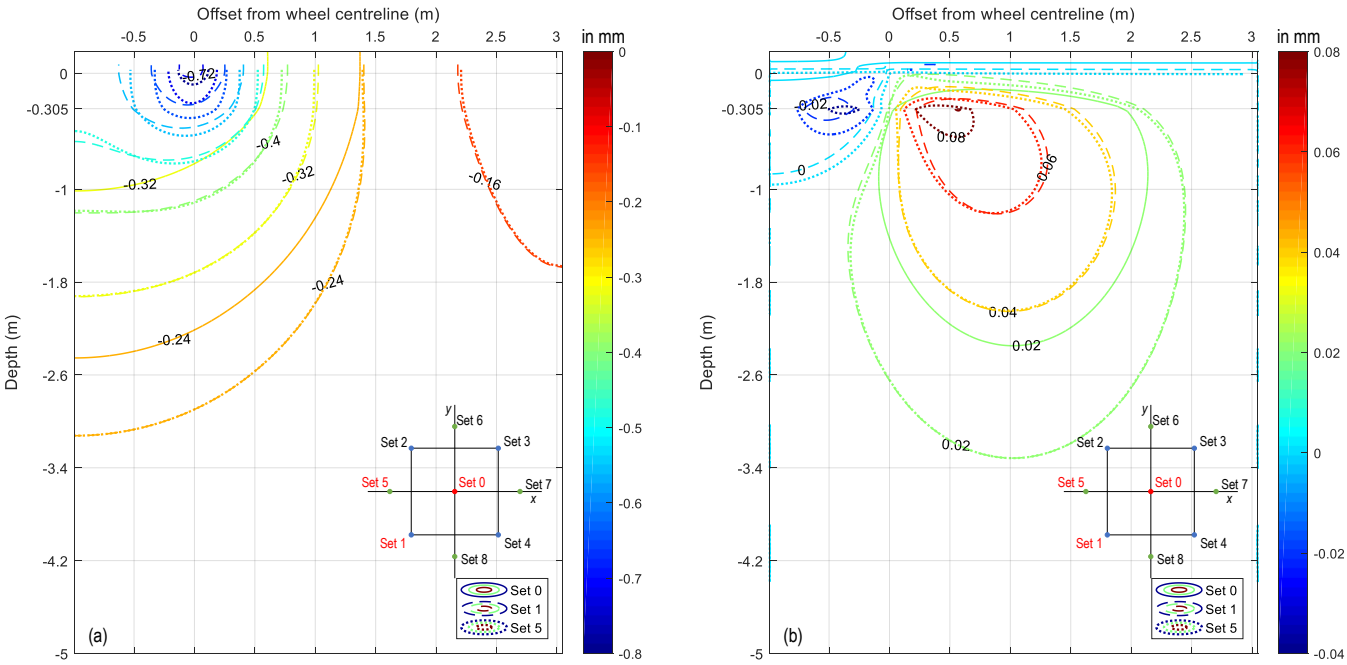

Figure 4.6 Contour plots of (a) vertical and (b) horizontal displacement of Set 0, Set 1 and Set 5

It is proposed that concrete pavements that are thin enough to have a distinctive trough in the wheel centreline should be designed for rutting as a traffic associated failure mechanism. This is typically done by determining the permanent deformation in the wheel path using a combination of numerical models and permanent deformation properties of the layer materials. The response in terms of deflected shape and resulting displacement in the substructure of thin concrete pavements is more complex than of thick concrete pavements when loaded with a two-wheel axle. The significantly different overlap of zones of influence and the hogging in the axle centreline supports the proposal that APT of UTCRCP should use an axle instead of a dual-wheel.

4.3 RESPONSE OF 50 MM THICK CONCRETE BOUND LAYER PAVEMENT

In Chapter 3 the model used by Kim (2007) was replicated. The bound layer material stiffness was changed from that of asphalt (2 759 MPa) to concrete (40 GPa). The thickness remained at 76 mm. In Section 4.1 bound layer thicknesses of 30 mm, 76 mm, 188 mm, 300 mm and 345 mm were used for RSM. However, UTCRCP uses a 50 mm HS-SFRC layer. A thickness of 50 mm is used for the remainder of this chapter.

The difference in the pavement response of 50 mm and 76 mm thick concrete bound layers was determined by evaluating the critical parameters and deflected shape. Table 4.4 shows that all the critical parameters increased when the thickness was reduced. This effect was anticipated.

The horizontal tensile stress in the 50 mm thick concrete bound layer exceeds the flexural strength of NSC, enforcing that HS-SFRC should be used for thin concrete bound layers supported by substructures that do not incorporate other bound materials.

Table 4.4 Critical parameters of 50 mm concrete layer and 76 mm concrete layer models

Thickness	Critical parameter			
	$\delta_{v\ surface}$ (mm)	$\sigma_{h\ bottom\ of\ BL}$ (kPa)	$\sigma_{v\ top\ of\ subgrade}$ (kPa)	$\varepsilon_{v\ top\ of\ subgrade}$ (μm/m)
50 mm	-0.862	6914	-33.8	-749
76 mm	-0.692	4637	-22.3	-466

Figure 4.7 shows the deflection bowl. It shows that the deflection around the load location increased as a result of the reduced concrete layer thickness. The difference in deflection diminishes between an offset of 0.5 m and 1 m to the right of the load location. In the axle centreline the deflection was greater for the 76 mm thick concrete layer model.

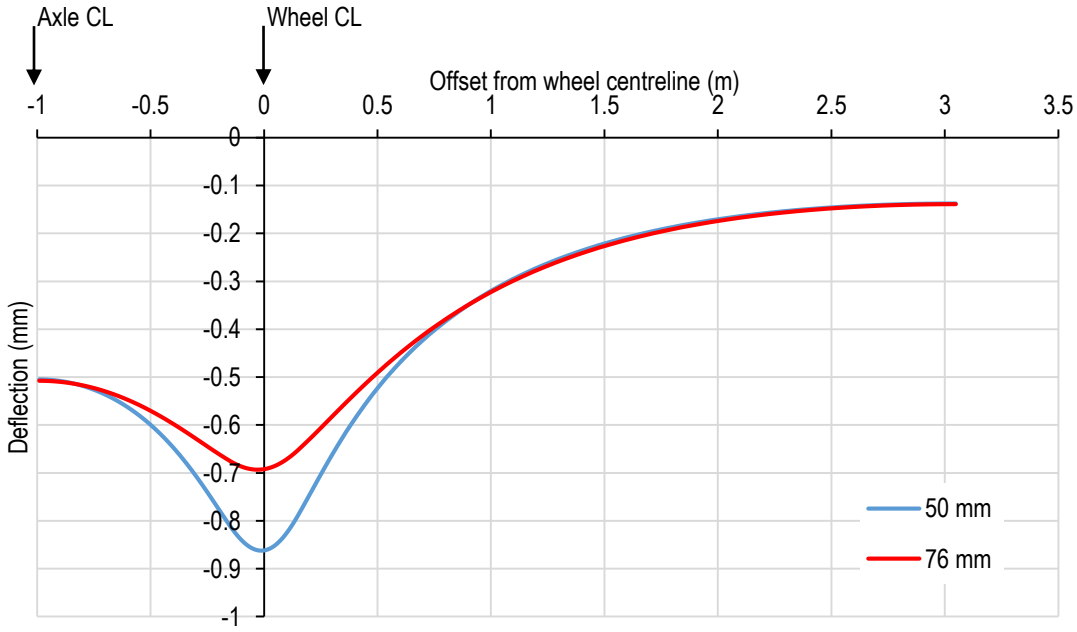

Figure 4.7 Transverse deflection bowls of models with 50 mm and 76 mm concrete layers

Thus far, only the transverse deflection bowls of pavement models have been discussed. Deflection bowls in the longitudinal direction of the pavements give a more complete description of pavement response. In physical modelling, longitudinal deflection bowls are measured when using multi-depth deflectometers. Figure 4.8 shows a schematic of longitudinal deflection bowls that are measured in the wheel centreline and axle centreline from the

transverse axle/wheel centreline. Depending on the relative stiffness, the deflection in the axle centreline should be smaller than in the wheel centreline.

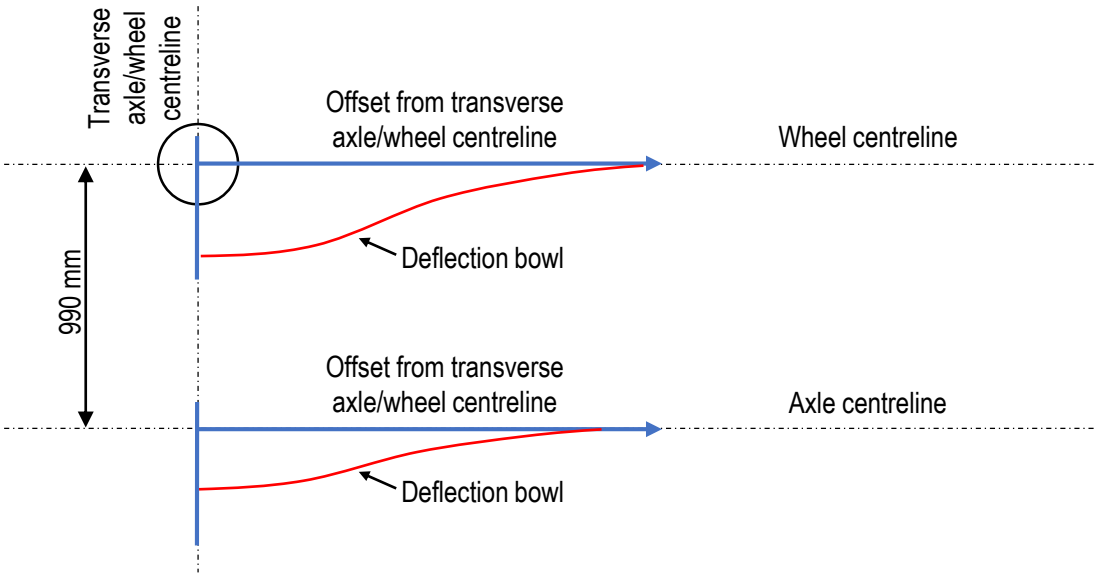

Figure 4.8 Schematic of longitudinal deflection bowls in the wheel and axle centreline

Figure 4.9 shows the longitudinal deflection bowls in the axle centreline and wheel centreline. The figure shows that the deflection is similar from an offset of approximately 0.8 m from the transverse axle/wheel centreline (CL). The deflected shape diverges closer to the transverse axle/wheel centreline, with the deflection in the axle centreline being smaller and the bowl being wider.

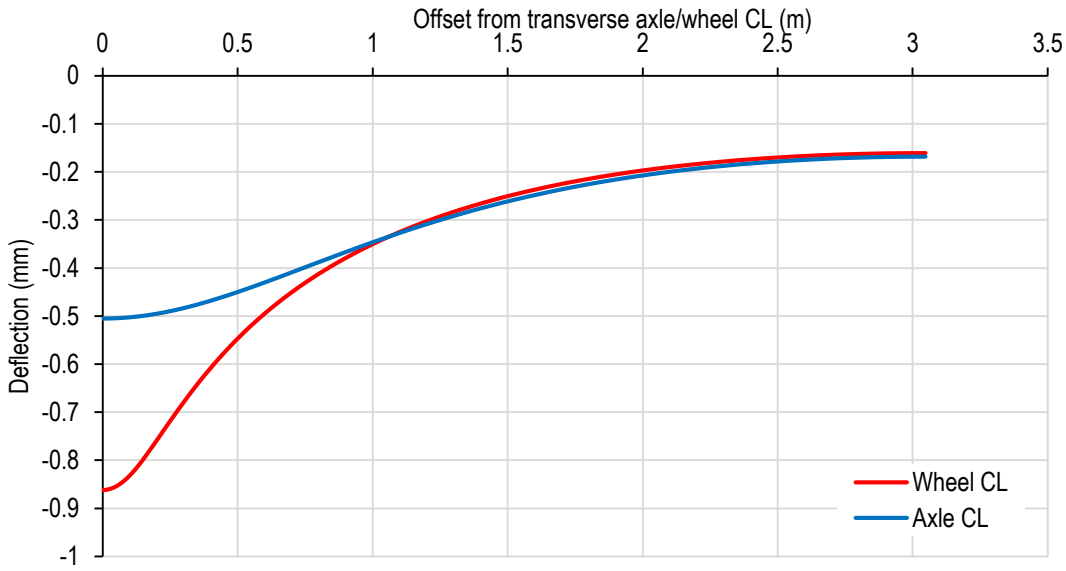

Figure 4.9 Longitudinal deflection bowls for 50 mm thick concrete bound layer model

4.4 EFFECT OF BASE MATERIAL STIFFNESS

In the previous section the concrete layer thickness and base material stiffness were varied simultaneously. The base material stiffness was varied in a range typical for unbound granular material. The effect of including bound granular material, in the form of cement stabilized granular material, in the design of UTCRCP is of interest. In this section the effect of varying the base material stiffness in the range of cement stabilized materials was investigated.

A concrete layer thickness of 50 mm was used, because this is the thickness originally suggested for UTCRCP. The material stiffness of cement stabilized material is variable, influenced by the extend of cracking of the pavement layer, as well as whether the overlaying layer is bound or unbound. A wide range of base material stiffness values (Young's Modulus) were used, varied in multiples of 1 400 MPa. Table 4.5 shows the values that were used. The maximum value was close to that used as the concrete Young's Modulus (40 000 MPa). The pavement response to a standard axle load is considered.

Table 4.5 Base material stiffness

Material stiffness (MPa)		
1 400	12 600	37 800

4.4.1 Effect of increasing base material stiffness

The effect of increasing the base material stiffness was investigated by considering the critical parameters (as in Kim, (2007)), the tensile stress at the bottom of the base layer, as well as the deflection bowls. The response of a pavement model with base material stiffness of 207 MPa (typical for granular material not cement stabilized) is included for reference. Table 4.6 shows the critical parameters of the respective base materials stiffnesses used. The subgrade properties remained constant with a depth of 20.955 m, Young's Modulus of 41 MPa and Poisson's Ratio of 0.45.

All the critical parameters decreased as the base material stiffness was increased. This is because load spreading through the base improved. The horizontal stress at the bottom of the concrete layer became a compressive stress as the base material stiffness was increased.

Table 4.6 Critical parameters of models with increasing base material stiffness

Material stiffness	Critical parameter			
	$\delta_{v\ surface}$ (mm)	$\sigma_{h\ bottom\ of\ BL}$ (kPa)	$\sigma_{v\ top\ of\ subgrade}$ (kPa)	$\varepsilon_{v\ top\ of\ subgrade}$ (μm/m)
207 MPa	-0.862	6914	-33.8	-749
1 400 MPa	-0.515	2185	-14.6	-294
12 600 MPa	-0.317	-394.6	-5.07	-71.0
37 800 MPa	-0.273	-319.6	-3.38	-38.1

Figure 4.10 shows the effect of increasing the base material stiffness on the horizontal stress at the bottom of the base layer. A tensile stress is induced, the relationship is logarithmic and ranges between 86.9 kPa and 605 kPa. As the stiffness of the base increases, the tensile stress increases and the ability of the layer to not crack (tensile strength) becomes more important.

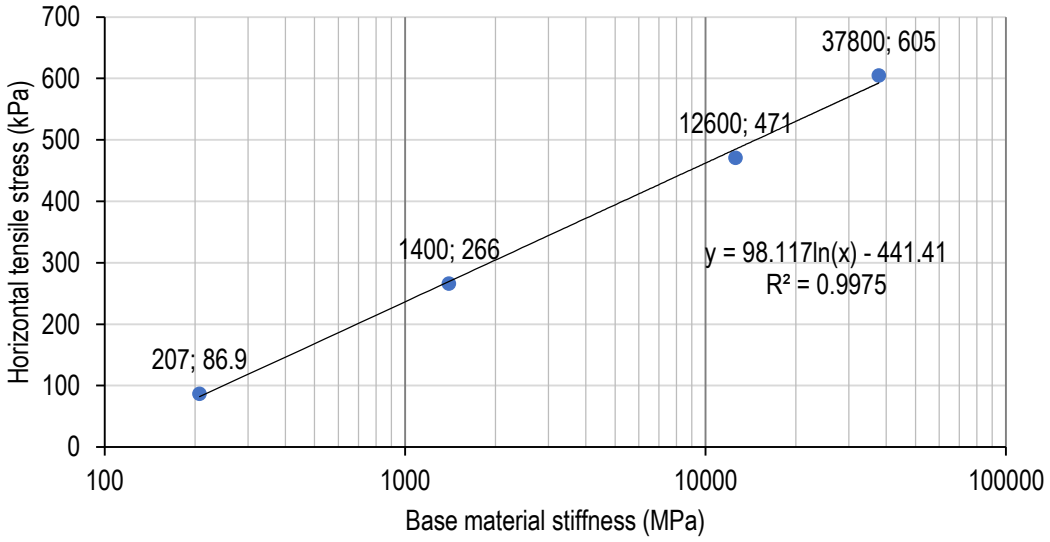

Figure 4.10 Horizontal tensile stress at bottom of base

In Figure 4.11 the horizontal tensile stresses in the base versus material stiffness are compared to the uncracked material stiffness and flexural strength combinations summarised in Section 2.8 from TRH 4: Structural Design of Flexible Pavements for Interurban and Rural Roads (Department of Transport, 1996) and TRH 13: Cementitious Stabilizers in Road Construction (Department of Transport, 1986). The function reported in Figure 4.10 was used to determine the load induced horizontal tensile stress for the material stiffnesses of the respective strength classes in Table 2.2. These stresses were divided by the flexural strength of the strength classes to calculate the stress level (S), which was also included in the Figure 4.11.

The range of the y-axis of Figure 4.11 is greater (0 to 2 500 MPa) than in Figure 4.10 (0 to 700 MPa).

The stress level ranged from a minimum of 0.24 for C1 materials to a maximum of 1.22 for C4 materials, with the number of cycles that can be endured decreasing as the strength decreased. The fatigue life of cemented materials loaded to a stress level under 0.50 is generally good, being able to absorb millions of load cycles (Xie *et al.*, 2018). For the three-layer pavement system modelled using 3D LE FE, the stress levels calculated for the base layer underneath a 50 mm HS-SFRC layer indicated that C1 and C2 materials would perform well under 80 kN axle loads. C3 and C4 materials would deteriorate faster.

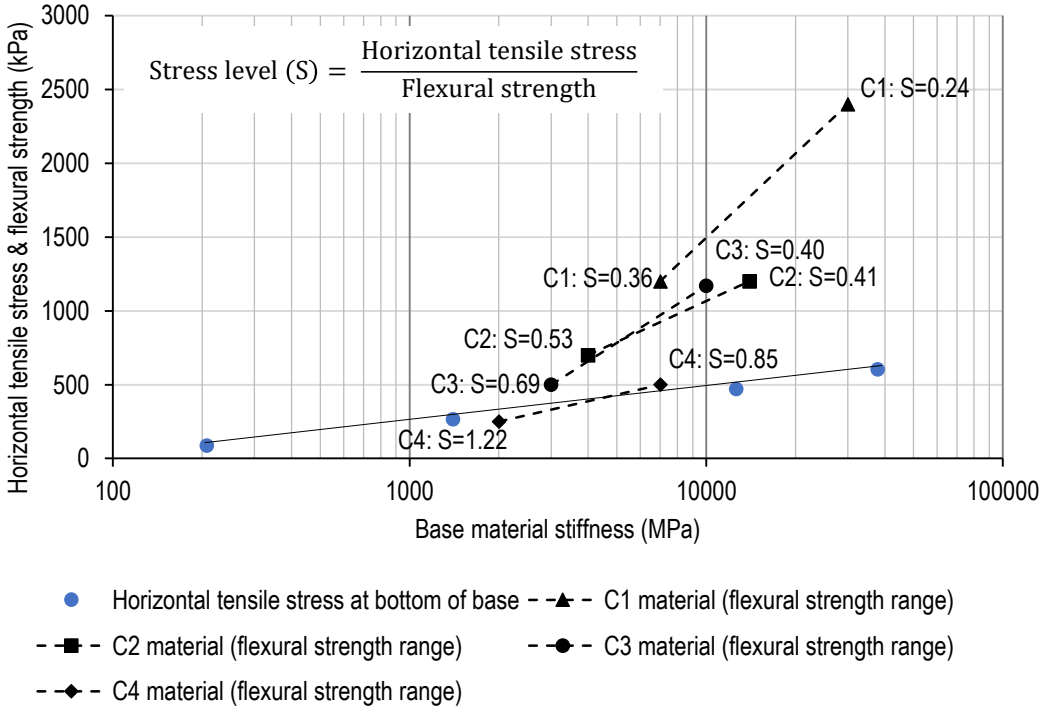

Figure 4.11 Comparison of material stiffness – flexural strength ranges to tensile stress values from models

The LE FE analysis showed that the inclusion of cement stabilized granular material would reduce all critical parameters. However, this analysis does not capture the possibility of the cemented material cracking due to material and traffic-loading variability. The effect of discretely cracked C1 and C2 materials underneath a 50 mm HS-SFRC layer could be detrimental to the layer underneath it, because cemented layer crack edges may cause stress concentrations in the adjacent layers. Physical modelling and FE modelling, that incorporates advanced material models for cemented granular materials, should be used to further investigate the use of cement stabilized granular materials underneath thin concrete layers. Further

investigations should also incorporate the repeated loading of traffic into account in numerical analyses.

Figure 4.12 shows the effect of increasing the base material stiffness on the deflection bowl, where the bound layer and base start acting as one layer and the deflection bowl shape becomes similar to that of the thick concrete layer models (as seen in Section 4.1).

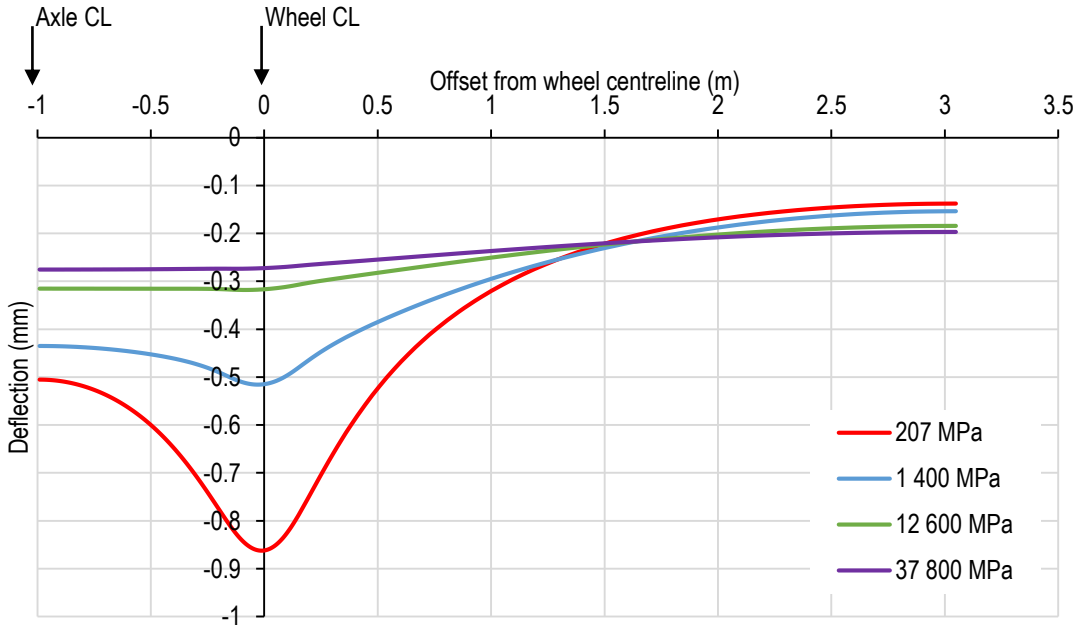

Figure 4.12 Deflected bowls of increasing base material stiffness

Figure 4.13 shows the longitudinal deflection bowls of the 50 mm model with a base material stiffness of 12 600 MPa. The deflection in the wheel and axle centreline was very similar with the deflection in the axle centreline being slightly greater for most of the length except at the load location.

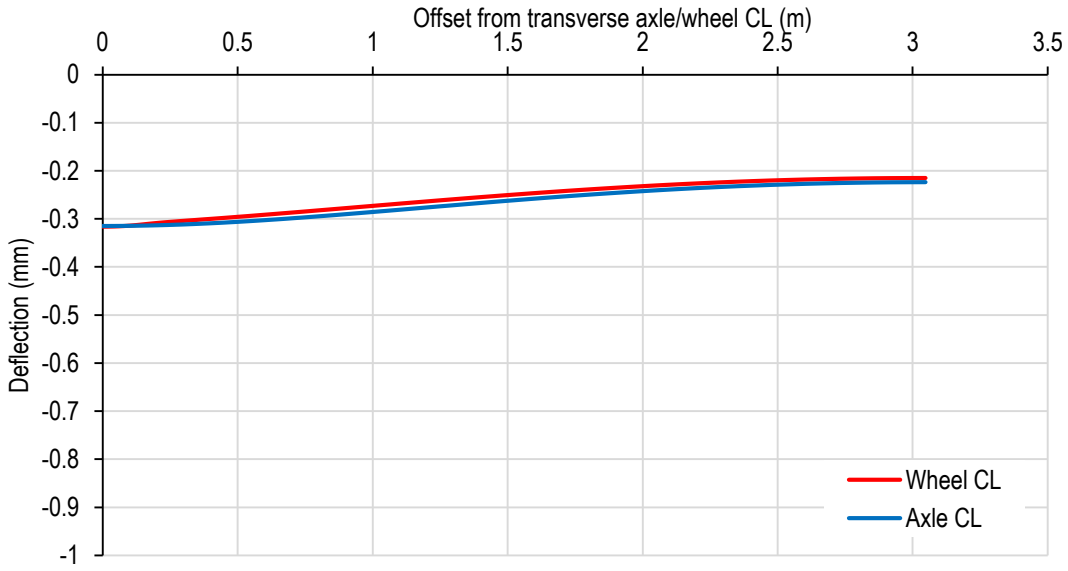

Figure 4.13 Longitudinal deflection bowls in wheel and axle centreline of 12 600 MPa base material stiffness model

4.5 INFLECTION POINT AND RELATIVE STIFFNESS

The inflection point is the point of a curve where a change in direction of curvature occurs, i.e. where the second derivative of the deflected shape is equal to zero. In Figure 4.14 the offset of the inflection points from the wheel centreline can be seen with respect to radius of relative stiffness. The radius of relative stiffness for spring foundation systems was used as in Equation 2.8. The modulus of subgrade reaction used in Equation 2.8 was determined as described in Appendix B. The values of radius of relative stiffness and inflection point offset, in Figure 4.14, can be viewed in Table 4.7.

The inflection point offset was always smaller than the radius of relative stiffness even though the inflection point was further away from the wheel centreline when axle loading was modelled (as pointed out in Section 3.3.3). It can be seen in Figure 4.14 that a range of radius of relative stiffness was not considered in the multivariable analyses and the high base material stiffness set. This range was from approximately 350 mm to 600 mm. The inflection point offset of concrete layers equal to and smaller than 76 mm were all smaller than 310 mm, regardless of base material stiffness. The inflection point offset of the high base material stiffness models (all had a concrete layer thickness of 50 mm) were all smaller than 250 mm. The inflection point offset of concrete layer thicknesses of 188 mm and greater were all greater than 550 mm, regardless of base material stiffness.

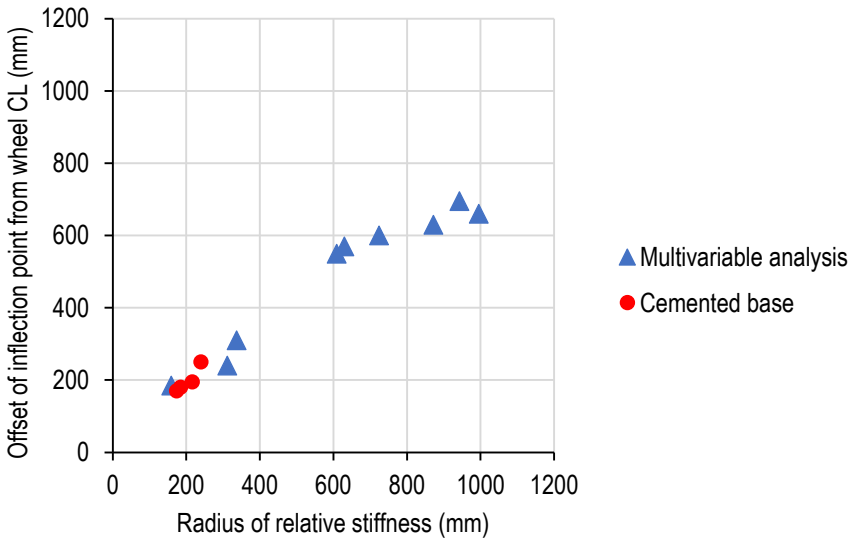

Figure 4.14 Correlation between radius of relative stiffness and inflection point offset

The difference in inflection point offset between the high base material stiffness deflection bowls and the high concrete layer thickness deflection bowls is interesting, because when the deflection bowls are viewed the shape of the high base materials stiffness deflections bowls seem to be similar to that of the thick concrete bound layer models. The inflection point offset for the thin concrete layer was influenced significantly by the stiffness of the adjacent layer. The inflection point offset became smaller as the relative stiffness between the concrete layer and cemented base layer became smaller.

The response of pavement models with radius of relative stiffnesses in the range that was not considered by the multivariable analyses should be investigated. The gradient of the relationship between radius of relative stiffness and offset of inflection point changed, with the gradient being lower for values of radius of relative stiffness greater than 600 mm. This could be influenced by the extent of the stress zone overlap for the wheels at the axle ends.

Table 4.7 Calculated radius of relative stiffness and determined inflection point offset

	Bound layer thickness (mm)	Base material stiffness (MPa)	Modulus of subgrade reaction (N/mm^3)	Radius of relative stiffness (mm)	Inflection point offset (mm)
Multivariable analyses	30	370	0.145	159	185
	76	137	0.117	337	310
	76	603	0.160	311	240
	188	370	0.145	630	570
	188	700	0.165	609	550
	188	40	0.083	724	600
	300	603	0.160	872	630
	300	137	0.117	943	695
	346	370	0.145	996	660
Cemented base models	50	207	0.129	240	250
	50	1400	0.196	216	195
	50	12600	0.365	185	180
	50	37800	0.473	174	170

4.6 SUMMARY

The effect of relative stiffness was investigated by varying the concrete bound layer thickness and base material stiffness simultaneously. The response surface equations showed that the concrete layer thickness had a dominant effect on the pavement response. The contribution of the base material stiffness became more significant when the concrete layer thickness was smaller than 100 mm.

Considering the types of overlap discussed in Chapter 3, only two types of overlap could be identified for the relative stiffness modelled using CCD. The deflection bowls varied between complete overlap and large partial overlap, with the displacement in the axle centreline always being downward. This indicates that small partial overlap, where the displacement in the axle centreline is vertically upward from the unloaded position, only occurs in the beam-on-elastic support simplification (see Chapter 3). The concrete thickness – base material stiffness combinations that did not have single curvature had interesting displacement patterns, with horizontal displacement toward the axle centreline and the offset of maximum vertical displacement changing with depth, moving from the wheel centreline to the axle centreline.

It was proposed that the distinctive deflection trough in the wheel centreline and hogging in the axle centreline of thin concrete layers could be an indicator that a pavement should be designed for rutting. This can be done by verifying that the permanent deformation in the wheel path is in an acceptable range by using a combination of numerical models and permanent deformation properties of the layer materials. These thin concrete pavements should also be modelled numerically and physically using complex load configurations, because important aspects of the pavement response is not modelled using a single wheel instead of an axle.

The effect of including bound granular material, in the form of cement stabilized granular material was investigated by varying the base material stiffness over a wider range. By doing this the relative stiffness was varied. Increasing the base material stiffness reduced all the critical parameters. It was found that there was a logarithmic relationship between the tensile stress at the bottom of the base layer and base material stiffness. Assuming linear elasticity, it was found that cemented bases underneath a 50 mm HS-SFRC layer that use C1 and C2 materials would perform well under standard axle loads of 80 kN because the stress level they are subjected to is relatively low. The stress level of C3 and C4 materials was higher and these materials are more likely to deteriorate fasters underneath a 50 mm HS-SFRC layer. Advanced material models for cement stabilized granular materials should be used to verify the behaviour of cemented bases directly underneath thin HS-SFRC layers.

A positive relationship exists between the radius of relative stiffness and offset of inflection point from the wheel centreline. The offset of inflection point was always smaller than the radius of relative stiffness. The inflection point offset of the transverse deflection bowl and radius of relative stiffness of the high material stiffness base models were small even though the deflection bowls were similar to that of the thick concrete layer models. This indicates that the relative stiffness between the thin HS-SFRC and cemented bases determined the offset of the inflection point, while the relative stiffness between two upper layers and subgrade determined the overall deflection.

The following questions identified during the literature review could be partially addressed from the summary in Chapter 4:

- Should UTCRCP be modelled as a flexible pavement where the substructure properties are important, and rutting is a traffic associated failure mechanism?

  Yes, the multivariable analysis showed that the response of thin concrete pavements is dependent on the substructure stiffness. It also showed that there is a steep increase in the vertical compressive stress and strain in subgrade from concrete layer thicknesses smaller than 150 mm. As for flexible pavements, including a cement stabilized bases would ensure

gradual load spreading. As the material stiffness becomes greater the deflected shape would reflect that of thick concrete pavements.

- Can concepts of relative stiffness be used to predict the extent of wheel load interaction and if a pavement should be modelled as a flexible pavement?

Yes, relative stiffness can be used. The use of an inflection point as an indicator of relative stiffness should be explored further. The relative stiffness effect of adjacent layers and the relative stiffness of effect of structural and foundation components of pavements should be determined.

- Is it useful to incorporate cement stabilized bases in UTCRCP to improve load spreading?

According to the LE FE modelling done, the incorporation of cement stabilized bases would reduce all the critical parameters and the stress levels in the base would fall within acceptable ranges. However, the possibility of the cement stabilized material cracking due to material variability and/or overloading should be taken into consideration before a conclusion can be made of cemented base usefulness. If C1 or C2 materials are used underneath a 50 mm HS-SFRC layer and the cemented layer does crack discretely, the unbound granular layer of subgrade underneath it will be subjected to stress concentrations. The use of cement stabilized base in UTCRCP should be investigated further.

- Should numerical and physical modelling of UTCRCP use axle loading instead of a single wheel and are important aspects of the pavement response ignored if axle loading is not used?

Yes, considering the deflected shape and vertical and horizontal displacement for the relative stiffnesses considered in the multivariable analysis concrete pavements thinner than 76 mm would be modelled more representatively using axle loading. The exact thickness need still needs to be determined, because a range of relative stiffness was not considered during the multivariable analysis.

With the effect of load configuration and relative stiffness thoroughly investigated using LE FE modelling it was opted to use physical modelling to verify the observations made and investigate the effect of true material response.

5 PHYSICAL MODELLING OF ROAD PAVEMENTS

5.1 INTRODUCTION

In the preceding chapters the effect of load configuration and relative stiffness on the response of road pavements to traffic loading was investigated using LE FE modelling. In this chapter, the response of road pavements to traffic loading was investigated using scaled physical models. Once again load configuration and relative stiffness were varied. Two sets of physical models were tested. The difference between the two sets was the load configuration. The first set of physical models were loaded using strip loading. The second set of models were loaded using an axle with rolling wheels.

The complex multi-layer systems of road pavements were simplified to two- and three-layer systems and the relative stiffness was varied by varying the layer thicknesses and material properties. For the strip loading load configuration, two two-layer systems and one three-layer system were tested. For the rolling wheel loading load configuration one two-layer systems and one three-layer system were tested.

A scaling factor of 1:10 was used. This factor was influenced by the practicality of constructing the respective layers. Scaled physical models were tested using the centrifuge facility at the University of Pretoria. The centrifuge was used to induce a representative stress field in the soil substructure of the scaled models. The facility at the University of Pretoria has a 150 G-ton geotechnical centrifuge. It is an Actidyn C67-4 model with a 3 m radius centrifuge arm and a 0.8 m x 1.0 m x 1.3 m model platform. Further details of the centrifuge are given in Jacobsz *et al.* (2014).

This chapter contains detail of the centrifuge modelling that was conducted for this research project. It provides a brief overview of centrifuge modelling and scaled concrete. The model composition and the preparation of the scaled concrete overlays are described, followed by the experimental setup, results and discussion of the respective load configurations. The chapter concludes with a summary of the centrifuge model behaviour.

5.1.1 Geotechnical centrifuge modelling

Full-scale testing of geotechnical systems is often unfeasible because of cost (Madabhushi, 2014). The difficulty of scaling geotechnical systems is that the stress state in small scale models are not representative of full scale and that the behaviour of soil is dependent on stress state.

Geotechnical centrifuges are used to induce a representative stress field in scaled models, thus ensuring representative geotechnical system responses. Centripetal acceleration is used to induce an artificial gravitational acceleration. A 1-N scale model tested at N times gravitational acceleration will have the same effective stress acting at relative corresponding points in the full-scale and model soil. Although the effect of increasing the gravitational acceleration is not constant for all variables, the effect on the variables of interest in this study is linear or constant. Table 5.1 shows general scaling laws (Madabhushi, 2014).

Table 5.1 Scaling laws of centrifuge testing

Variable	Scale factor
Model Scale	N
Acceleration	N
Linear dimensions	1/N
Area	$1/N^2$
Force	$1/N^2$
Stress	1
Strain	1
Density	1

5.1.2 Scaling of concrete

Care must be taken when interpreting small scale tests of reinforced concrete. This is because concrete is a brittle material and significant size effect exists. The size effect arises because the strength of reinforced concrete elements involves fracture of concrete which depends on the size of flaws within concrete (Knappett *et al.*, 2011). Significant overstrength is expected at scaling factors higher than 20.

Because of this constraint, it is common practice to design centrifuge models to have the correct scaled bending stiffness (EI) and use alternative materials (with different material stiffnesses). Typical materials include aluminium alloys (Laue & Arnold, 2008; Lemmen, 2015).

The brittle behaviour of concrete is not captured by aluminium and there has been a move toward developing scaled concrete that give reasonable strength and stiffness behaviour. Gypsum-based mortars have been developed (Knappett *et al.*, 2011). Scaled concrete has been used at the University of Pretoria for centrifuge modelling of soil-structure interaction (Kearsley *et al.*, 2014; Lemmen *et al.*, 2017). The general approach in designing mixture compositions for scaled concrete is to scale the slope of the particle size distribution of the

aggregate thus reducing the maximum particle size. The cement particles are not scaled to prevent variation of strength gain. Representative mechanical properties have been recorded (Kearsley *et al.*, 2014).

5.2 MODEL COMPOSITION

The behaviour of granular materials is dependent on its in-situ state. A variety of factors, such as moisture content, change the in-situ state and incorporating these factors can become complex. It is common practice to simplify the substructure when investigating slabs-on-grade. Often materials with relatively well understood response to load are used. This includes cork, rubber, foamed concrete and springs (Barros & Figueiras, 1999; Belletti *et al.*, 2008; Elsaigh *et al.*, 2011). The elasto-plastic response of granular materials was of interest in this study and the response of sand to loading is reasonably well understood. For the purposes of this study the substructure was primarily modelled using dry sand.

Typical pavements consist of subgrade with layers of unbound and bound granular materials constructed on top of it. The thicknesses of these layers vary between 80 and 200 mm. The complex multi-layer system of road pavements was simplified to two- and three-layer systems. The two-layer systems consisted of a substructure of compacted sand with an overlay of standard thickness scaled NSC or an overlay of ultra-thin scaled HS-SFRC. The first two-layer system is referred to as “thick concrete pavement model” and the second two-layer system is referred to as “thin concrete pavement model”. The three-layer system consisted of a compacted sand subgrade, a cement stabilized sand base and an overlay of ultra-thin HS-SFRC. This model is referred to as “thin concrete with cemented base model”. All bound and unbound granular layers were 15 mm representing 150 mm at full scale.

Figure 5.1 illustrates the component arrangement and scaled geometry of these systems. Figure 5.1 (a) shows the composition of the two-layer system representing rigid pavements. A 30 mm NSC slab was placed on compacted sand, which, when tested at 10G, would have the same self-weight and stiffness effect than a 300 mm thick concrete pavement layer. Figure 5.1 (b) and Figure 5.1 (c) show the composition of the models with the ultra-thin HS-SFRC overlays. The HS-SFRC overlays were 5 mm thick, thus modelling a 50 mm thick HS-SFRC layer. The cement stabilized sand base (also referred to as cemented sand base) was 15 mm thick, modelling a 150 mm stabilized base layer. The depth of the strip load model substructure to the strongbox base was 160 mm. The depth of the rolling wheel load model substructure to the strongbox base was 295 mm.

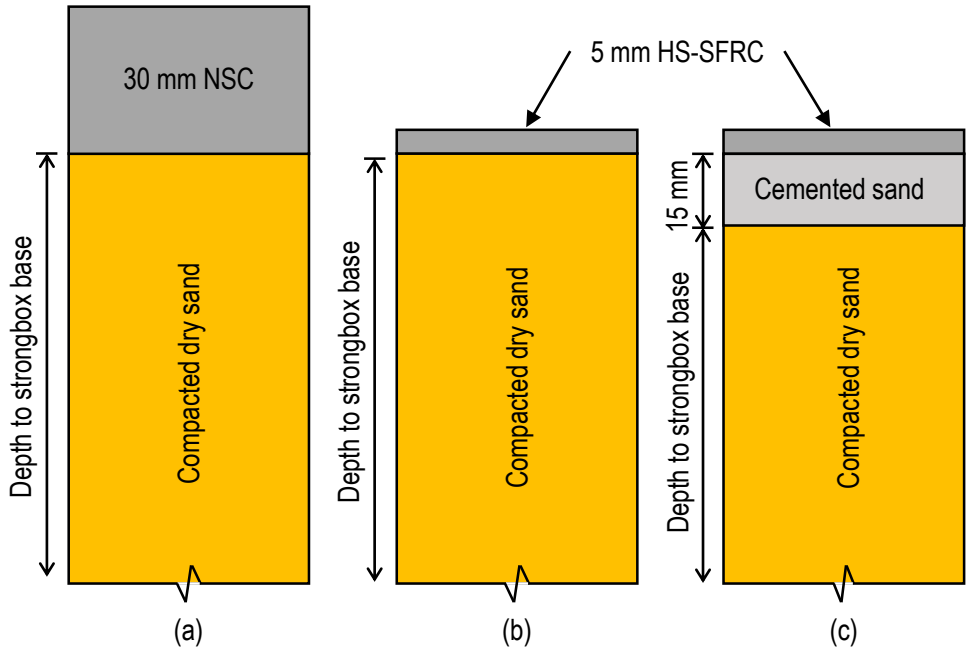

Figure 5.1 Multi-layer pavement systems with (a) thick NSC slab, (b) ultra-thin HS-SFRC slab and (c) ultra-thin HS-SFRC slab with cement stabilized base

The compacted sand consisted of dry silica sand. The cemented sand consisted of the same silica sand stabilized using cement and water. Scaled concrete was used for the concrete overlays. The material properties of the silica sand and cemented sand are provided in the experimental setup of the respective load configurations that were tested.

5.3 SCALED CONCRETE OVERLAYS

Kearsley *et al.* (2014) developed a scaled fibre reinforced concrete that is an approximate equivalent of HS-SFRC in terms of load deflection behaviour. The concrete mix design was adjusted, decreasing the maximum fine aggregate size and increasing the superplasticizer dosage. This was done to improve how castable the scaled concrete is. To replicate the effect of the high reinforcing content of the steel fibres and steel bar mesh, micro steel fibres and wire mesh were used. Table 5.2 shows the mix design and properties of the concrete.

Table 5.2 Scaled concrete mix designs

Concrete type	Scaled HS-SFRC	Scaled NSC
Material	Quantity (kg/m^3)	
Cement (CEM 42.5R)	450	350
Silica fume	50	N/A
Dolomite sand (<1.18 mm)	1850	2037
Micro steel fibres	80	N/A
Superplastisizer [a]	4.4	1.0
Mechanical properties		
Compressive strength (MPa)	104	57
Flexural strength (MPa)	31	18
Young's Modulus [b] (GPa)	42	35

a) Percentage by mass of cementitious material

b) $E_c=10f_{cube}^{0.31}$ ((Domone & Illston, 2010)

Figure 5.2 shows the micro steel fibres and prepared mesh. The fibres were 0.2 mm in diameter and 10 mm in length. The wire mesh had a diameter of 0.5 mm and had an aperture of 5 mm by 5 mm. To ensure bond between the mesh and concrete, the mesh was treated with hydrochloric acid to increase its surface roughness.

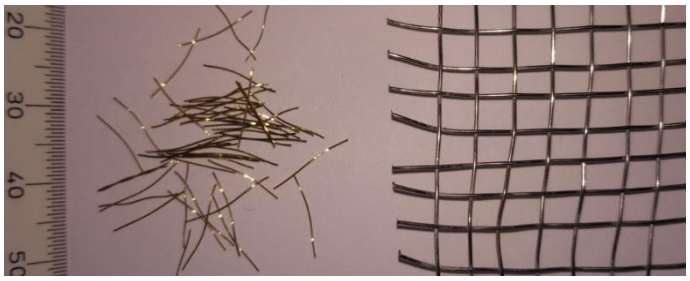

Figure 5.2 Micro-steel fibres and prepared mesh

The slabs were precast in a rigid smooth mould with the required plan area dimensions for the model setup and a thickness of 5 mm. Roughness was created on the exposed surface. When constructing the model, the rough surface was placed on the substructure to simulate a degree of friction. The mesh was positioned in the middle of the slab by compacting half the fresh concrete in the mould, placing the mesh and then inserting the other half of the concrete required to fill the mould.

5.4 STRIP LOADING: EXPERIMENTAL SETUP

As part of the scaled physical modelling, pavement models were loaded using strip loads, resulting in a plane strain setup. The difference between applying equal pressure over a strip area and square area was illustrated in Figure 2.16. For strip loads, higher stresses are experienced at greater depths and the zone of influence is wider. The difference between the two load configurations was explored in Chapter 3 where the difference between applying an equivalent pressure over a circular area or a strip was investigated. The three model compositions described in Section 5.2 were tested.

In the context of scaled physical modelling of pavements in a centrifuge, strip loading had some benefits as the complexity of load application was reduced and the pavement could be constructed against a stiff glass window allowing a conceptual model of the response to be developed from visual observation. Digital Image Correlation (DIC) was used to analyse the response. The plane strain assumption also eliminated the influence of the longitudinal model dimension, which allowed the dimension to be reduced up to what was easily constructible. This reduced material coast as well as the time required to build the models.

5.4.1 Model setup

The strip loading models were tested in an adjustable multi-purpose aluminium strongbox. Figure 5.3 shows a schematic of the strongbox and model setup in plan and in section. Three of the box sides, as well as the base, consisted of 50 mm thick aluminium panels. The fourth side of the box was an 80 mm glass panel that made visual observations of the model during testing possible. The inner dimensions of the strongbox were 395 x 400 x 600 mm. The length of the model was limited to 125 mm by placing spacers inside the strongbox. The resulting plan area dimensions of the model was 125 x 600 mm. Approximately 570 mm of the 600 mm model width was visible through the glass window. The substructure of the pavement models had a depth of 160 mm.

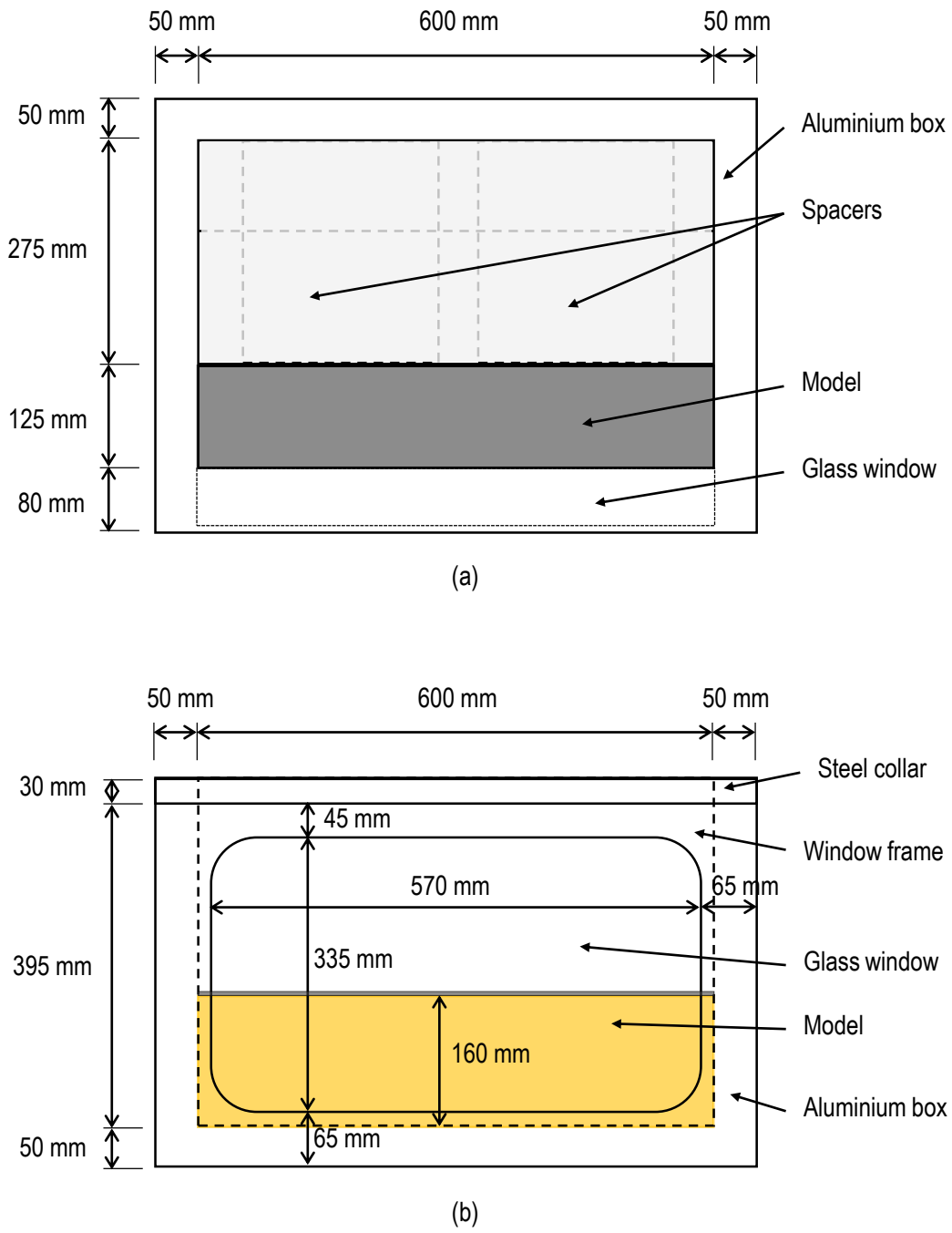

Figure 5.3 Schematic of strongbox in (a) plan and (b) profile

Figure 5.4 shows the load application system that was used for strip loading models. Rubber strips attached to a rigid footing were used to apply two strip loads. The width of the strip loads was 25 mm and they were spaced at 200 mm centre to centre. A stepper motor was used to apply load along the centre of the frame. The motor was attached to a steel stand that was attached to a steel collar at the top of the strongbox. A load cell was used to measure the load applied to models. The movement of the load frame was monitored using a Linear Variable Displacement Transducer (LVDT). A camera was placed 580 mm away from the glass window.

High-quality images were taken. Of the 600 mm model, 570 mm was visible through the glass window and 448 mm could be captured in these images. The entire 160 mm depth was captured.

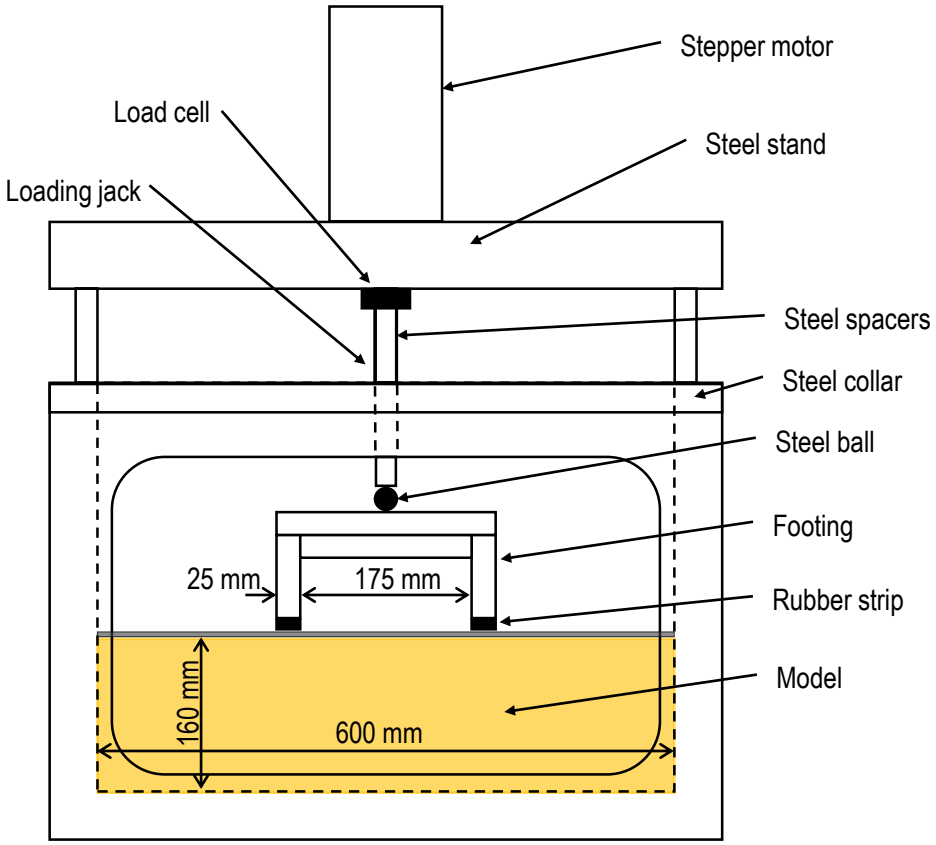

Figure 5.4 Load application system for strip loading models

5.4.2 Digital Image Correlation

Digital Image Correlation (DIC) was used to monitor the pavement response. DIC is a measurement technique often used in physical modelling to determine the displacements. High quality images are typically taken through a rigid, transparent panel (glass or Perspex) against which the model rests. The movement in models can be determined by tracking patches of pixles with specific texture through a sequence of photos taken during a test. White *et al.* (2003) discuss the theory and applicability of DIC for geotechnical applications. Patches are arranged according to the purpose of the analysis.

The patch arrangement for this experiment is described in the results section. Images were taken for every load cycle both when the model was loaded and unloaded.

5.4.3 Model preparation

5.4.3.1 Properties of silica sand

Silica sand, which was characterized by Archer (2014), was used to construct the substructure of the scaled models. Figure 5.5 shows a particle size distribution of the silica sand as obtained from a laser diffraction particle size analyser. The distribution was comparable to that reported by Archer (2014). The silica sand is referred to as Silica Sand 1.

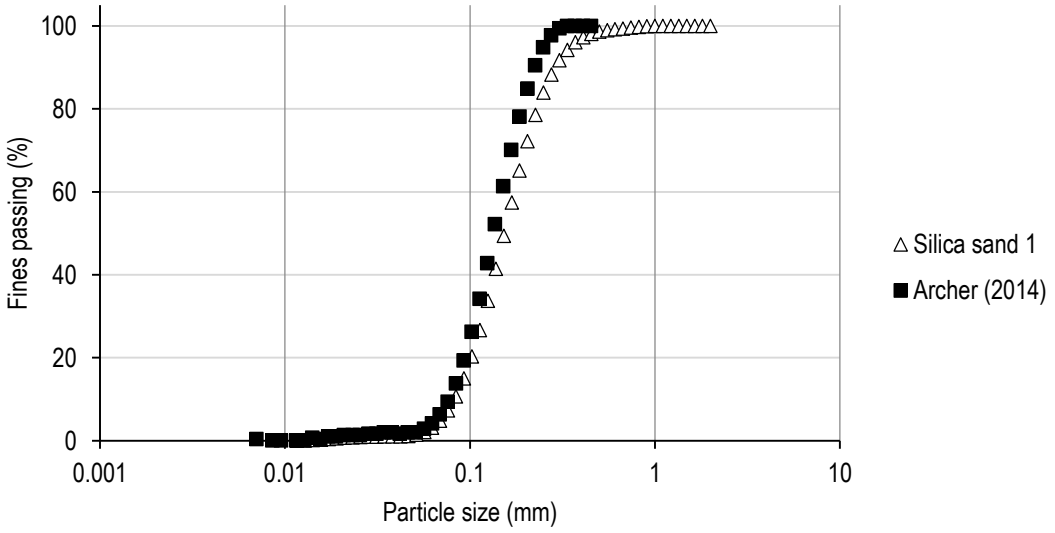

Figure 5.5 Particle size distribution for Silica Sand 1

Table 5.3 shows selected sand properties of silica sand as determined by Archer (2014). This table also contains the maximum friction angle for Silica Sand 1, determined from dry compacted and dry tested triaxial results where two initial mean effective principal stresses were used; 100 kPa and 200 kPa. An average density index of 0.95 was obtained for the two samples.

Table 5.3 Selected properties of Silica Sand 1

Property/Parameter	Value
Specific gravity	2.666
Maximum dry density (kg/m^3)	1 669
Minimum dry density (kg/m^3)	1392
Maximum void ratio, e_{max}	0.92
Minimum void ratio, e_{min}	0.60
Maximum friction angle, φ_{max}(°)	35.4

5.4.3.2 Mechanically stabilized layers

The response of concrete layers on compacted silica sand was modelled. The layers that consisted of silica sand were mechanically stabilized. Manual compaction, which consisted tamping a plate, was used. It was attempted to obtain the same density for all the layers. Dense sand was modelled, and the target density index and dry density were 0.97 and 1 669 kg/m^3 respectively. The mass of sand required to fill the required volume was weighed off and compacted into the strongbox. The first four layers of the substructure were compacted in layers of 25 mm and the last four pavement layers were compacted in 15 mm layers.

5.4.3.3 Cement stabilized layers

For the three-layer system the base was stabilized chemically using a CEM I 42.5 R Portland cement and water. Silica sand was used with 2.5% cement and 10% water by mass. The three materials were mixed in a 10-litre drum mixer and then manually compacted onto the already compacted dry sand. The target density was 1 720 kg/m^3. The cement stabilized layer was 15 mm thick. The newly constructed cement stabilized layer was covered and allowed to harden for 7 days before testing. The tensile strength obtained using the Brazilian disk test was 44 kPa (Gaspar, 2017).

5.4.4 Testing procedure

The models were constructed and placed on the centrifuge model platform. The camera was placed and focused. The strongbox was accelerated to 10G after which loading commenced. Load cycles of 550 kPa were applied.

This study focused on the loaded response to the first load cycle and the accumulation of permanent displacement after 5 cycles.

5.5 STRIP LOADING: RESULTS AND DISCUSSION

The response of the strip loading models was measured using DIC. As the response of the pavements was assumed to be symmetrical around the centreline of the footing, only the right half of the model was considered. Figure 5.6 shows not only the axle centreline (CL), which is also the axis of symmetry, but also the strip centreline (CL) where the load is applied.

The image texture in the patches are tracked to measure displacement. For the purposes of this project, rows of patches at discrete depths were used to determine the model response. Figure 5.6 also shows the arrangement of patches used. The patch rows were placed on the concrete layer to track its displacement and at four depths in the substructure (in multiples of 15 mm).

Although the total depth of the model substructure was 160 mm, the response was only evaluated to a depth of 60 mm.

A single patch on the footing on the strip centreline was used to plot the vertical displacement in the wheel centreline versus time. The displacement of the respective models at maximum load, during the first load cycle, as well as the permanent displacement after the first and fifth load cycle were considered.

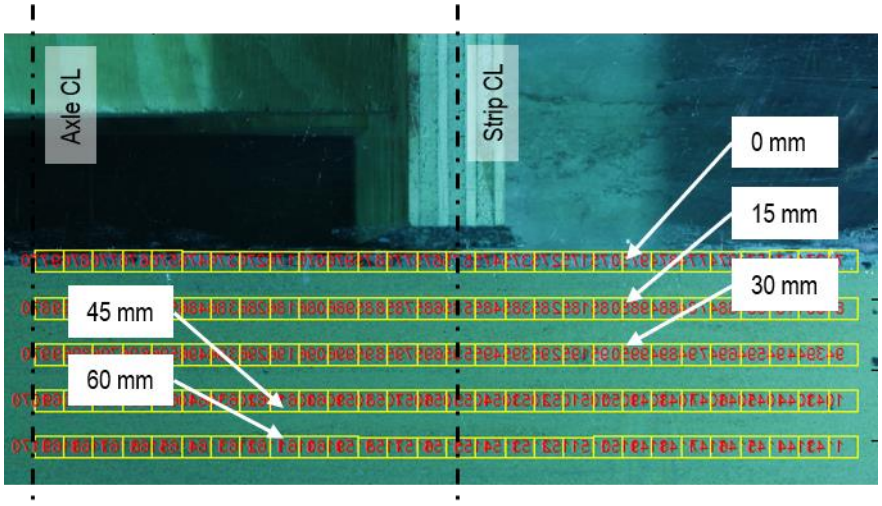

Figure 5.6 Patch row arrangement

Transverse deflection bowls were used to investigate the response of pavements to traffic loading in Chapter 3 and Chapter 4, where LE FE modelling was used. The shape of the deflection bowl and magnitude of deflection was found to be dependent on the relative stiffness of the pavement system, while load configuration also had an influence on the deflection bowl shape and magnitude of deflection. Wheel loads on thin concrete pavements resulted in troughs forming around the load locations, while upward bending occurred along the axle centreline. The deflection of thick concrete pavements resulted in the maximum deflection in the axle centreline. The shape of deflection bowls of three-layer systems with cemented bases were dependent on the material stiffness of the cemented base. Medium stiffness cemented bases (12 600 MPa) still allowed the formation of a deflection trough around the load location, with reduced difference between the displacement in the wheel centreline and axle centreline.

Strip loading (or assuming plane strain conditions) resulted in deflections an order of magnitude greater than for 3D load conditions, where pressure was applied on circular or square areas. The deflection bowl shape for axle loading of the plane strain and the transverse deflection bowl of the 3D loading differed. The difference in displacement of the wheel/strip centreline and axle centreline was reduced for the plane strain FE model.

5.5.1 Vertical displacement versus time

Figure 5.7 shows the vertical displacement of the footing measured in the strip centreline for the three models during the first five load cycles. The initial loading rate differed and became similar by cycle five. Point A (indicated in the figure) was reached when the full load was applied to the model, while Point B is the vertical displacement when the models were unloaded.

There was significant settlement during the first load cycle, during which the most permanent vertical displacement occurred. The thin concrete pavement model clearly showed accumulation of permanent displacement. The thin concrete with a cemented base pavement model underwent the most displacement during the first load cycle, where after the displacement of the model seemed to have stabilized and there was little to no accumulation of permanent strain measured. The thick concrete pavement model displaced the least. The loaded vertical displacement after five cycles ranged between 0.7 mm for the thick concrete pavement model and 1.2 mm for the thin concrete pavement model.

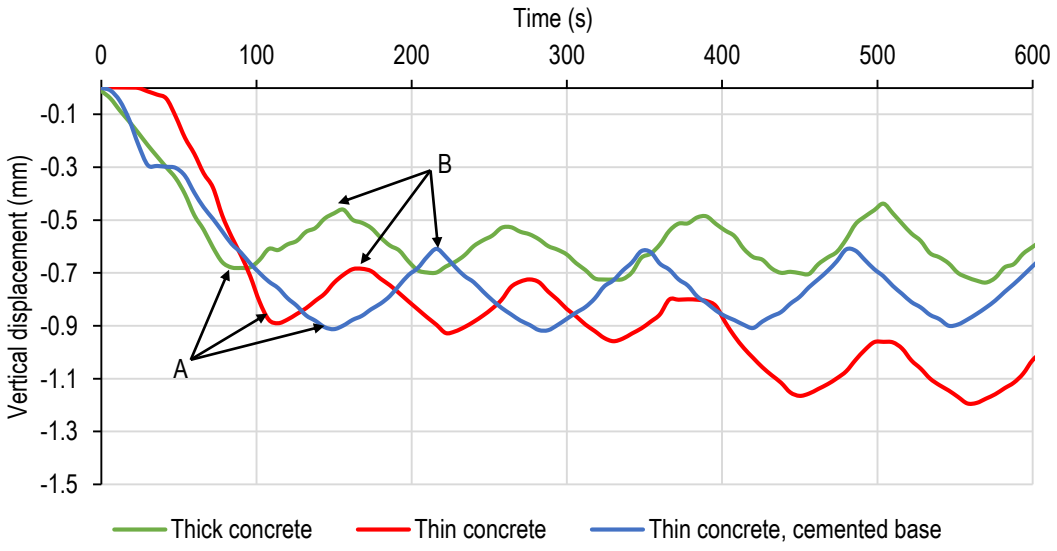

Figure 5.7 Vertical displacement versus time

5.5.2 Deflection at maximum load of first cycle

Figure 5.8 shows the transverse deflection profiles of the three strip loading models that were tested. The deflection was normalized to the maximum deflection of the respective models. Generally, the deflected shapes of scaled concrete slabs on compacted sand reflected behaviour as predicted by the LE FE models for the respective relative stiffnesses. The row of patches at depth 15 mm was used to characterize the deflected shape of the respective pavement systems.

The thick concrete pavement model had minimal differential displacement and seemed to punch into the soil. The thin concrete pavement model had differential displacement, with the maximum deflection occurring along the strip centreline. The deflection bowl was relatively symmetrical around the strip centreline, except for clear downward/negative curvature in the axle centreline. This was not seen toward the right, free-end of the concrete layer, where the concrete could move upward without bending. The deflection bowl of the plane strain FE model was not symmetrical around the wheel/strip centreline either. The observed difference could be due to boundary effects. The strip loading models were not deep. Because the substructure could not move downward, the sand moved to the side toward the axle centreline and then upward. The deflection bowl of the thin concrete layer on a cemented base also had maximum deflection in the strip load centreline. The deflection bowl was slightly wider than for the thin concrete pavement model. These results show that plane strain physical models could be used to investigate the response of concrete pavements comparatively.

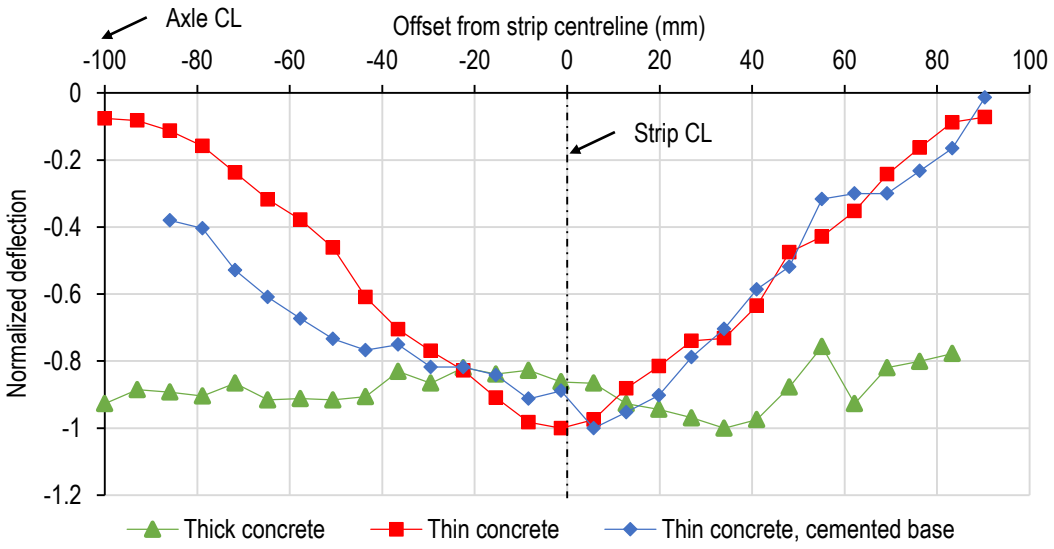

Figure 5.8 Normalized deflection at maximum load of first cycle

5.5.3 Permanent displacement

Figure 5.9 to Figure 5.11 show the normalized permanent vertical displacement of the respective models after one load cycle and after five load cycles. The displacement at depths 0 mm, 15 mm, 30 mm, 45 mm and 60 mm are shown. The displacement at depth 0 mm is the movement at the bottom of the concrete layer. The displacement is normalized using the maximum vertical displacement after five cycles. The uppermost rows should show the most permanent displacement and the displacement of deeper rows should be a fraction of that.

Figure 5.9 shows the permanent vertical displacement with depth of the thick NSC layer on compacted dry sand after one and five load cycles. The magnitude of permanent vertical

displacement decreased with depth. Permanent displacement accumulated from one cycle to five cycles. In Figure 5.9 (a) no residual differential vertical movement remained in the concrete slab. The displacement at depth 15 mm showed the same trend, but the displacement at depths 30 mm to 60 mm increased noticeably toward the axle centreline.

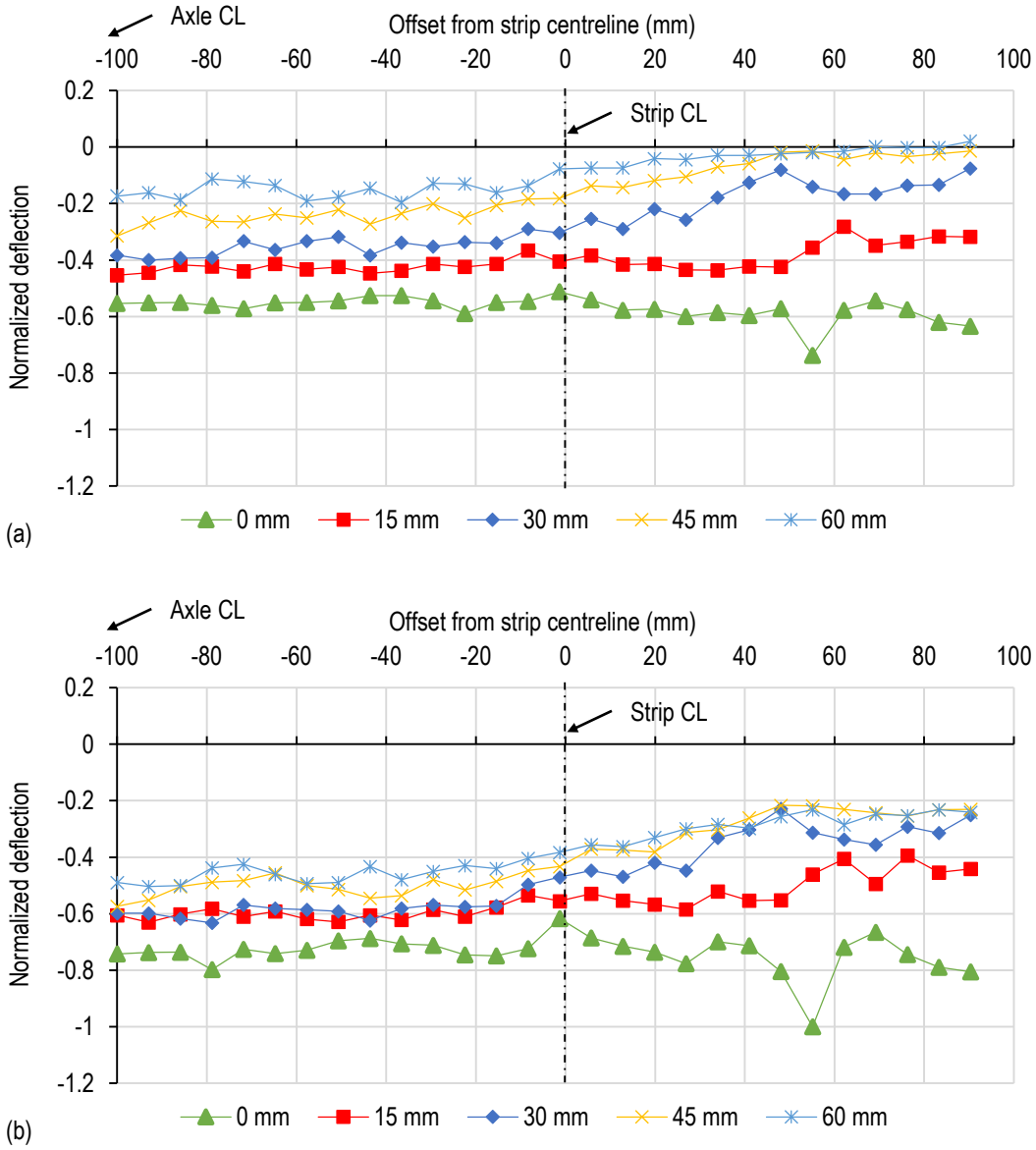

Figure 5.9 Permanent displacement of thick concrete pavement model after (a) one load cycle and (b) five load cycles

Figure 5.9 (b) shows that permanent deformation accumulated at all the depths to the fifth cycle. The permanent displacement trends from the first cycle remained similar. Displacement was slightly greater around the axle centreline. After the first load cycle the displacement reduced with depth. After the fifth load cycle there was a smaller difference in the displacement with depth.

The limited differential vertical displacement in Figure 5.9 was a result of the good load spreading ability of the thick normal strength concrete slab on compacted sand. The substructure was subjected to an approximately uniformly distributed load from the slab to the substructure across the whole plan area of the slab. The slightly greater vertical deformation around the axle centreline could be due to the overlapping stress distribution zones of the two load strips, resulting in slightly higher stress around the axle centreline.

Figure 5.10 shows the permanent vertical displacement of the thin HS-SFRC layer on compacted dry sand. Figure 5.10 (a) shows that differential permanent vertical displacement occurred around the strip load. This resulted in a deflection bowl with a trough around the strip load and a peak in the axle centreline. Not only did the displacement decrease with depth, but the difference between the trough and peak also decreased with depth.

The displacement of depth 0 mm represents the vertical displacement at the bottom of the thin concrete layer. Unlike for the thick concrete pavement model, there was residual differential vertical displacement after the model was unloaded. The permanent displacement of the concrete layer was less than that of the sand at depth 15 mm, just underneath it. This is contrary to the reducing permanent displacement from depth 15 mm to 60 mm below the surface.

Figure 5.10 (b) shows how the entire system settled downward after five load cycles were applied. Two trends can be observed when comparing the permanent displacement after one and five load cycles. The first was that the vertical distance between the troughs and peaks at depths 15 mm to 60 mm increased as more load cycles were applied. The second observation was that the difference in maximum displacement with depth increased as more load cycles were applied. This shows that the distance between the consecutive layers from 15 mm to 60 mm decreased, as the layers moved into each other (or the model deformed permanently). The extent to which the layers moved into each other decreased with depth and distance away from the strip load.

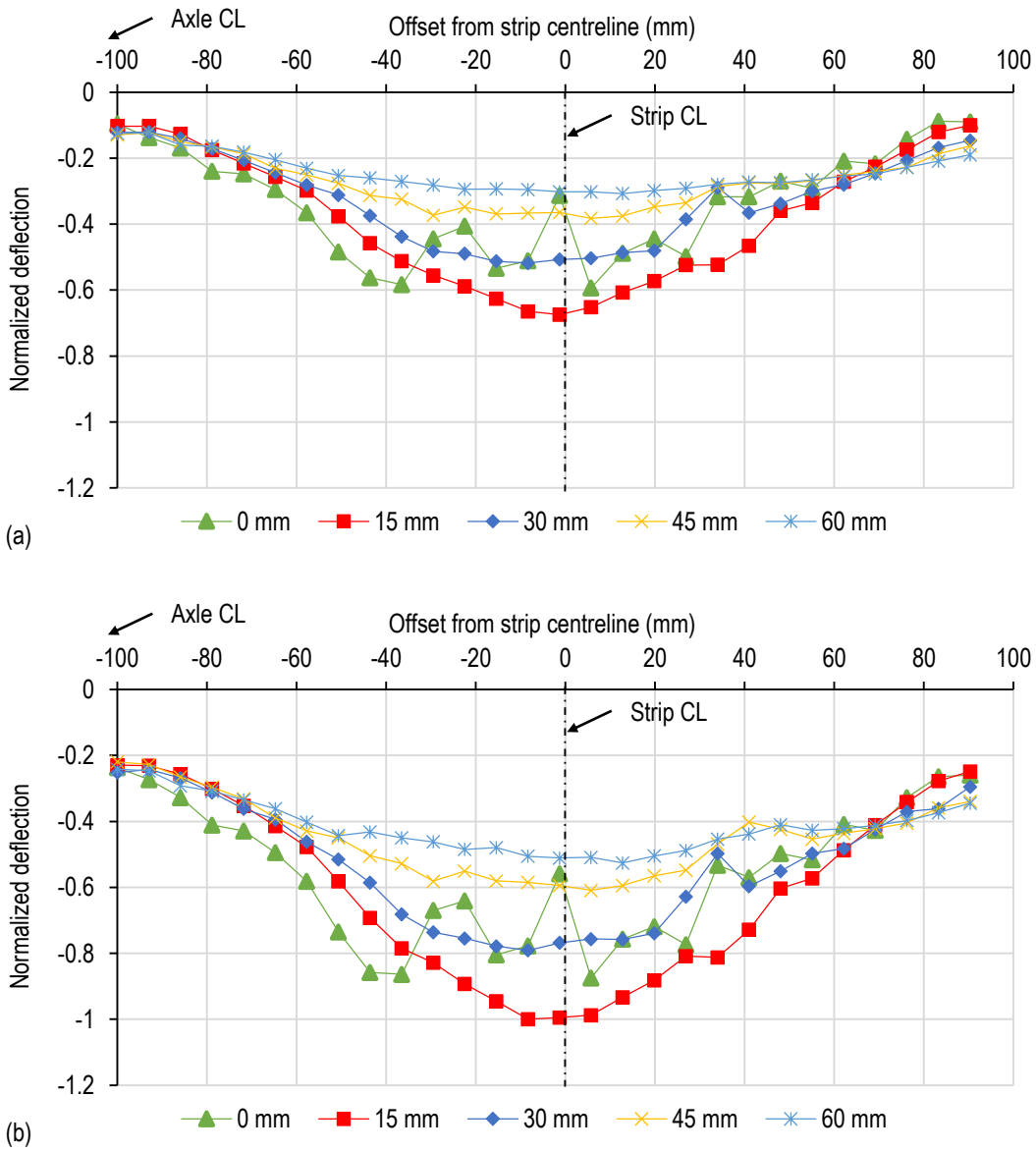

Figure 5.10 Permanent displacement of thin concrete pavement model after (a) one cycle and (b) five cycles

The development of differential permanent vertical displacement around the load application location showed that there was poor load spreading from the thin HS-SFRC layer to the compacted dry sand. The increase in the vertical difference between the troughs and peaks, as well as the decreasing distance between the layers in the substructure, indicates that there could have been non-vertical movement in the sand and possibly vertically upward movement along the centreline of the axle, relative to the rest of the structure. The relative upwards movement would not have been observed had an axle not been used to load the system. If continuity is assumed between all the layers, the concrete layer should have displaced more than the sand at a depth of 15 mm. The fact that the permanent displacement of the concrete layer was less than the layer directly underneath it indicates that the thin flexible concrete slab rebounds after the

system is unloaded, resulting in a discontinuity, or gap, forming between the concrete layer and the substructure.

Figure 5.11 shows the permanent displacement of the thin HS-SFRC layer with a cemented sand base on compacted dry sand. The permanent displacement with depth of this model was different to that of the two models discussed earlier. Bowl-shaped displacement could be seen at depths 0 mm (displacement of the concrete layer) and 15 mm (displacement at the interface between the cemented sand and dry sand). Close to the axle centreline, the concrete layer displaced less than the substructure at depth 15 mm. The differential vertical displacement decreased at depths 45 mm and 60 mm.

The response of the three-layer model was a combination of the two two-layer pavement systems discussed before. A deflection bowl formed around the load application location close to the surface, but the combination of the concrete and cemented sand layer distributed the load sufficiently so that minimal differential vertical deformation occurred from a depth of 45 mm downward. The load distribution through the thin concrete slab was however not adequate to prevent the cemented base from possible cracking. The sudden change in slope for depth 0 mm, 15 mm and 30 mm from offset 0 mm to -40 mm to offset -40 mm to -100 mm supports the suggestion that the base cracked.

After five load cycles the permanent displacement at depth 0 mm and 15 mm had reduced, while the permanent displacement at greater depths had accumulated. The reduction was unexpected. It can be attributed to the cemented base layer sticking to the glass and possibly resulting in the DIC not being representative of the true response of the model. It is also possible that loads were redistributed to areas further away from the load location, which could happen if the concrete slab spans across a damaged zone or gap in the substructure transferring the applied load to undamaged sections in the stabilized layer.

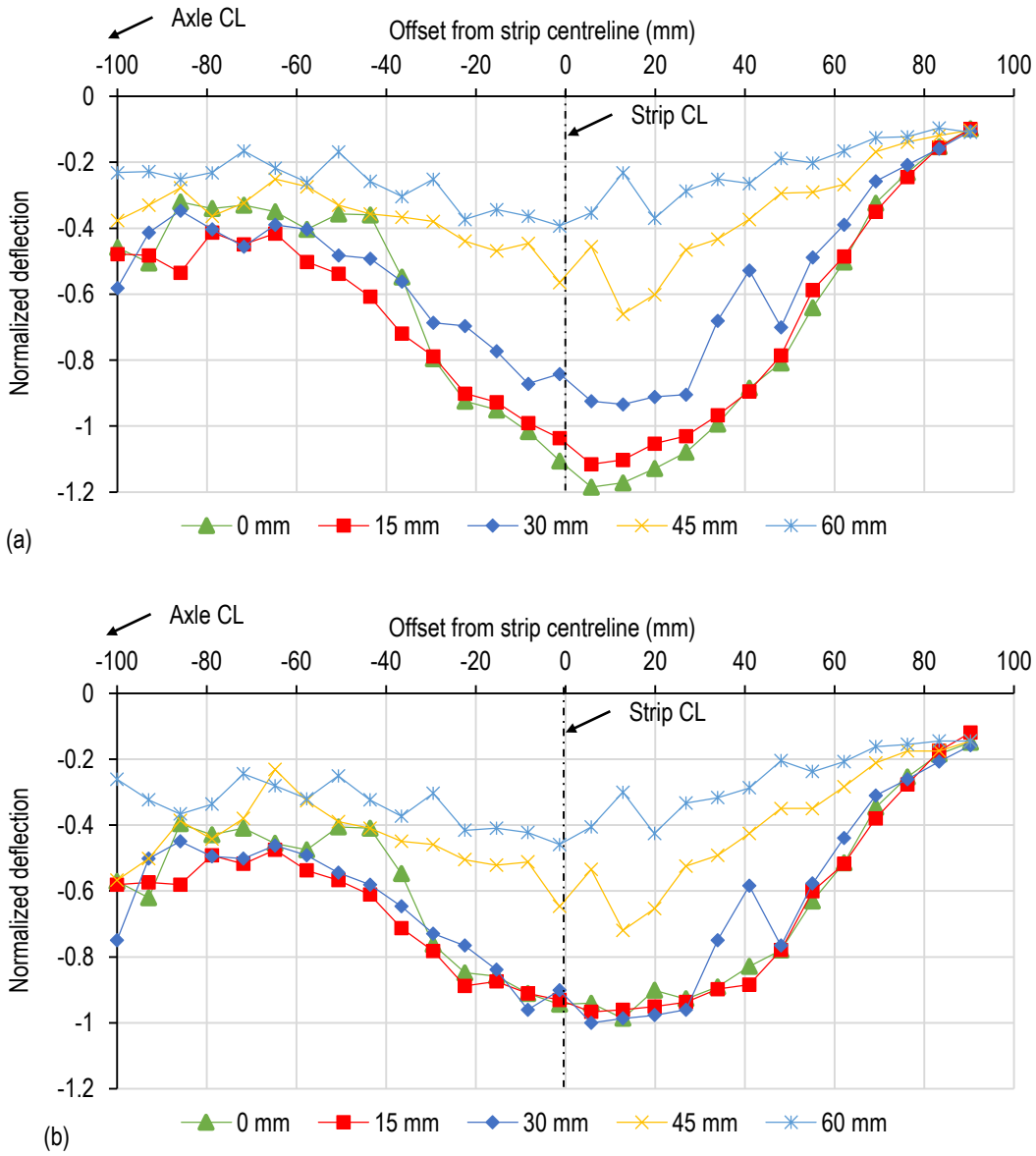

Figure 5.11 Permanent deformation of thin concrete with cemented base pavement model after (a) one cycle and (b) five cycles

5.5.4 Summary

The deflection at maximum load during the first load cycle showed that the thick concrete pavement model had little differential vertical displacement and seemed to punch into the soil. The thin concrete pavement model deflected with a trough around the load location. Contrary to the deflection bowl determined by the plane strain FE model, the deflection bowl was approximately symmetrical around the strip load centreline. It was proposed that this is due to the boundary effects and elasto-plastic behaviour of the sand. The models were not deep and the substructure could have displacement horizontally with sand moving to the axle centreline from the left and right strip loads and then being pushed upward. The deflection bowl of the

thin concrete with cemented base pavement model was slightly wider than for the thin concrete pavement model, which was only supported by compacted sand.

There was an accumulation of permanent displacement for all three strip loading models. As more load cycles were applied to the thick concrete model, the permanent displacement with depth became more equal. In the thin concrete pavement model, the concrete layer detached from the substructure. The difference between the permanent displacement in the wheel centreline and axle centreline became greater as more cycles were applied. The permanent displacement in the thin concrete with cemented base pavement model changed from having a trough around the load location to very little differential vertical displacement at greater depths.

Despite the excessive deformation caused, strip loading could be used to develop a conceptual and comparative understanding of the response of the various pavement models to loading. It is proposed that if strip loading is to be used in future, the pressure exerted should be reduced to match the deflection bowls expected for wheel loads. Additionally, it is proposed that the response of road pavements to rolling wheel loads should be investigated.

5.6 ROLLING WHEEL LOADING: EXPERIMENTAL SETUP

To investigate the response of UTCRCP to more representative load conditions, a rolling wheel load was applied to scaled models in the centrifuge. This resulted in 3D load conditions, with a demarcated zone of the model being subjected to stress at any given time. The zone moves, subjecting the pavement to principal stress rotation.

A model strongbox and measurement setup were constructed for the purpose of applying a rolling wheel load in the centrifuge. The model setup is referred to as the Centrifuge Pavement Tester (CPT). A moving weighted two-wheel axle was used to apply the load. The response of the pavement was monitored using a measurement system similar to MDDs. Two of the model compositions described in Section 5.2 were tested; one model with a thin concrete layer on compacted dry sand and one model with a thin concrete layer on a cemented sand base supported by compacted dry sand.

5.6.1 Model setup

Figure 5.12 and Figure 5.13 show the elements of the CPT. All elements of the setup were attached to a 50 mm aluminium base that had plan dimensions of 800 x 1200 mm. As with the plane strain model three of the model box sides, as well as the base, consisted of 50 mm thick aluminium panels. The fourth side of the box consisted of a 30 mm thick glass window. The

inside dimensions of the box measured 600 x 460 x 300 mm. Models constructed in the box would have a height of 300 mm, length of 460 mm and cross-sectional width of 600 mm.

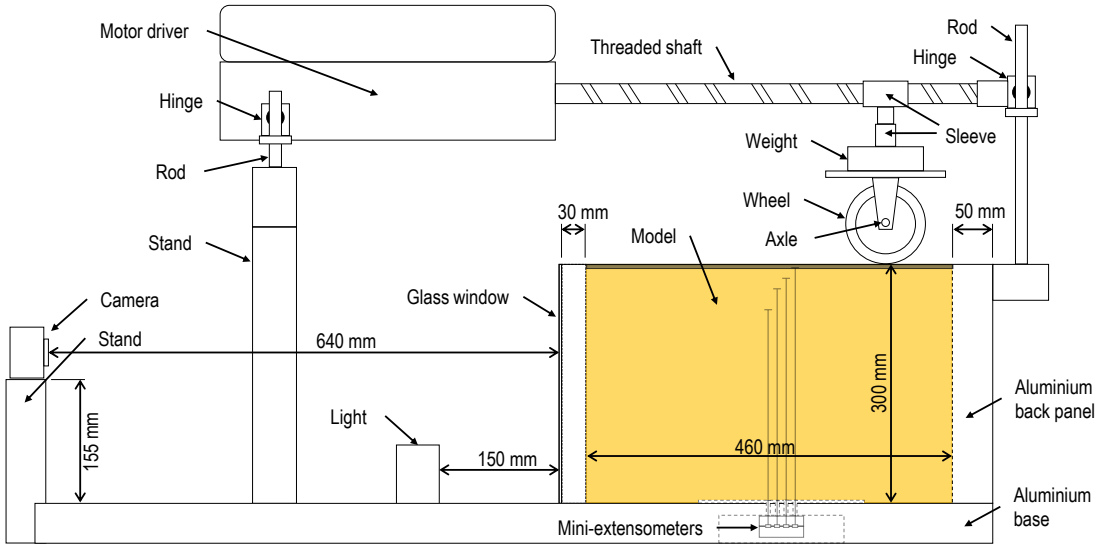

Figure 5.12 Schematic side view of Centrifuge Pavement Tester

A two-wheel axle applied load to the pavement system. The wheels had solid rubber tyres of which the contact area was elliptical with a width of 22 mm and length of 33 mm (depending of the load). The wheels were spaced 220 mm centre to centre at opposite ends of the axle. Weights were placed symmetrically on the axle to apply the desired axle load to the pavement model.

To roll the loaded wheels across the pavement surface, the axle was attached to a sleeve that moved along a motor driven rotating threaded shaft. The wheels rested on the pavement surface and the axle was attached to the threaded shaft sleeve through loose sleeve system that allowed the axle to move freely in the vertical direction. The axle moved bi-directionally along a 460 mm long path length at 10 mm/second. The pavement system was unloaded when the axle came to rest on top of the 30 mm glass window. The pressure that the wheels applied to the pavement models could be altered by adjusting the weights.

The response of the pavement model was monitored using a measurement system similar to MDDs as well as DIC. The measurement system similar to MDDs, is referred to as mini-extensometers and can be seen in Figure 5.13. The figure shows the location of the measurement mechanism embedded in the strongbox base. Needles extended from the mechanism into the model. The mini-extensometers were used to measure the vertical displacement at four depths below the pavement surface layer in both the wheel and axle centreline.

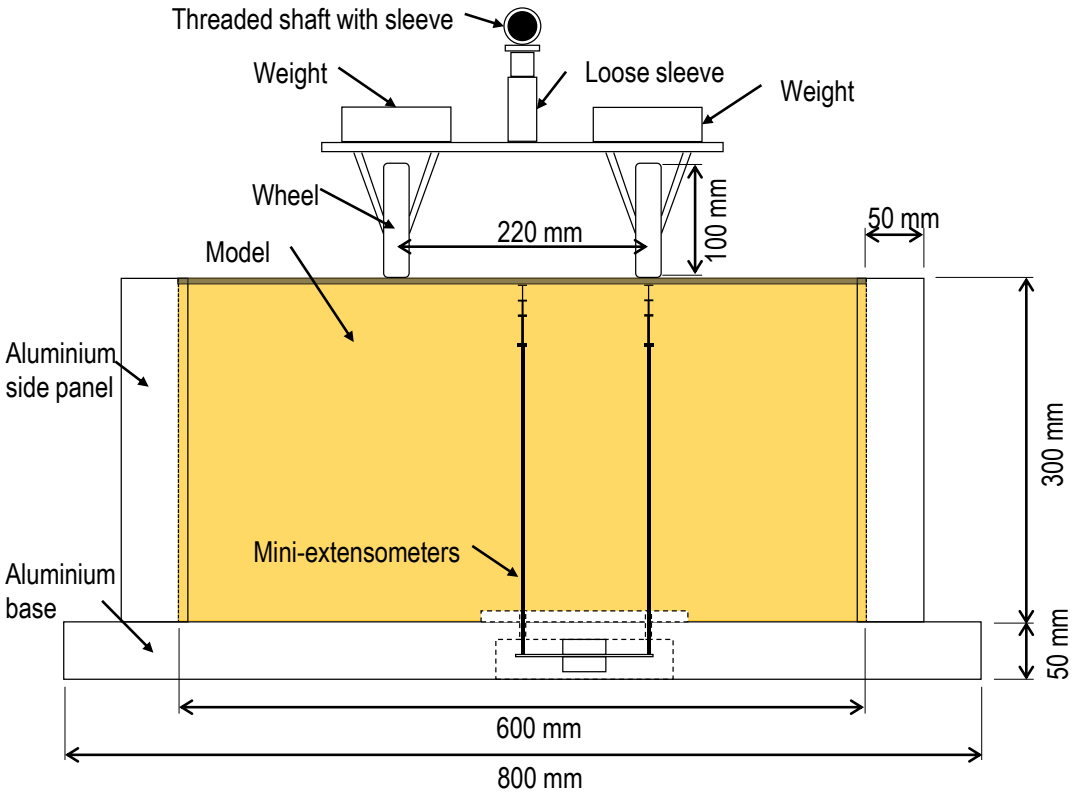

Figure 5.13 Profile section of Centrifuge Pavement Tester

The transverse cross section of the pavement system was visible through the 30 mm thick clear glass window. The exposed surface of the model was illuminated by LED lights that were placed approximately 150 mm from the glass window and positioned to minimise glare. To be able to observe as much of the exposed cross-section as possible with one camera, the camera was placed 640 mm from the glass window, at a height of 155 mm from the base surface. Figure 5.14 shows the CPT during model preparation and when placed on the centrifuge model platform.

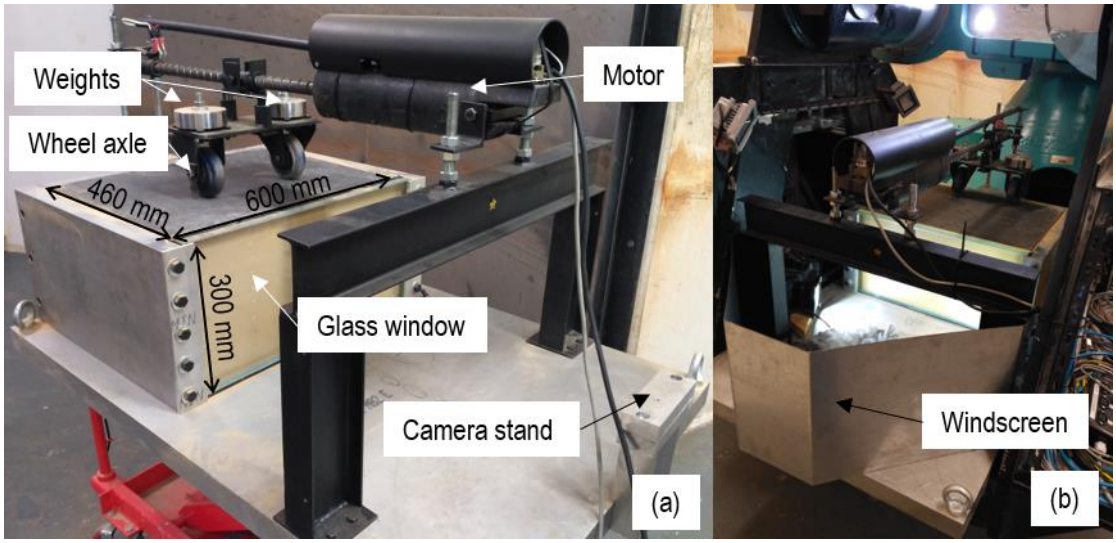

Figure 5.14 Centrifuge Pavement Tester (a) after model preparation and (b) placed in centrifuge

5.6.2 Mini-extensometers

The in-situ measurement system used to monitor deformation in the pavement systems is shown schematically in Figure 5.15. An annotated photo can be seen in Figure 5.16. The mechanism consisted of a steel bending beam that was rigidly clamped between two aluminium blocks. The bending beam dimensions were 50 x 3.75 mm with a thickness of 0.62 mm. It was instrumented with 120 Ω strain gauges, assembled in a full Wheatstone bridge, positioned close to the clamped end of the bending beam where large bending moments would develop when the end of the beam displaced in the vertical direction.

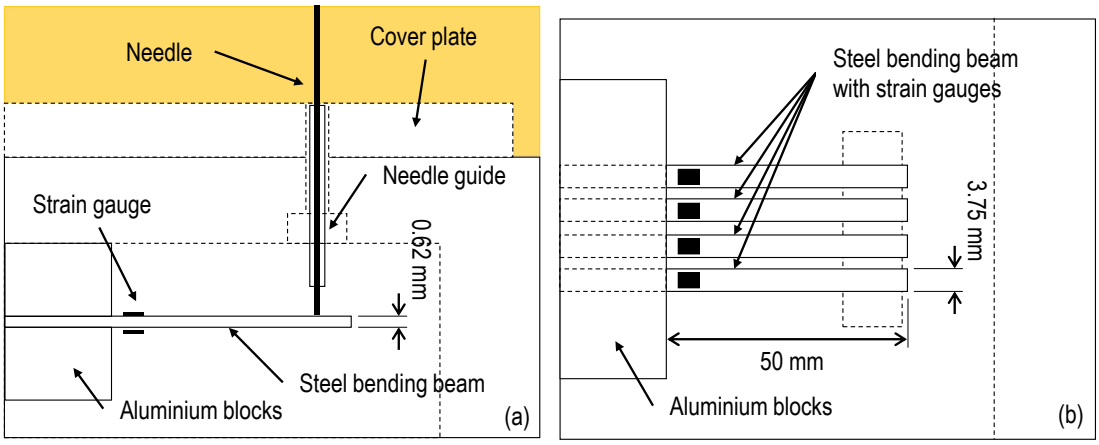

Figure 5.15 Measurement mechanism in (a) profile and (b) plan

A needle, that was embedded in the model, rested on the loose end of the bending beam causing it to deflect as vertical movement occurred in the model. Hypodermic needles were used. The embedded needles had a diameter of 0.81 mm and were flexible. To ensure that the needles

rested on their respective bending beams, each needle was guided within another hypodermic needle that was fixed to the CPT base as indicated in Figure 5.16.

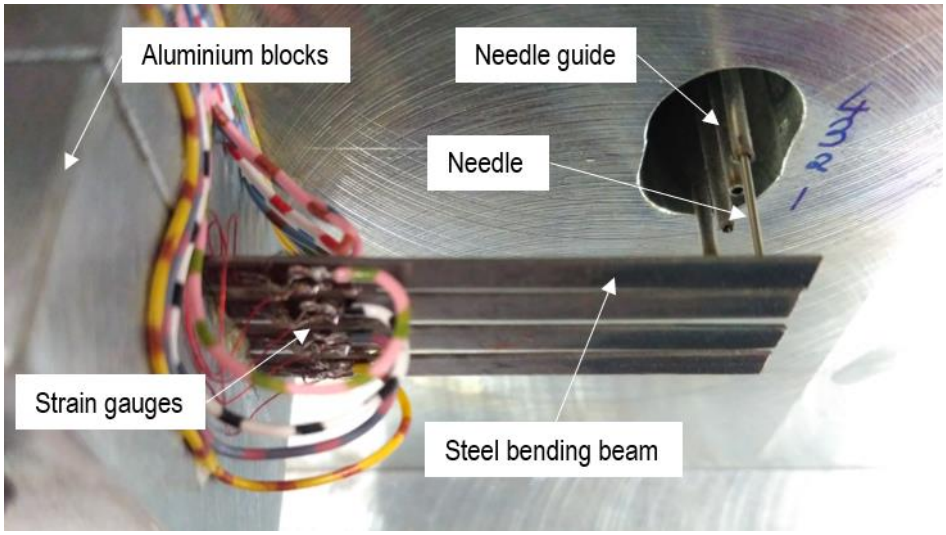

Figure 5.16 Measurement mechanism viewed from below

Two sets of four bending beams were embedded in the CPT base making it possible to measure movement at four depths in one of the wheel paths and along the centreline of the axle. Figure 5.17 shows the embedded measurement system along with the positioning of the needle sets. The depth at which movement was monitored could be customised. For the purposes of this study, displacement was monitored directly underneath the concrete slab and at depths of 15 mm, 30 mm, and 60 mm in the substructure below the bottom of the concrete slab.

A thin platform was epoxied to the top end of each needle (as seen in Figure 5.18 (a)). This was done to ensure that the needles moved with the substructure. During model preparation, the needle-end platforms were positioned at different depths in the model. The substructure was constructed around the needles, taking care to ensure that the surrounding material was compacted to the same degree as the rest of the model.

The bottom end of each needle rested on the bending beam, which could be reached through a hole that was drilled in the CPT base. Although the internal diameter of the guiding needles was 0.85 mm, fine sand moved into the 0.04 mm gap resulting in constricted needle movement. To mitigate this problem, geotextile was placed over the holes and the needles were pushed through it, ensuring that the needles could still move freely (as seen in Figure 5.18 (b)).

The mechanism of the mini-extensometers was similar to that of spring-loaded LVDTs, where the displacement that each needle would measure would be the displacement of the layer above the needle as the platform at the end of the needle pushed against the upper layer due to pre-loading of the steel bending beams.

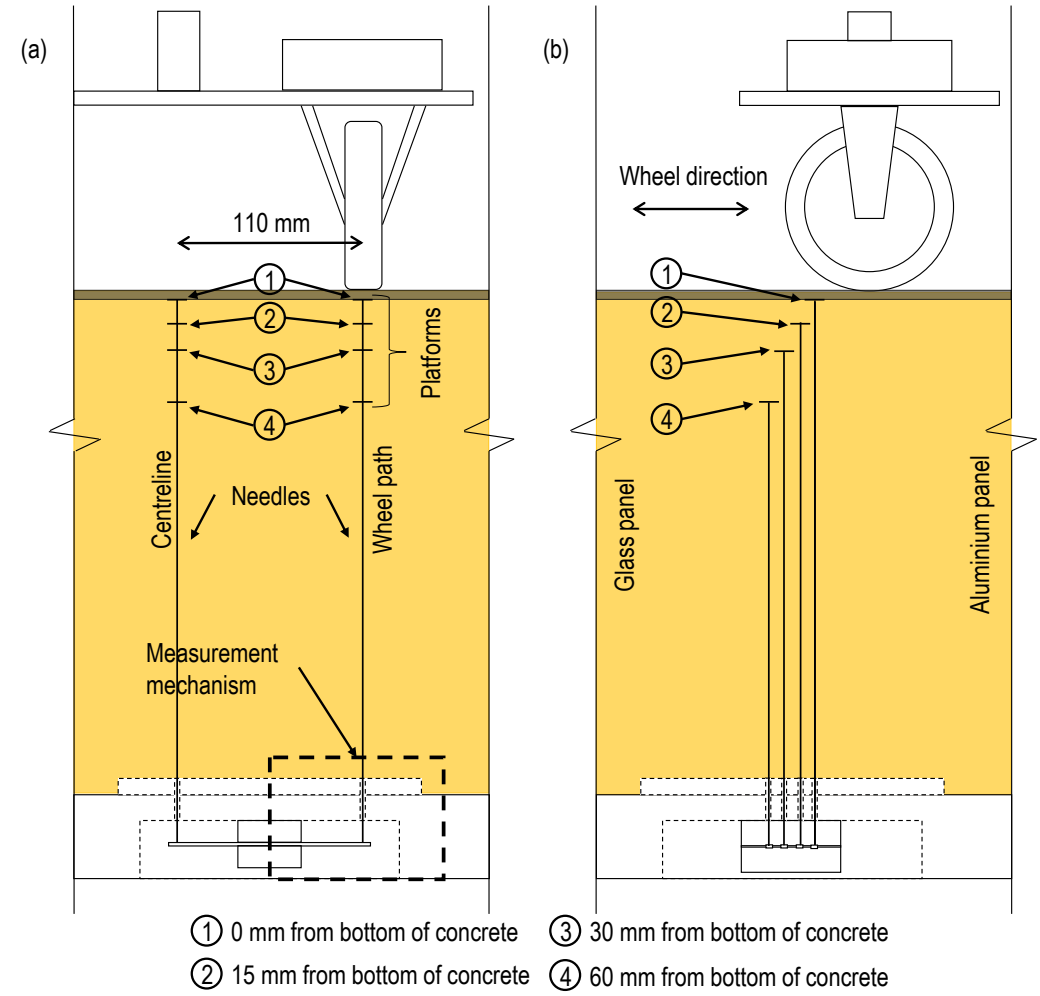

Figure 5.17 Configuration of embedded mini-extensometers (a) front view and (b) side view

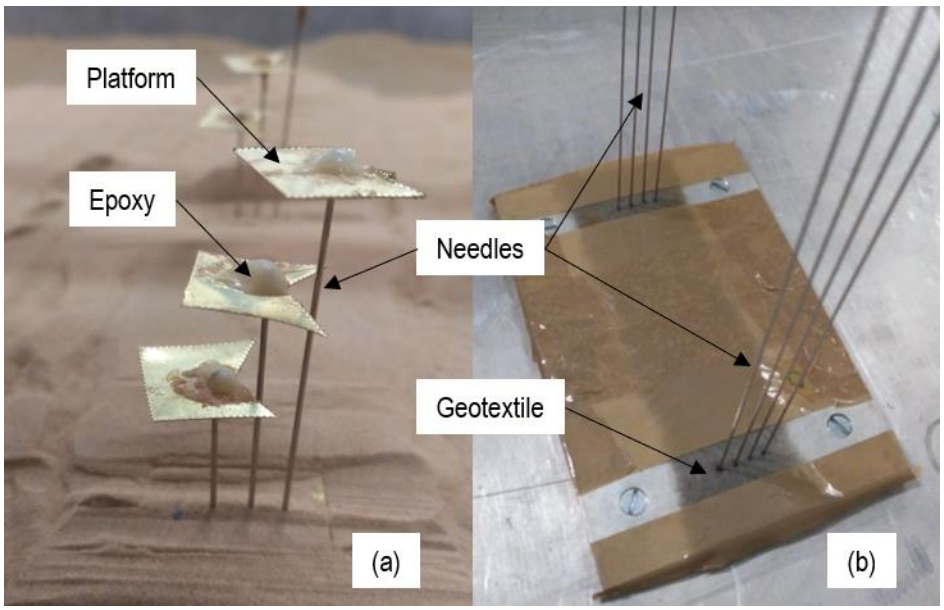

Figure 5.18 Embedded needles (a) with platforms and (b) placed in strongbox before model construction

5.6.3 Model preparation

5.6.3.1 Properties of silica sand

Silica sand was used to construct the substructure of the scaled models. Figure 5.19 shows a particle size distribution of the silica sand that was used for the rolling wheel load models. A laser diffraction particle size analyser was used. The silica sand was finer than that characterized by Archer (2014) and is referred to as Silica Sand 2.

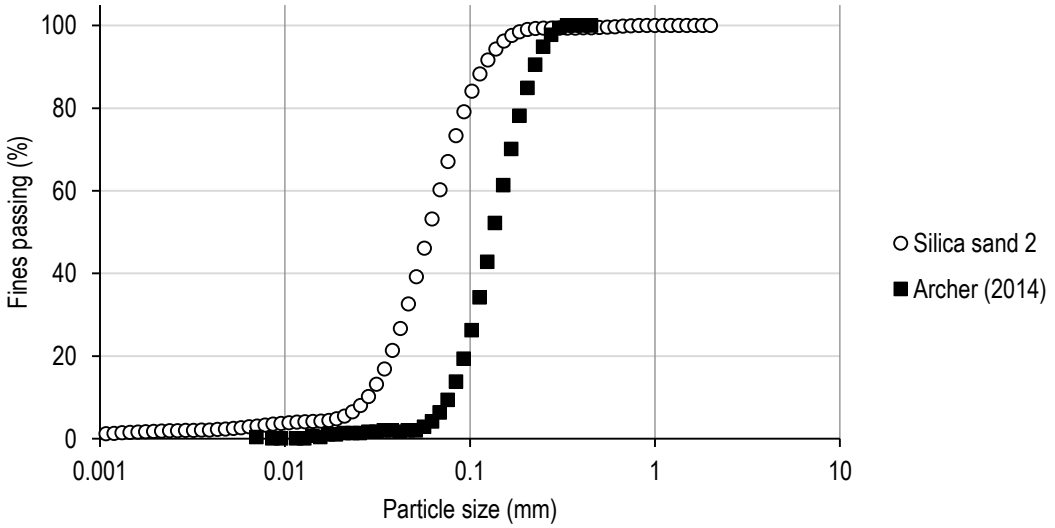

Figure 5.19 Particle size distribution of Silica Sand 2

Selected properties of Silica Sand 2 were determined as shown in Table 5.4. The maximum and minimum density and void ratio of soil was obtained using ASTM D4254 – 16 and ASTM D4253 – 16. A maximum friction angle of Silica Sand 2 was determined from dry compacted and dry tested in the triaxial apparatus. Two initial confining stresses were used; 100 kPa and 200 kPa. An average density index of 0.82 was obtained for the triaxial samples.

Table 5.4 Selected properties of Silica Sand 2

Property/Parameter	Value
Specific gravity	2.689
Maximum dry density (kg/m^3)	1 627
Minimum dry density (kg/m^3)	1 363
Maximum void ratio, e_{max}	0.973
Minimum void ratio, e_{min}	0.653
Maximum friction angle, φ_{max}(°)	35.3

5.6.3.2 Mechanically stabilized layers

The layers that consisted of silica sand were mechanically stabilized. Manual compaction, which consisted tamping a plate, was used. It was attempted to obtain the same density for all the layers. Dense sand was modelled, and the target density index and dry density were 0.97 and 1 617 kg/m^3 respectively. The required mass to fill the required volume was weighed off and compacted into the volume. The substructure was compacted in layers of decreasing thickness. The upper four layers had thicknesses of 15 mm each.

5.6.3.3 Cement stabilized layers

A cemented base layer was constructed using silica sand chemically stabilized with a CEM I 42.5 R Portland cement and water. The cement content was 5% by mass and the water content was 8% water by mass. The three materials were mixed in a 10 litre drum mixer and then compacted on the already compacted dry sand. The target density was 1 720 kg/m^3. The cemented base layer was 15 mm thick. The layer was covered and allowed to harden for 7 days before testing. The tensile strength obtained using the Brazilian disk test was 120 kPa (Gaspar, 2017).

5.6.4 Testing procedure

The models were constructed and placed on the model platform. The strongbox was accelerated to 10G after which the loaded axle was moved over the pavement models. A pressure of 550 kPa was applied to the models through the wheels. This is representative of a standard 80 kN axle load. The pressure was not adjusted during testing.

This study focused on the loaded response to the first load cycle and the loaded and unloaded displacement after one and five cycles.

5.7 ROLLING WHEEL LOADING: RESULTS AND DISCUSSION

The response of the rolling wheel loading models was monitored by the continuous measurement of vertical displacement in one of the wheel path centrelines and in the axle centreline. The displacement directly underneath the concrete layer (0 mm) and at depths 15 mm, 30 mm and 60 mm into the substructure was measured. The total depth of the model was 300 mm.

In this section the response of the two pavement models subjected to rolling wheel loading is discussed using longitudinal deflection bowls of the first load cycle and loaded and unloaded vertical displacement distributions after one and five load cycles. A brief discussion of the

vertical displacement versus time is followed by an in-depth discussion of the selected measures of pavement response.

5.7.1 Vertical displacement versus time

The vertical displacement in the wheel centreline (CL) versus time for both the thin concrete model and the thin concrete with cemented base are shown in Figure 5.20. The movement of the axle was bi-directional on the pavement model. The axle rested on the 30 mm thick glass panel at the start of testing. When loading was started, the wheel moved off the glass panel onto the model, rolling toward the opposite end. The figure illustrates the displacement in the pavement as the wheels rolled over the location of the mini-extensometer platforms embedded in the model. The vertical displacement peaks, or reaches a maximum, when the wheel is positioned on top of the mini-extensometer platform. The first maximum displacement of the mini-extensometer placed underneath the concrete layer of the first bi-directional cycle is indicated by point A1 in Figure 5.20.

Due to space constraints in the centrifuge, the axle did not move off the pavement at the opposite end of the model. The axle stopped at a horizontal distance of 155 mm away from the sensors and then started moving back to the glass panel end. The turning point is indicated by point B1 in Figure 5.20. The second maximum displacement peak is indicated by point C1. The model was unloaded when the axle moved onto the glass panel. The permanent displacement after the first bi-directional cycle is indicated by point D1. The same pattern of loading can be seen for each bi-directional cycle and are again highlighted in Figure 5.20 for the fifth cycle (by A5, B5, C5 and D5). A similar pattern can be seen in Appendix D for the vertical displacement versus time in the axle centreline of the two models.

The initial loading (first load cycle) of the model resulted in the most permanent vertical displacement. The initial loading also resulted in steep vertical displacement, indicating the mini-extensometer were immediately in the zone of influence of the axle loading even at a horizontal distance of approximately 230 mm from the axle load. Each subsequent cycle contributed to the permanent vertical displacement. The loaded vertical displacement measured under the concrete layer after five bi-directional cycles was 0.6 mm, half of what was measured for the strip loading model. The rate of accumulation of permanent vertical displacement stabilized for both models within 60 load cycles.

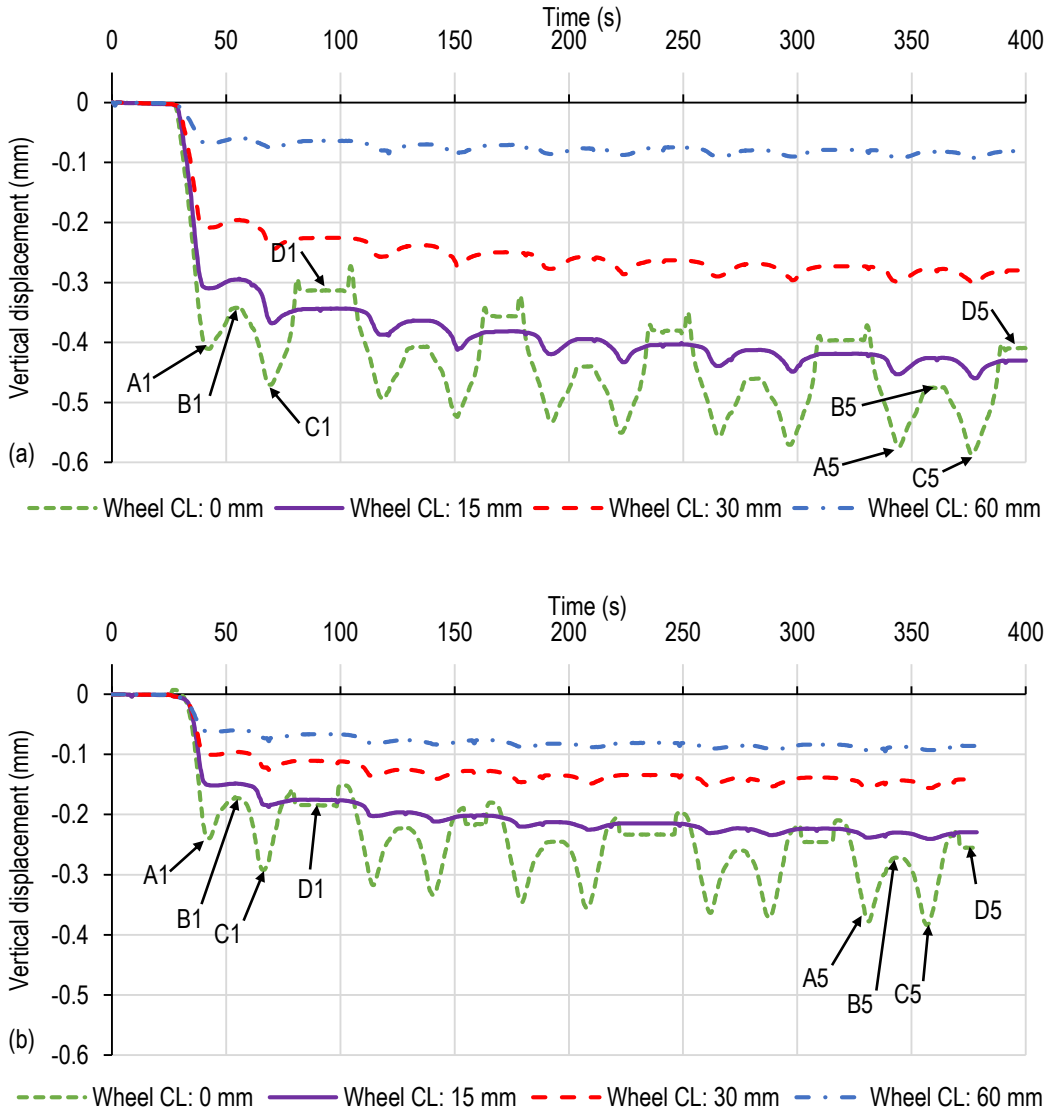

Figure 5.20 Vertical displacement in wheel centreline versus time of (a) thin concrete pavement model and (b) thin concrete slab with cemented base pavement model

Greater vertical displacement was measured at shallower depths while the pavement models remained loaded. When the thin concrete model was unloaded the permanent vertical displacement of the concrete layer was smaller than what was measured at a depth of 15 mm in the substructure (see D1 in Figure 5.20 (a)). When the thin concrete with cemented base pavement model was unloaded the vertical displacement of the concrete layer remained greater than what was measured at a depth of 15 mm in the substructure.

The response of the pavement models was explored in detail using the longitudinal deflections bowls determined from the vertical displacement measured in the wheel centreline and axle centreline. The deflection bowls were determined for the first load cycle, i.e. up to point A1 in Figure 5.20. Furthermore, the displacement measured at the respective depths when the

pavement was loaded (at point C1, C5 etc) and unloaded (at point D1, D5 etc) were used to compile the vertical displacement distributions in the wheel centreline and axle centreline. The vertical displacement distributions were used to investigate the accumulation of permanent displacement of the pavement models.

5.7.2 Deflection at maximum load of first cycle

Deflection bowls were determined along the wheel centreline and axle centreline respectively. Figure 5.21 shows the orientation of the measured deflection bowls, which were in the longitudinal direction along the wheel and axle centreline, respectively.

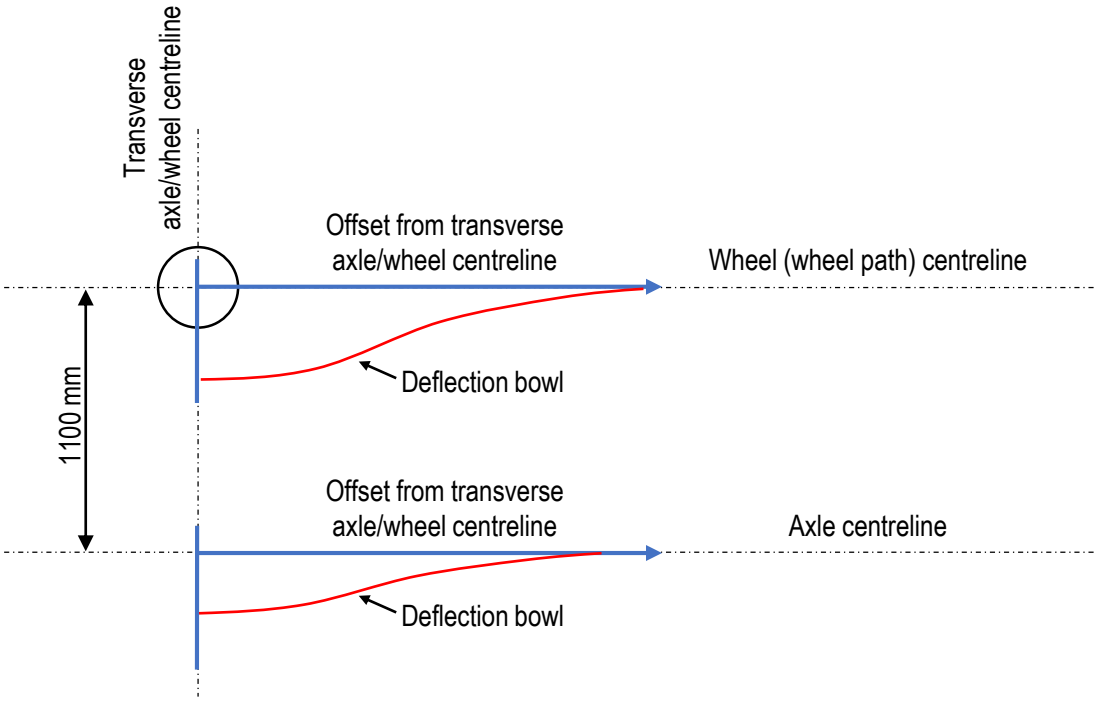

Figure 5.21 Offset from transverse axle/wheel centreline

Figure 5.22 shows the deflection bowls of the thin concrete pavement model determined from the first load cycle. The deflection bowls at depth 0 mm (directly underneath the concrete layer) and at depth 15 mm in the wheel centreline (CL) and axle centreline (CL) are shown. The width of the deflection bowl could not be greater than 230 mm, as that is the maximum distance from where the models were loaded. The deflection reduced with depth and the deflection in the axle centreline was smaller than the deflection in the wheel centreline.

A scaling factor of 10 was used for the model, which means that dimensions are 10 times greater at full scale. At full scale the maximum deflection in the wheel centreline would have been approximately 4 mm, while the maximum deflection in the axle centreline was approximately

3 mm. This was significantly greater than the values determined using FE modelling in Section 4.2.1, where the response of a 50 mm concrete pavement model with LE constitutive material models was determined. The vertical displacement in the wheel centreline was 0.85 mm and axle centreline was 0.5 mm. The smaller displacement of the FE model was predominantly due to a relatively high material stiffness used for the base. The stress-dependence of the sand material stiffness and elasto-plastic behaviour of sand were not taken into account when using LE material models.

The ratio of the maximum deflection in the axle centreline and wheel centreline of the physical model was 0.775, while the ratio of the FE model was 0.585. This indicated that the extent of overlap was greater for the physical model. The difference in vertical displacement with depth was greater in the wheel centreline than in the axle centreline.

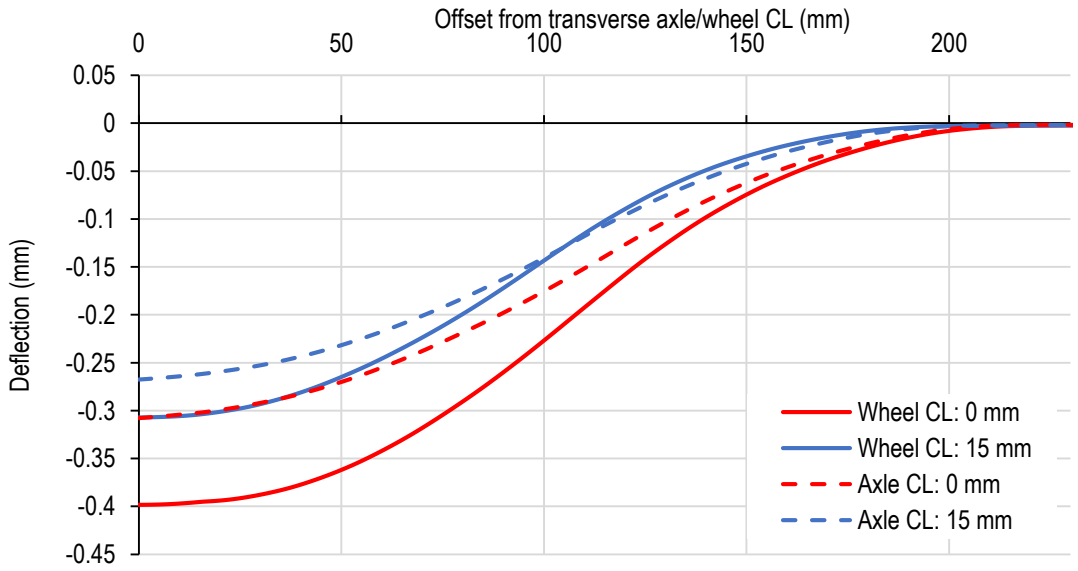

Figure 5.22 Wheel and axle centreline deflection bowls of thin concrete pavement model at depth 0 mm and 15 mm

Figure 5.23 shows the deflection bowls at depths 30 mm and 60 mm, where deflection was smaller than at shallower depths. At depth 30 mm the deflection in the wheel centreline and axle centreline had a similar magnitude. The deflection bowl in the axle centreline was slightly flatter and wider. At depth 60 mm the deflection in the wheel centreline was smaller than in the axle centreline. This correlates with the FE modelling contour plots in Chapter 3 and 4 that showed that the maximum vertical displacement of thin bound layer pavements modelled with two-wheel axle loading, moves toward the axle centreline with depth. For the combination of concrete layer and compacted sand in the thin concrete pavement model, the maximum displacement is in the axle centreline at depths between 30 mm and 60 mm. This observation shows that the maximum strain in the subgrade of UTCRCP does not necessarily occur under

the load location when complex load configurations are used and that the wheel interaction may result in critical parameters at locations other than what is typically assumed.

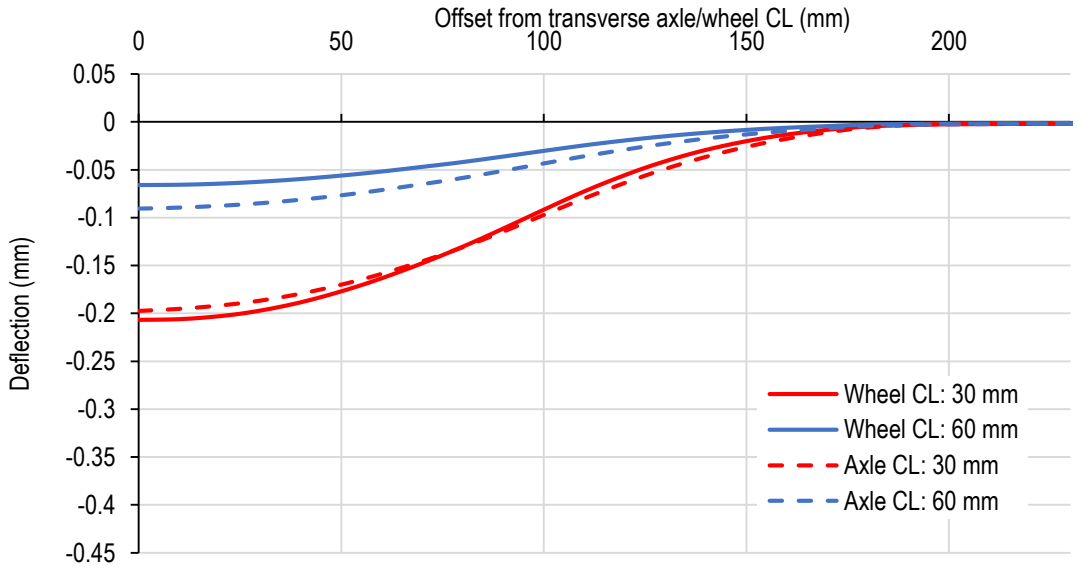

Figure 5.23 Wheel and axle centreline deflection bowls of thin concrete pavement model at depth 30 mm and 60 mm

Figure 5.24 and Figure 5.25 show the deflection bowls of the thin concrete with cemented base pavement model. The deflection of the model that incorporated a cemented base was smaller. This was because the load spreading through the cemented base was improved in comparison to the dry compacted sand. The width of the deflection bowl of the concrete layer was smaller than for the model without a cemented base. This can be because the relative stiffness between the concrete layer and cemented base determined the pavement response.

The radius of relative stiffness decreased when the stiffness of the supporting layer increased (as illustrated when the inverse beta value was discussed in Section 3.5) and a similar trend could be seen for the model with high base material stiffnesses (discussed in Section 4.4) where the inflection point offset from the wheel centreline decreased as the base material stiffness increased. The effect of the reduced deflection bowl width could also be amplified by the concrete layer being able to detach from the substructure. The shape of the deflection bowls could also be a result of the cemented base cracking during the first load cycle.

Figure 5.24 shows that the deflection of the concrete layer (depth 0 mm) was slightly upward from an offset of 120 mm to 170 mm. This indicates that a hogging moment, where tensile stresses are induced at the top of the concrete layer, occurs in front of wheel loading in a thin concrete layer placed on a cemented base. The wheel centreline and axle centreline deflection

bowls measured at depth 0 mm were dissimilar to those seen in Figure 4.13 for the high base material stiffness model.

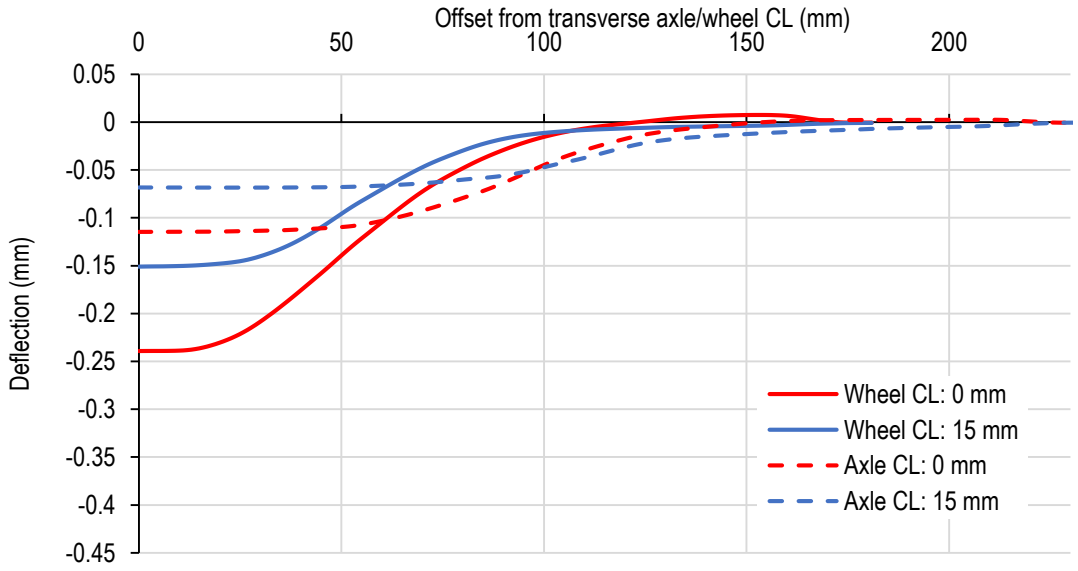

Figure 5.24 Deflection bowls of thin concrete with cemented base pavement model at depth 0 mm and 15 mm

Figure 5.25 shows the deflection at depths 30 mm and 60 mm of the thin concrete with cemented base pavement model. The deflection bowls were shallow and narrow, with no difference between the deflection in the axle centreline at depth 30 mm and 60 mm. The deflection bowls in the axle centreline and at greater depths (further away from the wheels) were relatively flat and wide.

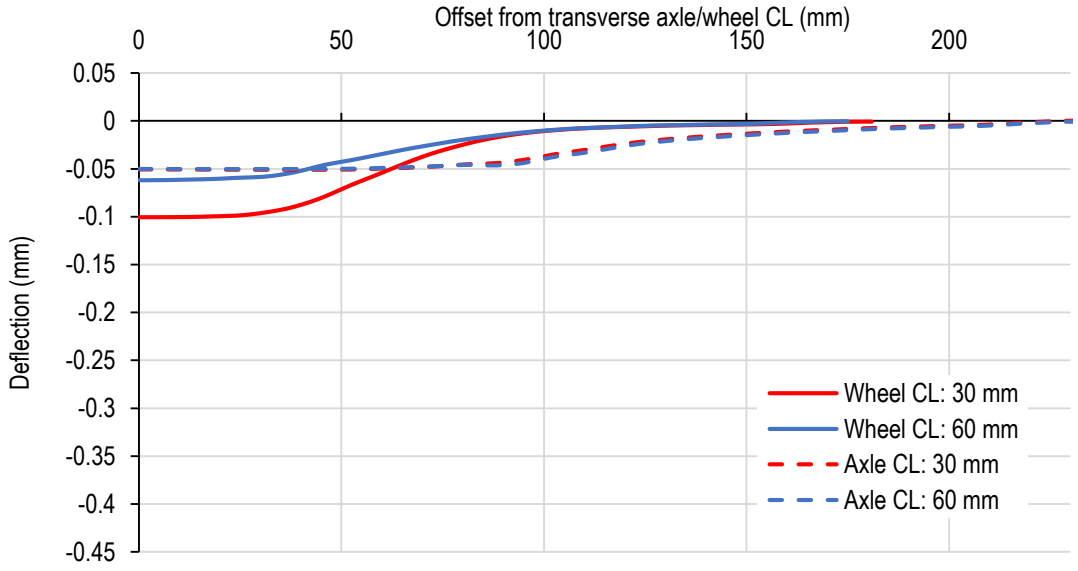

Figure 5.25 Deflection bowls of thin concrete with cemented base pavement model at depth 30 mm and 60 mm

5.7.3 Vertical displacement distribution

The loaded and unloaded Vertical Displacement Distributions (VDDs) were isolated from the vertical displacement data. VDDs show the vertical displacement with depth. Unloaded VDDs show the permanent displacement and accumulation of permanent displacement with number of cycles. Figure 5.26 shows the loaded and unloaded VDD of the thin concrete pavement model in the wheel centreline as more wheel passes were applied. Each wheel pass was considered as a load cycle. Figure 5.26 (a) shows how the vertical displacement decreased with depth when the model was loaded. The figure also shows how the system steadily displaced downward as more cycles were applied. The difference between the loaded displacement at the top of the system and at the bottom of the system increases with every load application, while the magnitude of vertical displacement remains inversely related to depth below the concrete layer.

By comparing Figure 5.26 (a) to Figure 5.26 (b) it can be seen that the shapes of the loaded VDD differed from the unloaded VDD. After the initial load application, the permanent displacement underneath the concrete layer was less than at a depth of 15 mm. The difference between the permanent displacement at 0 mm and 15 mm decreased as more cycles were applied. As mentioned in the description of the mini-extensometers, their mechanism was similar to that of spring-loaded LVDTs, where the displacement that each needle would measure would be the displacement of the layer above the needle.

The fact that the displacement of the concrete layer was less than what was measured in the substructure indicated that the concrete lifted, off the substructure when the pavement was unloaded, indicating that a discontinuity and gap between the concrete layer and substructure had formed. A similar trend was seen not only by Gerber (2011) as discussed in the literature review, but also in the plane strain physical models discussed in this chapter.

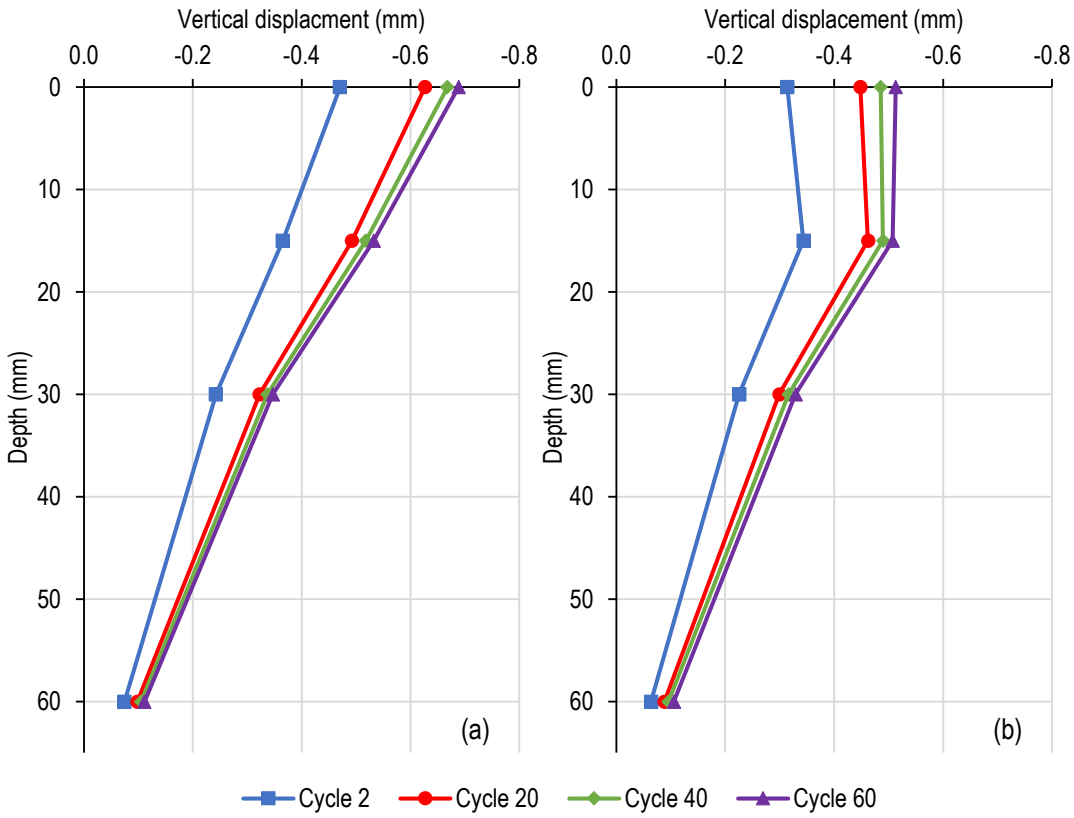

Figure 5.26 VDD of thin concrete pavement model in wheel centreline when (a) loaded and (b) unloaded

Figure 5.27 shows the VDD in the axle centreline of the thin concrete pavement model. The shape of the VDD along axle centreline was different to the shape in the wheel path. The displacement at 0 mm in comparison to 15 mm was less along the axle centreline, than it is in the wheel centreline. This difference could be attributed to the zones of influence of the respective wheel loads only overlapping deeper in the pavement substructure, as well as an anticipated upward deflection in the axle centreline as predicted by the FE models in Chapter 3 and 4.

The permanent displacement along the axle centreline followed the general shape of the loaded displacement, but similar to the permanent displacement in the wheel centreline, the permanent displacement at 0 mm was approximately the same than at 15 mm. Although the permanent displacement in the wheel centreline is similar to that in the axle centreline, significant displacement differences can be seen when the wheel load is present, indication that UTCRCP behaves as a flexural pavement.

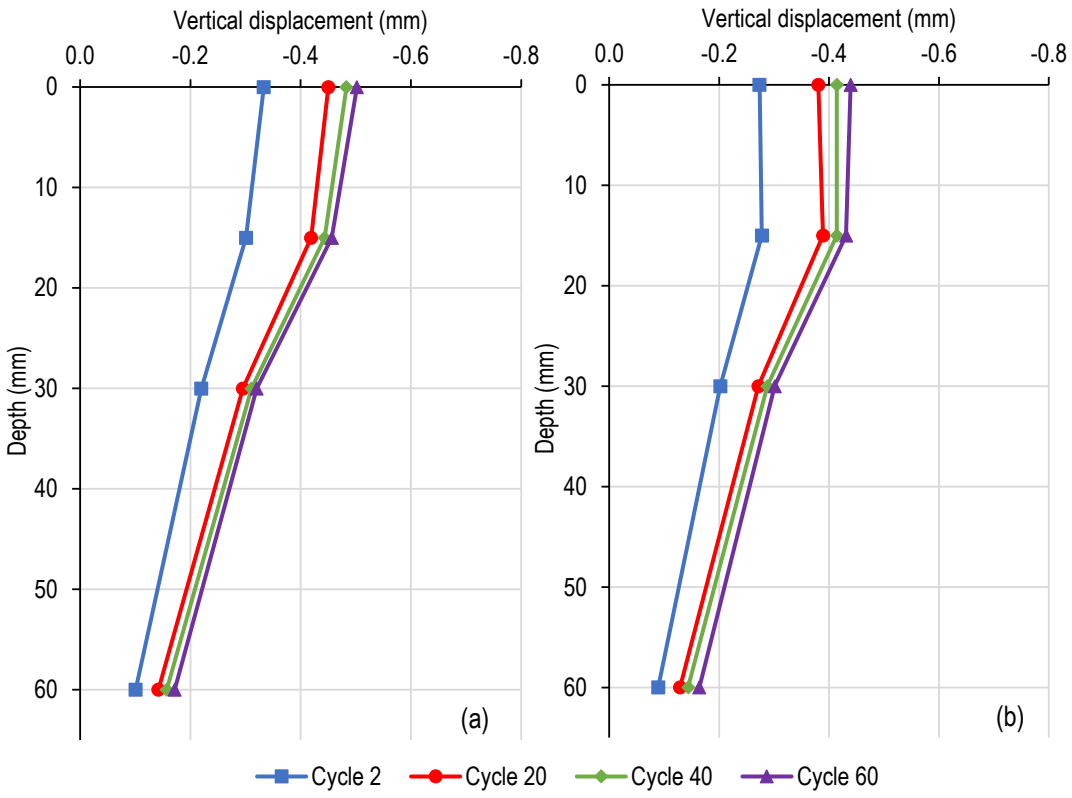

Figure 5.27 VDD of thin concrete pavement model in axle centreline when (a) loaded and (b) unloaded

Figure 5.28 shows the loaded and unloaded VDD in the wheel centreline of the thin concrete with cemented base pavement model. The vertical displacement of this model was monitored at depth 0 mm, between the concrete layer and cemented base, at depth 15 mm between the cemented base and the rest of the compacted sand substructure. The compacted sand substructure was also monitored at depth 30 mm and 60 mm from the top of the substructure. It should be noted that the layers below the stabilized layer displaced less than in the model that consisted of only the HS-SRFC layer and compacted sand.

The response of the thin concrete with cemented base pavement model in the wheel centreline was similar to the thin concrete pavement model in the wheel centreline. The first wheel pass caused the greatest permanent displacement, the rate of accumulation of permanent displacement decreased as more load cycles were applied and the magnitude of loaded displacement decreased with depth. Unlike for the two-layer system, the difference between the displacement at 0 mm and 15 mm increased, with more displacement occurring at 0 mm in comparison to at 15 mm. This indicates that the cemented base deteriorated as more load cycles were applied.

The permanent displacement in Figure 5.28 (b) mimics this trend. Initially the permanent displacement at 0 mm and 15 mm was approximately the same, where after it gradually increased with the surface deflecting more than the cement stabilized layer. This trend is different than the trend of thin concrete layer on compacted sand, where it was suggested that the concrete layer lifts up off the compacted sand when it is unloaded, leaving a gap. The cracking of cemented bases under ultra-thin concrete layers should be investigated using FE modelling to clarify this trend.

The permanent displacement at depth 0 mm in the wheel path was greater than at depth 15 mm in the wheel path. After 40 bi-directional wheel passes the displacement of 15 mm, 30 mm and 60 mm was more stable than at 0 mm where the rate of accumulation of permanent displacement had not stabilized. The permanent vertical displacement in the layers under the stabilized layer is also less than that seen in Figure 5.26 (b) where the permanent displacement in the wheel centreline of the two-layer system is shown.

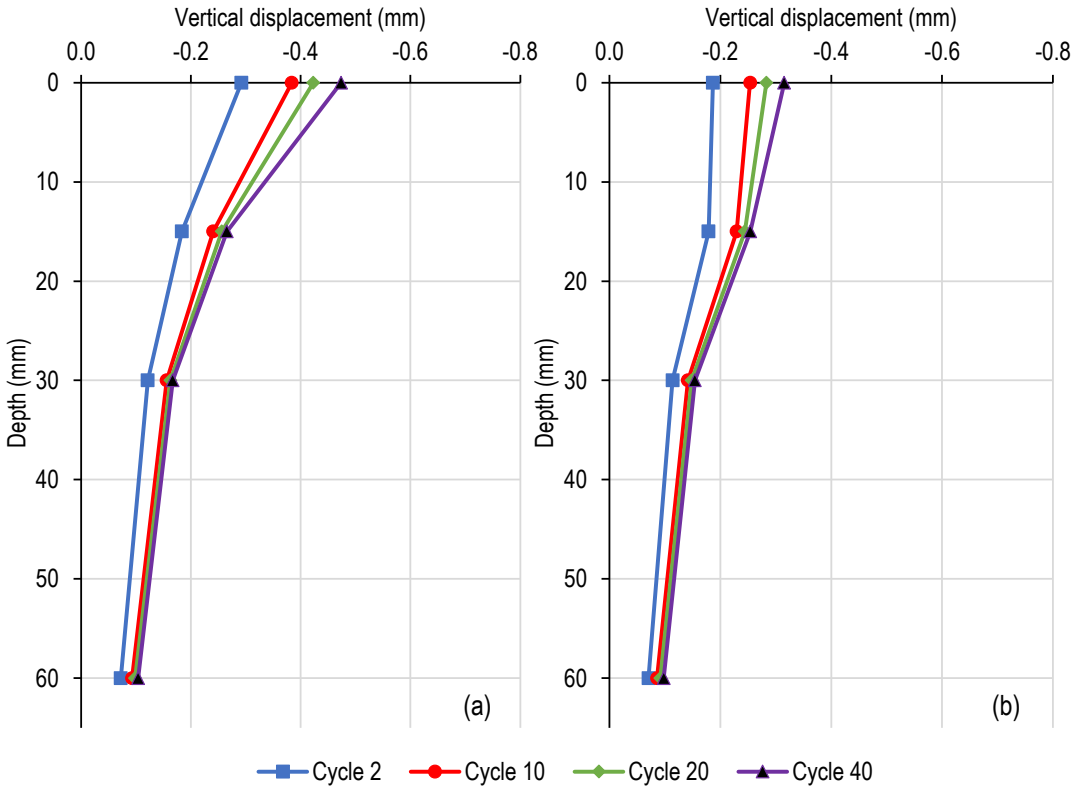

Figure 5.28 VDD of thin concrete with cemented base pavement model in wheel centreline when (a) loaded and (b) unloaded

Figure 5.29 shows the VDD in the axle centreline for the thin concrete with cemented base pavement model. The displacement in the axle centreline stabilized after few cycles. The displacement was small in comparison to that measured in the wheel centreline and in the axle

centreline of the thin concrete pavement model and no clear trend of loaded and unloaded vertical displacement could be identified.

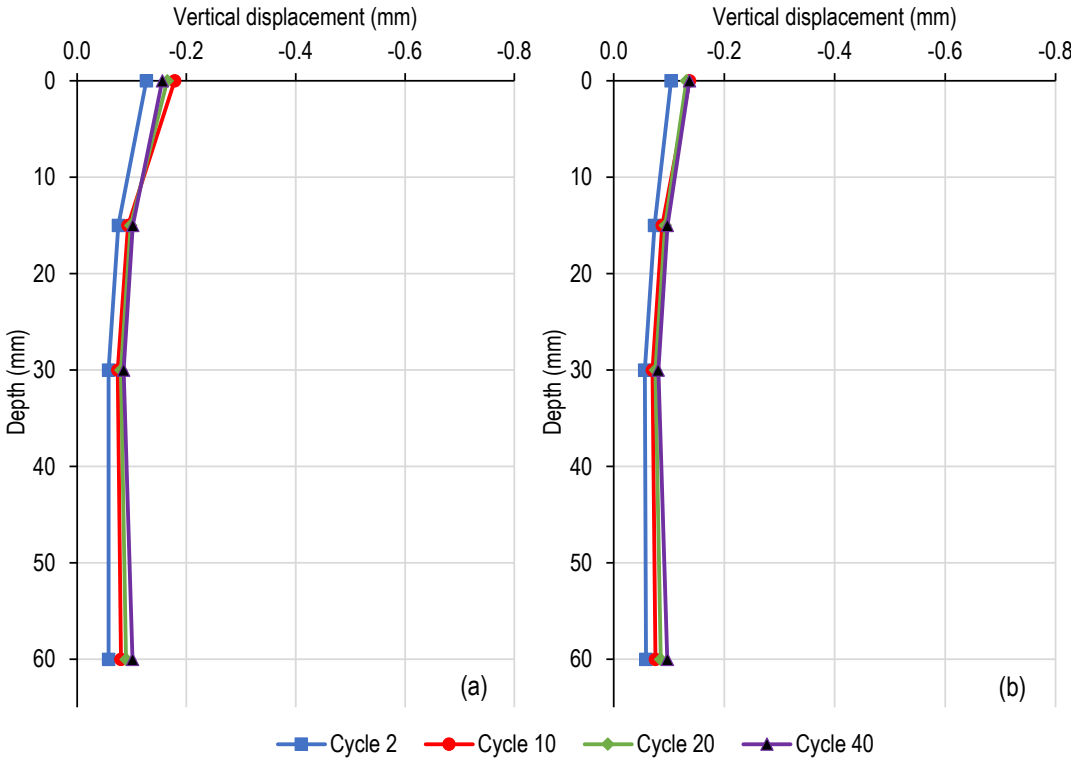

Figure 5.29 VDD of thin concrete with cemented base pavement model in axle centreline when (a) loaded and (b) unloaded

5.7.4 Summary

The deflection bowls determined from the mini-extensometers, placed in the wheel centreline and axle centreline, were in the longitudinal direction of the pavement. The scaled deflections of the physical models were much greater than what was numerically modelled in Chapter 4. This was probably predominantly due to linear elastic assumptions and a relatively high material stiffness being selected for the base in the numerical model.

The difference in vertical displacement may be because there may have been settlement during the first load cycle due to the concrete layer being placed on the model and not cast on the compacted sand. The ratio of the deflection in the axle centreline to the deflection in wheel centreline was also greater for the physical model than for the FE models. This indicated that there was greater overlap of the stress zones induced by the wheels on the opposite sides of the axle. This is in part because the relative stiffness between the scaled HS-SFRC layer and compacted sand could have been greater than between the bound layer and substructure in the FE model. The deflection in the axle centreline at a depth of 60 mm was greater than the

deflection at the same depth in the wheel centreline. This indicated that the stress zones started overlapping between depth 30 mm and 60 mm.

The deflection bowl of the thin concrete layer with cemented base pavement model was shallower and narrower than thin concrete pavement model. This was possibly due to the interaction between the thin concrete layer and the cemented base layer where the radius of relative stiffness would have been reduced by the increase in stiffness of the base layer (and ultimately the entire substructure). The deflection bowls in the axle centreline and at greater depths (further away from the wheels) were relatively flat and wide.

VDDs were used to investigate the loaded and unloaded response with number of cycles applied. The difference between the loaded displacement at the top of the system (depth 0 mm) and at depth 60 mm increased with every load application. The permanent displacement measured at 0 mm, directly underneath the concrete layer, was approximately the same as the displacement measured at depth 15 mm reducing when the pavement was unloaded. This indicates that the concrete layer rebounds when unloaded, leaving a gap between the concrete layer and substructure in the wheel path.

A gap forming between the concrete layer and substructure would influence how stress in UTCRCP is distributed with depth. The HS-SFRC layer would span over the gap. The concrete layer would be able to absorb the tensile stress induced by traffic loading if it has a high enough steel content, which is ensured by the steel fibres and the high area of steel in the longitudinal direction due to the 50 x 50 mm mesh. The load would be transferred to the edges of the gap formed in the substructure, inducing high stresses and causing permanent deformation at the gap edges.

When the pavement was loaded, the VDD in the axle centreline of the thin concrete pavement model had a different shape than in the wheel centreline. The vertical displacement reduced with depth, but the difference in displacement did not reduce smoothly. The difference in displacement between depth 0 mm and 15 mm was smaller than the difference between depth 15 mm and 30 mm. In comparison to the displacement in the wheel centreline, the difference between the displacement at depth 0 mm and 60 mm did not increase as significantly in the axle centreline. The differences between the wheel centreline VDDs and axle centreline VDDs could have been caused by overlapping stress zones and shows that there is interaction between the two wheels at opposite ends of the axle for the relative stiffness of the model and when true material behaviour is taken into consideration.

The VDDs of the thin concrete with cemented base pavement model showed that the difference between the displacement at 0 mm and 15 mm increased as more load cycles were applied. This

indicates that the cemented base deteriorated with load applications. As for the thin concrete pavement model, there was a degree of rebound when the model was unloaded. The vertical displacement in the axle centreline of the model with a cemented base was small.

5.8 CONCLUSIONS

The trend of a rebounding concrete layer was observed for both thin concrete pavement models tested using different load configurations. The trend of increasing difference between the deflection at depth 0 mm in the wheel or strip centreline and axle centreline could be observed for both load configurations. For the models with cemented base a change from significant differential vertical displacement at shallow depths to fairly uniform vertical displacement at greater depths could be observed for the load configurations. The rolling wheel load models underwent limited displacement in the axle centreline.

The following questions identified during the literature review could be partially addressed from the summary in Chapter 5:

- Is it viable to simplify loading configurations to strip loading and how does strip and 3D loading affect pavement response?

  Yes, although the vertical displacement was greater for the strip load model the similar trends, such as deflected shape and gap formation, were observed for both load configurations. It is proposed that strip loading is used for qualitative and comparative purposes combined with the option of reducing the strip load pressure to match the plane strain deflected shapes to 3D loading deflected shapes.

- Should UTCRCP be modelled as a flexible pavement where the substructure properties are important, and rutting is a traffic associated failure mechanism?

  Yes, the physical modelling showed that differential vertical displacement occurred around the load location and became more prominent as more load cycles were applied. Additionally, it was observed that a gap formed between the bottom of the concrete layer and the top of the substructure. This indicates that rutting that occurs in UTCRCP may not be observed from the surface of the pavements.

- Is it useful to incorporate cement stabilized bases in UTCRCP to improve load spreading?

  The inclusion of a cemented base was useful in that the vertical displacement was reduced. The permanent displacement did not accumulate notably for the strip load model, but from

the VDDs for the rolling wheel models it could be seen that the cemented base deteriorated during the first 60 load cycles. The use of cemented bases and the use of different strength classes should thus be further investigated in future studies.

- Should numerical and physical modelling of UTCRCP use axle loading instead of a single wheel and are important aspects of the pavement response ignored if axle loading is not used?

  From the LE FE modelling the differences between single wheel and axle loading was apparent. The strip loading model showed that axle loading (or using two strips) resulted in a pavement response that was symmetrical around the axle centreline. The representativeness of using an axle instead of a single wheel load for the rolling wheel load models could not be evaluated definitively because a single wheel was not modelled and there were no mini-extensometer readings between the wheel path and the edge of the model.

Pavement response during physical modelling was monitored by taking measurements at discrete locations in the pavements. Although visual observation and DIC can help to form a more complete picture of pavement response these methods have limitations. It was decided to further investigate the response of UTCRCP to traffic loading by making use of a constitutive material model based on the critical state framework for sand. The model is referred to as the Nor-Sand model. The use of Nor-Sand should make it possible to model the non-linear, stress-dependent elasto-plastic behaviour of sand and by extension, granular materials.

6 INCORPORATION OF CRITICAL STATE SOIL MECHANICS IN FE MODELLING OF ROAD PAVEMENTS

6.1 INTRODUCTION

It has been shown that the numerical modelling of pavements would benefit from using complex material models (Belletti *et al.*, 2008). Stress-dependence, non-linearity, plastic strain and lack of tensile strength should be modelled to capture the true behaviour of granular material. In Chapter 5 compacted dry sand was used to model the substructure of the centrifuge pavement models, and it would be beneficial to further investigate the response of thin HS-SFRC layers on compacted sand using advanced constitutive material models for sand.

The critical state soil concept demonstrates that all possible states of soil exist within a characteristic surface. Numerical models that are based on the critical state soil concept exist. The most well-known models are the Cam-Clay and the Modified Cam-Clay model (Roscoe & Burland, 1968; Schofield & Wroth, 1968). Nor-Sand is an advanced constitutive material model based on the critical state soil concept, developed for sand (Jefferies, 1993).

Nor-Sand can be used in conjunction with 3D FE analysis to investigate the response of the centrifuge models. This chapter gives background on Nor-Sand, and a brief description of the material input parameters and FE model input parameters it requires. The suitability of using Nor-Sand to model road pavements is assessed by conducting sensitivity analyses for the FE model input parameters. A FE model with geometry similar to that used in Chapter 3 and Chapter 4 was used.

6.2 THE NOR-SAND SOIL MODEL

Nor-Sand is a generalized Cambridge-type constitutive model for sand. It is derived from the critical state theory and uses the “state parameter” concept (Been & Jefferies, 1985). Existing Cam-Clay models cannot be used to model the softening and dilatancy of dense sands. This is a significant deficiency as most applications of sand involve dense sand. The “state parameter” concept is used to overcome this deficiency. The concept postulates an infinity of isotropic normal consolidation loci, which forces a separation of intrinsic state from overconsolidated state (Jefferies, 1993).

Nor-Sand attempts to accurately reproduce dilation and softening on the dry side (dense) of the critical state and contraction and hardening on the wet side (loose) of critical state. In the

following section the general concept of the Nor-Sand model is explained. The mathematical formulation of the critical state, yield surface and hardening law are also given.

6.2.1 Theory of Nor-Sand Soil Model

Figure 6.1 is a schematic diagram of the Nor-Sand soil model in $\ln p' - e$ space, where p' is the mean effective principal stress. It shows the infinity of Normal Consolidation Lines (NCL), the Critical State Line (CSL) and the swelling/compression line (S/C line) of a sample in overconsolidated state.

An overconsolidated sample would move along the S/C line as p' increases, where the stress state is elastic. When the sample reaches the NCL and starts moving down it (as p' continues to increase) the stress state becomes elasto-plastic. The sand sample deforms continually at constant volume under constant effective stress when it reaches the CSL. A normally consolidated sample would be in an elasto-plastic stress state immediately when p' starts increasing, moving down the NCL until it reaches the CSL (Cheong, 2006; Jefferies, 1993).

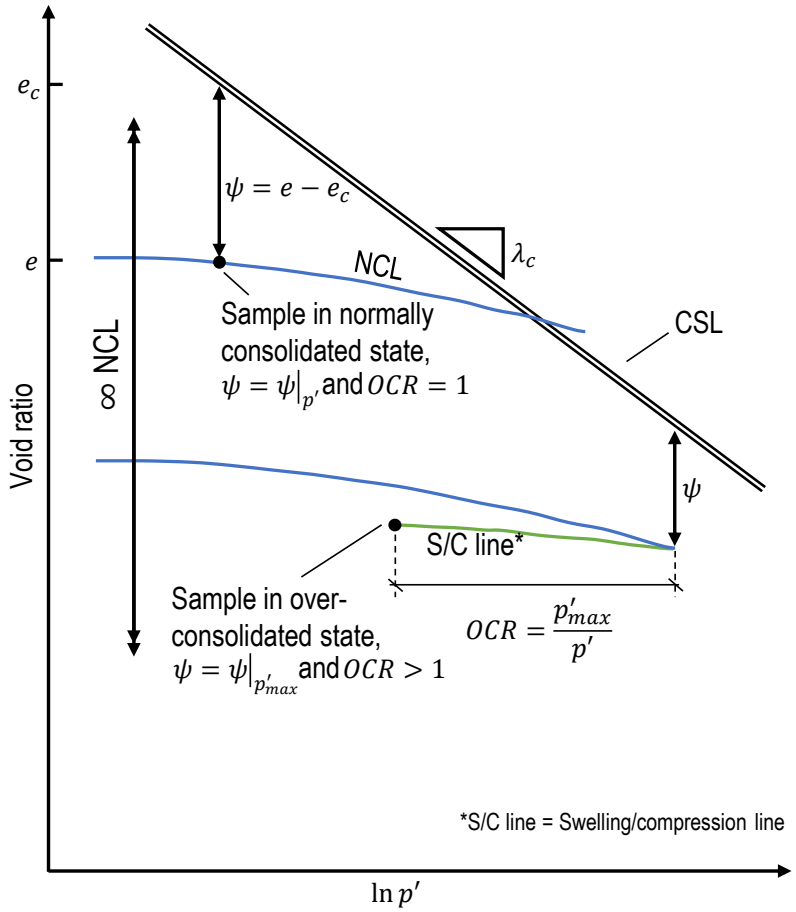

Figure 6.1 Nor-Sand Soil model in *lnp'-e* space (adapted from Jefferies (1993))

Also demonstrated in Figure 6.1 are the state parameter (ψ) and the overconsolidation ratio (OCR). The state parameter (as in Equation 6.1) is the difference between the current void ratio (e) and void ratio on the CSL (e_c) at the current mean effective principal stress.

$$\psi = e - e_c \qquad \textbf{Equation 6.1}$$

The OCR is the ratio of the mean effective principal stress when the S/C line reaches the current NCL (p'_{max}) over the current mean effective principal stress. It is used as a measure of distance inside the yield surface from the NCL. The infinity of NCL is accommodated in the soil state description by using the OCR and the state parameter to describe the current NCL (Jefferies, 1993).

6.2.1.1 Critical state

Critical state behaviour for sandy soils defines an ultimate state at which sand deforms continually at constant volume and under constant shear and confining stress. The following equations expresses the CSL in $p' - q$ space (Equation 6.2) and $\ln p' - e$ space (Equation 6.3):

$$q_c = M p'_c \qquad \textbf{Equation 6.2}$$

$$e_c = \Gamma - \lambda_c \ln p'_c \qquad \textbf{Equation 6.3}$$

The subscript c indicates critical state. M is the critical stress ratio and gradient of the CSL in $p' - q$ space. The critical void ratio on the CSL at a mean principal effective stress of 1 kPa is denoted by Γ. The slope of CSL in $\ln p' - e$ space is also illustrated in Figure 6.1 and denoted by λ_c.

The flow rule used in Nor-Sand is different than for Cam-Clay. It has also been proven that M as a material constant does not represent sand behaviour well. It has proposed that M should be modelled as a function of Lode angle (Cheong, 2006; Cornforth, 1964). Additionally, Nor-Sand is adjusted to model the bi-linearity of the CSL in $\ln p' - e$ space by making use of density index calculated using the maximum, minimum and current void ratios. The break in the CSL is possibly due to particle crushing and occurs at a stress level of 1 MPa (Cheong, 2006). These aspects of the Nor-Sand model will not be discussed in more detail, because it is unlikely that pavements subjected to traffic loading will reach critical state or a stress level of 1 MPa.

6.2.1.2 Yield surface

The yield surface of the Nor-Sand model is written as seen in Equation 6.4. It is a function of the initial state parameters, plastic deformations and the current stresses.

$$\eta - \frac{M}{N}\left[1 + (N-1)\left(\frac{p'}{p'_i}\right)^{\frac{N}{1-N}}\right] = 0 \qquad if\ N \neq 0 \qquad \textbf{Equation 6.4 (a)}$$

$$\eta - M\left[1 + \ln\left(\frac{p'_i}{p}\right)\right] = 0 \qquad if\ N = 0 \qquad \textbf{Equation 6.4 (b)}$$

As in Equation 2.5, $\eta = \frac{q}{p'}$. The critical stress ratio and gradient of the CSL in $p' - q$ space is denoted by M. Another parameter used in the Nor-Sand model is the mean effective principal stress at image state. It is denoted by p'_i and is the mean effective principal stress at critical state. It is used to scale the size of the yield surface (Jefferies, 1993).

The location of the image state mean principal stress is shown in Figure 6.2 (a), which also illustrates the scaling of the yield surface. The shape of the yield surface is a function of N, which is a material property relating to volumetric work (Cheong, 2006). Figure 6.2 (b) shows the effect of N on the shape of the yield surface, where the "$N = 0$" yield surface corresponds to the shape of the Cam-Clay yield surface.

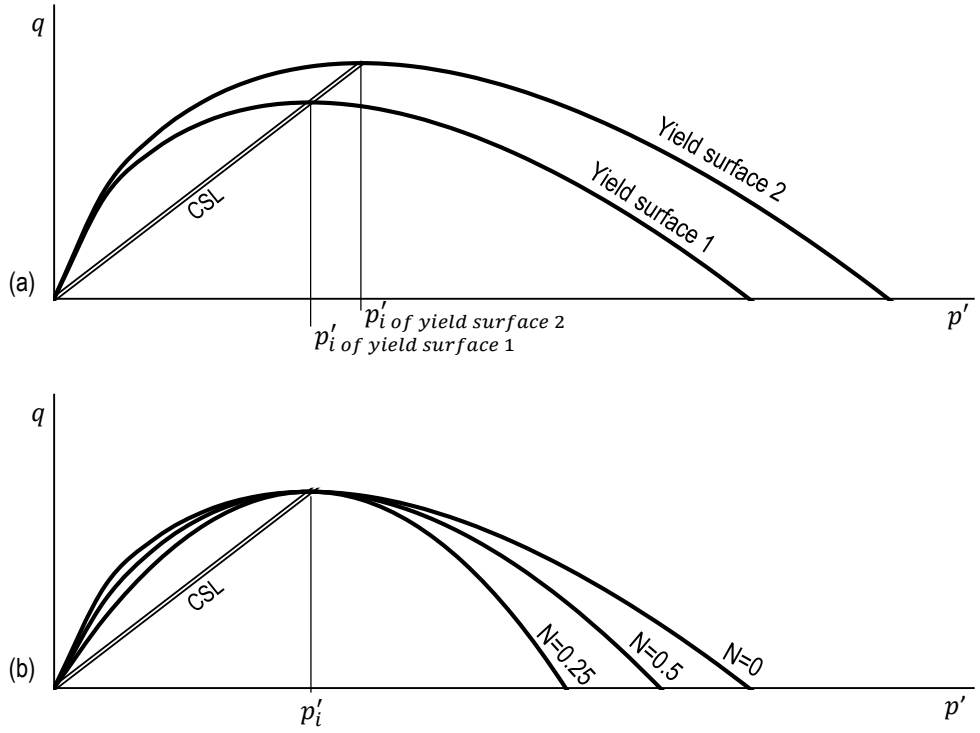

Figure 6.2 Effect of (a) p'_i in scaling the yield surface and (b) N on the yield surface shape (adapted from Jefferies (1993))

6.2.1.3 Hardening law

The hardening law describes the evolution of the yield surface, which is scaled by the principal mean stress at image state, p'_i. The state parameter, introduced in Section 6.2.1, is used for this

purpose. The void ratio at image state is used (which is also on the CSL). Equation 6.1 becomes Equation 6.5, where the subscript i indicates image state.

$$\psi_i = e - e_{c,i} \qquad \textbf{Equation 6.5}$$

The yield surface is constrained using a relationship between maximum dilatancy and the state parameter at image state. This relationship is described using the maximum dilatancy coefficient (χ), which has an average of 3.5. The maximum dilatancy is transformed to a limiting hardness, where the yield surface size calculated using χ cannot be larger than the limiting yield surface given by Equation 6.6:

$$\frac{p'_{i,max}}{p'} = \left(1 + \chi\psi_i \frac{N}{M}\right)^{\frac{N-1}{N}} \quad if\ N \neq 0 \qquad \textbf{Equation 6.6 (a)}$$

$$\frac{p'_{i,max}}{p'} = exp\left(-\frac{\chi\psi_i}{M}\right) \qquad if\ N = 0 \qquad \textbf{Equation 6.6 (b)}$$

The simple hardening rule in Equation 6.7 incorporates the limited maximum hardness, where h is a dimensionless hardening/softening modulus.

$$\frac{\dot{p}_i}{\dot{\varepsilon}_s^p} = h(p'_{i,max} - p'_i) \qquad \textbf{Equation 6.7}$$

6.3 RESPONSE MODELLED USING NOR-SAND

The response of loose and dense sand is depicted in Figure 6.3 (a), where the stress-strain response in shear and the volumetric strain with respect to shear strain can be seen. The strain-softening and initial contraction and subsequent dilation of dense sand is depicted. The strain-hardening and contraction of loose sand is depicted. Contraction is modelled as a negative volumetric strain, and dilation is modelled as positive volumetric strain. The measured stress-strain response of loose and dense Erksak Sand reported by Cheong (2006) can be seen in Figure 6.3 (b), along with the response computed in ABAQUS using a user subroutine for Nor-Sand. The stress-strain response is shown in terms of the stress ratio of deviatoric stress over mean effective principal stress. The same sign convention as in Figure 6.3 (a) is followed where volume increase is positive. The figure shows that Nor-Sand can accurately model the response of sand for large deformations.

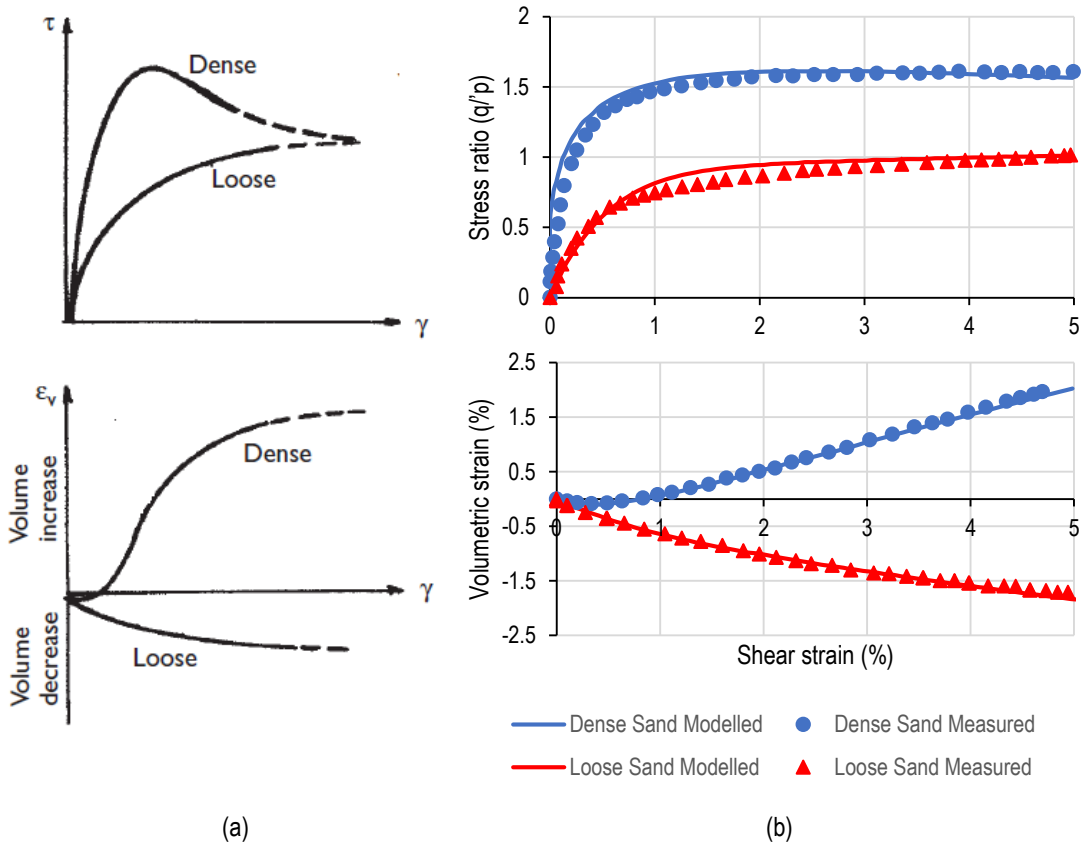

Figure 6.3 (a) Idealised response of loose and dense sand from Craig (2004) and (b) measured and modelled stress-strain response of Erksak Sand (adapted from Cheong, 2006)

Typical resilient strains in asphalt pavements under standard axle wheel loads fall in a range below 0.1% axial strain (Brown, 1996). Although pavement type and distance from the load location plays a role in the expected strains, loading of pavements is not deemed to be a large deformation problem. However, modelling the substructure of pavements using a stress dependent, elasto-plastic material model based on the critical state framework should result in a more accurate representation of actual pavement behaviour. The reason for this is that the critical state soil concept marries possible stress states with volume and excludes high levels of tensile stress.

The Nor-Sand model requires the following nine material input parameters to describe elastic, plastic and critical state behaviour:

- Elasticity
  - A – dimensionless shear modulus
  - n – pressure exponent
  - ν – Poisson's Ratio

- Plasticity
  - N – 'N' value in flow rule
  - h – plastic hardening modulus
  - χ – maximum dilatancy coefficient
- Critical state condition
  - M – critical stress ratio in triaxial compression
  - e_{max} – maximum void ratio
  - e_{min} – minimum void ratio

In ABAQUS, an initial stress state is assigned which is dependent on the self-weight induced vertical stress and lateral earth pressure at-rest (K_0). An OCR and a void ratio are also assigned to the sand section modelled. The initial void ratio, K_0, and OCR are referred to as the FE model input parameters.

6.3.1 Elasticity

The elastic strain of sand is anisotropic, depends on mean stress and void ratio, and although it has been studied by several researchers, a consensus has not been reached over the relationship between these factors (Jefferies & Shuttle, 2002). Nor-Sand was developed to model the critical state behaviour of sand. The details of elasticity were not considered to be crucial and the relationship used does not capture the dependence of material stiffness on strain level. Nonetheless, the formulation used is similar to more complex material models in pavement modelling, where the material stiffness is modelled as a function of confining stress.

Nor-Sand uses the elastic bulk modulus, K, and shear modulus, G, as well as a constant Poisson's Ratio, ν, to determine deformation. The shear modulus is modelled as a function of mean effective principal stress using a power relationship, as shown in Equation 6.8:

$$G = Ap'^{n} \qquad \textbf{Equation 6.8}$$

Where A is a dimensionless shear modulus constant with a typical range from 300 to 3000, and n is a pressure exponent with a typical range from 0.4 to 1.0 (Cheong, 2006). The mean effective principal stress is denoted by p'. The bulk modulus can be deduced from the shear modulus using the expression in Equation 6.9:

$$K_B = \frac{2(1+\nu)}{3(1-2\nu)}G \qquad \textbf{Equation 6.9}$$

The shear modulus can be related to Young's Modulus using the expression in Equation 6.10:

$$G = \frac{E}{2(1+\nu)} \qquad \textbf{Equation 6.10}$$

Figure 6.4 shows the range of Young's Moduli that can be calculated using the stress dependence in Equation 6.8 and the minimum and maximum values of the A and n ranges. The range of Young's Moduli is illustrated for a mean stress range from 0 kPa to 150 kPa. The material stiffness of sand is generally lower than that of granular material typically used in pavements. At a mean stress of 150 kPa and a pressure exponent (n) of 0.4, the Young's Modulus varies between 5.8 MPa and 58 MPa for a shear modulus constant from 300 to 3000. At a mean stress of 150 kPa and a pressure exponent of 1, the Young's Modulus varies between 117 MPa and 1170 MPa for a shear modulus constant from 300 to 3000. Ideally the elastic shear modulus is measured using bender elements but it can also be obtained from the elastic stress-strain behaviour of sand (Jefferies & Shuttle, 2005). The elastic parameters can be calibrated simultaneously by trial-and-error fitting of elastic data.

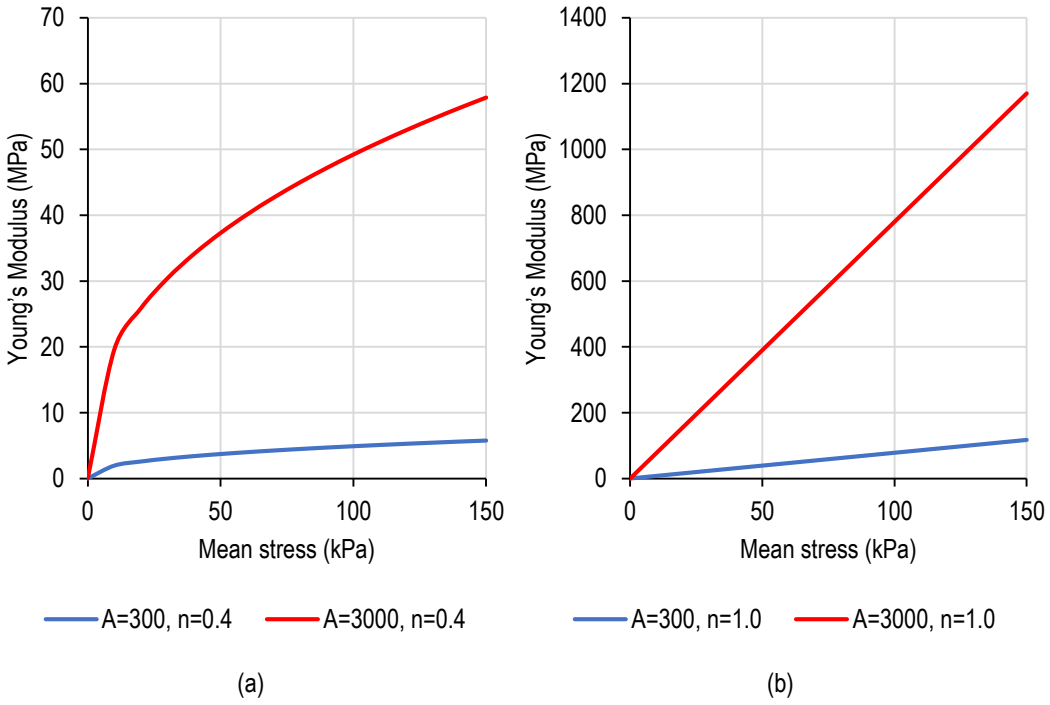

Figure 6.4 Young's Modulus range modelled using Nor-Sand stress-dependence relationship for (a) *n*=0.4 and (b) *n*=1 and *A* varied from 300 to 3000

6.3.2 Plasticity

The plasticity behaviour of Nor-Sand is modelled using the material input parameters; N, h and χ. The flow rule parameter, N, determines the shape of the yield surface in $p' - q$ space. The

parameter can be varied between 0.1 and 0.4. The hardening rule controls the evolution of the yield surface size incorporating the plastic hardening modulus, h. This parameter can be varied between 50 and 1000. The hardening rule also constrains the yield surface expansion in a formulation that incorporates the starting void ratio and the maximum dilatancy coefficient, χ, which can be varied between 2 and 5.

For these parameters, the effect of the plastic hardening modulus is easily illustrated with a stress-strain curve. Figure 6.5 (a) shows the stress-strain curves where the plastic hardening parameter is increased, while all other parameters remain constant. It illustrates how increasing the parameter results in steeper stress-strain behaviour. Figure 6.5 (b) shows the effect of the plastic hardening modulus on volumetric strain where negative volumetric strain is contractive. The figure illustrates how, for increasing hardening modulus, the expansion of the volumetric strain starts at a smaller shear strain as the maximum yield surface size is also reached at a smaller shear strain.

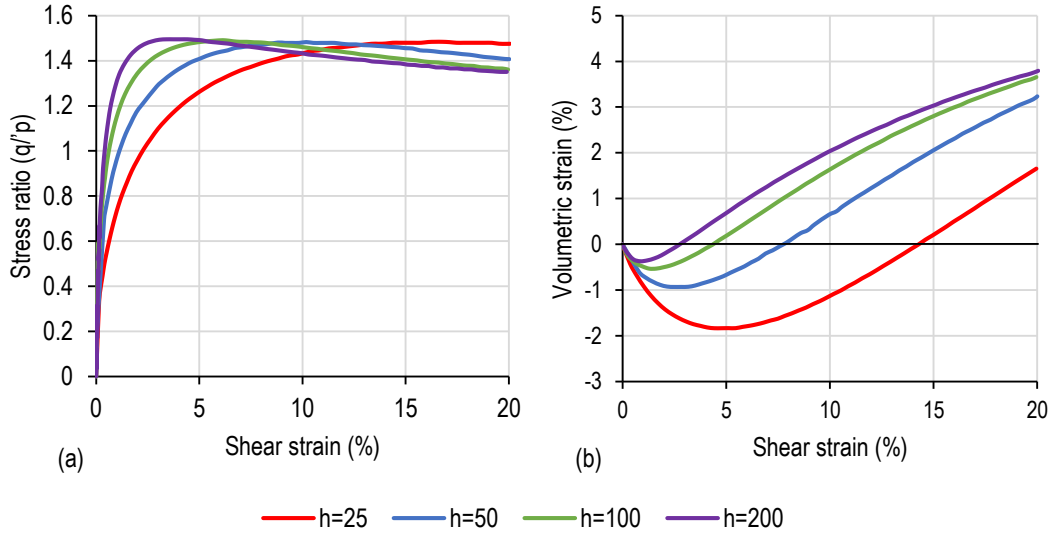

Figure 6.5 Effect of increasing hardening modulus on (a) stress-strain and (b) volumetric strain-strain behaviour (adapted from Cheong, 2006)

The plastic material input parameters are obtained by trial-and-error until the computed stress-strain curve fits the test data. The hardening rule could have a significant influence on modelling the response of pavements because it influences the stress-strain behaviour at relatively small permanent strains.

6.3.3 Critical state condition

Critical state behaviour for sandy soils defines an ultimate state at which the sand deforms continually at a constant volume and under constant shear and confining stress (Craig, 2004).

The parameters that describe the critical state condition in Nor-Sand are the maximum and minimum void ratio and the critical stress ratio in triaxial compression. These parameters are used to describe the critical state surface in $p' - q - v$ space within which all states of sand exist.

The critical stress ratio, M, is the gradient of the critical state line in $p' - q$ space. The value of M prescribed for Nor-Sand falls between 0.6 and 1.4 (Cheong, 2006). The minimum and maximum void ratios are used to determine the critical state void ratio. Typical values are 0.4 to 0.6 and 0.7 to 1 for the minimum and maximum void ratio, respectively (Cheong, 2006). Using these two parameters make it possible to model the bi-linearity of the critical state line in $e - \ln\ p'$ space. The change in line gradient occurs at approximately 1 MPa and is possibly due to particle crushing. At low stresses in pavements, particle crushing is unlikely to occur as a result of a single load cycle, but crushing may occur due to the repetitive nature of pavement loading. This is however not modelled by the formulation of Nor-Sand used in this project. The critical state void ratio is used in conjunction with the current void ratio in the state parameter concept, which is used to model overconsolidation and normal consolidation.

Figure 6.6 shows that the critical stress ratio is a measure of soil strength and increasing the ratio results in an increase in stress ratio at which failure occurs. The critical stress ratio can be related to the angle of shearing resistance of soil.

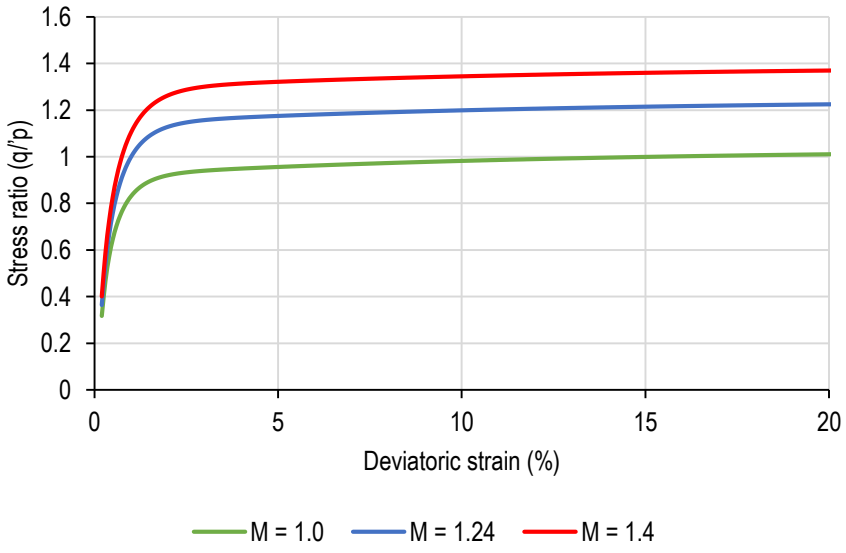

Figure 6.6 Effect of varying critical stress ratio (Osman, 2018 – personal communication)

M is the slope of the critical state line in the $p' - q$ plane and is determined through soil strength tests such as triaxial and shear box tests. The maximum and minimum void ratio of soil can be obtained using the ASTM standard test methods, ASTM D4254 – 16 and ASTM D4253 – 16.

6.3.4 Nor-Sand soil model in ABAQUS

Nor-Sand is modelled in ABAQUS/Standard using a user subroutine referred to as a UMAT file. Typically, a UMAT file is written in FORTRAN format. Cheong (2006) implemented a refined version of the Nor-Sand UMAT code initially implemented by Dasari & Soga (2000). The model was modified to improve its performance for 3D FE analysis. The UMAT code and a description of the modifications are available in Cheong (2006). The UMAT code requires the nine material input parameters discussed. A subroutine in the UMAT code assigns a void ratio and OCR with depth to the soil body that the Nor-Sand soil model is assigned to. The version of UMAT used in this research was not formulated to model cyclic loading.

6.3.5 FE model input parameters

The FE model input parameters are the initial void ratio, the coefficient of lateral earth pressure at-rest (K_0), and the OCR. In a pavement system all three of these parameters are to some extent dependent on compaction. The starting void ratio determines whether a loose, medium dense or dense sand is being modelled. A sand that has been compacted will typically have a lower void ratio. The initial stress state is dependent on K_0, which is used to calculate the horizontal stress component. K_0 is variable with depth (Chen & Fang, 2008). Values for K_0 up to 13 have been estimated for upper pavement layers (Levenberg & Garg, 2014). A value of 6 has been determined for compacted dry sand, depending on the soil strength. The OCR of the upper pavement granular layers have been estimated to be up to 207 (Levenberg & Garg, 2014).

6.4 INCORPORATING NOR-SAND IN 3D FE MODELLING OF PAVEMENTS

The suitability of using Nor-Sand to model road pavements was assessed by incorporating it in the base of the axle loading FE model that was used in Chapter 3 and Chapter 4 and conducting sensitivity analyses to the FE model input parameters. Material input parameters as calibrated for Erksak Sand available in the literature were used (Cheong, 2006). Table 6.1 shows the values of the material input parameters used in conjunction with the UMAT file. The response of Erksak Sand modelled in ABAQUS at a mean effective principal stress of 100 kPa was shown in Figure 6.3 (b).

Table 6.1 Erksak Sand material input parameters

Part description	Parameters	Value
Elasticity	Shear modulus constant (A)	3000
	Pressure exponent (n)	0.55
	Poisson's Ratio (ν)	0.3
Plasticity	'N' value in flow rule (N)	0.2
	Hardening parameter (h)	280
	Maximum dilatancy coefficient (χ)	5
Critical state condition	Critical state ratio (M)	1.2
	Maximum void ratio (e_{max})	0.807
	Minimum void ratio (e_{min})	0.527

Table 6.2 shows the combinations of FE model input parameters used in the sensitivity analyses. Dense, medium dense and loose sand were modelled with a K_0 of 1 and OCR of 1.1. Combinations of medium dense sand, an OCR of 1.1 and varying K_0 values were modelled and combinations of medium dense sand, a K_0 of 1 and varying OCR values were modelled. A combination of dense sand, a K_0 of 3 and an OCR of 5 were modelled to represent a more representative combination of the FE model input parameters for compacted sand in the pavement context. For comparison, a LE analysis was done where a base material stiffness, in terms of Young's Modulus, of 35 MPa was used. This value was selected as an approximate average of the base material stiffnesses of the stress-dependent material stiffness modelled for Erksak Sand using the Nor-Sand model.

A density index for soil of 0.95, 0.5 and 0.05 were selected for dense, medium dense and loose sand respectively and the initial void ratio (e) was calculated accordingly. The coefficient of lateral earth pressure at-rest was varied over a wide range from 1 to 12. Selecting a K_0 of 12 is high for dry sand, but not unrealistic for granular materials used in road pavements (Levenberg & Garg, 2014). The minimum OCR of 1.1 was selected to ensure that the model was not deforming plastically at the start (from the first increments of the step in which the load is applied) of the analysis. The maximum OCR used was 20 to minimize permanent deformation.

Table 6.2 Combinations of model input parameters

Combination	Initial void ratio	K_0	OCR
Set 1	0.541	1	1.1
Set 2	0.667	1	1.1
Set 3	0.793	1	1.1
Set 4	0.667	3	1.1
Set 5	0.667	12	1.1
Set 6	0.667	1	5
Set 7	0.667	1	20
Set 8	0.541	3	5

As in Chapter 3 and Chapter 4, a pressure of 550 kPa was applied over a circular area with a radius of 152.4 mm, representing a standard axle load of 80 kN, where 40 kN is applied per wheel. The properties of the concrete layer remained constant with a thickness of 50 mm, Young's Modulus of 40 GPa and Poisson's Ratio of 0.17. The material properties of the subgrade also remained constant with Young's Modulus of 41 MPa and Poisson's Ratio of 0.45. In terms of the model depth, adjustments had to be made to the two-wheel axle model in Chapter 3 and 4 to enable the use of Nor-Sand. Before the effect of the model input parameters can be discussed, the adjustments and their effect are discussed.

For the sensitivity analyses to the FE model input parameters the overall pavement response and the base response (which, along with the subgrade forms part of the substructure) were considered. The overall pavement response is discussed in terms of:

- the critical parameters defined in Section 3.2 which include:
    - vertical deflection of the model surface in the wheel centreline
    - horizontal tensile stress at the bottom of the Bound Layer (BL)
    - vertical compressive stress and strain at the top of the subgrade, and
- transverse deflection bowls

The base response was discussed in terms of:

- the material stiffness distribution,
- induced stress,
- Vertical Displacement Distributions (VDDs), and
- vertical distribution of volumetric strain.

6.4.1 Adjustments to axle load FE model

Advanced soil and granular material models are typically dependent on initial stress conditions. In ABAQUS the initial stress conditions are calculated in the Geostatic Step, which is typically the first step of geotechnical analyses. Ideally, the gravity loads and initial stresses should equilibrate and produce zero deformations (Dassault Systemes Simulia Corp, 2014).

The great depth, and poor element aspect ratio away from the area of interest of the pavement model adapted from Kim (2007) resulted in non-convergence during the Geostatic Step. Convergence was achieved by reducing the model depth and changing the element type. It was known that approximately equilateral 3D models converge in the Geostatic Step. It was opted to change the depth to 4.038 m, which was the dimension of the long plan side of the axle loading model. The thickness of the concrete bound layer remained 50 mm and the thickness of the base remained 305 mm. This resulted in a subgrade depth of 3.683 m. Quadratic tetrahedron elements (C3D10) were used.

The road pavement model was modelled in two parts, i.e. the bound layer part and the substructure part. Using two parts allows for interaction to be modelled in future. Initially, the two parts were modelled as one part by assigning a contact property that did not allow tangential movement and prevented nodes from detaching once attached. This was done to enable comparison with the pavement model that was modelled as one part. The substructure was split into the base and subgrade according to the dimensions of the preceding paragraph and given their respective material properties. Figure 6.7 shows the two parts and the mesh.

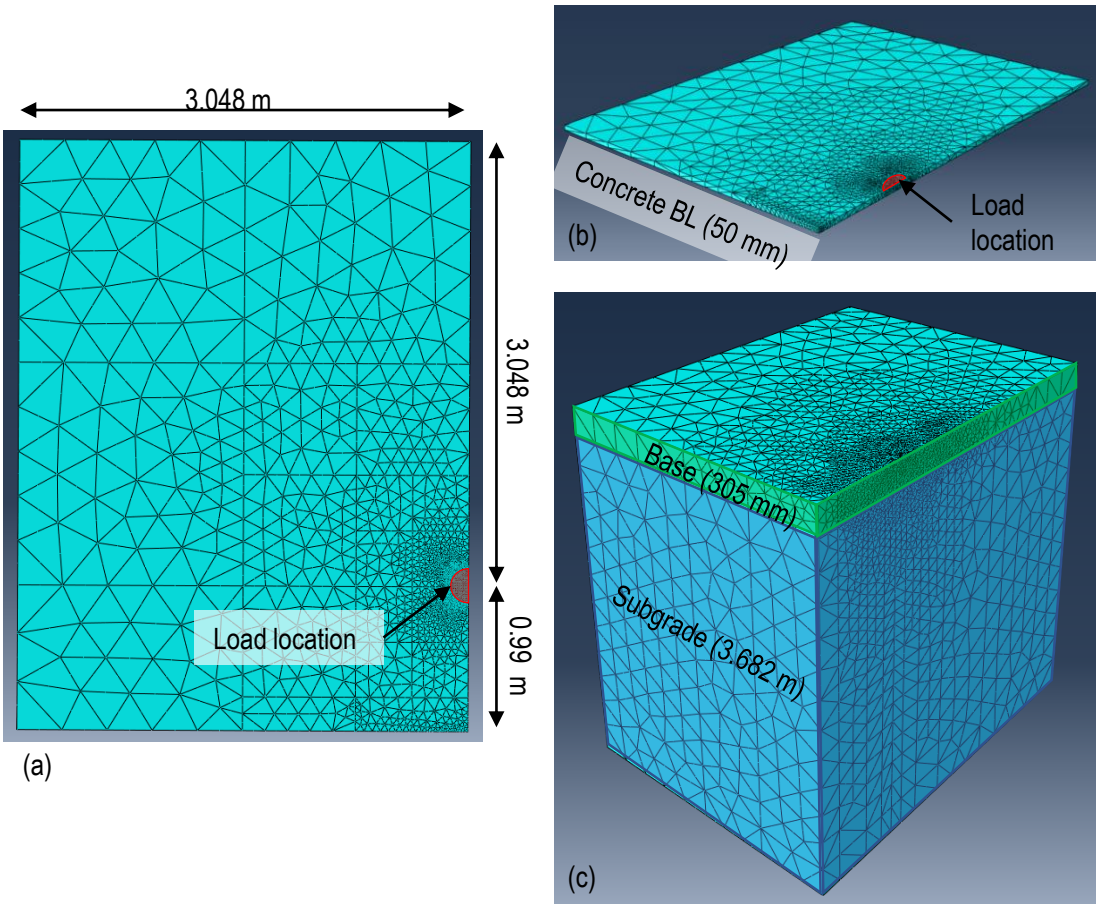

Figure 6.7 Model adjusted for Nor-Sand from Kim (2007) with (a) plan view, (b) isometric view of bound layer part and (c) isometric view of substructure

Table 6.3 shows the critical parameters of the full depth model with a 50 mm concrete bound layer and the adjusted model with the reduced depth and quadratic tetrahedron elements. The material input parameters used in Section 3.2 for the substructure remained constant, while the concrete Young's Modulus was 40 GPa and the Poisson's Ratio was 0.17. The deflection of the reduced model was less than for the full depth model. The difference and percentage difference in deflection were 0.16 mm and 18.6%, respectively. The other critical parameters were not notably affected by the changes.

Table 6.3 Critical parameters of adjusted models

Model	Critical parameter			
	$\delta_{v\ surface}$ (mm)	$\sigma_{h\ bottom\ of\ BL}$ (kPa)	$\sigma_{v\ top\ of\ subgrade}$ (kPa)	$\varepsilon_{v\ top\ of\ subgrade}$ (μm/m)
Full depth, C3D20R	-0.862	6914	-33.8	-749
Reduced depth, C3D10	-0.706	6911	-33.9	-811

Figure 6.8 shows the transverse deflection bowls of the full depth and reduced depth models. The vertical displacement of the original model was greater than the model with reduced depth. If the deflection bowl of the original model is overlain on top of the reduced depth model, using the maximum displacement as the reference point to shift it, it can be seen that the deflected shapes were very similar. This confirms the minimal effect the depth change had on the stress and strain in Table 6.3.

It is however interesting to note that the concrete layer of the reduced depth model moved vertically upward from a distance 2.25 m away from the wheel centreline (CL). This was observed even though the interaction did not allow the concrete bound layer to detach from the substructure. The upward displacement indicates that thin concrete pavements constructed on shallow layerworks with horizontal rock faces close to the surface may deflect upward at free edges under traffic loading.

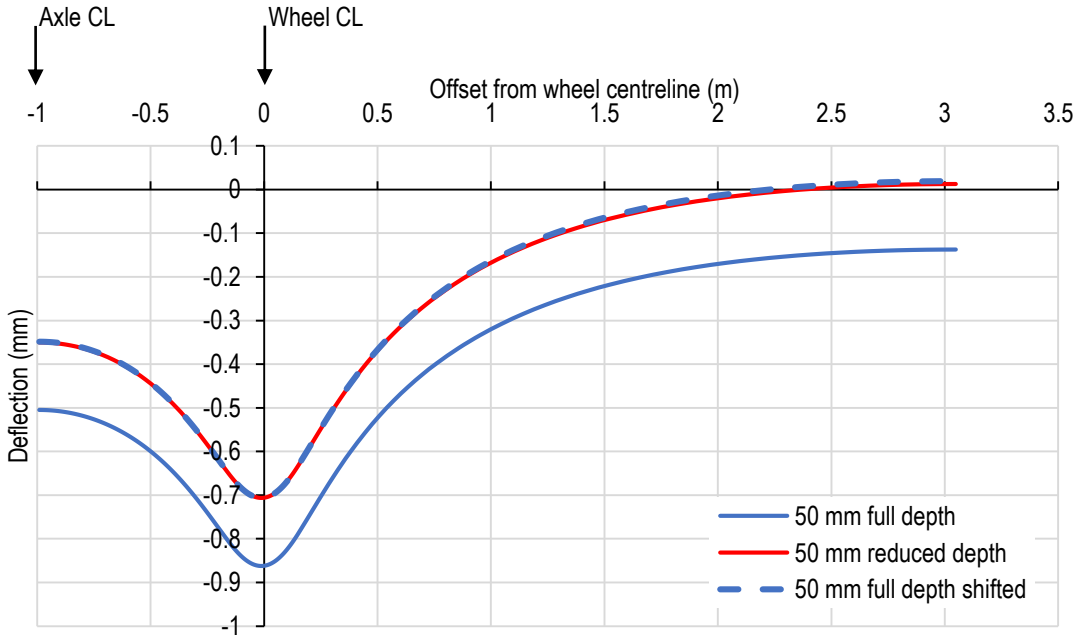

Figure 6.8 Transverse deflection bowls of the full depth and reduced depth models, and shifted full depth transverse deflection bowl

The reduced depth model with C3D10 elements was used to investigate the effect of assigning Nor-Sand as a material model to the base and varying the FE model input parameters. A relative density of 1.6 was used for the entire substructure and 2.4 was used for the concrete bound layer. Layer interaction was not modelled, and the assigned contact property did not allow tangential movement and prevented nodes from detaching once attached.

6.4.2 Effect of initial void ratio

Varying the void ratio varies the density. Soil or granular material with a high void ratio has a low density and a less dense soil or granular material would have less resistance to deformation. For the FE model input parameter combinations (see Table 6.2), Set 1 had the lowest void ratio and the highest density, while Set 3 had the highest void ratio and lowest density. The substructure would typically be compressed for the load conditions of pavements, resulting in the void ratio decreasing, and the density increasing.

6.4.2.1 Overall pavement response

Table 6.4 shows the critical parameters for the three FE model input parameter sets with different initial void ratios (equivalent to dense, medium and loose sand). The critical parameters of the LE analysis using a material stiffness, in terms of Young's Modulus, of 35 MPa is also included. As expected, increasing the void ratio resulted in less resistance to deformation and increased surface deflection in the wheel centreline. The transverse horizontal tensile stress at the bottom of the concrete bound layer also increased. The transverse horizontal tensile stress was in the range of the flexural strength of HS-SFRC with 80 kg/m^3 steel fibres seen in Figure 2.7, which was between 10 and 15 MPa. Unexpectedly, the compressive vertical stress and strain at the top of the subgrade decreased as the void ratio increased.

Comparing the critical parameters of the LE analyses to that of Set 1, Set 2 and Set 3, shows that the surface deflection and tensile stress in the bound layer reduced, while the vertical compressive stress and strain in the subgrade increased, when linear elasticity was assumed for the base. The fact that all the critical parameters for the LE analysis fell outside the range of values obtained using Nor-Sand when varying the sand from loose to dense is significant. It indicates that LE design assumptions could result in an underestimation of the requirements for the bound layer flexural strength and the surface deflection, while the requirement for subgrade strength is overestimated.

Table 6.4 Effect of initial void ratio on critical parameters

Combination (e, K_0, OCR)	Critical parameter			
	$\delta_{v\ surface}$ (mm)	$\sigma_{h\ bottom\ of\ BL}$ (kPa)	$\sigma_{v\ top\ of\ subgrade}$ (kPa)	$\varepsilon_{v\ top\ of\ subgrade}$ (μm/m)
Set 1 (0.541, 1, 1.1)	1.619	13 153	37.2	586
Set 2 (0.667, 1, 1.1)	1.896	14 045	32.2	464
Set 3 (0.793, 1, 1.1)	2.397	15 194	25.9	330
LE 35 MPa	1.062	10 723	38.8	737

Figure 6.9 shows the negative correlation between the surface deflection and vertical compressive stress at the top of the subgrade under the wheel centreline of the FE models that incorporated Nor-Sand in the base. The figure also shows the positive correlation between the two critical parameters in the LE multivariable analyses in Chapter 4. The reduction of the critical parameters in the subgrade was a result of the combination of material stiffness stress-dependence and elasto-plasticity that is taken into account by Nor-Sand. The fact that the combination of a thin concrete layer and decreasing density sand resulted in reduced stress and strain in the subgrade motivates that design procedures of UTCRCP should be re-examined.

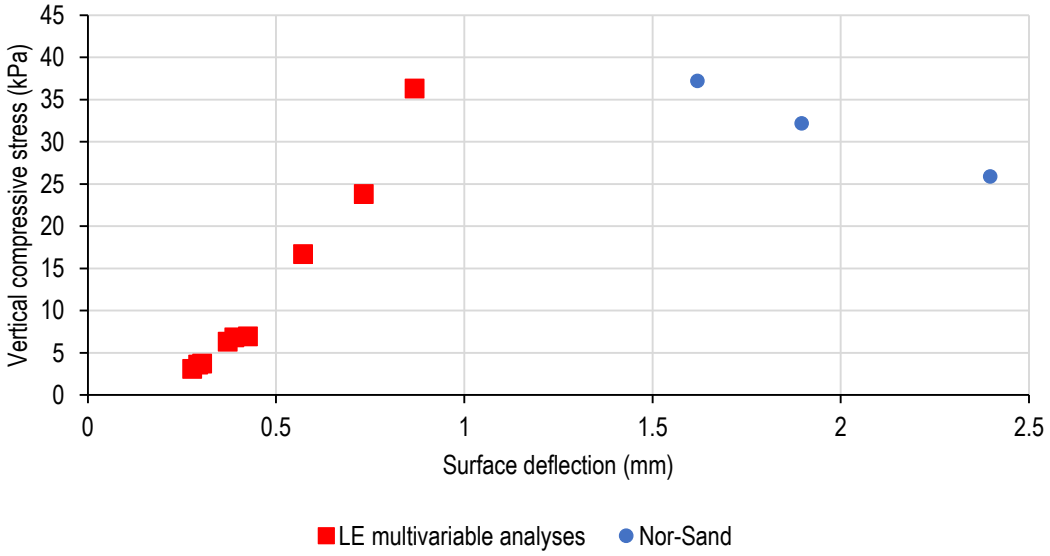

Figure 6.9 Relationship between surface deflection and vertical compressive stress in wheel centreline at top of subgrade with varying initial void ratio

Figure 6.10 shows the effect of void ratio on the transverse deflection bowls. The deflected shape of the thin concrete layer was the same as for the 3D LE models in Chapter 3 and 4, with a trough around the load location and hogging type deflection in the axle centreline. This indicates that the material stiffness of the base would have to be reduced significantly for the relative stiffness between the concrete layer and the substructure to be high enough to cause single curvature of the concrete layer.

Figure 6.10 shows that the deflection increased as the void ratio increased. When considering the normalized deflection bowls in Appendix E, it can be seen that the deflection bowl of the loose sand was the widest, and the difference between the vertical displacement in the wheel centreline and axle centreline was the smallest.

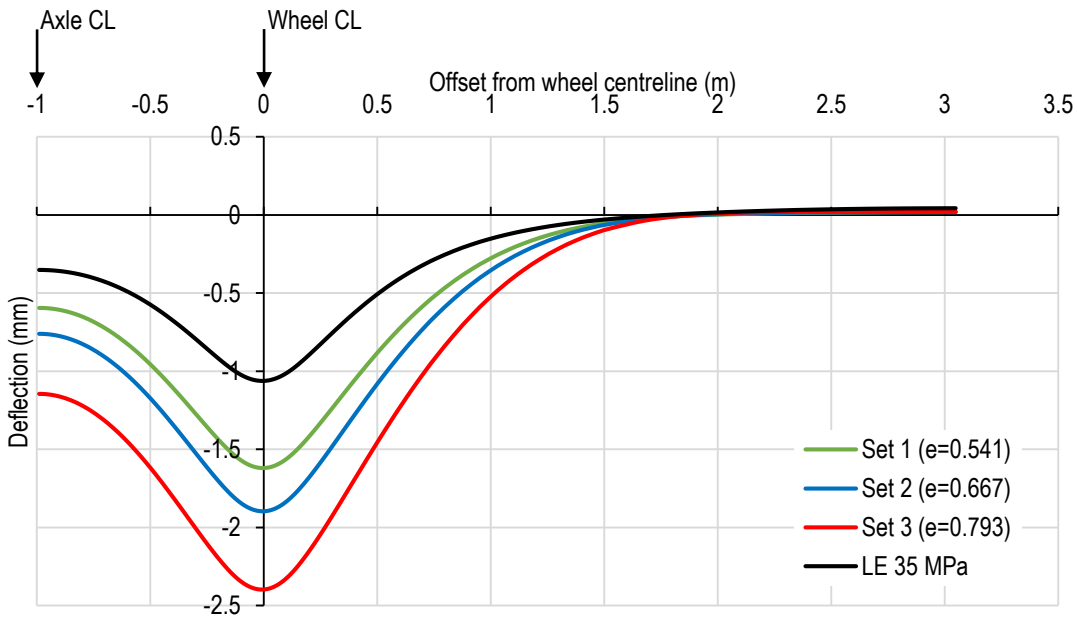

Figure 6.10 Effect of initial void ratio on transverse deflection bowls

6.4.2.2 Base response

Figure 6.11 shows the distribution of material stiffness, in terms of Young's Modulus, calculated from the shear modulus and Poisson's Ratio using Equation 6.10. The limits of the contour plots were 5 000 to 55 000 kPa. The maximum material stiffness of Set 1, Set 2 and Set 3 were 51 923 kPa, 47 566 kPa and 45 474 kPa respectively.

The highest material stiffness was induced in Set 1, which modelled dense sand. Considering Figure 6.3 (b) the stress-strain curve of the dense sand was steeper than of the loose sand. The result of the compounded effect of a steep stress-strain curve and stress-dependent material stiffness is shown in Figure 6.11. Stress was absorbed close to the load location due to the steeper stress-strain curve. This resulted in an increase in stress, which resulted in an increase in material stiffness, which caused an increase in stress. Ultimately, a high proportion of the load induced stress is concentrated close to the load location. The increase in vertical compressive stress and strain at the top of the subgrade, as the initial void ratio decreased is a result of the compounded effect of the stress-strain curve slope and stress-dependent material stiffness.

The compressive stress and strain in the axle centreline at the top of the subgrade increased as the void ratio increased, varying from 12.4 kPa and 69.5 μm/m for dense sand, 13.5 kPa and 87.3 μm/m for medium dense sand and 14.9 kPa and 114.8 μm/m for loose sand. This was due to the zones of influence of the wheels overlapping further as the density decreased. The zones of influence overlapping further could be a result of the compounding effect of the stress-strain

curve and stress-dependent material stiffness or could be a result of the change in radius of relative stiffness due to the relative stiffness between the concrete bound layer and base layer being greater. The zones of influence overlapping further could also be result of a combination of the two.

The material stiffness of the base due to initial stress conditions, before the wheel load was applied, was between 9 625 kPa (underneath the concrete layer) and 21 630 kPa (above the subgrade). The material stiffness of the subgrade was 41 000 kPa. The contour patterns in Figure 6.11 show how the base was compressed between two layers that have relatively high material stiffnesses in comparison to its own stiffness.

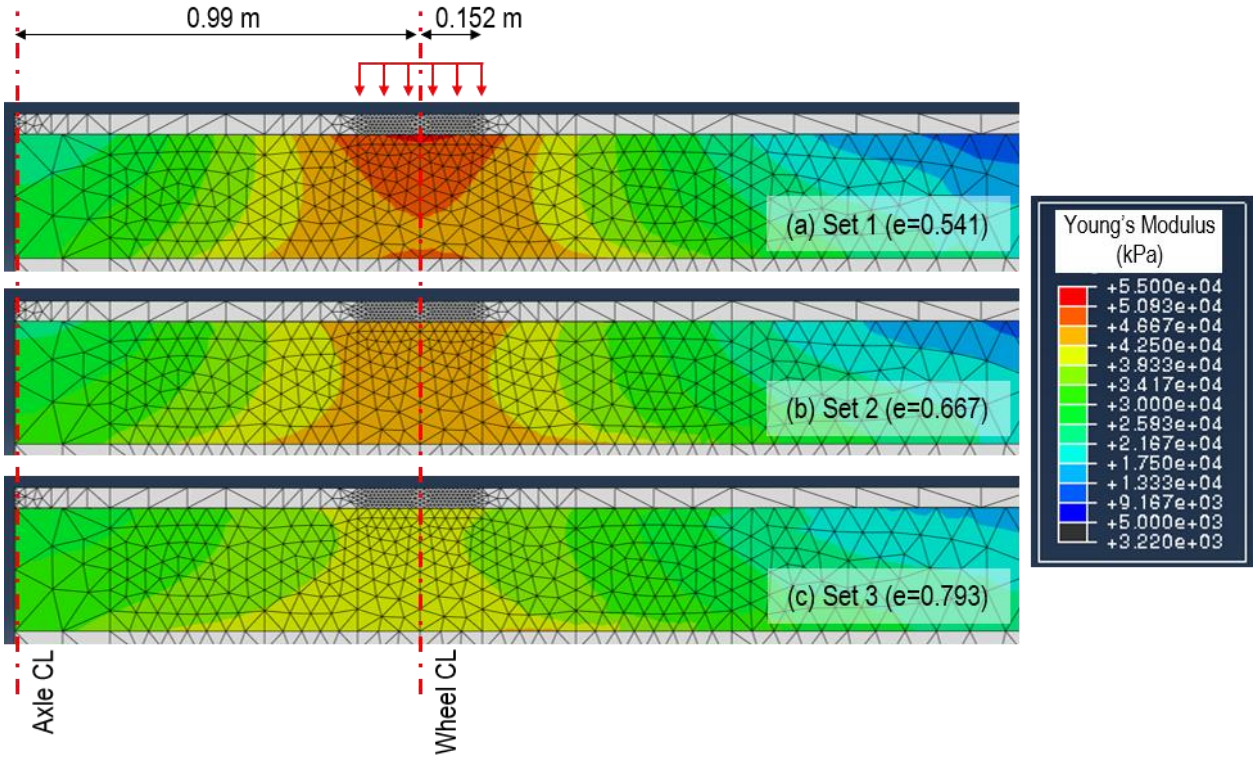

Figure 6.11 Stress-dependent material stiffness development in base for (a) Set 1, (b) Set 2 and (c) Set 3 with varying initial void ratio

As the material stiffness is a function of the stress conditions, Figure 6.11 is also a representation of mean stress distribution. The vertical and horizontal stresses induced at the top and bottom of the base layer in the wheel and axle centreline are summarised in Table 6.5. The horizontal stress applies to the transverse direction of the pavement. The horizontal stress in the longitudinal direction was approximately the same as in the transverse direction. All the vertical and horizontal stresses induced were in compression.

The horizontal stress in the wheel centreline at the top of the base was greater than at the bottom of the base for Set 1. The reverse occurred in the axle centreline. The horizontal stress in the wheel centreline at the top and bottom of the base for Set 2 did not differ much, while a greater stress was induced at the bottom of the base in the axle centreline. For Set 3, the horizontal stress was greater at the bottom of the base in the wheel and axle centreline. The same trends were observed for the vertical stresses.

Table 6.5 Effect of initial void ratio on stress in wheel and axle centreline at top and bottom of base for Set 1, Set 2 and Set 3

	Centreline	σ_h (kPa)		σ_v (kPa)	
		Top	Bottom	Top	Bottom
Set 1	Wheel	-24.8	-20.9	-45.2	-37.3
	Axle	-5.94	-10.2	-7.41	-12.0
Set 2	Wheel	-21.9	-21.2	-35.2	-32.1
	Axle	-7.39	-11.3	-8.73	-13.3
Set 3	Wheel	-17.4	-19.7	-24.8	-25.8
	Axle	-9.07	-13.0	-10.2	-14.8

The percentage difference between the starting void ratio of the Set 1, Set 2 and Set 3 and their respective minimum void ratios at full load application was 0.92%, 1.09% and 1.64% at the top of the base in the wheel centreline. The percentage difference increased as the void ratio increased.

Figure 6.12 shows the vertical displacement distribution in the base for the respective void ratio sets. The vertical displacement at the bottom of the base did not differ notably for the respective models, while displacement to the top increased as greater initial void ratios were used. The figure shows that the vertical displacement of Set 3, which had the highest void ratio, was the greatest at the surface and the smallest at the bottom of the base. The vertical displacement of the LE model was the smallest because the material model did not include stress dependent, elasto-plastic material behaviour.

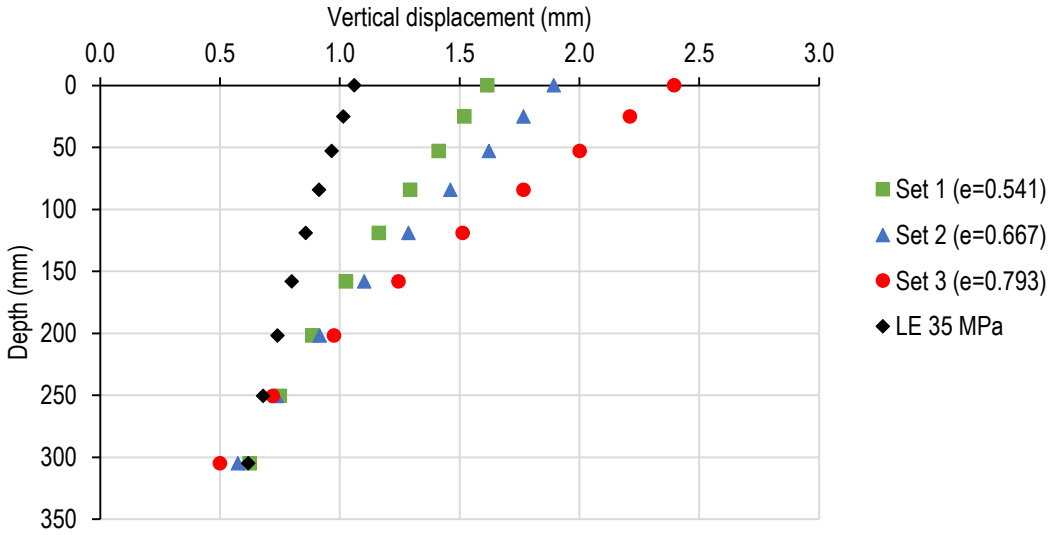

Figure 6.12 Effect of initial void ratio on base vertical displacement distribution

Figure 6.13 (a) shows the total and permanent volumetric strain in the base with depth when the pavement is loaded. Figure 6.13 (b) shows the ratio of permanent volumetric strain over total volumetric strain in the base with depth. The total volumetric strain increased as the initial void ratio increased. The ratio of permanent over volumetric strain remained relatively constant with depth for each set. The ratio increased as the initial void ratio increased.

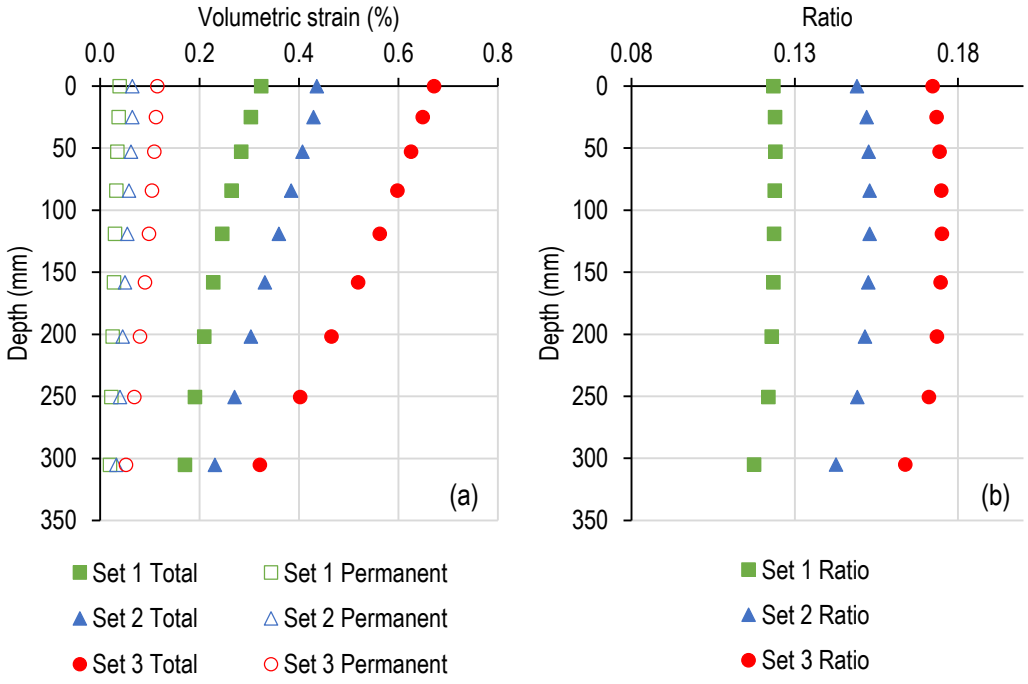

Figure 6.13 Effect of initial void ratio on the vertical distribution of (a) total and permanent volumetric strain and (b) ratio of permanent and volumetric strain in the base

6.4.3 Effect of coefficient of lateral earth pressure at-rest

The coefficient of lateral earth pressure at-rest influences the initial stress conditions of the base layer. The initial stress conditions influence the starting material stiffness, which influences the overall pavement response. The values used to investigate the effect of the coefficient of lateral earth pressure at-rest were 1, 3 and 12.

6.4.3.1 Overall pavement response

The critical parameters at full load application are shown in Table 6.6. Increasing the coefficient of lateral earth pressure at-rest caused a reduction in the surface deflection and transverse horizontal tensile stress at the bottom of the concrete layer. Increasing K_0, also caused an increase the vertical compressive strain at the top of the subgrade. The same trend was not observed for the vertical compressive stress.

Table 6.6 Effect of K_0 on critical parameters

Combination (e, K_0, OCR)	Critical parameter			
	$\delta_{v\ surface}$ (mm)	$\sigma_{h\ bottom\ of\ BL}$ (kPa)	$\sigma_{v\ top\ of\ subgrade}$ (kPa)	$\varepsilon_{v\ top\ of\ subgrade}$ (μm/m)
Set 2 (0.667, 1, 1.1)	1.896	14 045	32.2	464
Set 4 (0.667, 3, 1.1)	1.259	12 213	38.3	609
Set 5 (0.667, 12, 1.1)	1.186	10 664	28.6	1177
LE 35 MPa	1.062	10 723	38.8	737

Figure 6.14 shows the effect that K_0 had on the transverse deflection bowls. Similar to when the void ratio was varied, all the deflection bowls had a trough around the load location and hogging in the axle centreline. The magnitude of deflection for Set 4 and Set 5 was in the same range. This was surprising considering the difference in initial stress distribution, and resulting initial material stiffness, due to high values of K_0. The deflection bowl of Set 5 was slightly shallower and wider than that of Set 4. These results indicate that the effect of horizontal stresses induced by compaction reaches a limit, where after it no longer influences the deflection of pavements. The deflection bowl of the LE analyses with a material stiffness of 35 MPa is included and had a similar magnitude than Set 4 and Set 5. The normalized deflection bowls can be seen in Appendix E.

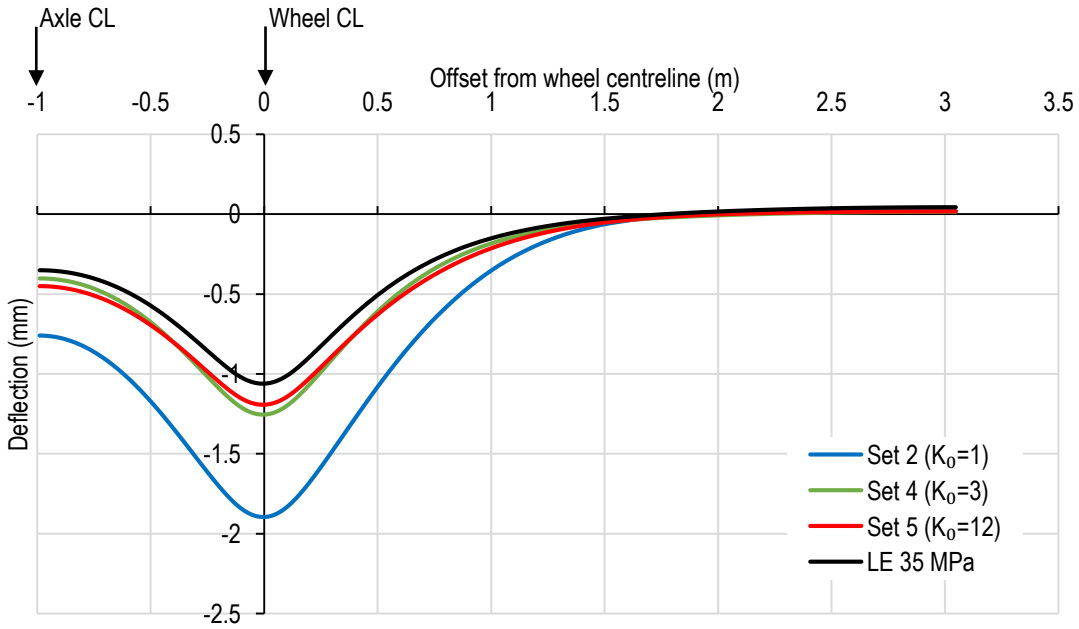

Figure 6.14 Effect of K_0 on the transverse deflection bowls

6.4.3.2 Base response

Figure 6.15 shows the distribution of material stiffness, in terms of Young's Modulus, calculated from the shear modulus and Poisson ratio. The range of material stiffness reported is greater than for Figure 6.11, where only the void ratio was varied. The material stiffness limits were 5 000 kPa to 90 000 kPa. The greater range resulted in a loss of detail for the contours of Set 2 and Set 4. It can however be seen that a higher material stiffness was induced for a wider zone in Set 4 than in Set 2.

The material stiffness contours for Set 5 shows the effect of starting with greater values for material stiffness. The material stiffness of the base due to initial stress conditions, before the wheel load was applied, was between 27 703 kPa (underneath the concrete layer) and 67 577 kPa (above the subgrade). When the load was applied the highest material stiffness and stress were still situated at the bottom of the base in the wheel centreline, reducing at shallower depths.

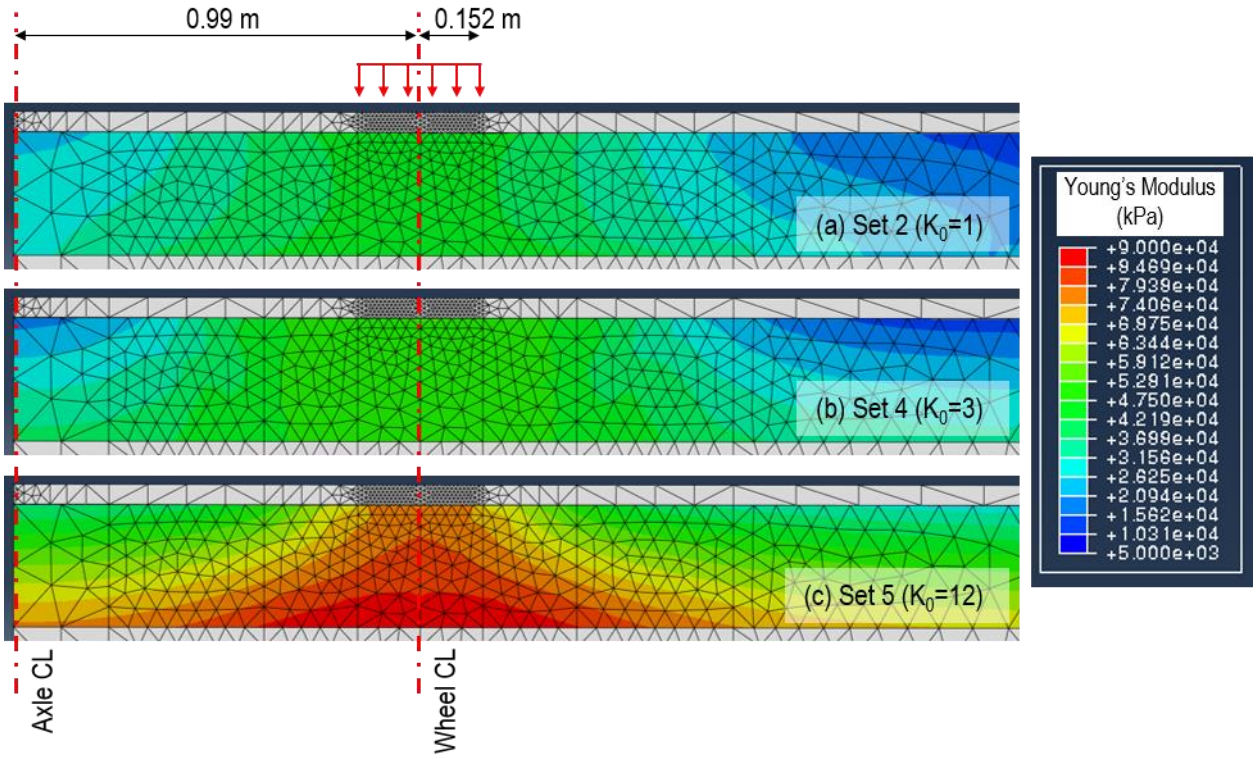

Figure 6.15 Stress-dependent material stiffness development in base for (a) Set 2, (b) Set 4 and (c) Set 5 with varying *K0*

The vertical and horizontal stresses induced at the top and bottom of the base layer in the wheel and axle centreline under full load application are summarised in Table 6.7. All the stresses in the base were in compression. The horizontal and vertical stresses in the wheel centreline increased as the coefficient of lateral earth pressure at-rest increased. For Set 5, where K_0 was 12, the horizontal stress in the wheel centreline was greater at the bottom of the base than at the top. In the axle centreline both horizontal and vertical stresses were greater at the bottom than at the top of the base.

Table 6.7 Effect of *K0* on stress in wheel and axle centreline at top and bottom of base for Set 2, Set 4 and Set 5

	Centreline	σ_h (kPa)		σ_v (kPa)	
		Top	Bottom	Top	Bottom
Set 2	Wheel	-21.9	-21.2	-35.2	-32.1
	Axle	-7.39	-11.3	-8.73	-13.3
Set 4	Wheel	-27.0	-26.8	-44.4	-38.3
	Axle	-5.76	-25.5	-3.31	-11.0
Set 5	Wheel	-54.3	-113	-84.0	-28.1
	Axle	-21.6	-99.0	-5.50	-13.7

Figure 6.16 shows the effect of K_0 on the VDD in the base. The figure shows that the vertical displacement was the greatest and reduced the most with depth for Set 2, which had a K_0 of 1. The vertical displacement of Set 4 and Set 5 overlap twice with depth. The displacement of Set 4 was greater than for Set 5 at the top and at the bottom of the base. Between a depth of approximately 50 mm and 175 mm the vertical displacement of Set 5 was greater than Set 4. High initial stress conditions, caused by high values of coefficient of lateral earth pressure at-rest, resulted in vertical displacement magnitude comparable to what was determined for the LE analyses where 35 MPa was used for the base material stiffness.

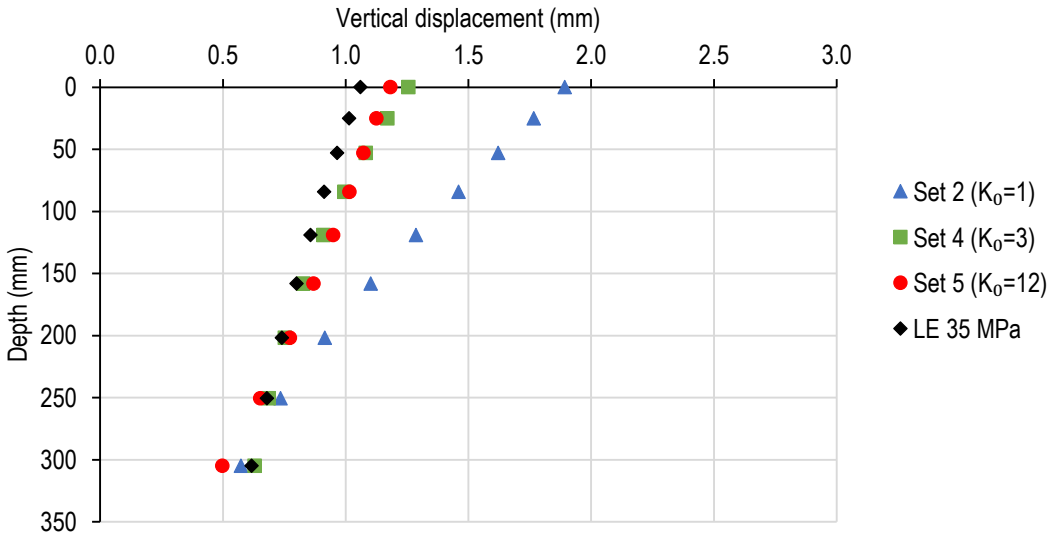

Figure 6.16 Effect of K_0 on the vertical displacement distribution

Figure 6.17 (a) shows the total and permanent volumetric strain in the base with depth when the pavement is loaded. The total volumetric strain of both Set 2 and Set 4 reduced with depth, while the total volumetric strain of Set 5 with a K_0 of 12 reduced to a depth of 50 mm and then increased again. Figure 6.17 (b) shows the ratio of permanent over total volumetric strain in the base with depth. The proportion of permanent strain to total volumetric strain varied with depth for Set 5, showing that there was more permanent deformation at the bottom of the base for Set 5 than at the top.

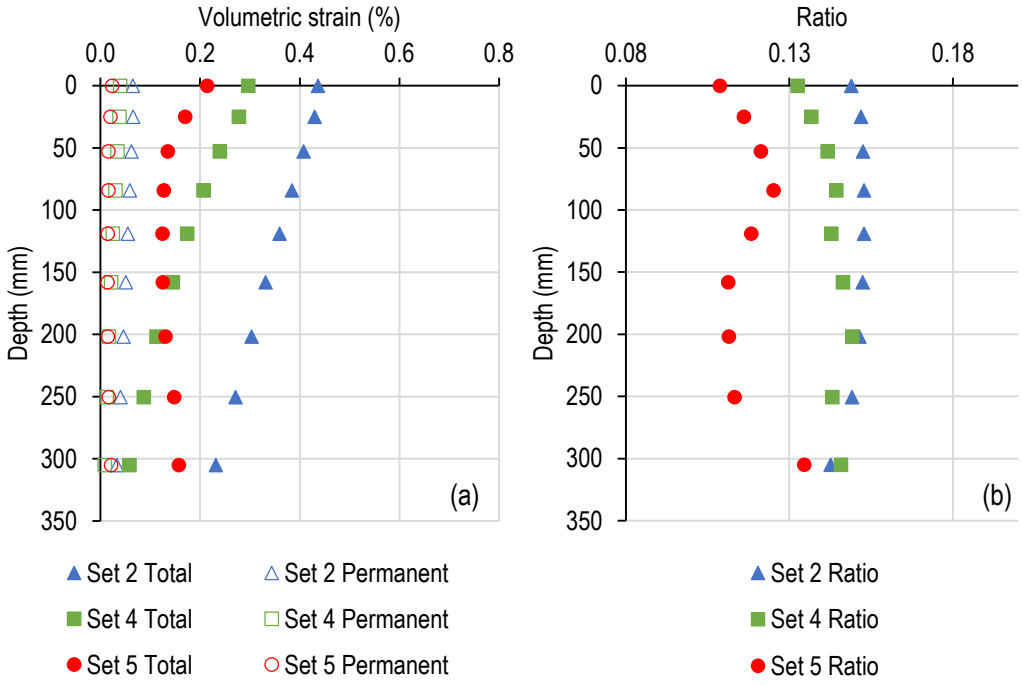

Figure 6.17 Effect of K_0 on the vertical distribution of (a) total and permanent volumetric strain and (b) ratio of permanent and volumetric strain for Set 2, Set 4 and Set 5

6.4.4 Effect of overconsolidation ratio

In the context of pavement engineering, an apparent overconsolidation ratio can be associated with the compacted soil of the substructure. The OCR is a description of how much less the current stress conditions are than the maximum stress that has been experienced in the past and how much stress can be absorbed until permanent deformation occurs. In $p' - q$ space the OCR is used to determine the size of the yield surface and thus the length of the stress path before a soil element reaches the yield surface.

6.4.4.1 Overall pavement response

Less permanent deformation will occur in a base with a high OCR. Table 6.8 shows the effect of increasing the OCR on the critical parameters, where the surface deflection and transverse horizontal tensile stress at the bottom of the base decreased and the vertical compressive stress and strain at the top of the subgrade increased with increasing OCR.

Table 6.8 Effect of OCR on critical parameters

Combination (e, K_0, OCR)	Critical parameter			
	$\delta_{v\ surface}$ (mm)	$\sigma_{h\ bottom\ of\ BL}$ (kPa)	$\sigma_{v\ top\ of\ subgrade}$ (kPa)	$\varepsilon_{v\ top\ of\ subgrade}$ (μm/m)
Set 2 (0.667, 1, 1.1)	1.896	14 045	32.2	464
Set 6 (0.667, 1, 5)	1.428	12 843	35.1	590
Set 7 (0.667, 1, 20)	1.231	11 722	41.5	756
LE 35 MPa	1.062	10 723	38.8	737

Figure 6.18. shows that a negative correlation exists between the surface deflection and vertical compressive stress at the top of the subgrade when the OCR was varied. When an OCR of 20 was used the surface deflection was reduced, but the vertical compressive stress at the top of the subgrade was increased. When an OCR of 1.1 was used the deflection increased, but the vertical compressive stress at the top of the subgrade decreased. The figure also shows the positive correlation between the two critical parameters in the LE multivariable analyses in Chapter 4. This trend was similar to when the void ratio was varied in Section 6.4.2.

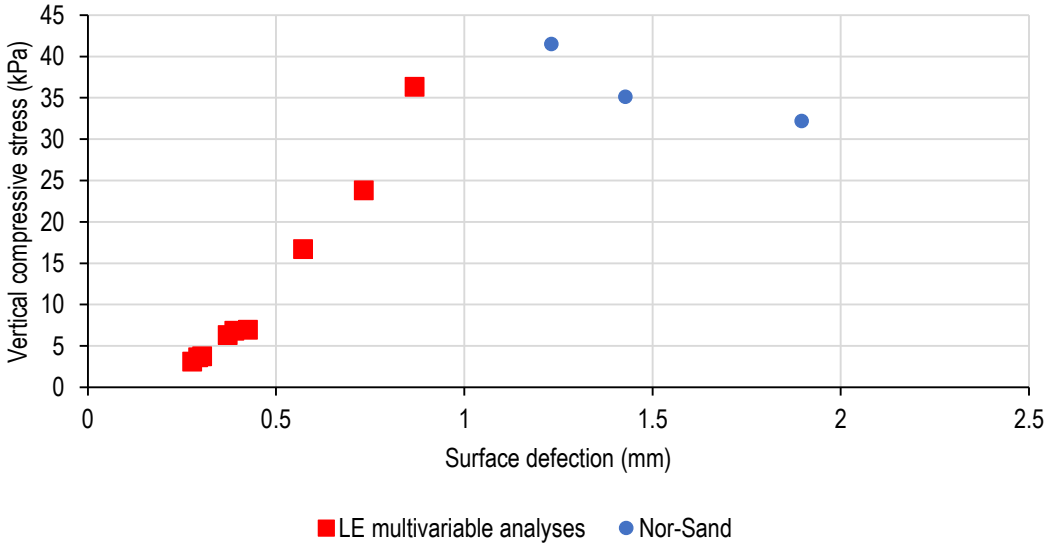

Figure 6.18 Relationship between surface deflection and vertical compressive stress in wheel centreline at top of subgrade with varying OCR

Figure 6.19 shows the transverse deflection bowls of Set 2, Set 6 and Set 7. It also shows the deflection bowl of the LE analyses. As for when the void ratio and coefficient of lateral earth pressure at-rest were varied, all the deflection bowls had a trough around the load location and hogging in the axle centreline. The figure shows that the magnitude of deflection reduced as the OCR increased.

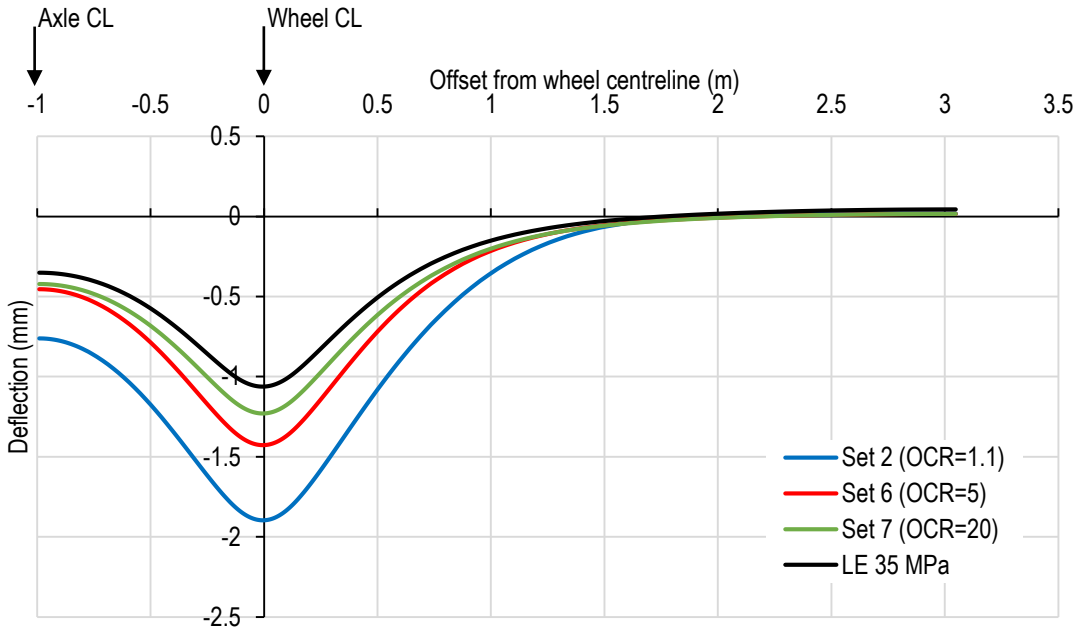

Figure 6.19 Effect of OCR on the transverse deflection bowls

6.4.4.2 Base response

Figure 6.20 shows the distribution of material stiffness, in terms of Young's Modulus, for Set 2, Set 6 and Set 7. The contour range limits were 5 000 kPa to 60 000 kPa. As the OCR increased and less permanent deformation occurred, the zone with a material stiffness between 23 330 kPa and 41 670 kPa reduced in width. The material stiffness in the vicinity of the load location increased, concentrating the induced stress close to the wheel centreline and surface.

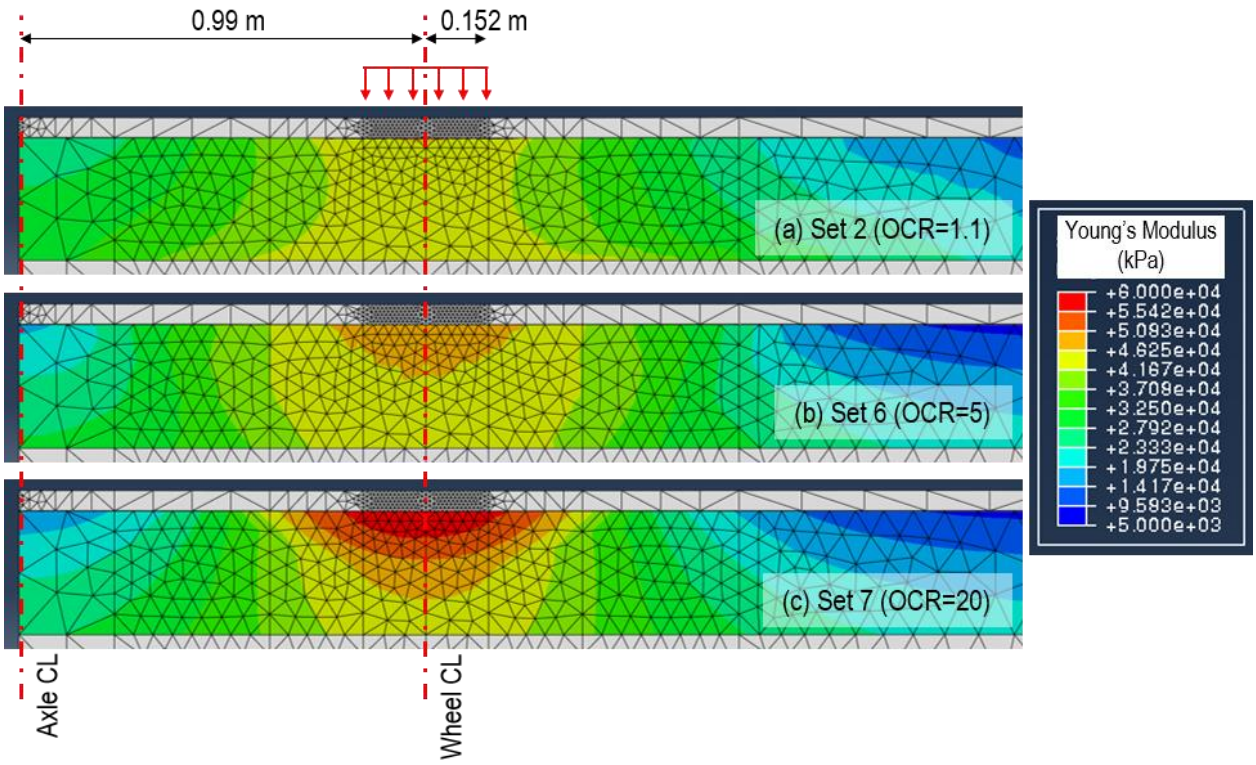

Figure 6.20 Stress-dependent material stiffness development of (a) Set 2, (b) Set 6 and (c) Set 7 with varying OCR

The vertical and horizontal stresses induced at the top and bottom of the base layer in the wheel and axle centreline are summarised in Table 6.9. All the stresses in the base were in compression. The difference between the horizontal stress in the wheel centreline at the top of the base and at the bottom of the base increased as the OCR was increased. The horizontal stress at the top of the base in the axle centreline reduced as the OCR increased, while the horizontal stress at the bottom of the base remained constant. The vertical stress in the wheel centreline at the top of the base was greater than at the bottom of the base for all the model input parameter sets. The vertical stress in the axle centreline was greater at the bottom of the base than at the top of the base for all the model input parameter sets.

Table 6.9 Effect of OCR on stress in wheel and axle centreline at top and bottom of base for Set 2, Set 6 and Set 7

	Centreline	σ_h (kPa)		σ_v (kPa)	
		Top	Bottom	Top	Bottom
Set 2	Wheel	-21.9	-21.2	-35.2	-32.1
	Axle	-7.39	-11.3	-8.73	-13.3
Set 6	Wheel	-23.6	-19.8	-38.8	-35.0
	Axle	-4.06	-11.7	-5.89	-12.8
Set 7	Wheel	-33.1	-14.0	-55.2	-41.6
	Axle	-3.38	-11.2	-4.75	-11.5

Figure 6.21 shows the effect of OCR on the VDD in the base. Increasing the OCR reduced the vertical displacement. This effect diminished with depth with the vertical displacement from a depth of approximately 250 mm being similar. The relationship between the vertical displacement at the top of the base and the OCR was non-linear with the effect of the OCR on reducing the vertical displacement reaching a plateau.

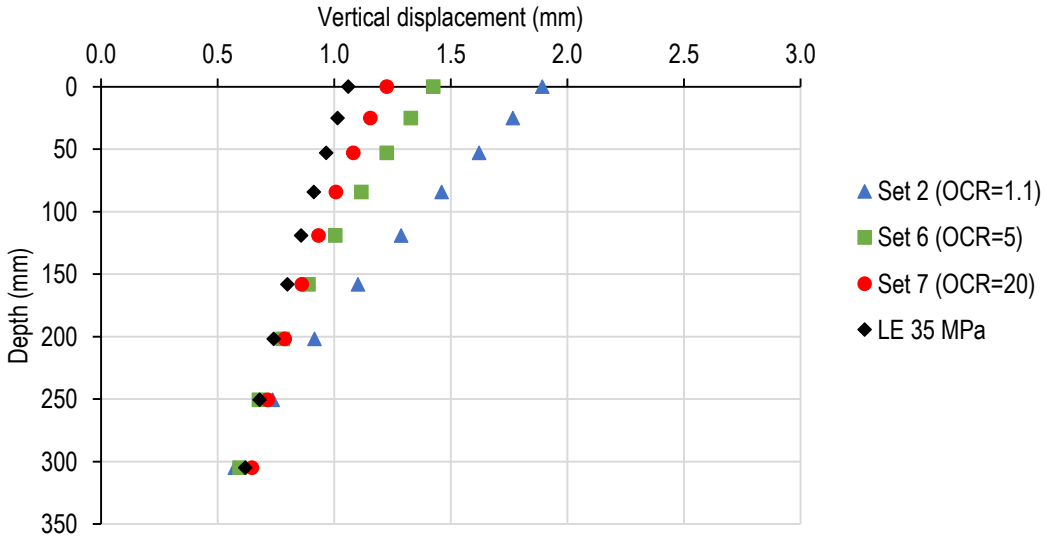

Figure 6.21 Effect of OCR on the vertical displacement distribution

Figure 6.22 (a) shows the vertical distribution of total and permanent volumetric strain and Figure 6.22 (b) shows the vertical distribution of the ratio of the permanent volumetric strain to the total volumetric strain. An OCR of 20 was used for Set 7 in an attempt to prevent any permanent deformation from occurring. The vertical distribution of total volumetric strain of Set 7 was the most non-linear. The ratio of permanent volumetric strain to total volumetric strain for an OCR of 1.1 and 5 was similar, while the ratio of permanent volumetric strain to total volumetric strain for an OCR of 20 reduced to the mid-depth of the base with the minimum being 0.08.

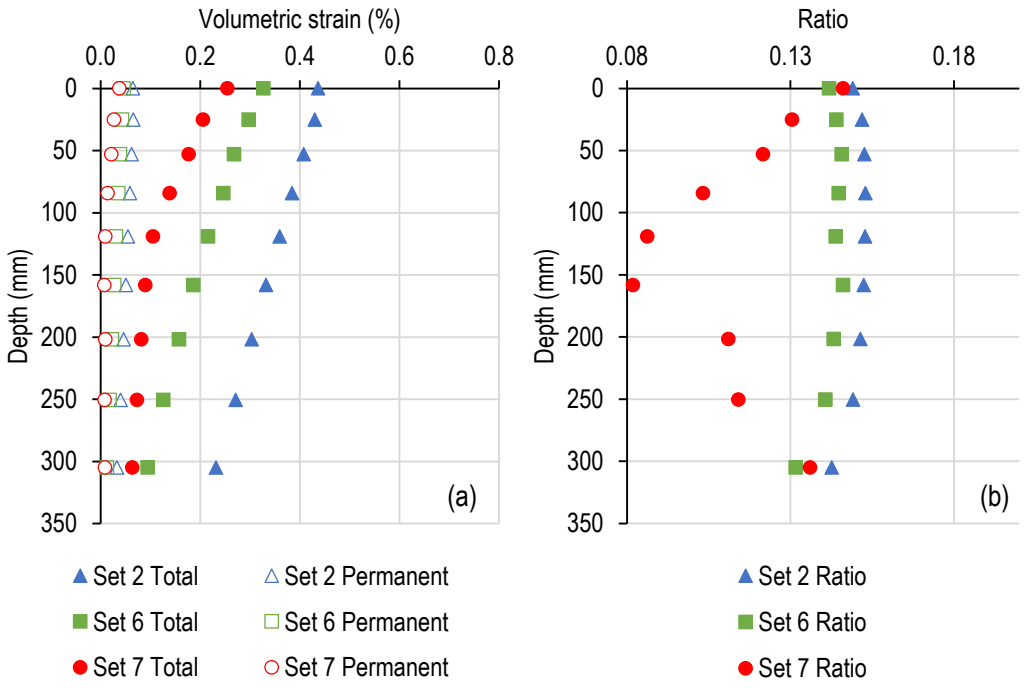

Figure 6.22 Effect of OCR on the vertical distribution of (a) total and permanent volumetric strain and (b) ratio of permanent and volumetric strain

6.4.5 Realistic combination of void ratio, coefficient of lateral earth pressure at-rest and OCR for pavements

Set 8 was used to model a realistic combination of void ratio, K_0 and OCR for pavements where the granular material would have been compacted to increase the density, creating an apparent overconsolidation ratio and accumulated lateral stresses. A void ratio of 0.541 was used along with a K_0 of 3 and OCR of 5.

6.4.5.1 Overall pavement response

Table 6.10 shows the critical parameter values of Set 8, as well as Set 1, Set 4, Set 6 and LE 35 MPa. Set 1 had the same initial void ratio as Set 8, Set 4 had the same K_0 as Set 8 and Set 6 had the same OCR as Set 8. The vertical deflection in wheel centreline and the tensile

stress at the bottom of the concrete bound layer in wheel centreline of Set 8 were smaller than for the other sets using Nor-Sand. The vertical compressive stress and strain of Set 8 in the axle centreline was greater than the other sets.

Table 6.10 Effect of realistic combination of void ratio, coefficient of lateral earth pressure at-rest and OCR for pavements

Combination (e, K_0, OCR)	Critical parameter			
	$\delta_{v\ surface}$ (mm)	$\sigma_{h\ bottom\ of\ BL}$ (kPa)	$\sigma_{v\ top\ of\ subgrade}$ (kPa)	$\varepsilon_{v\ top\ of\ subgrade}$ (μm/m)
Set 1 (0.541, 1, 1.1)	1.619	13 153	37.2	586
Set 4 (0.667, 3, 1.1)	1.259	12 213	38.3	609
Set 6 (0.667, 1, 5)	1.428	12 843	35.1	590
Set 8 (0.541, 3, 5)	1.159	11 334	43.8	546
LE 35 MPa	1.062	10 723	38.8	737

Figure 6.23 shows the transverse deflection bowls of Set 1, Set 4, Set 6, Set 8 and LE 35 MPa. As could be anticipated, the deflected shape of Set 8 had a trough around the load location and hogging type deflection in the axle centreline. The figure shows the magnitude of vertical deflection for Set 8, which had the densest base, less permanent deformation (due to an OCR of 5) and a high mean normal effective stress due to a K_0 of 3. The vertical deflection of Set 8 was not much different from that of Set 4, which was a medium sand with a K_0 of 3. The normalized deflection bowls can be seen in Appendix E.

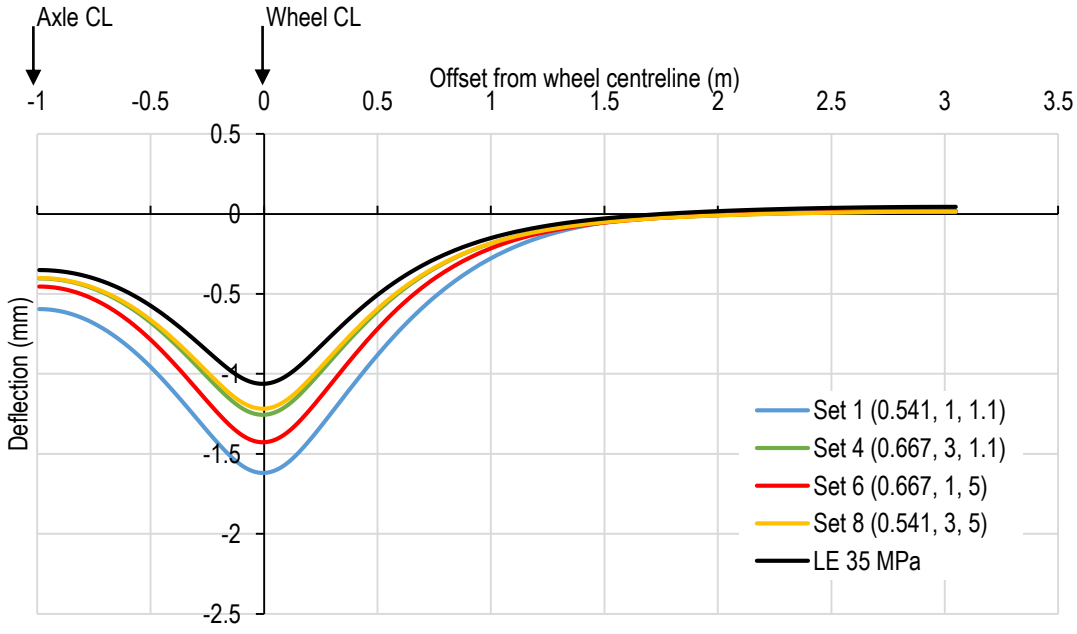

Figure 6.23 Deflection bowls of Set 1, Set 4, Set 6, Set 8 and LE 35 MPa

6.4.5.2 Base response

Figure 6.24 shows the distribution of material stiffness, in terms of Young's Modulus, of Set 1, Set 4, Set 6 and Set 8. The range of the contour plots is from 5 000 kPa to 62 000 kPa. The wide range of material stiffness contours results in the contours of Set 1, Set 4 and Set 6 having less detail. Set 8 had the highest material stiffness. The material stiffness reduced in concentric circles around and away from the load location. The similarity of the deflection bowls of Set 4 and Set 8 in terms of magnitude and the dissimilarity of the material stiffness range and variation indicates how different combinations of void ratio, initial stress conditions and OCR can result in similar measured pavement responses.

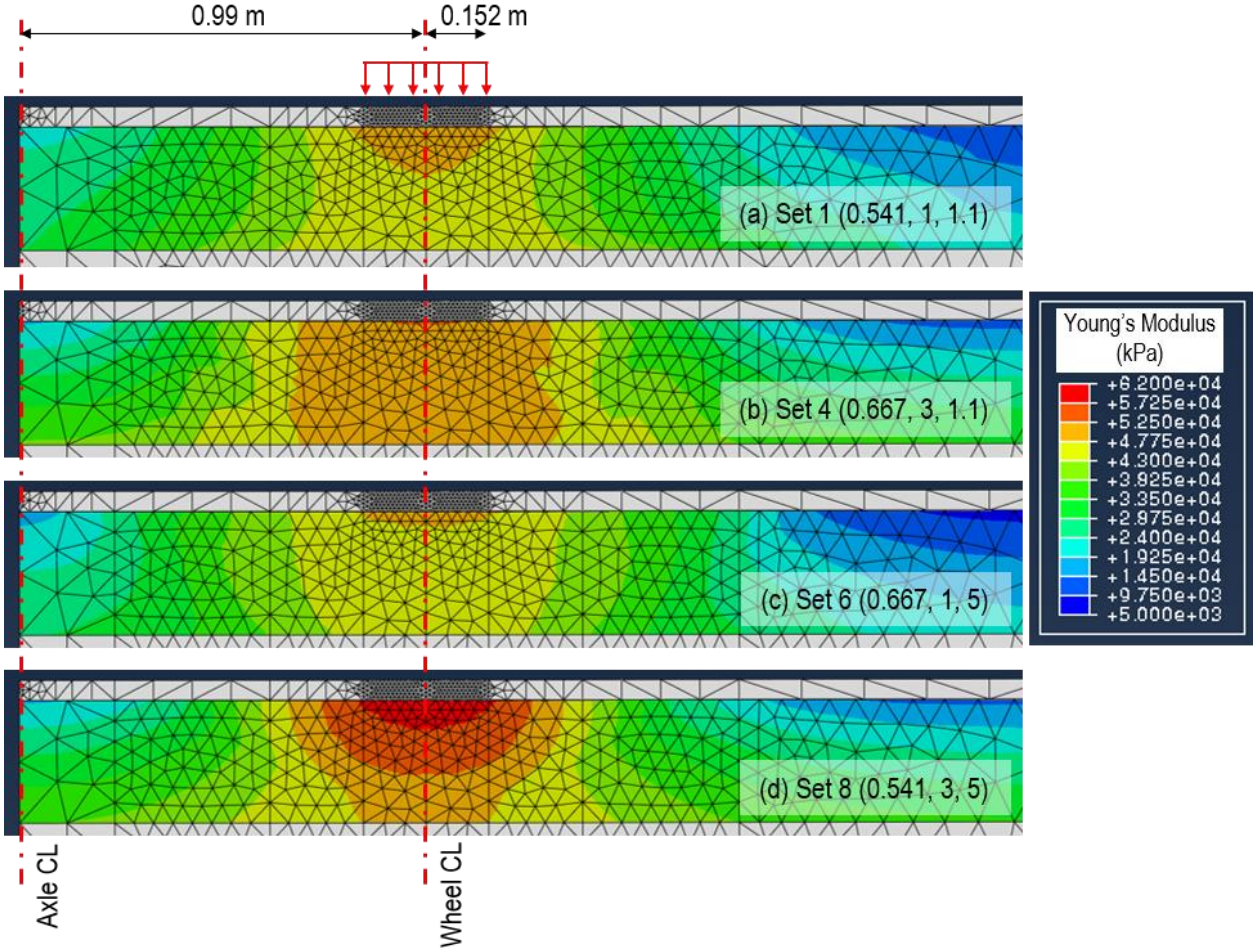

Figure 6.24 Material stiffness contours of (a) Set 1, (b) Set 4, (c) Set 6 and (d) Set 8

The vertical and horizontal stresses induced at the top and bottom of the base layer in the wheel and axle centreline are summarised in Table 6.11. The stresses in the wheel centreline was greater at the top of the base than at the bottom and the reverse was true for the stresses in the axle centreline.

Table 6.11 Stress in wheel and axle centreline at top and bottom of base for Set 2, Set 4, Set 6 and Set 8

	Centreline	σ_h (kPa)		σ_v (kPa)	
		Top	Bottom	Top	Bottom
Set 2	Wheel	-21.9	-21.2	-35.2	-32.1
	Axle	-7.39	-11.3	-8.73	-13.3
Set 4	Wheel	-27.0	-26.8	-44.4	-38.3
	Axle	-5.76	-25.5	-3.31	-11.0
Set 6	Wheel	-23.6	-19.8	-38.8	-35.0
	Axle	-4.06	-11.7	-5.89	-12.8
Set 8	Wheel	-34.2	-20.3	-63.4	-43.8
	Axle	-5.53	-24.5	-4.0	-11.3

Figure 6.25 shows the VDD of Set 1, Set 4, Set 6, Set 8 and LE 35 MPa. By comparing Set 1 and Set 8 it can be seen how increasing K_0 and OCR reduces the vertical displacement. The vertical displacement of these two sets converge from a depth of 200 mm. The VDD of Set 4 and Set 8 were more similar to that of Set 6 and Set 8. This shows that K_0, and as a result the initial stress condition and material stiffness distribution, have a dominant effect on the pavement response.

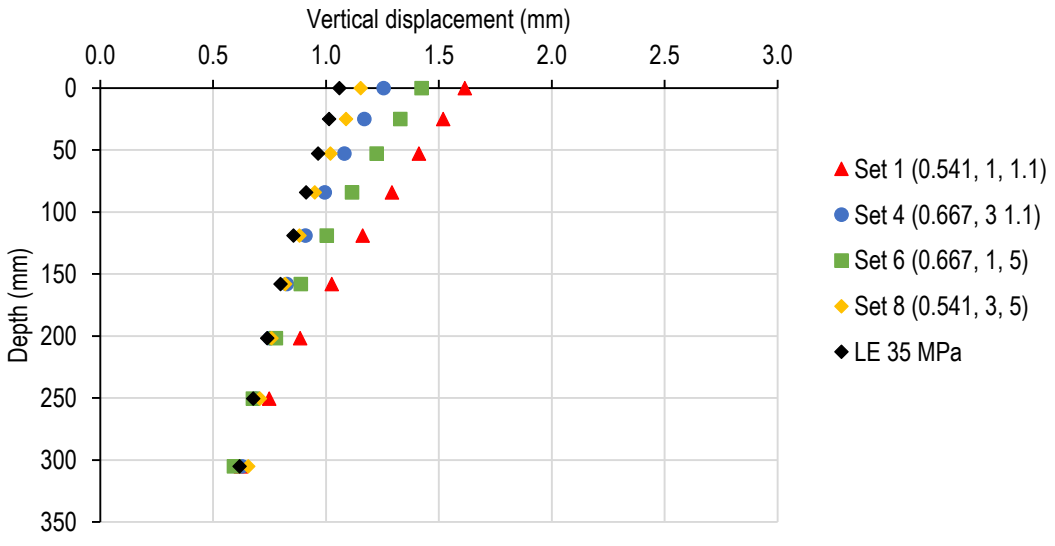

Figure 6.25 Vertical displacement distribution of Set 1, Set 4, Set 6, Set 8 and LE 35 MPa

Figure 6.26 (a) shows the vertical distribution of total and permanent volumetric strain when the pavement is loaded and Figure 6.26 (b) shows the vertical distribution of the ratio of the

permanent volumetric strain over total volumetric strain. The volumetric strain of Set 8 was the smallest. The ratio of the permanent volumetric strain over total volumetric strain remained relatively constant with depth, while the ratio for Set 8 varied. The maximum ratio was toward the bottom of the base, indicating the most permanent strain occurred at the bottom of the base for Set 8.

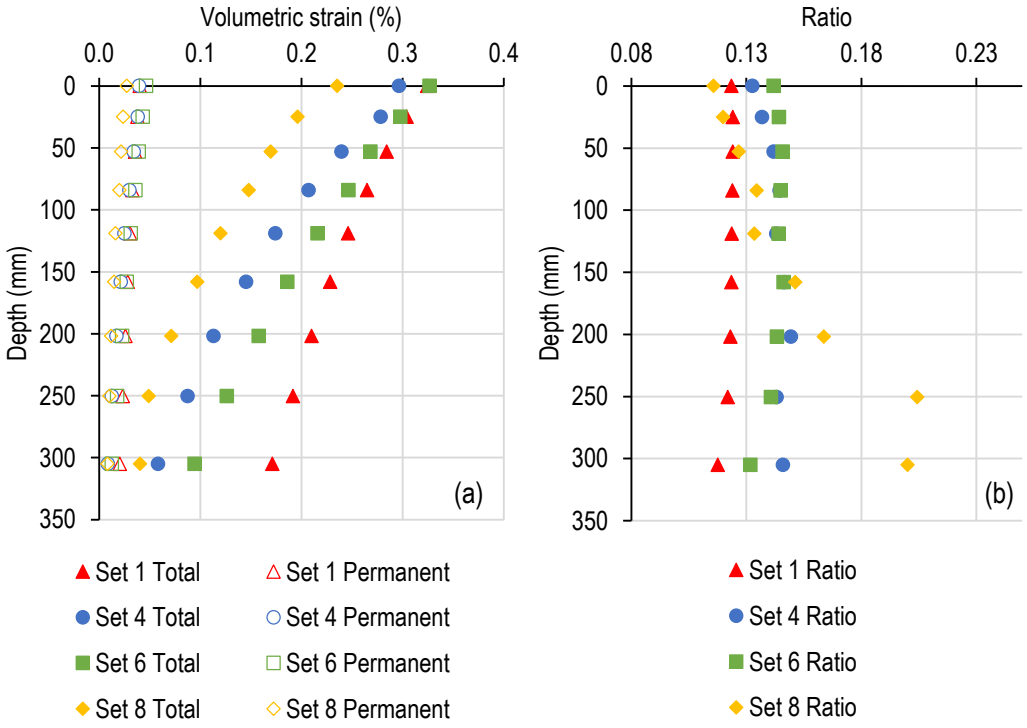

Figure 6.26 Vertical distribution of (a) total and permanent volumetric strain and (b) ratio of permanent and volumetric strain

6.5 SUMMARY

Nor-Sand is a material model developed for sand in the critical state framework. It requires three material input parameters to model elasticity, three material input parameters to model plasticity and three material input parameters to model critical state behaviour. The Nor-Sand model, that was developed to be used in conjunction with FE analyses, requires initial stress conditions to be defined. The initial stress conditions are dependent on the material density, model depth and the coefficient of lateral earth pressure at-rest (K_0). The Nor-Sand model also requires an initial void ratio and OCR to be assigned. The initial void ratio, OCR and K_0 are defined as the FE model input parameters.

Using Nor-Sand in the pavement context was explored by using material input parameters obtained from literature (Cheong, 2006) and varying the FE model input parameters. The depth and element type of the axle load FE model used in Chapter 3 and 4 were altered to ensure

convergence in the Geostatic Step. The depth was reduced from 21.336 m to 4.038 m and quadratic tetrahedron elements were used. The critical parameters were not affected significantly, except for the deflection which was reduced. The deflection bowl shape of the full and reduced depth models was approximately the same. The reduced model deflected upward from 2.25 m from the wheel centreline, indicating that UTCRCP constructed on shallow horizontal rock faces may deflect upward.

The initial void ratio was varied between dense, medium and loose sand, while keeping the OCR and K_0 constant at 1.1 and 1, respectively. As the void ratio increased and the density decreased, the deflection and horizontal stress at the bottom of the concrete layer increased, while the vertical stress and strain at the top of the subgrade in the wheel centreline decreased. This was as a result of the compounded effect of the steeper stress-strain curve of denser sand and stress-dependent material stiffness, which concentrated the load induced stress close to the load location. The contours of the material stiffness indicated that the base layer was compressed between two layers that were more stiff than itself. The VDDs showed that the decrease in vertical displacement with depth reduced as the void ratio decreased.

The coefficient of lateral earth pressure at-rest was varied while using an initial void ratio for medium sand and an OCR of 1.1. Surface deflection and horizontal tensile stress at the bottom of the concrete layer were reduced as K_0 increased. The vertical compressive stress and strain at the top of the subgrade in the wheel centreline increased as K_0 increased. Changing K_0 from 1 to 3 resulted in a widening of the high material stiffness zone in the base. Increasing K_0 further to 12, resulted in the highest material stiffness being situated at the bottom of the base, even at full load application. The magnitude of deflection of Set 4 (with a K_0 of 3) and Set 5 (with a K_0 of 12) was in the same range. This was surprising considering the difference in material stiffness distribution in the base.

The OCR was varied while using an initial void ratio for medium sand and a coefficient of lateral earth pressure at-rest of 1. A similar trend for the critical parameters was observed as for when the initial void ratio was varied. The deflection and horizontal tensile stress at the bottom of the concrete layer decreased as the OCR increased. The vertical compressive stress and strain at the top of the subgrade increased as the OCR increased. As the OCR increased the material stiffness close to the load location concentrated the induced stress close to the wheel centreline and surface. When the void ratio or the OCR were varied, a negative relationship existed between the surface deflection and vertical compressive stress at the top of the subgrade. A positive relationship existed between these two critical parameters, where the compressive stress in the subgrade increased as the deflection increased for LE multivariable analyses in Chapter 4.

The deflected shape of all the combinations of FE model input parameters had a trough at the load location and hogging deflection in the axle centreline. The material stiffness of the substructure would have to be reduced significantly for the relative stiffness between the concrete layer and the substructure to be high enough to cause single curvature of the concrete layer.

The following questions identified during the literature review could be partially addressed from the summary in Chapter 6:

- Is it useful to incorporate stress-dependent, elasto-plastic soil material models to numerically model the substructure of pavements that use thin concrete overlays?

  Yes, Nor-Sand made is possible to investigate the effect of initial conditions (void ratio, stress state and OCR) on the response of UTCRCP. The effect of including sand between two more stiff pavement components (concrete and subgrade) could also be modelled more accurately and influence of stress dependence and stress-strain behaviour on the critical parameters could be captured. However, it is unlikely that UTCRCP will be built on sand and it is proposed that other advanced soil models, that are representative of granular materials, are incorporated to model the response of UTCRCP.

- Is it useful to incorporate cement stabilized bases in UTCRCP to improve load spreading?

  The use of cement stabilized bases was not investigated in this chapter, but the potential use of the concept of inverse pavements was investigated by inadvertently modelling a sand layer between two more stiff layers. Using a less stiff layer between a thin concrete layer and cement stabilized layer would result in lower stresses in the cemented layer during the first cycle due to stress redistribution. The effect of further cyclic loading of this type of inverted pavement should be investigated.

- Is it necessary to include significant amounts of steel reinforcement in the longitudinal and transverse direction?

  Yes, considering the high tensile stresses that were induced in the concrete layer placed on compacted sand, it is essential to include significant amounts of steel in both directions.

- Should numerical and physical modelling of UTCRCP use axle loading instead of a single wheel and are important aspects of the pavement response ignored if axle loading is not used?

Yes, the symmetry of the deflected shape of the FE models being in the axle centreline indicates that it is still more representative to use axle loading. The wheel load interaction does seem to have reduced if the ratio of the vertical deflection in the axle centreline over the wheel centreline is considered to be a measure.

The incorporation of Nor-Sand in the pavement applications could assist in improving our understanding of the response of UTCRCP to loading. Assigning Nor-Sand to the base layer, between a concrete layer and the subgrade, resulted in a layer with varying material stiffness which was relatively low in comparison to that of the adjacent layers. This resulted in the base layer being squashed between the bound layer and subgrade. Typically, the material stiffness and strength of pavement layers reduce with depth. The compounding effect of stress-strain behaviour and stress-dependent material stiffness concentrated the stress close to the load location and surface. Low material stiffnesses were induced for bases with low densities or OCRs, resulting in improved stress distribution through the base and reduced stress and strain in the subgrade. These trends would not have been observed without an advanced material model.

7 RESPONSE OF ULTRA-THIN HS-SFRC LAYERS ON SAND TO TRAFFIC LOADING

7.1 INTRODUCTION

The usefulness of advanced material models based on the critical state concept framework in road pavements was demonstrated in Chapter 6. In this chapter, the pavement responses modelled using Nor-Sand and 3D FE modelling are calibrated and compared to experimental data.

The response of the two-layer rolling wheel load model is used. The details of the 3D FE model are given and the determination of the material input parameters of Silica Sand 2 discussed. The material input parameters of Silica Sand 2 were compared to Erksak Sand. The response of the physical and FE models was compared by making use of the VDDs. The effect of the two sand material input parameters was considered. The model input parameters were varied to calibrate the FE model against the physical model. The effect of the combination of permanent deformation and loss of contact between the concrete bound layer and substructure was considered.

7.2 FE MODEL CONFIGURATION

The general-use FE analyses program ABAQUS/Standard (Dassault Systemes Simulia Corp, 2016) was used. The FE model was based on the rolling wheel load centrifuge model. Nor-Sand was used to model the sand substructure. Silica Sand 2 was used in the rolling wheel load models and the material input parameters of the sand was determined by fitting a numerically modelled stress-strain curve to a measured stress-strain curve.

7.2.1 FE model of rolling wheel load physical model

The rolling wheel load centrifuge model had a width of 600 mm, a length of 460 mm and a depth of 300 mm. To represent UTCRCP, a model that consisted of a 5 mm thin HS-SFRC layer on compacted sand was subjected to rolling wheels on an axle. The centrelines of the wheels of the axle were 220 mm apart and the contact area was elliptical with a width of 22 mm and length of 33 mm. Although the geometry of the rolling wheel load centrifuge model was used, a rolling wheel load was not applied. The pavement response was measured by making use of mini-extensometers placed directly underneath the concrete layer, at depth 15 mm, 30 mm and 60 mm.

While the scaled physical model was tested in a centrifuge at 10G, a full-scale FE model was used. A 50 mm concrete bound layer on 3 m compacted sand substructure was modelled for the two-layer model. Quarter symmetry was used. Pressure was applied over an area to simulate static loading. Figure 7.1 shows the geometry of the FE model. At full scale the scaled physical model would have had a depth of 3 m. Due to quarter symmetry, half the width (3 m) and half the length (2.3 m) were modelled. The load was applied over half of an elliptical area with a length of 330 mm and width of 220 mm. The load area was placed 1.1 m from the axle centreline and on the axis of symmetry in the longitudinal direction.

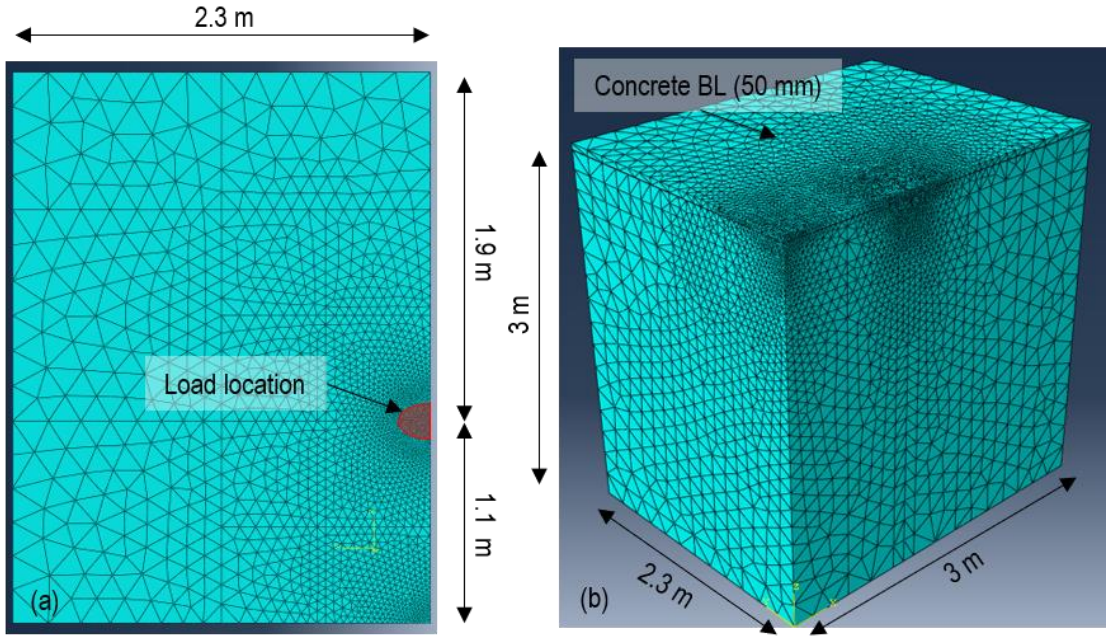

Figure 7.1 FE model of rolling wheel load model in (a) plan view and (b) isometric view

The concrete layer was modelled using linear-elasticity. As in the previous chapters a material stiffness in terms of Young's Modulus of 40 000 MPa and a Poisson's Ratio of 0.17 were selected. Nor-Sand was used to model the sand substructure. The two pavement components, bound layer and substructure, were modelled as two parts allowing an interaction property to be assigned between the concrete bound layer and compacted sand.

Roller support boundary conditions were used for the vertical boundaries for both the concrete bound layer and substructure in the transverse and longitudinal axes of symmetry. Roller support boundary conditions were only applied to the substructure for the other two vertical boundaries. Vertical movement of the bottom of the model was also constrained using roller support boundary conditions. The total load area was 57 020 mm^2 for the ellipse. For a standard axle wheel load of 80 kN, a pressure of 702 kPa had to be applied per wheel. Quadratic

tetrahedron elements (C3D10) were used. The mesh fineness increased closer to the load location and axle centreline.

Tangential and normal behaviour were assigned to the interaction property between the concrete bound layer and substructure. A penalty friction formulation, which consists of a Coulomb friction model, was used for the tangential behaviour. A friction coefficient of 0.5 was assigned. The normal behaviour was modelled using "Hard" contact, allowing separation after contact. "Hard" contact minimizes penetration of the slave nodes into the master surface and does not allow tensile stress transfer across the interface surfaces.

7.2.2 Determination of material input parameters

Nine material input parameters are required for Nor-Sand. These are three parameters that describe the elastic behaviour, three parameters that describe plastic behaviour and three that describe the critical state condition. As mentioned in Section 6.2, the parameters used to model the critical state condition can be determined using standard test procedures. The other parameters are determined though trial-and-error by fitting the numerically calculated stress-strain response to the measured stress-strain response.

Silica Sand 2 was used for the rolling wheel load centrifuge models. The minimum and maximum void ratio as well as the peak angle of friction were determined for Silica Sand 2 as reported in Table 5.4. The remaining material input parameters were determined by fitting a stress-strain curve generated by a numerical model of Nor-Sand in MATLAB (The Mathworks Inc., 2017) to the measured stress-strain curve from the triaxial test done of Silica Sand 2 at a confining pressure of 100 kPa (Section 5.6.3). The sample with a diameter of 50 mm and length of 100 mm was dry compacted and dry tested. The loading rate was 2.286 mm/min and the applied load was measured using a load cell. The strain was measured by mounting two LVDTs on the sample.

The starting void ratio was 0.716 and the density index was 0.804 as determined for the triaxial sample. By manually changing the elastic material input parameters the values of A and n were selected to be 3000 and 0.55. Poisson's Ratio of 0.35 was selected using the same procedure (kry references). The modelled stress-strain curve was most sensitive to the plasticity material input parameters. The parameter values were determined by minimizing the sum of squares of the difference between the measured and modelled stress-strain curve. The values for N, H and χ determined were 0.125, 50 and 2.

A summary of the material input parameters of Erksak Sand and Silica Sand 2 can be seen in Table 7.1. The shear modulus constant and pressure exponent of Erksak Sand and Silica Sand 2

were the same, while the Poisson's Ratio was greater for Silica Sand 2. The plasticity material input parameters of Silica Sand 2 were smaller than for Erksak Sand, while all the critical state conditions parameters of Silica Sand 2 were greater than for Erksak Sand.

Table 7.1 Material input parameters of Erksak Sand and Silica Sand 2

Part description	Parameters	Erksak Sand	Silica Sand 2
Elasticity	Shear modulus constant (A)	3000	3000
	Pressure exponent (n)	0.55	0.55
	Poisson's Ratio (ν)	0.3	0.35
Plasticity	'N' value in flow rule (N)	0.2	0.125
	Hardening parameter (H)	280	50
	Maximum dilatancy coefficient (χ)	5	2
Critical state condition	Critical state ratio (M)	1.2	1.47
	Maximum void ratio (e_{max})	0.807	0.973
	Minimum void ratio (e_{min})	0.527	0.653

The effect of the difference in plasticity and critical state condition parameters can be seen in Figure 7.2, which shows the modelled stress-strain curve for Erksak Sand and the measured and modelled stress-strain curves of Silica Sand 2. The measured Silica Sand 2 stress-strain response showed that peak stress of a sample at a density index of 0.804 and at a confining pressure of 100 kPa was reached at an axial strain of approximately 15%. The stress-strain behaviour of Erksak sand at the same confining pressure and density index reached the peak stress at approximately 2.5% axial strain and had significant strain softening.

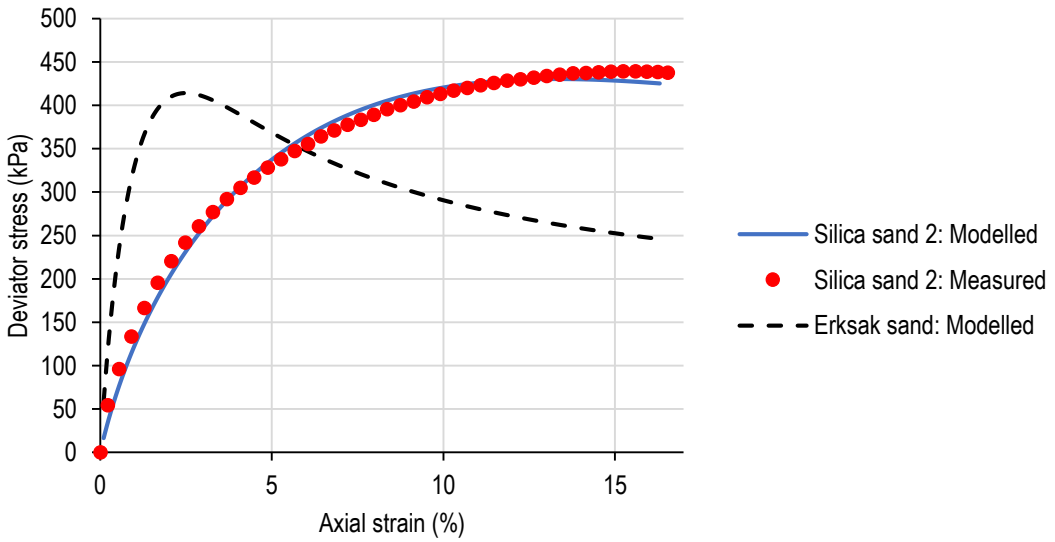

Figure 7.2 Measured and modelled stress-strain response of Silica Sand 2

7.3 COMPARISON OF PHYSICAL MODEL AND 3D FE MODEL

The response modelled using Nor-Sand with the material input parameters of Silica Sand 2 and representative model input parameters should be comparable to what was measured for the centrifuge models. Because the sand was compacted into a rigid strongbox it was anticipated that the coefficient of lateral earth pressure at-rest, K_0, and overconsolidation ratio (OCR) would both be greater than 1. None of the model input parameters were determined during testing. A value of 3 was selected for K_0 and a value of 5 was selected for the OCR.

The effect of two void ratios was considered. The maximum density determined for Silica Sand 2 was 1627 kg/m^3. The density obtained for the compacted sand in the centrifuge model was 1688 kg/m^3. Due to this discrepancy it was opted to use the average density of the Silica Sand 2 triaxial test samples to calculate the initial void ratio. The void ratio was 0.708 and the density index was 0.829 resulting in a dense sand being modelled. It was opted to also model a loose sand by changing the initial void ratio to 0.957 and a density index of 0.05. For comparison, the substructure was also modelled using the material input parameters of Erksak Sand. The same density index of dense Silica Sand 2 was used.

Figure 7.3 shows the VDDs in the wheel and axle centrelines of the FE model with dense and loose Silica Sand 2 and dense Erksak Sand. The figure shows the VDD of the rolling wheel load model adjusted to full scale. The VDDs in Figure 7.3 are to a depth of 600 mm below the concrete layer. The VDDs to the full depth of the FE model (3000 mm) can be seen in Appendix F. Figure 7.3 (a) shows the VDDs of the physical and FE models and Figure 7.3 (b)

shows the VDDs of only the FE models. The scale of vertical displacement of Figure 7.3 (b) is larger than Figure 7.3 (a).

When scaled to full scale, the vertical displacement measured in the wheel and axle centreline was approximately 4 mm and 3 mm respectively. The vertical displacement modelled numerically was approximately 3 mm smaller than what was measured for the physical model in both centrelines.

The vertical displacement of the physical model reduced gradually over the total depth of 600 mm. In the FE models where the Silica Sand 2 was modelled, the vertical displacement reduced rapidly down to a depth of 100 mm, where after the rate of decrease in vertical displacement became less rapid. In the FE model where dense Erksak Sand was modelled, the reduction in vertical displacement was gradual and did not have a distinct slope change.

The maximum vertical displacement modelled numerically in the wheel centreline was up to 1 mm and thus significantly greater than what was modelled in Chapter 3 and Chapter 4 using linear elastic material models. The vertical displacement that was modelled using Erksak Sand for the full depth of the substructure was smaller than what was modelled for when only the base was modelled with Nor-Sand in Section 6.3.5. Of the model input parameters, the void ratio of the base-only model was slightly smaller. The smaller vertical displacement can be explained by the smaller depth of the current FE model of the physical model (3 m instead of 3.987 m), the pressure being applied over a greater area and the stress-dependent material stiffness that is calculated for the full depth of the model. The subgrade material stiffness was 41 MPa in Chapter 6, while at the start of the analyses using Nor-Sand, the stiffness ranged from 14.4 MPa underneath the concrete layer to 109 MPa at the bottom of the model.

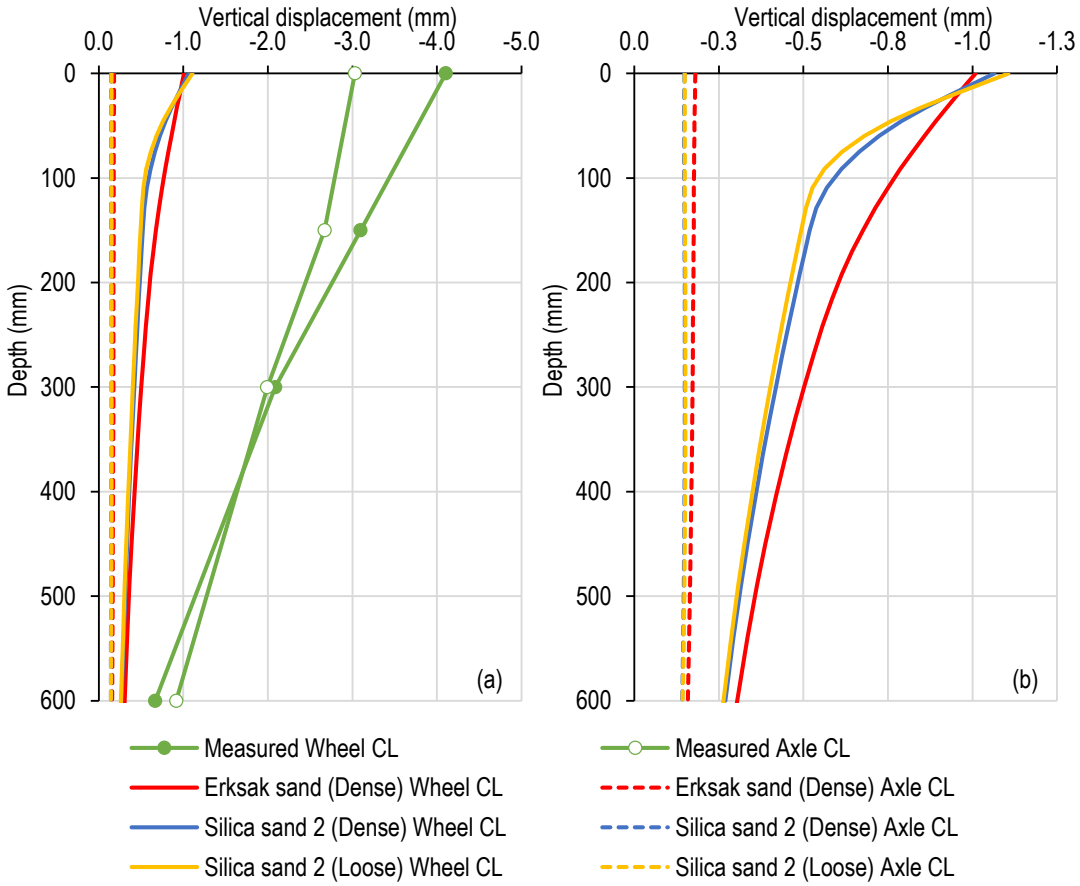

Figure 7.3 Comparison of vertical displacement distributions of (a) physical and FE models and (b) FE models

The larger scale of the vertical displacement axis of Figure 7.3 (b) makes it possible to see the difference between the VDDs of the FE models. For the depth considered, the vertical displacement in the axle centreline did not reduce with depth. The VDDs of the full depth in Appendix F shows that the vertical displacement varied little between the top of the substructure and approximately 500 mm, where after it reduced toward the substructure bottom. The vertical displacement of the Silica Sand 2 FE models reduced slightly to the top of the substructure. The vertical displacement of the Erksak sand FE model increased slightly to the top of the substructure.

The change in slope of the wheel centreline VDDs of the FE models that used Silica Sand 2 is clearer in Figure 7.3 (b). The vertical displacement modelled with loose sand was greater than that modelled with dense sand close to the top of the subgrade. At a depth of approximately 40 mm the vertical displacement modelled with the loose sand is less than that modelled with the dense sand. This was also seen in Figure 6.12, where the void ratio of the base layer was varied. The difference between the loose and dense sand was not large for Silica Sand 2. The difference was greater for Erksak Sand (where the initial void ratio was varied in Chapter 6),

even though Nor-Sand was only used in the base layer. The difference in the effect of the initial void ratio is related to the difference in the stress-strain behaviour of Erksak Sand and Silica Sand 2.

A range of factors could have caused the difference between vertical displacement distribution of the physical and numerical models. In terms of the physical modelling, some settlement of the model would have occurred during initial loading, due to the fact that the concrete layer was precast and placed on the compacted sand during construction. Additionally, the lateral earth pressure at-rest and the OCR were not determined for the physical model. The measured results were adjusted while also varying the model input parameters to get a better fit with the experimental data as described below.

7.3.1 Variation of model input parameters

High values for OCR and coefficient of lateral earth pressure at-rest reduces the vertical displacement of road pavements, because the OCR controls the permanent deformation and K_0 influences the stress-dependent material stiffness. Two FE analyses were run to systematically find suitable model input parameters. In the first analyses, the OCR was reduced from 5 to 3, while the coefficient of lateral earth pressure at-rest remained constant at 3. In the second analyses, the coefficient of lateral earth pressure at-rest was reduced further to 1, while the OCR remained at 3. Attempting to reduce the OCR further resulted in FE analyses that would not converge during the load step. A void ratio of 0.707 for dense sand was used.

Figure 7.4 shows the effect of decreasing the model input parameters on the VDDs in the wheel and axle centreline. Reducing only the OCR from 5 to 3 resulted in the vertical displacement increasing to a depth of approximately 150 mm. The depth at which the slope of the VDD changed also moved downward. The vertical displacement in the axle centreline was affected marginally. Keeping the OCR at 3 and reducing K_0 to 1 increased the vertical displacement further. The slope change depth moved downward even further to a depth of approximately 350 mm. The difference between the first and second analyses is due to the reduction in stress-dependent material stiffness, as well as the interaction between permanent deformation and stress-dependent material stiffness.

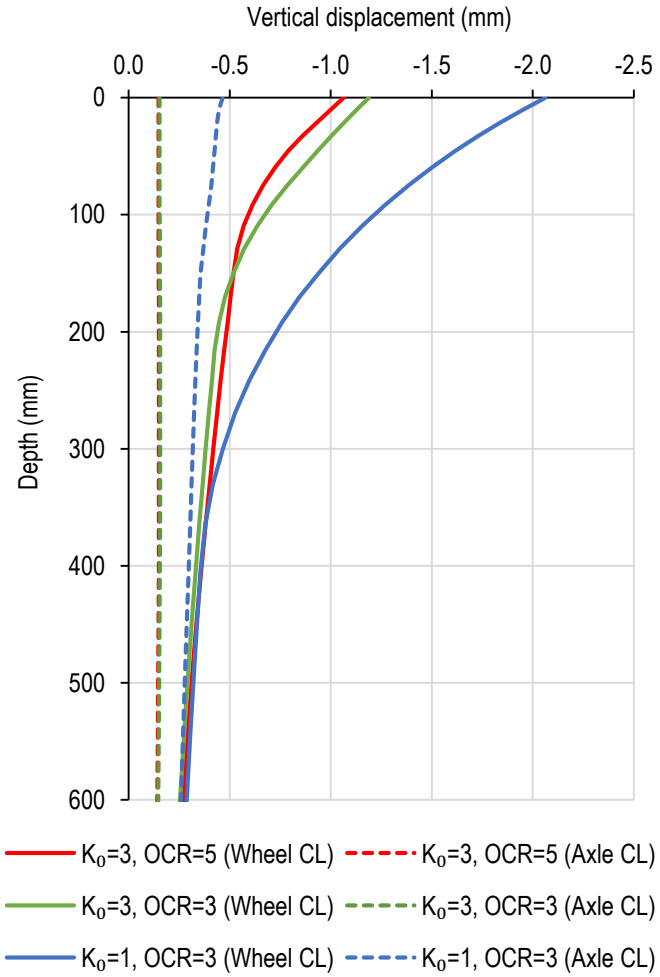

Figure 7.4 Effect of model input parameters on vertical displacement distributions

The VDDs of the FE models to the full depth can be seen in Appendix F, where the effect of reducing the model input parameters on the vertical displacement in the axle centreline can be seen more clearly. The vertical displacement of the FE model using K_0=1 and OCR=3 decreased when the full model depth was considered.

In Figure 7.5 (a) the vertical displacement obtained when using a coefficient of lateral earth pressure at-rest of 1 and an OCR of 3 for dense and loose sand is compared to what was measured during the physical modelling. Once again, the difference between the response of dense and loose sand was not significant, except for the loose sand deflecting more at shallow depths and less than the dense sand from a depth of approximately 50 mm. The vertical displacement at the top of the substructure of the FE model was approximately half of what was measured for the physical model. Once again, the shape of the VDDs were different with the slope of the FE model changing more gradually with depth.

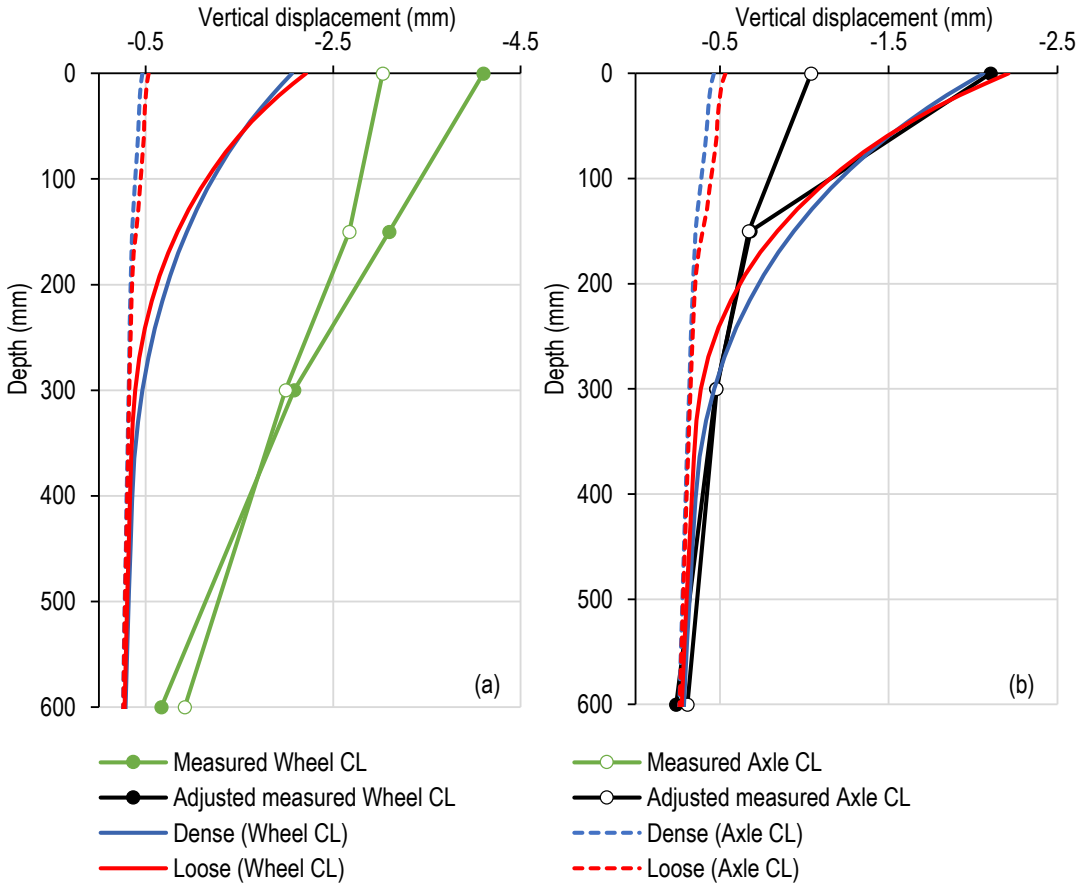

Figure 7.5 Comparison of FE model using K_0=1 and OCR=3 Silica sand 2 to (a) measured vertical displacement and (b) adjusted measured vertical displacement

In Figure 7.5 (b) the vertical displacement of the same FE analysis was compared to the adjusted measured vertical displacement. The adjustment was done by subtracting the permanent vertical displacement after the first load cycle from the measured vertical displacement when the model is fully loaded during the second load cycle. The vertical displacement calculated using K_0=1 and OCR=3 matched the adjusted measured vertical displacement well. The magnitude of displacement was in the same range and the shape of the VDDs were also similar.

7.4 UNLOADING OF FE MODELS

The results from physical modelling suggested that a gap forms between the ultra-thin HS-SFRC layer and the substructure. The concept of a gap forming between the concrete layer and substructure was verified by making use of the 3D FE model of the physical model. An additional analysis step was added to model reduction of pressure exerted by the wheel load to zero. The FE models discussed in Section 7.3.1, where the OCR and coefficient of lateral earth pressure at-rest was varied, were used. Figure 7.6 shows loaded and permanent vertical

displacement in the transverse direction of the FE pavement model. An initial void ratio of 0.707 was used, while one FE model had a K_0 of 3 and OCR of 3 and one FE model had a K_0 of 1 and OCR of 3. This figure is similar to the deflection bowls discussed throughout this project except that it also gives the vertical displacement after the pavement has been unloaded.

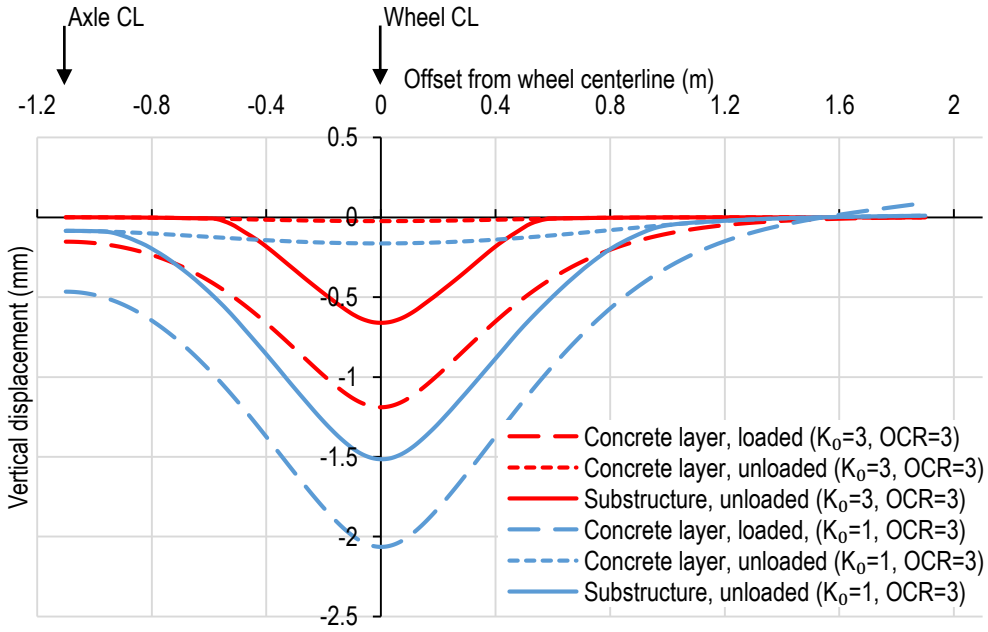

Figure 7.6 Transverse vertical displacement

The deflection bowls of the two models show that the model with a K_0 of 1 deflected more when loaded. The unloaded vertical displacement shows that the substructure of both models deformed permanently. The difference between the loaded and unloaded vertical displacement of the substructure was approximately 0.6 mm for the model with a K_0 of 3, while the difference was approximately 1.2 mm for the model with a K_0 of 1 The concrete layer of both models spans over the gap that formed due to the permanent displacement, verifying the observation from the physical modelling. Because the OCR remained constant between the two models, the width and depth of the gap is likely dependent on the relative stiffness of the concrete layer and substructure.

The gap that formed between the concrete layer and compacted dry sand would be more pronounced than what would form between a concrete layer and well-constructed granular layers. Nonetheless, the repetitive nature of traffic loading could result in a similar gap forming between the concrete layer and substructure, which could change the manner in which load is distributed with pavement depth.

7.5 SUMMARY

The material input parameters of Silica Sand 2 for Nor-Sand were determined from standard soil tests and fitting a calculated stress-strain curve to a measured stress-strain curve. The stress-strain response that was measured for Silica Sand 2 reached the maximum stress at an axial strain of 15%, which was a large strain in comparison to Erksak Sand.

A FE model of the rolling wheel load physical model was compiled. Nor-Sand was used to model the substructure response. Loose and dense sand were modelled. An OCR of 5 and a coefficient of lateral earth pressure at rest of 3 were assumed. The vertical displacement of the FE model was significantly smaller than what was measured for the physical models and it was opted to vary the model input parameters to get a better fit.

Reducing the model input parameters increased the vertical displacement, but the magnitude was still significantly smaller than what was measured. It was opted to adjust the measured vertical displacement by subtracting the permanent vertical displacement after the first bi-directional cycle from the loaded response during the second bi-directional cycle. This resulted in the measured vertical displacement having the same magnitude and shape as the numerically determined vertical displacement.

A variety of factors could have influenced the initial discrepancy between the numerical and physical pavement response. The adjusted vertical displacement matched, but besides settlement of the physical models it is anticipated that one of the factor that should be addressed is the method of embedding the mini-extensometers during the construction of the scaled physical models. Additionally, it is suggested that the elastic properties of the sand be measured using bender elements and that the coefficient of lateral earth pressure at-rest is determined. This can be done using an experimental setup similar to Chen & Fang (2008) where soil pressure transducers were attached to the model wall.

During the physical modelling it was observed that a gap forms between the concrete layer and substructure. It was attempted to verify the formation of a gap by including an unloading step to the FE analysis. The Nor-Sand material model used in this research was not formulated to allow cyclic loading by making use of a bounding surface, although such models do exist. Nonetheless, the FE pavement model of the scaled physical model could be unloaded for the material input parameters of Silica Sand 2 and selected model input parameters. The model input parameter combinations that allowed the models to be unloaded were dense sand and a K_0 of 3 and OCR of 3 and dense sand and a K_0 of 1 and OCR of 3.

After one load cycle a clear gap formed between the concrete layer and substructure. The width and depth of the gap was dependent on the model input parameters, with the model using a K_0

value of 1 having a deeper and wider gap. In the unloaded state the concrete spans over the gap and upon reloading, the load transfer to the substructure will initially be carried on the sides of the original wheelpath.

The following questions identified during the literature review could be partially addressed from the summary in Chapter 7:

- Should numerical and physical modelling of UTCRCP use axle loading instead of a single wheel and are important aspects of the pavement response ignored if axle loading is not used?

  For the FE model where the entire substructure was modelled using Nor-Sand, the transverse deflection bowls showed that the wheel load interaction was reduced further than when the Nor-Sand was used to model the base. The transverse deflection bowl was almost symmetrical around the wheel centreline.

- Should UTCRCP be modelled as a flexible pavement where the substructure properties are important, and rutting is a traffic associated failure mechanism?

  Yes, as for all the other numerical and physical models of representing UTCRCP, a trough formed around the load location indicating that a rut would form in the load path when the pavement is subjected to traffic loading. As for the physical model it was observed that a gap form between the bottom of the concrete layer and top of the substructure when the pavement is unloaded, indicating that the rut may not be observed from the surface of the pavements.

- Is it useful to incorporate stress-dependent, elasto-plastic soil material models to numerically model the substructure of pavements that use thin concrete overlays?

  Yes, the vertical displacement distribution measured and modelled numerically using Nor-Sand was similar and the material model can be used to further explore the response of concrete layers on sand to loading. However, for practical applications a model more representative of granular materials needs to be incorporated in the FE modelling of UTCRCP.

8 CONCLUSIONS AND RECOMMENDATIONS

8.1 CONCLUSIONS

The aim of this study was to investigate the response of UTCRCP to traffic loading by considering load configuration, relative stiffness and the stress dependent, elasto-plastic behaviour of granular materials.

8.1.1 Findings from literature reviewed

Findings on various past research studies on UTCRCP were reviewed. These reviews indicated that:

- The design methodology of UTCRCP in South Africa was extrapolated from conventional concrete pavement design methodology, not considering rutting as a failure mechanism.
- In terms of APT of UTCRCP in South Africa only one side of an axle is considered, using a dual-wheel. UTCRCP performed well under traffic loading regardless of support conditions, but tended to deflect significantly depending on support conditions.
- In terms of steel mesh spacing it was found that there is little benefit in using rectangular mesh apertures in concrete slabs, because the direction of least steel content determines the load absorption ability.
- In terms of including cement stabilized granular material to improve load spreading and reduce deflection, it is anticipated that its use may result in a type of reflection cracking where the layer underneath the cemented layer is subjected to stress concentrations and accelerated deterioration, while the HS-SFRC layer above the cemented layer is not notably affected.

8.1.2 Investigating the effect of load configuration and relative stiffness on pavement response using LE numerical modelling

The following conclusions could be made concerning the effect of load configuration and relative stiffness on pavements using LE FE modelling:

- When a three-layer pavement system, incorporating a thin bound layer, is loaded using an axle:
    - A greater proportion of the load induced stress is absorbed by a concrete bound layer than an asphalt bound layer.

    - The deflection bowl of a pavement using a concrete bound layer is greater than that using an asphalt bound layer, resulting in more notable interaction of wheels at opposite ends of an axle.
    - The high horizontal stresses induced in the thin HS-SFRC layer highlight the importance of reinforcing the layer in the transverse and longitudinal directions.
- When a three-layer pavement system, incorporating a thin concrete bound layer, is subjected to plane strain loading:
    - The percentage difference between the vertical deflection critical parameter of the plane strain and 3D models exceeded 1000%, while the difference between the stress and strain critical parameters were all less than 450%.
    - The normalized transverse deflection bowls differ significantly. The difference between the deflection in the axle and wheel/strip centreline is smaller for the plane strain model, due to the larger zone of influence of strip loads.
- A positive correlation exists between the radius of relative stiffness and inflection point of transverse deflection bowls. Changing the load configuration from single wheel to axle loading moved the inflection point further from the wheel centreline.
- When a beam-on-elastic support model was used to investigate wheel interaction for different relative stiffnesses:
    - Three types of deflection bowl overlapping were identified; no overlap, partial overlap (subdivided into large and small partial overlap) and complete overlap.
    - The reciprocal of β, which is the equivalent of the radius of relative stiffness for 3D analyses of pavements, can be used to predict the extent of overlap.
- For all load configurations the wheel interaction was dependent on the relative stiffness of the pavement

The following conclusions were made concerning the effect of relative stiffness on concrete pavements using LE FE models:

- When varying the concrete bound layer thickness and base material stiffness simultaneously:
    - Concrete layer thickness had a dominant effect on pavement response in terms of critical parameters, while the effect of base material stiffness became more significant for concrete layer thicknesses smaller than 100 mm.
- When varying the base material stiffness over a wide range to simulate cement stabilized bases:

  - Although increasing the base material stiffness reduced all the critical parameters and resulted in acceptable ranges of stress level in the base layer, it is anticipated that discrete crack formation in bases using C1 or C2 materials will cause stress concentrations in adjacent layers. This may result in accelerated deterioration of the layer.
  - As the base material stiffness increased, the transverse deflection bowl became similar to that of pavements with concrete bound layers with thicknesses greater than 188 mm.
- When considering the radius of relative stiffness and offset of inflection point from the wheel centreline:
  - A positive relationship exists between the offset of inflection point from the wheel centreline and radius of relative stiffness, where the offset of inflection point from the wheel centreline is always smaller.
  - The offset of the inflection point from the wheel centreline was small, even though visual inspection indicated that the transverse deflection bowl was similar to that of pavements using thick concrete bound layers. This indicated that there is interaction between the concrete bound layer and cemented base.

8.1.3 Investigating the effect of load configuration and relative stiffness using centrifuge modelling

The following conclusions were made regarding the effect of load configuration and relative stiffness using centrifuge modelling:

- The strip loading models showed that:
  - The thick concrete model had little differential vertical displacement and punched into the substructure. The maximum deflection in the axle centreline.
  - The maximum deflection of the thin concrete model was in the strip centreline with a peak in the axle centreline.
  - Although the deflection bowls of the physical and FE models of the thin concrete pavement model were similar, in that there was a trough at the strip centreline and a peak in the axle centreline, the deflection in the axle centreline of the FE model was greater. The axle centreline deflection of the physical model was very small, almost forming a symmetrical bowl around the strip centreline. The difference is explained by boundary effects, with the physical model of strip loading being shallow, and the elasto-plastic behaviour of sand, with the FE model using linear-elasticity.

  - For the substructure of the thin concrete model the difference between permanent vertical displacement in the strip centreline and the axle centreline increased as more load cycles were applied. The permanent displacement of the concrete layer was less than that of the substructure, indicating that the concrete detached from the supporting layers, forming a gap.
  - Strip loading can be used to develop a conceptual and comparative understanding of pavements.
- The rolling wheel load models showed that:
  - The full-scale deflection of the scaled physical model for the first load cycle was greater than what was modelled for the 50 mm thick concrete FE model subjected to axle load configuration. This could be because linear elasticity was assumed for the substructure and relatively high material stiffnesses were assumed for the base. Additionally, the substructure of the physical model was subjected to principal stress rotation and the elasto-plastic behaviour of sand was not modelled.
  - The ratio of the deflection in axle centreline to wheel centreline for the thin concrete model was large. This indicates that the radius of relative stiffness between the concrete layer and substructure was large and that there was overlap, at shallower depths of the stress zones induced by the wheels at opposite ends of the axle.
  - The longitudinal deflection bowls of the thin concrete layer with cemented base model were shallower and narrower than the thin concrete layer models. This was not the same as what was observed for the LE FE modelling, where interlayer interaction was not modelled. The observation of the physical model indicates that there is interaction between the concrete layer and base, and that the two pavement layers did not deflect as one into the underlying sand (as was seen for the LE FE modelling).
  - The VVD of the permanent displacement of the thin concrete model indicated that a gap formed between the concrete layer and the sand substructure.
  - The VDDs in the axle centreline of the thin concrete layer model reduced less with depth than in the wheel centreline. This is due to the stress influence zones of the two wheels overlapping.
  - The difference between the wheel and axle centreline deflection increased as more wheel passes were applied.
  - The cemented base deteriorated notably even after the first wheel pass was applied and continued to do so as more wheel passes were applied. As for the thin concrete model, the concrete layer detached from the substructure.

- The trend of a gap forming between the thin concrete layer and substructure was observed for both the strip loading and rolling wheel load models.
- The trend of increasing difference between the deflection in the wheel and axle centreline for the thin concrete model was observed for both load configuration types.

8.1.4 Investigating the effect of incorporating stress-dependent, elasto-plastic constitutive material modelling on pavement response

The following conclusions could be made regarding the incorporation of Nor-Sand in the base of a three-layer pavement model and varying the model input parameters:

- When increasing the void ratio (reducing the density):
    - The material stiffness, in terms of Young's modulus, of the sand layer was smaller than that of the material stiffness of the layers adjacent to the base. This resulted in a base that was compressed between two relatively stiff layers.
    - Deflection and tensile stress in the wheel centreline increased and the vertical compressive stress and strain in the subgrade decreased. This indicated a type of load redistribution due to the material stiffness increasing less close to the load location and the radius of relative stiffness between the concrete layer and substructure being larger because the material stiffness of the base increasing less.
- When increasing the coefficient of lateral earth pressure at-rest:
    - A wider zone of high material stiffness formed and critical parameters (deflection, horizontal tensile stress in bound layer, compressive stress and strain at the top of subgrade all in the wheel centreline) decreased.
    - Neither the deflection of the pavement model, nor the vertical displacement in the wheel centreline were significantly affected (for the range from 3 to 12).
- When increasing the OCR:
    - An inverse relationship between the surface deflection and vertical compressive stress in the subgrade existed, with the stress decreasing as the OCR was decreased.
    - The deflection of the FE models decreased non-linearly as the OCR was increased.
    - Permanent strain was still induced in the base at an OCR of 20, which was concentrated to the top and bottom of the base in the wheel centreline.

- In pavement design, the stiffness of material in the pavement layers reduces with depth. By incorporating Nor-Sand, a less stiff material was introduced between two relatively stiff materials and the true effect of doing so could be explored.
- Incorporating Nor-Sand allowed the effect of geotechnical concepts such as stress-dependent material stiffness, void ratio, coefficient of lateral earth pressure at-rest and overconsolidation and the interaction between all these concepts to be explored for pavement engineering.

The following conclusions could be made when incorporating Nor-Sand to model the response of the rolling wheel load model of a thin concrete layer on a compacted sand substructure:

- The measured vertical displacement distributions and the numerically modelled vertical displacement distributions could be matched when the initial settlement of the centrifuge models was taken into account.
- The gap observed in the physical modelling could be modelled using Nor-Sand, verifying that the concrete layer detaches when the pavement is unloaded and that the load distribution upon reloading may be altered. The width and depth of the gap was dependent on the model input parameters.

8.2 RECOMMENDATIONS

8.2.1 Practice and design for UTCRCP

The following aspects related to the design and practical application of UTCRCP could be addressed:

It is essential that the concrete layer of UTCRCP include significant steel reinforcement in the longitudinal and transverse directions. In comparison to conventional concrete pavements, where the inclusion of steel reinforcement does not have a structural purpose, but is used to control thermal crack widths, the steel mesh in UTCRCP is included for structural purposes. When the concrete layer is subjected to traffic loading high tensile stresses will be induced at the bottom of the concrete layer underneath wheel loads and relatively high stresses will be induced between wheel loads (in the axle centreline and in between axles), where these stresses will span in both the transverse and longitudinal directions of the pavements.

The incorporation of cement stabilized bases would reduce all the critical parameters and the stress levels in the base would fall within acceptable ranges according to the LE FE modelling that was done. The centrifuge modelling showed how the relatively weak cemented bases

deteriorated underneath thin concrete layers. Before a conclusion can be made regarding the use of cement stabilized materials underneath thin HS-SFRC layers, the possibility and detrimental effect of discrete crack formation in the cemented base should be taken into consideration.

The physical and numerical models of ultra-thin concrete layers on sand showed that a gap formed where the concrete layer detached from the supporting layers when the pavement was in an unloaded state. This was already seen after the first load cycle. This will likely happen for UTCRCP subjected to real traffic loading and would result in rutting of the substructure going unnoticed. Although the thin HS-SFRC layer might endure the high stresses and deflections when it is unsupported in the wheel path, the riding quality would be affected.

8.2.2 Future research

From the research conducted the following recommendations for future research are made:

- The effect of interlayer interaction should be investigated in the context of soil-structure interaction and relative stiffness of pavements.
- Strip loading could be used to develop a conceptual and comparative understanding of the response of pavements. The effect of reducing the pressure exerted to attempt to match the deflection bowls expected for wheel loads should be investigated.
- The 2D deflection bowls determined from the beam-on-elastic support equations should be compared to 3D slabs-on-grade, considering degrees of overlap and wheel interaction.
- The response of UTCRCP using APT with an axle instead of a dual-wheel should be investigated.
- From the multivariable analyses it is suggested that the transition from single curvature to multiple curvature is determined by only considering concrete layer thicknesses smaller than 188 mm.
- Although the development and use of the mini-extensometers in the centrifuge modelling was moderately successful, ways to improve the measurement technique need to be investigated.
- A glass window was included in the rolling wheel load model to measure and observe the pavement response using DIC. This was unsuccessful due to timing difficulties, camera speeds and the movement of the axle wheels from the pavement model onto the side of the model box. Ways to improve the model setup to successfully use DIC needs to be investigated.

- Ways to determine the coefficient of lateral earth pressure at-rest in centrifuge modelling should be investigated and the coefficient of lateral earth pressure at-rest needs to be determined.
- The effect of gap formation on the response of UTCRCP should be investigated.
- A version of Nor-Sand that allows cyclic loading to be modelled should be used to model the response of pavements and investigate the effect of gap formations.
- Contact stress distribution between thin concrete layer and its supporting layers should be investigated using advanced material models.

9 REFERENCES

Aiban, S.A. & Znidarcic, D. 1995. Centrifugal modelling of bearing capacity of shallow foundations on sands. *Journal of Geotechical Engineering.* 121(10), pp. 704-712.

ARA Inc. ERES Consultants Division. 2004. *Guide for Mechanistic-Empirical Design of New and Rehabilitated Pavement Structures, NCHRP 1-37A Final Report*. Washington D.C.

Archer, A. 2014. *Using small-strain stiffness to predict the settlement of shallow foundations on sand.* Masters dissertation. University of Pretoria.

ASTM Committee D18. ASTM Standard D4254-16-2006: *Standard Test Methods for Minimum Index Density and Unit Weight of Soils and Calculation of Relative Density.*

ASTM Committee D18. ASTM Standard D4253-16-2011: *Standard Test Methods for Maximum Index Density and Unit Weight of Soils Using a Vibratory Table*.

ASTM Committee D04. ASTM Standard D1195-93-1997: *Standard Test Method for Repetitive Static Plate Load Tests of Soils and Flexible Pavement Components, for Use in Evaluation and Design of Airport and Highway Pavements.*

Atkinson, J.H. & Bransby, P.L. 1978. *The Mechanics of Soils. An Introduction to Critical State Soil Mechanics.* Maidenhead, England: McGraw-Hill.

Barros, J.A.O. & Figueiras, J.A. 1998. Experimental behavior of fiber concrete slabs on soil. *Mechanics of Cohesive-Frictional Materials.* 290(January 1996), pp. 277-290.

Barros, J.A.O. & Figueiras, J.A. 1999. Flexural behaviour of SFRC: testing and modeling. *Journal of Materials in Civil Engineering*. 11(November), pp. 331-339.

Barros, J.A.O. & Figueiras, J.A. 2001. Model for the analysis of steel fibre reinforced concrete slabs on grade. *Computers and Structures.* 79(1), pp. 97-106.

Bayton, S.M., Elmrom, T. & Black, J.A. 2018. Centrifuge modelling utility pipe behaviour subject to vehicular loading. In: McNamara *et al* (eds) *Physical Modelling in Geotechnics; Proceedings of the 9th International Conference, 17-20 July 2018*. London, United Kingdom: Taylor & Francis Group. pp. 163-168.

Been, K. & Jefferies, M.G. 1985. A state parameter for sands. *Géotechnique*. 35(2), pp. 99-112.

Belletti, B., Cerioni, R., Meda, A. & Plizzari, G. 2008. Design aspects on steel fiber-reinforced concrete pavements. *Journal of Materials in Civil Engieering.* 20(9), pp. 599-607.

Beuth Verlag GmbH. 1974. DIN 4018 Subsoil: *Calculation of Bearing Pressure Distribution under Spread Foundations.*

Bowles, J.E. 1996. *Foundation analysis and design, 5th ed.* New York: McGraww-Hill.

Bowman, A. & Haigh, S.K. 2016. The Cambridge Airfield Pavement Tester. In: *Physical Modelling in Geotechnics; Proceedings of the 3rd European Conference, 1-3 June 2016.* Nantes, France: pp. 105-110.

Briggs, M.A., Valsangkar, A.J. & Thompson, A. 2016. Behaviour of fibre-reinforced concrete beams on grade. *International Journal of Physiscal Modeling in Geotechnics.* 16(4), pp. 152-159.

Broms, B. 1971. Lateral earth pressures due to compaction of cohesionless soils. *Proceeding of the 4th Conferenece on Soil Mechanics, 1971.* Budapest, Hungary: pp. 373-384.

Brown, S.F. 1967. *Stresses and deformations in flexible layered pavement systems subjected to dynamic loads.* PhD Thesis. University of Nottingham.

Brown, S.F. 1996. Soil mechanics in pavement engineering. *Géotechnique*. 46(3), pp. 383-426.

Brown, S.F. 2004. Accelerated pavement testing in highway engineering. *Proceedings of the Institution of Civil Engineers.* 157(3), pp. 173-180.

Brown, S.F. & Selig, E.T. 1991. The design of pavement and rail track foundations. In: O'Reilly, M.P. & Brown, S.F. (eds), *Cyclic Loading of Soils: From Theory to Design, 1st ed.* London, United Kingdom: Blackie. pp. 249-305.

Brown, S.F., Tam, W.S. & Brunton, J.M. 1986. Development of an analytical method for the structural evaluation of pavements. In: *Proceedings of the 2nd International Conference on Bearing Capacity of Road and Airfields.* Plymouth, United Kingdom. pp. 267-276.

Burmister, D.M. 1945a. The general theory of stresses and displacements in layered systems I. *Journal of Applied Physics.* 16(February), pp. 89-95.

Burmister, D.M. 1945b. The general theory of stresses and displacements in layered systems II. *Journal of Applied Physics.* 16(March), pp.126-127.

Burmister, D.M. 1945c. The general theory of stresses and displacements in layered systems III *Journal of Applied Physics.* 16(May), pp. 296-303.

Burmister, D.M. 1958. Evaluation of Pavement Systems of the WASHO Road Test by Layered System Methods. *Bulletin 177 Highway Research Board.* pp. 26-54.

Burmister, D.M. 1962. Application of layered system concepts to interpretations and evaluations of asphalt pavement performance and to design and construction. In: *Proceedings of the International Conference on Structural Design of Asphalt Pavements.* Ann Arbor, MI, USA: University of Michgan. pp. 441-453.

Chan, F.W.K. 1990. *Permanent Deformation of Granular Layers in Pavements.* PhD Thesis. University of Nottingham.

Chen, D.H., Won, M., Chen, X. & Zhou, W. 2016. Design improvements to enhance the performance of thin and ultra-thin concrete overlays in Texas. *Construction and Building Materials.* 116(July), pp.1-14.

Chen, T.-J. & Fang, Y.-S. 2008. Earth Pressure due to Vibratory Compaction. *Journal of Geotechnical and Geoenvironmental Engineering.* 134(4), pp. 437-444.

Cheong, T.P. 2006. *Numerical modelling of soil-pipeline interaction.* PhD Thesis. University of Cambridge.

Cho, Y.-H., McCullough, B.F., & Weissmann, J. 1996. Considerations on Finite-Element Method Application in Pavement. *Transportation Research Record.* 1539(1), pp. 96-101.

Chou, F.J. & Tutumluer, E. 2001. Stress path testing for proper characterization of unbound aggregate base behaviour. *Transportation Reseach Record.* 1757, pp. 692-99.

Clayton, C.R.I. 2011. Stiffness at small strain: research and practice. *Géotechnique*. 61(1), pp. 5-37.

Cornforth, D.H. 1964. Some experiments on the effect of strain condition on the strength of sand. *Géotechnique*. 14(2), pp. 143-167.

Craig, R.F. 2004. *Craig's Soil Mechanics, 7th ed.* London, United Kingdom: Spon Press.

Council for Scientific and Industrial Research 2017. Heavy Vehicle Simulator [Online]. Availble at: https://www.csir.co.za/heavy-vehicle-simulator [Accessed 13 June 2017]

Dasari, G.R. & Soga, K. 2000. *A guide book for soil models and soil-pipe analysis using ABAQUS.* Report submitted to Tokyo Gas Ltd. Tokyo, Japan.

Dassault Systemes Simulia Corp. 2014. *ABAQUS Documentation.* Providence, RI, USA.

Dassault Systemes Simulia Corp. 2016. *ABAQUS.* Johnston, RI, USA.

Dave, T.N. & Dasaka, S.M. 2018. Experimental model study on traffic loading induced earth pressure reduction using EPS geofoam. In: McNamara *et al* (eds) *Physical Modelling in Geotechnics; Proceedings of the 9th International Conference, 17-20 July 2018*. London, United Kingdom: Taylor & Francis Group. pp. 169-174.

De Beer, M. 1990. *Aspects of the design and behaviour of road structures incorporating lightly cementitious layers.* PhD Thesis. University of Pretoria.

De Bruin, P.W. & Jordaan, G.J. 2004. The effect of heavy vehicle compositions on design traffic loading calculations (E80s). In: *Proceedings of the 23th Annual Southern African Transport Conference.* Pretoria, South Africa.

Denneman, E. 2011. *Fracture in High Performance Fibre Reinforced Concrete Pavement Materials*. PhD Thesis. University of Pretoria.

Denneman, E., Kearsley, E.P. & Visser, A.T. 2010. Size-effect in high performance concrete road pavement materials. In: van Zijl & Boshoff (eds) *Advances in Cement-Based Materials*. London, United Kingdom. CRC Press. pp. 53-58.

Department of the Navy. 1982. *Foundations and Earth Strucutres: Design Manual 7.2.* Alexandria, VA, USA.

Department of Transport. 1986. *TRH13: Cementitious Stabilizers in Road Construction*. Pretoria, South Africa.

Department of Transport. 1991. *TRH16: Traffic Loading for Pavements and Rehabilitation Design*. Pretoria, South Africa.

Department of Transport. 1996. *TRH 4: Structural Design of Flexible Pavements for Interurban and Rural Roads*. Pretoria, South Africa.

Domone, P. & Illston, J. 2010. *Construction Materials, 4th ed*, Oxon, United Kingdom: Spon Press.

Dondi, G. 1994. Three-dimensional finite element analysis of a reinforced paved road. *In Proceedings of the 5th International Conference on Geotextiles, Geomembranes and Related Products*. Singapore. pp. 95-100.

Donovan, P., Sarker, P. & Tutumluer, E. 2016. Rutting prediction in airport pavement granular base/subbase: A stress history based approach. *Transportation Geotechnics.* 9(2016), pp. 139-160.

Duncan, J.M. & Seed, R.B. 1987. Compaction-induced earth pressures under K_0-conditions. *Journal of Geotechnical Engineering.* 112(1), pp. 1-22.

Duncan, J.M., Williams, G.W., Sehn, A.L. & Seed, R.B. 1991. Estimation earth pressures due to compaction. *Journal of Geotechnical Engineering*. 117(12), pp. 1833–1847.

Dynatest. 2017. Heavy Vehicle Simulator (HVS) [Online]. Availble at: http://www.dynatest.com/hvs. [Accessed 13 June 2017].

Elsaigh, W.A. 2007. *Modelling the behaviour of steel fibre reinforced concrete pavements.* PhD Thesis. University of Pretoria.

Elsaigh, W.A., Kearsley, E.P. & Robberts, J.M. 2011. Modeling the Behaviour of Steel-Fiber Reinforced Concrete Ground Slabs II: Development of Slab Model. *Journal of Transportation Engineering.* 137(12), pp. 889-896.

Fern, E.J., Robert, D.J. & Kenichi, S. 2016. Modeling the Stress-Dilatancy Relationship of Unsaturated Silica Sand in Triaxial Compression Tests. *Journal of Geotechnical and Geoenvironmental Engineering.* 142(11).

Ferretti, E. & Bignozzi, M.C. 2012. Stress and strain profiles along the cross-section of waste tire rubberized concrete plates for airport pavements. *Computers, Materials and Continua.* 27(3), pp. 231-273.

Gaspar, T.A.V. 2017. *The tensile behaviour of three unsaturated soils subjected to the Brazilian Disc Test.* Masters dissertation. University of Pretoria.

Gerber, J.A.K. 2011. *Charaterization of cracks on Ultra-Thin Continuously Reinforced Concrete Pavements.* Masters dissertation. Stellenbosch University.

Hallak, A. 2012. Soil-Structure Interaction and Foundation Vibrations [Online]. Available at: https://www.slideshare.net/ahmadhallak1973/soil-structure-interaction-amec-presentationfinal?qid=eea2ecf3-23b5-442e-84ed-5791caeed555&v=default&b=&from_search=1. [Accessed 13 July 2019].

Hernández, N., Ossa, A. & Rangel, F.A. 2016. Four decades of circular test track at the Institute of Engineering UNAM contributing to pavement research in Mexico., In: Aguiar-Moya *et al*. (eds) *The Roles of Accelerated Pavement Testing in Pavement Sustainability: Engineering, Environment, and Economics.* Switzerland: Springer International Publishing. pp. 17-34.

Hjelmstad, K.D. & Taciroglu, E. 2000. Analysis and Implementation of Resilient Modulus Models for Granular Solids. *Journal of Enigneering Mechanics.* 126(August), pp. 821-830.

Horak, E. 2008. Benchmarking the structural condition of flexible pavements with deflection bowl parameters. *Journal of the South African Institute of Civil Engineering.* 50(2), pp. 2-9.

Huang, Y.H. 1969. Influence Charts for Two-Layer Elastic Foundations. *Journal of Soil Mechanics and Foundation Division.* 95(March), pp. 709-713.

Huang, Y.H. 1993. *Pavement Analysis and Design. 2nd ed*. New Jersey, USA: Pearson Prentice Hall.

Ioannides, A.M. 2006. Concrete pavement analysis: The first eighty years. *International Journal of Pavement Engineering.* 7(4), pp. 233-249.

Jacobsz, S.W., Kearsley, E.P. & Kock, J.H.L. 2014. The geotechnical centrifuge facility at the University of Pretoria. In: Gaudin & White (eds.) *Physical Modelling in Geotechnics; Proceedings of the 8th International Conference, 14-17 January 2014.* Perth, Australia: Taylor & Francis. pp. 169-174.

Jefferies, M.G. 1993. Nor-Sand: a simple critical state model for sand. *Géotechnique*. 43(1), pp. 91-103.

Jefferies, M.G. & Shuttle, D.A. 2002. Dilatancy in general Cambridge-type models. *Géotechnique*. 52(9), pp. 625-638.

Jefferies, M.G. & Shuttle, D.A. 2005. NorSand: Features, calibration and use. *Geotechnical Special Publication.* (128), pp. 204-236.

Jordaan, G.J. 1984. *Bituminous pavement rehabilitation design*. Masters dissertation. University of Pretoria.

Juspi, S. 2007. *Experimental validation of shakedown concept for pavement analysis and design.* PhD Thesis. University of Nottingham.

Kannemeyer, L., Perrie, B.D., Strauss, P.J. & Du Plessis, L. 2007. Ultra-Thin Continuously Reinforced Concrete Pavement research in South Africa. In: *Proceedings of the International Conference on Concrete Roads, 16-17 August 2007.* Midrand, South Africa: Cement & Concrete Institute. pp. 97-124.

Kearsley, E.P. & Mostert, H.F. 2010. Enabling the effective use of high performance fibre reinforced concrete in infrastructure. In: van Zijl & Boshoff (eds) *Advances in Cement-Based Materials.* London, United Kingdom: CRC Press. pp. 53-58.

Kearsley, E.P., Vd Steyn, W.J. vdM. & Jacobsz, S.W. 2014. Centrifuge modelling of Ultra Thin Continuously Reinforced Concrete Pavements (UTCRCP). In: Gaudin & White (eds.) *Physical Modelling in Geotechnics; Proceedings of the 8th International Conference, 14-17 January 2014.* Perth, Australia: Taylor & Francis. pp. 1101–1106.

Khazanovich, L., Yu, H.T., Rao, S., Galasova, K., Shats, E. & Jones, R. 2000. *User's Guide; ISLAB2000 - Finite Element Analysis Program for Rigid and Composite Pavements.* Urbana Champaign, Ill: ERES Consultants.

Kim, I.T. & Tutumluer, E. 2005. Unbound Aggregate Rutting Models for Stress Rotations and Effects of Moving Wheel Loads. Journal of the Transportation Research Record. 1913, pp. 41-49.

Kim, M. 2007. *Three-dimensional finite element analysis of flexible pavements considering nonlinear pavement foundation behaviour*. PhD Thesis. University of Illinois at Urbana-Champaign.

Kim, M., Tutumluer, E. & Kwon, J. 2009. Nonlinear Pavement Foundation Modeling for Three-Dimensional Finite-Element Analysis of Flexible Pavements. *International Journal. Geomechanics.* 9(October), pp. 195-208.

Klar, A., Vorster, T.E.B., Soga, K. & Mair, R.J. 2005. Soil-pipe interaction due to tunnelling: Comparison between Winkler and elastic continuum solutions. *Géotechnique.* 55(6), pp. 461-466.

Knappett, J.A., Reid, C., Kinmond, S. & O'Reilly, K. 2011. Small-scale modeling of reinforced concrete structural elements for use in a geotechnical centrifuge. *Journal of Structural Engineering.* 137(11), pp. 1263-1271.

Laue, J. & Arnold, A. 2008. Physical modelling of soil-structure interaction of flexible raft foundations. In: *Proceedings of the BGA International Conference on Foundations, 24-27 June 2008.* Dundee, Scotland: IHS BRE Press.

Lee, M.K. & Barr, B.I.G. 2004. An overview of the fatigue behaviour of plain and fibre reinforced concrete. *Cement and Concrete Composites.* 26(2004), pp. 299-305.

Lekarp, F., Isacsson, U. & Dawson, A. 2000a. State of the Art. I: Resilient response of unbound aggregates. *Journal of Transportation Engineering.* (January/February), pp. 66–75.

Lekarp, F., Isacsson, U. & Dawson, A. 2000b. State of the Art. II: Permanent strain response of unbound aggregates. *Journal of Transportation Engineering.* (January/February), pp. 76-83.

Lemmen, H.E. 2015. *The Influence of Footing Stiffness on the Behaviour of Surface Strip Foundations on Sand.* Masters dissertation. University of Pretoria.

Lemmen, H.E., Jacobsz, S.W. & Kearsley, E.P. 2017. The influence of foundation stiffness on the behaviour of surface strip foundations on sand. *Journal of the South African Institute of Civil Engineering.* 59(2), pp. 19-27.

Levenberg, E. & Garg, N. 2014. Estimating the coefficient of at-rest earth pressure in granular pavement layers. *Transportation. Geotechnics*. 1(2014), pp. 21-30.

Li, Q., Xiao, D.X., Wang, K.C.P., Hall, K.D. & Qiu, Y. 2011. Mechanistic-empirical pavement design guide (MEPDG): a bird's-eye view. *Journal of Modern Transportation.* 19(2), pp. 114-133.

Losberg, A. 1960. *Structurally reinforced concrete pavements.* PhD Thesis. Chalmers Tekniska Hogskola.

Lukiantchuki, J., Oliveira, J.R.M.S., Pessin, J. & Almeida, M. 2018. Centrifuge modelling of traffic simulation on a construction waste layer. *International Journal of Physical Modelling in Geotechnics*. 18(6), pp. 290-300.

Lv, S., Xia, C., Liu, H., You, Li., Qu, F., Yang, Yi & Washko, S. 2019. *International Journal of Pavement Engineering*.

MacDonald, B.J. 2011. *Practical Stress Analysis with Finite Elements, 2nd ed.* Dublin, Ireland: Glasnevin Publishing.

Madabhushi, G. 2014. *Centrifuge modelling for Civil Engineers.* London, United Kingdom: Taylor & Francis.

Maina, J.W., Denneman, E. & De Beer, M. 2008. Introduction of new road pavement response modelling software by means of benchmarking. In: *Proceedings of the 27th Annual Southern African Transport Conference.* Pretoria, South Africa.

Maina, J.W. & Matsui, K. 2004. Developing software for elastic analysis of pavement structure responses to vertical and horizontal surface loadings. *Transportation Research Record 1896, TRB, National Research Council.* Washington, D.C. pp. 107-118.

Mayne, P.W. & Kulhawy, F.H. 1982. K_0-OCR relationships in soil. *Journal of the Geotechnical Engineering Division.* 108(June), pp. 851-869.

Montgomery, D.C. 2001. *Design and analysis of experiments, 5th ed.* New York, NY, USA: John Wiley & Sons.

Neville, A.M. & Brooks, J.J. 2010. *Concrete technology, 2nd ed.* Harlow, United Kingdom: Pearson.

O'Flaherty, C.A. 1967. *Highway Engineering Volume II, 2nd ed.* London, United Kingdom: Edward Arnold Ltd.

O'Reilly, M.P. & Brown, S.F. 1991. *Cyclic loading of Soils: from theory to design, 1st ed.* London, United Kingdom: Blackie & Son Ltd.

Owen, G. 2009. *Fulton's Concrete Technology, 9th ed.* Midrand, South Africa: Cement & Concrete Institute.

Pappin, J.W. 1979. *Characteristics of a granular material for pavement design.* PhD Thesis. University of Nottingham.

Pereira, D.D.S., Balbo, J.T. & Khazanovich, L. 2006. Theoretical and field evaluation of interaction between ultra-thin whitetopping and existing asphalt pavement. *International Jounral of Pavement Engineering.* 7(4), pp. 251-260.

Powrie, W. 2004. *Soil mechanics: concepts and applications, 2nd ed.* London, United Kingdom: Spon Press.

Roscoe, K.H. & Burland, J.B. 1968. On the generalised stress-strain behaviour of 'Wet' clay. In: Heyman & Leckie (eds) *Engineering plasticity*. Cambridge, United Kingdom: Cambridge University Press. pp. 535-609.

Roesler, J.R., Cervantes, V.G. & Amirkhanian, A.N. 2012. Accelerated performance testing of concrete pavement with short slabs. *International Journal of Pavement Engineering.* 13(6), pp. 494-507.

Saad, B., Mitri, H. & Poorooshasb, H. 2005. Three-dimensional dynamic analysis of flexible conventional pavement foundation. *Journal of Transportation Engineering.* 131(6), pp. 460-469.

Saad, B., Mitri, H. & Poorooshasb, H. 2006. 3D FE analysis of flexible pavement with geosynthetic reinforcement. *Journal of Transportation Engineering.* 132(5), pp. 402-415.

SABITA. 1993. *GEMS - The design and use of granular emulsion mixes.* Cape Town, South Africa: South African Bitumen and Tar Association.

Saboya, F., Tibana, S., Reis, R.M., Farfan, A.D. & de Assis Melo, C.M. 2020. Centrifuge and numerical modeling of moving traffic surface loads on pipeline buried in cohesionless soil. *Transportation Geotechnics.* 23(2020), pp. 1-11.

SANRAL. 2013. Pavement Design. In: *South African Pavement Engineering Manual.* South Africa: SANRAL Ltd.

SANRAL. 2014. Road Prism and Pavement Investigations. In: *South African Pavement Engineering Manual.* South Africa: SANRAL Ltd.

Schofield, A.N. & Wroth, C.P. 1968. *Critical state soil mechanics*. London: McGraw-Hill.

Smit, M.S. 2015. *The effect of mixture proportions on the properties of high strength concrete pavements.* Masters dissertation. University of Pretoria.

Smit, M.S., Kearsley, E.P. & Jacobsz, S.W. 2018a. Scaled physical modelling of ultra-thin continuously reinforced concrete pavement. In: McNamara *et al* (eds) *Physical Modelling in Geotechnics; Proceedings of the 9th International Conference, 17-20 July 2018*. London, United Kingdom: Taylor & Francis Group. pp. 179-184.

Smit, M.S., Kearsley, E.P. & Jacobsz, S.W. 2018b. The effect of relative stiffness on soil-structure interaction under vehicle loads. In: McNamara *et al* (eds) *Physical Modelling in Geotechnics; Proceedings of the 9th International Conference, 17-20 July 2018*. London, United Kingdom: Taylor & Francis Group. pp. 185-190.

Stat-Ease Corporation. 2019. *Design Expert 11 Software for Design of Experiments.* Minneapolis, MN, USA.

Strauss, P.J. 2018. Personal communication. Pretoria, South Africa.

Strauss, P.J., Slavik, M., Kannemeyer, L. & Perrie, B.D. 2007. Updating cncPave: Inclusion of Ultra-Thin Continuously Reinforced Concrete Pavement (UTCRCP) in the mechanistic, empirical and risk based concrete pavement design method. In: *Proceedings of the International Conference on Concrete Roads, 16-17 August 2007.* Midrand, South Africa: Cement & Concrete Institute. pp. 204-218.

Sweere, G.T.H. 1990. *Unbound granular basis for roads.* PhD Thesis. University of Delft.

Su Jung, Y., Zollinger, D.G. & Wimsatt, A.J. 1993. Test Method and Model Development of Subbase Erosion for Concrete Pavement Design. *Journal of the Transportation Research Record*. 2154, pp. 22-31.

The Mathworks Inc. 2017. *MATLAB version 9.2 (R2017a)*. Natick, Massachusetts.

Theyse, H.L., De Beer, M. & Rust, F.R. 1996. Overview of South African Mechanistic Pavement Design Method. *Transportation Reseach Record.* 1539, pp. 6-17.

Ugural, A.C. & Fenster, S.K. 2012. *Advanced Mechanics of Materials and Applied Elasticity, 5th ed.* Westford, MA, USA: Pearson Education.

Ulditz, P. 1987. *Pavement analysis.* New York, USA: Elsevier.

Uzan, J. 1985. Characterization of granular materials. *Transportation Reseach Record.* 1022, pp. 52-59.

Van Aswegen, E. 2013. *Effect of density and moisture content on the resilient response of unbound granular material.* PhD Thesis. University of Pretoria.

Van de Ven, M.F.C. & De Fortier Smit, A. 2000. The role of the MMLS devices in APT. In: *Proceedings of the 19th Annual Southern African Transport Conference, 17-20 July 2000.* Pretoria, South Africa.

Vining, G. 2011. Technical advice: Residual plots to check assumptions. *Quality Engineering.* 23(1), pp. 105-110.

Vishwakarma, R.J. & Ingle, R.K. 2017. Simplified approach for the evaluation of critical stresses in concrete pavement. *Structural Engineering and Mechanics*. 61(3), pp. 389-396.

Vishwakarma, R.J. & Ingle, R.K. 2018. Effect of Panel Size and Radius of Relative Stiffness on Critical Stresses in Concrete Pavement. *Arabian Journal for Science and Engineering*. 43(10), pp. 5677-5687.

Visser, A. 2017. Potential of South African road technology for application in China. *Journal of Traffic and Transportation Engineering (English Ed)*. 4(2), pp. 113-117.

Vorster, T.E.B., Klar, A., Soga, K. & Mair, R.J. 2005. Estimating the Effects of Tunneling on Existing Pipelines. *Journal of Geotechnical and Geoenvironmental Engineering*. 131(November), pp. 1399-1410.

Werkmeister, S., Dawson, A.R. & Wellner, F. 2004. Pavement Design Model for Unbound Granular Materials. *Journal of Transportation Engineering*. 130(5), pp. 665-674.

Westergaard, H.M. 1926. Stresses in concrete pavements computed by theoretic analysis. *Public Roads*. 7(2), pp. 25-35.

White, D.J., Take, W. A. & Bolton, M.D. 2003. Soil deformation measurement using particle image velocimetry (PIV) and photogrammetry. *Géotechnique*. 53(7), pp. 619-631.

Xie, J., Tang, L., Lv, S., Zhang, N., Huang, T. & Liu, H. 2018. Standardization of Fatigue Characteristics of Cement-Treated Aggregate Base Materials under Different Stress States. *Applied Sciences*. 8, pp. 1-23

Zaghloul, S. & White, T. 1993. Use of a Three-Dimensional, Dynamic Finite Element Program for Analysis of Flexible Pavement. *Transportation Reseach Record.* 1388, pp. 60-69.

APPENDIX A – EFFECT OF POISSON'S RATIO AND BOUND LAYER-SUBSTRUCTURE INTERACTION ON PAVEMENT RESPONSE

Effect of Poisson's Ratio on pavement response

Poisson's Ratio is a dimensionless material property of the lateral strain over the longitudinal strain. Concrete has a low Poisson's Ratio, which indicates that if a concrete cylinder is compressed in the axial direction, the radial (or lateral) strain will be relatively small. If the concrete cylinder is confined in the radial direction, it would experience less stress than if it was a material with a higher Poisson's Ratio, such as asphalt or unbound granular materials.

The Poisson's Ratio of the base layer was varied to investigate the pavement response sensitivity. The concrete bound layer FE model in Section 3.2.3 was used. The total depth of the model was 21.336 m. The bound layer thickness and base thickness were 76 mm and 305 mm respectively. The properties of the bound layer, base and subgrade can be viewed in Table 3.3. The critical parameters used in Chapter 3 were used to measure the sensitivity. These were the maximum vertical deflection under the wheel, tensile stress at the bottom of the bound layer and compressive stress and strain at the top of the subgrade.

The Poisson's Ratios used were 0.1, 0.25, 0.4 and 0.495. The Poisson's Ratio of soils and granular material ranges between 0.2 – 0.5 (Bowles, 1996). The original model by Kim (2007) and the models in Chapter 3 used a value of 0.4 for the base. The maximum Poisson's Ratio that can be used in ABAQUS/Standard (Dassault Systemes Simulia Corp, 2016) is 0.495.

In Table A.1 the critical parameters increased as the Poisson's Ratio increased. The percentage difference between the realistic Poisson's Ratio's (0.25 and 0.495) and the model value 0.4 varied between 0.5% and 2%, indicating that the response of the LE FE road pavement model reported is not significantly sensitive to a change in Poisson's Ratio. It should be noted that if the base layer was thicker (> 305 mm) its influence would be more significant.

Table A.1 Critical parameters of models with varying Poisson's Ratios

Poisson's Ratio	Critical parameter			
	$\delta_{v\ surface}$ (mm)	$\sigma_{h\ bottom\ of\ BL}$ (kPa)	$\sigma_{v\ top\ of\ subgrade}$ (kPa)	$\varepsilon_{v\ top\ of\ subgrade}$ (μm/m)
0.1	-0.674	4416	-21.8	-465
0.25	-0.685	4540	-22	-464
0.4	-0.692	4637	-22.3	-466
0.495	-0.695	4682	-22.7	-473

Effect of bound layer-substructure interaction on pavement response

Although including interaction between layers would be more realistic, it is computationally expensive. As suggested by Kim (2007), quadratic elements were used in Chapter 3. To reduce the computational time required to investigate the effect of interaction it was decided to use linear elements for the subgrade, as it is very deep, and a large section of the subgrade would only be affected minimally by the applied load.

Mechanical interaction properties were assigned for the bound layer – base interaction. Normal and tangential properties were used. The normal behaviour selected was "hard" contact, which minimizes the penetration of the slave surface into the master surface at the constraint locations and prevents transfer of tensile stress across the interface. The normal behaviour also allowed separation after contact. The tangential behaviour had a penalty friction formulation and was isotropic. A coefficient of friction can be assigned (Dassault Systemes Simulia Corp, 2014).

The effect of using linear elements, instead of quadratic elements, in the subgrade was examined for a coefficient of friction of 0.1, as a low value would be more detrimental to the critical parameters. The values in Table A.2 indicate that the effect of element type on the critical parameters was minimal.

Table A.2 Effect of linear and quadratic elements in subgrade on critical parameters

Element type	Critical parameter			
	$\delta_{v\ surface}$ (mm)	$\sigma_{h\ bottom\ of\ BL}$ (kPa)	$\sigma_{v\ top\ of\ subgrade}$ (kPa)	$\varepsilon_{v\ top\ of\ subgrade}$ (μm/m)
Linear	-0.777	5269	-29	-518
Quadratic	-0.776	5268	-29.2	-521

"Hard" contact is the simplest "Pressure-Overclosure" behaviour. The normal behaviour of the interaction property was not varied. The coefficient of friction (μ) of the tangential behaviour was varied. Typical values for the coefficient of friction for concrete cast on soil varies between 0.3 and 0.7 (Department of the Navy, 1982). The values considered were 0.1, 0.35, 0.7 and 0.9. The interaction was also modelled as frictionless. The value of 0.35 was the lower end of friction coefficients of concrete on clean fine sand, while 0.6 was the upper end of concrete on clean gravel or coarse sand. The values 0.1 and 0.9 were included to inspect the effect of friction coefficient over a wider range.

The critical parameters in Table A.3 shows the effect of including interaction the pavement model response. Allowing the concrete bound layer to move tangentially and detach vertically

from the base, resulted in increased critical parameters. This was expected because the concrete bound layer could now slide on, as well as detach from the substructure. It no longer had the stiffness of a perfectly bonded composite system. The stress and strain experienced during loading would be more localized around the load location as the concrete layer can detach from the substructure push into it in this area.

Allowing the bound layer to detach from the substructure had a more noticeable effect than varying the friction coefficient. From frictionless tangential behaviour to a friction coefficient of 0.9 the critical parameters did not decrease significantly.

Table A.3 Effect of variation of friction on critical parameters

Interaction	Critical parameter			
	$\delta_{v\ surface}$ (mm)	$\sigma_{h\ bottom\ of\ BL}$ (kPa)	$\sigma_{v\ top\ of\ subgrade}$ (kPa)	$\varepsilon_{v\ top\ of\ subgrade}$ (μm/m)
No interaction	-0.692	4637	-22.3	-466
Frictionless	-0.778	5276	-29.1	-520
μ = 0.1	-0.777	5269	-29	-519
μ = 0.35	-0.777	5251	-28.9	-517
μ = 0.6	-0.774	5235	-28.7	-514

APPENDIX B – DETERMINATION OF MODULUS OF SUBGRADE REACTION

Finite element model configuration

The modulus of subgrade reaction was determined by simulating a plate load test as described in ASTM Standard D1195 – 93 (ASTM Committee D04, 1997). The geometry of the single wheel model described in Chapter 3, without the bound layer, was used. The model used quarter symmetry and the load was applied through the quarter of a circular plate with a diameter of 762 mm. The plate was rigid. A pressure was applied to the plate. The setup is illustrated in Figure B.1.

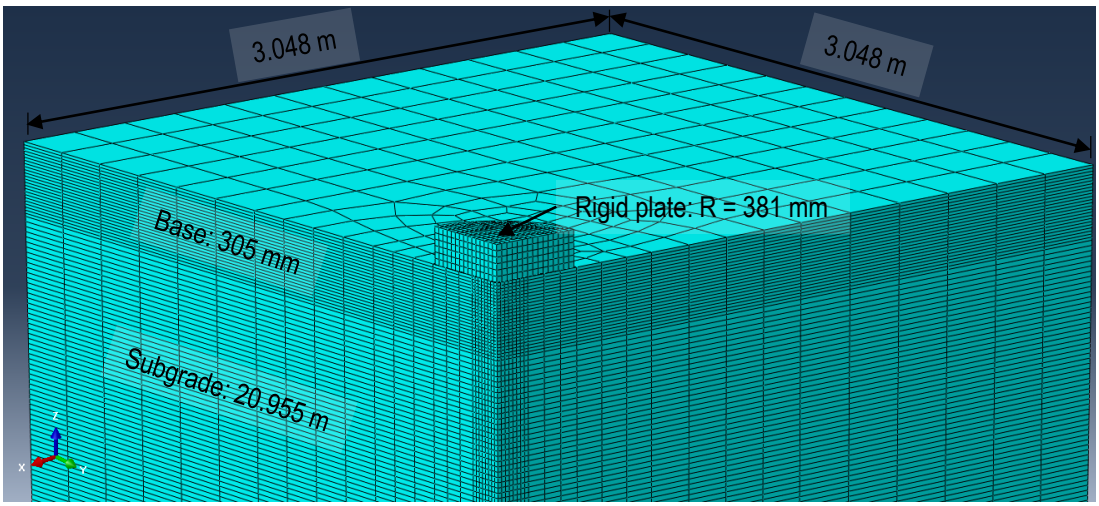

Figure B.1 FE model of plate load setup

The deflection was measured as the displacement of the node at the surface of the substructure in the centreline of the model and plate. The modulus of subgrade reaction was determined for various substructure stiffnesses, where the base material stiffness was varied, while the subgrade materials stiffness remained constant. The base material stiffness remained constant in Chapter 3 and was varied Chapter 4.

Modulus of subgrade reaction

Figure B.2 shows the load-deflection of the various substructure stiffnesses. The deflection was linear. The calculated modulus of subgrade reaction can be viewed in Table B.1. All the values, except those of high base material stiffnesses, were comparable with those given in Bowles (1996) for typical values for different soil types.

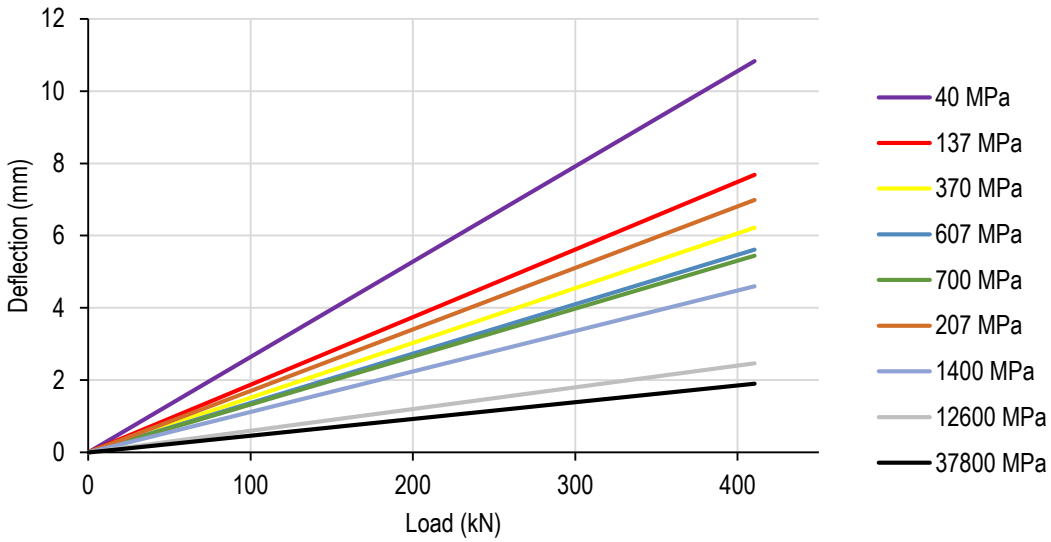

Figure B.2 Load-deflection of substructure stiffnesses

Table B.1 Modulus of subgrade reaction of substructure stiffnesses

Modelling	Base material stiffness (MPa)	Modulus of subgrade reaction (N/mm^3)
Replica	207	0.129
Multivariable analysis	40	0.083
	137	0.117
	370	0.145
	607	0.160
	700	0.165
High base material stiffnesses	1400	0.196
	12600	0.365
	37800	0.473

APPENDIX C – MODEL EQUATIONS AND ANOVA OF MULTIVARIABLE ANALYSES

Table C.1 Model equations and ANOVA of models derived for critical parameters

$\delta_{v\ surface}$(mm)				$\sigma_{h\ bottom\ of\ BL}$ (kPa)			
Factors	Coded	Actual	p-value		Coded	Actual	p-value
Response	$\delta_{v\ surface}^{-0.71}$	$\delta_{v\ surface}^{-0.71}$	N/A	Response	$\sigma_{h\ bottom\ BL}^{-0.99}$	$\sigma_{h\ bottom\ BL}^{-0.99}$	N/A
constant	1.955	0.6382	N/A	constant	8.35E-04	4.31E-05	N/A
A	0.494	7.43E-03	<<	A	7.46E-04	6.24E-07	<<
B	0.070	8.04E-04	<<	B	6.42E-05	3.01E-07	<<
AB	-0.046	-1.78E-06	<<	AB	8.39E-06	3.22E-10	0.0516
A^2	-0.079	-6.28E-06	<<	A^2	1.97E-04	1.57E-08	<<
B^2	-0.012	-2.28E-07	0.0014	B^2	-6.31E-06	-1.16E-10	0.0526
Lack of fit (Sum of squares)		0.0003		Lack of fit (Sum of squares)		3.59E-10	
R^2		0.999		R^2		0.9990	
Model p-value		<<		Model p-value		<<	
Adequacy of precision		321		Adequacy of precision		433	

$\sigma_{v\ top\ of\ subgrade}$ (kPa)				$\varepsilon_{v\ top\ of\ subgrade}$ (μm/m)			
Factors	Coded	Actual	p-value	Factors	Coded	Actual	p-value
Response	$\sigma_{v\ top\ subgrade}^{-0.22}$	$\sigma_{v\ top\ subgrade}^{-0.22}$	N/A	Response	$\varepsilon_{v\ top\ subgrade}^{-0.22}$	$\varepsilon_{v\ top\ subgrade}^{-0.22}$	N/A
constant	0.656	0.371	N/A	constant	0.350	0.180	N/A
A	0.116	1.77E-03	<<	A	0.075	9.94E-04	<<
B	8.19E-03	8.00E-05	0.0009	B	4.51E-03	5.15E-05	<<
AB	-8.51E-03	-3.26E-07	0.0048	AB	-5.08E-03	-1.95E-07	<<
A^2	-2.05E-02	-1.63E-06	<<	A^2	-8.31E-03	-6.63E-07	<<
B^2	1.21E-03	2.23E-08	0.4715	B^2	3.23E-04	5.95E-09	0.3404
Lack of fit (Sum of squares)		1.23E-04		Lack of fit (Sum of squares)		4.88E-06	
R^2		0.999		R^2		0.999	
Model p-value		<<		Model p-value		<<	
Adequacy of precision		115		Adequacy of precision		375	

APPENDIX D – VERTICAL DISPLACEMENT IN AXLE CENTRELINE VERSUS TIME FOR CENTRIFUGE WHEEL LOADING MODELS

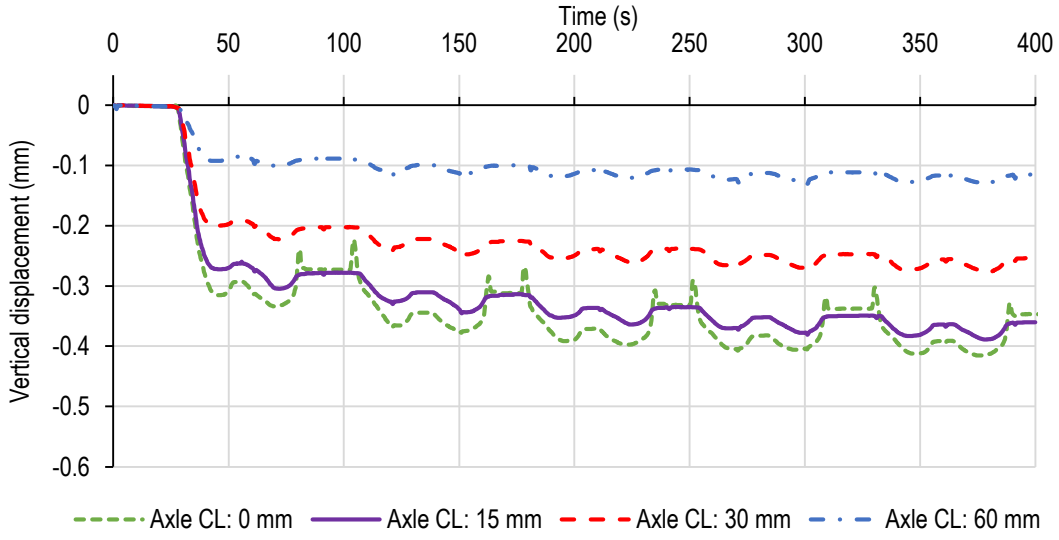

Figure D.1 Vertical displacement in axle CL versus time of thin concrete model

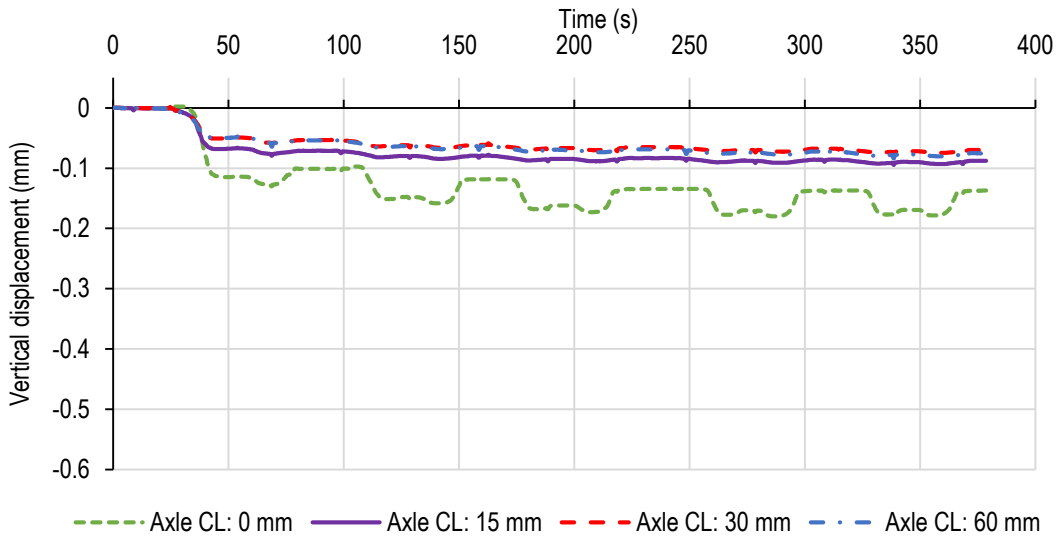

Figure D.2 Vertical displacement in axle CL versus time of thin concrete model with cemented base

APPENDIX E – NORMALIZED DEFLECTION BOWLS OF MODELS WITH NOR-SAND BASE MATERIAL BEHAVIOUR

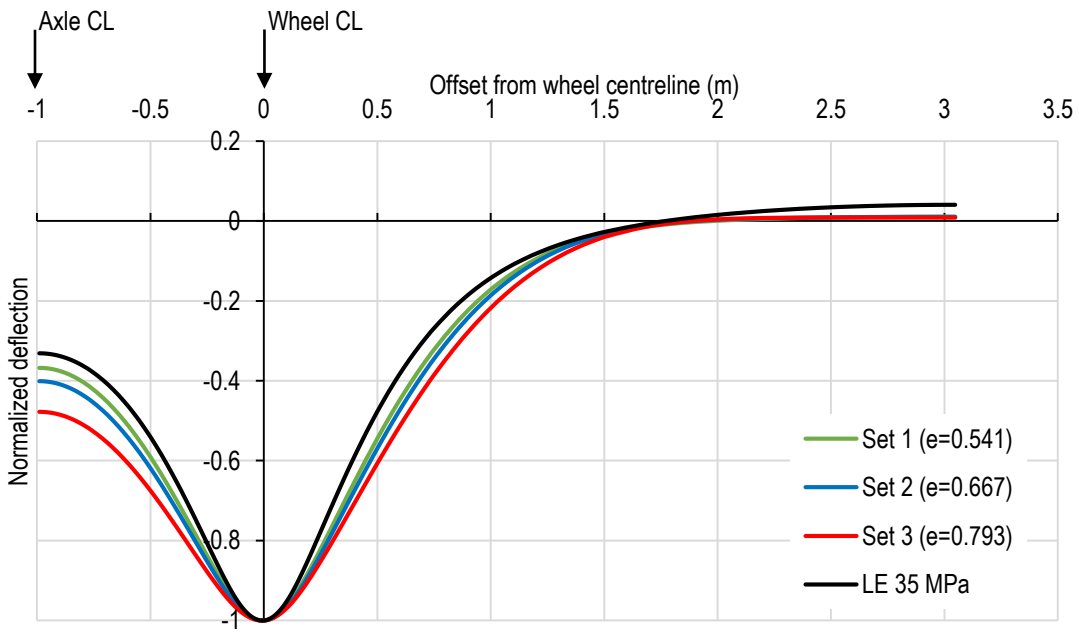

Figure E.1 Effect of void ratio on normalized deflection bowls

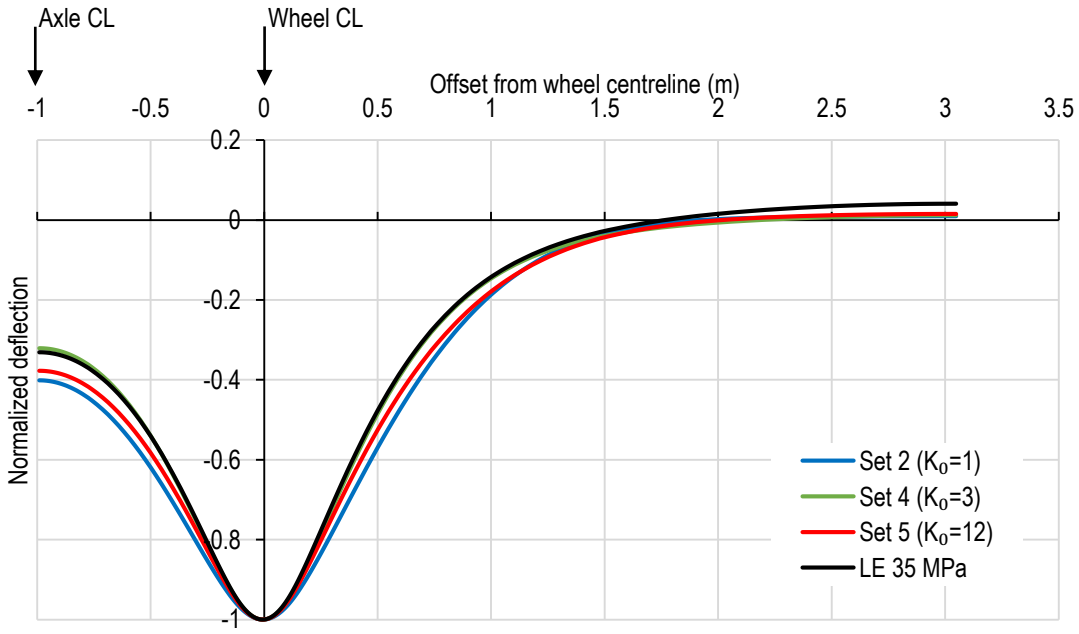

Figure E.2 Effect of K_0 on normalized deflection bowls

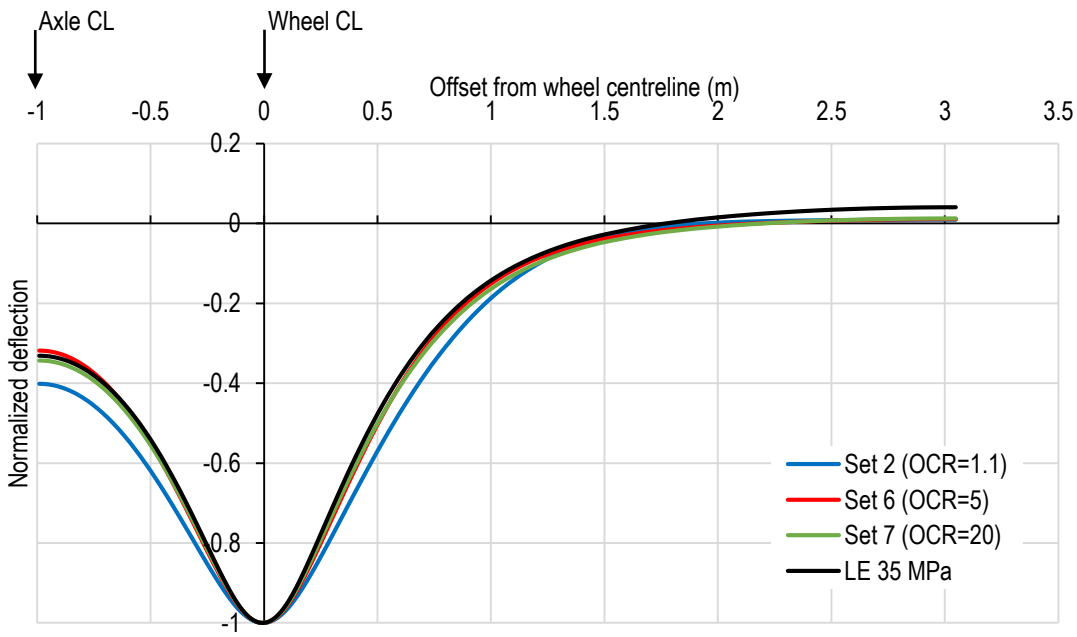

Figure E.3 Effect of OCR on normalized deflection bowls

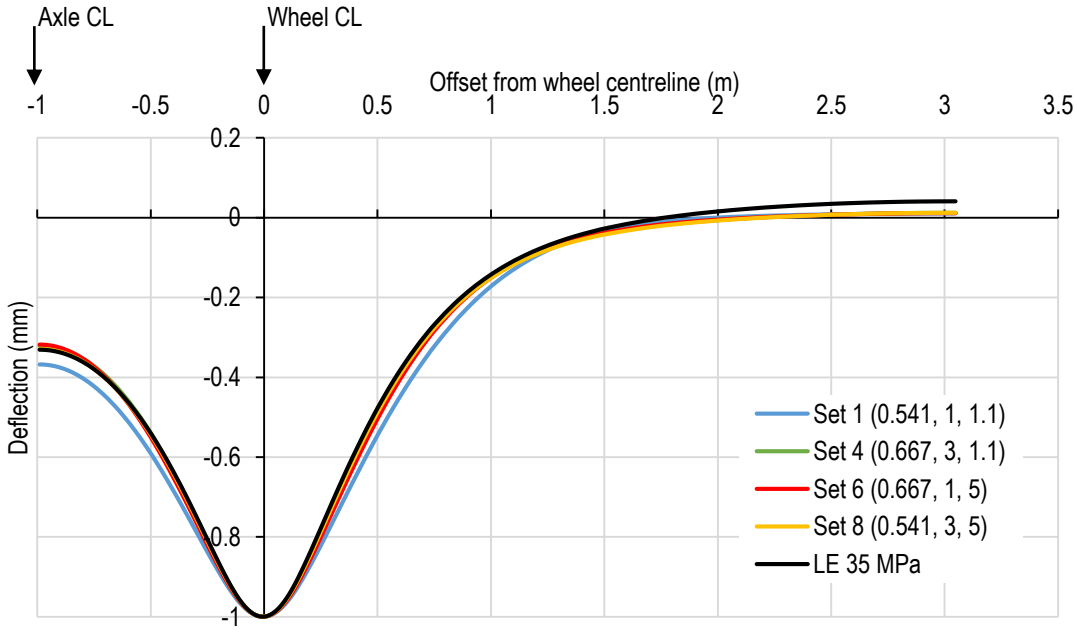

Figure E.4 Normalized deflection bowls of Set 1, Set 4, Set 6, Set 8 and LE 35 MPa

APPENDIX F – FULL DEPTH VERTICAL DISPLACEMENT DISTRIBUTIONS

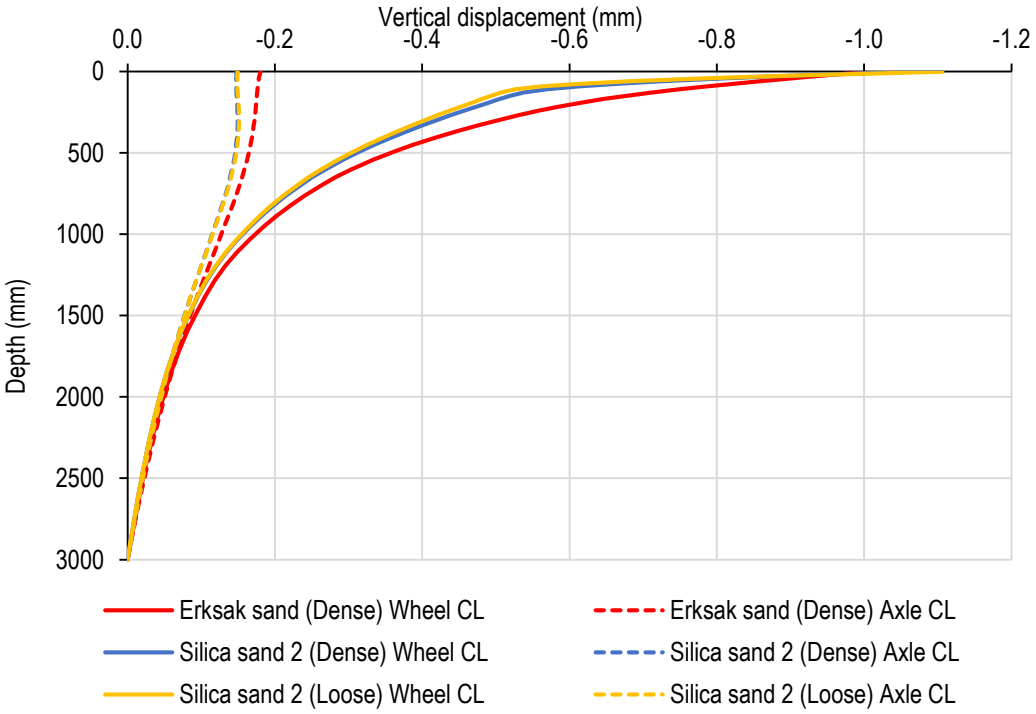

Figure F.1 Comparison of full depth vertical displacement distribution of Erksak sand and Silica sand 2

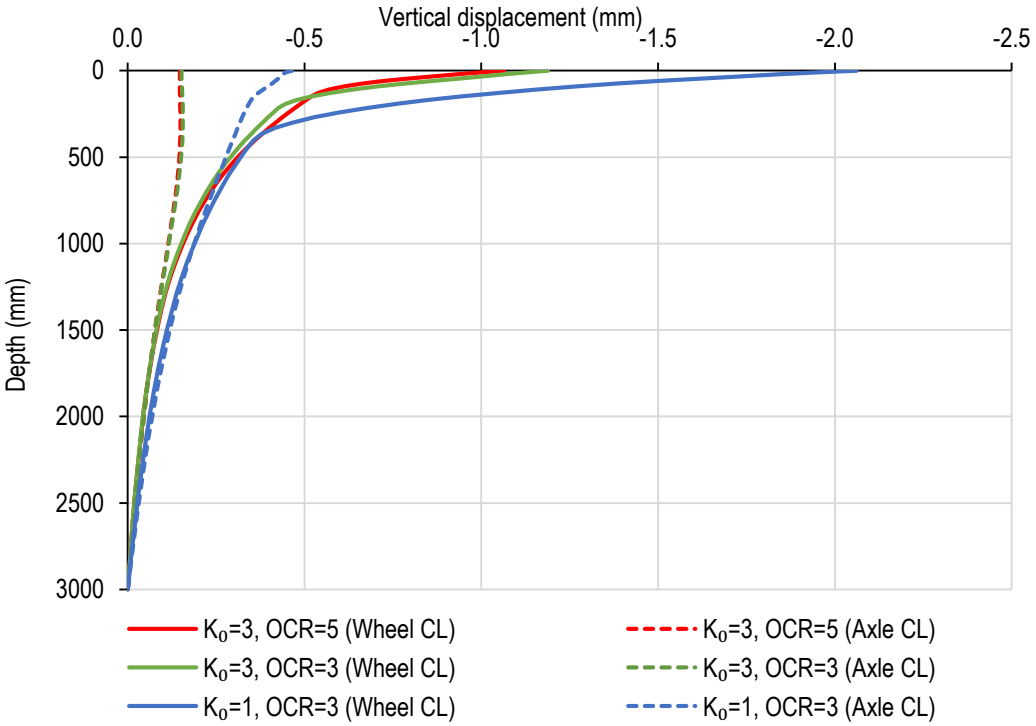

Figure F.2 Effect of model input parameters on full depth vertical displacement distributions